



## **RUNOUT**

**Major risk from rapid, large-volume landslides in Europe:  
The design and testing of new techniques  
for hazard assessment and mitigation.**

## **FINAL REPORT**



**RUNOUT Project Meeting, Gran Canaria, November 1998  
Photo: Alejandro Lomoschitz**

## **EUROPEAN COMMISSION**

***Programme Environment and Climate 1994-1998  
ENV4-CT97-0527***

**2000**

**Project RUNOUT, Final Report**  
**PL971219 Contract No. ENV4-CT97-0527**

**Major risk from rapid, large-volume landslides in Europe:  
the design and testing of new techniques for hazard assessment  
and mitigation**

**Contents**

<b>Executive summary</b>	i
<b>Part I. Modelling catastrophic giant landslides</b>	
1. Forecasting giant, catastrophic slope collapse	1
2. The flow of giant rock landslides	8
3. Modelling fragment interaction within sturzstroms	28
<b>Part II. Field sites: Giant, rapid landslides</b>	
4. The Vajont landslide, Italy	35
5. The K�fels sturzstrom, �tz valley, Austria	39
<b>Part III. Field sites: Giant, slow landslides</b>	
6. Monitoring and hazard analysis at the Tessina landslide, Italy	51
7. The long-term evolution of the Tessina landslide	89
8. Bad Goisern, Stambach Valley, Austria: The Zwerchwand rockfall/topple and Stambach mud slide	111
9. The Barranco de Tirajana Basin, Gran Canaria, Spain	123
<b>Part IV. Comparative studies</b>	
10. The stability of episodically reactivated landslides: Stambach, Austria, and Tessina, Italy	131
11. Surface Deformation Monitoring using rapid static GPS	141
12. Use of spaceborne remote sensing for monitoring giant landslides: Barranco de Tirajana, Gran Canaria, Spain, and Tessina, Italy	160
<b>Part V. Landslide hazard awareness and training</b>	
13. Raising public awareness on landslides in the Barranco de Tirajana, Gran Canaria, Spain	192
14. The development of multi-media training material for landslide hazard zonation: applications to Project RUNOUT	200

## **Executive summary**

*Programme Environment and Climate 1994-1998.  
PL971219. Contract Number ENV4-CT97-0527*

### **RUNOUT: Major risk from rapid, large-volume landslides in Europe: the design and testing of new techniques for hazard assessment and mitigation.**

*Goals. To develop a physical model for rapid, large-volume landslides, or sturzstroms; to quantify precursors to catastrophic slope failure and to establish baseline data for high-risk landslide areas, representative of the range of geological settings in Europe; to design strategies for optimizing networks monitoring large-volume slope movement; to prepare thematic databases and maps for assessing the hazards from large-volume landslides, to integrate these with a dedicated Geographical Information System (GIS), and to establish guidelines for raising public awareness of landslide hazards.*

#### **Summary**

The primary goals for Project RUNOUT were to develop and test physical models for the catastrophic collapse and runout of giant landslides, and to use these to improve strategies for mitigating the hazard from such mass movements. These goals have been achieved, together with the creation of databases for the improved monitoring of unstable slopes and methodologies for raising the awareness of landslide hazards among vulnerable populations. Field data were obtained from five test sites: the sturzstrom deposits from Köfels (Austria) and Vajont (Italy) and the recently-active, slower landslides at Tessina (Italy), the Barranco de Tirajana (BdT, Spain) and Bad Goisern (Austria). During the course of the project, movements at Tessina increased significantly, raising concern for the exposed communities of Funes and Lamosano. As a result, group resources were reassigned from the Bad Goisern landslide to the Tessina reactivation. In addition, teams originally assigned to redesigning the Tessina alert network were recruited for observing the new movements while leaving the existing alert system in place. Computer simulations of sturzstroms have been verified for 2D landslides (ignoring lateral spreading) and are currently being extended to the 3D case. The results have been integrated into GIS packages for separate test sites, and have provided the foundation for a GIS-based methodology for landslide-hazard training programmes.

Seven Partners collaborated in the project: (1) Cheltenham and Gloucester College of Higher Education (CGCHE), (2) Joint Research Centre (JRC), (3) University College London (UCL; coordinating institution), (4) University of Las Palmas, Gran Canaria (ULPGC), (5) University of Ferrara (UNIFE), (6) University of Vienna (UNIVIE), and (7) University of Portsmouth (UOP). The final project status is summarized in Table 1. Full reports follow in Chapters 1 to 14, contributors to which are identified in Table 2. Key results and deliverables are described below. Colour versions of the report, together with electronic versions of maps and GIS outputs are provided on the accompanying CD ROM.

#### **Project results**

*Modelling catastrophic, large-volume landslides (Chapters 2, 3, 5; work package 1)*

Applied to rapid large-volume slope movements, limits to dynamic regimes in granular flow have been quantified by scaling analysis and computer simulations. The essential features of sturzstrom emplacement can be explained if they lose kinetic energy through viscous deformation in one or more basal boundary layers. The boundary layers consist of rock fragments in a fine grained rock matrix. Crushed by the weight of overlying rock, the basal

matrix acts as a viscous fluid. Comparison with results from computer simulations yields constraints on programme algorithms. During collapse itself, basal resistance is small compared with the gravitational force driving movement, so that there is a nearly perfect conversion from potential to kinetic energy until the landslide runs out on a subhorizontal surface. The new analysis provides a physical justification for using the volume of unstable material to forecast the potential runout length of a sturzstrom.

*Precursors to giant landslides (Chapters 1, 4, 6-10, 12; work packages 2, 3)*

The transition from slow to rapid deformation has been analysed by comparing pre-failure conditions before (1) slow landsliding at the test sites Tessina, BdT and Bad Goisern, and (2) the catastrophic collapse of Mt Toc into the Vajont reservoir in 1963. Results from Project RUNOUT identify the transition with the onset of progressive, brittle failure within deep-seated instabilities. Brittle failure under gravity does not occur at shallow depths since the applied stresses are smaller than the peak resistances of continuous rock. Shallow landslides are thus associated (1) with the movement of loose material, such as soil, or of chemically weakened or previously fractured rock, and (2) with very small stress drops for which initial accelerations are too small to trigger catastrophic movements. The rapid accelerations required for catastrophic collapse can only be achieved by fracturing rock with a large difference between peak and residual strength. Such rock invariably has also a large peak strength, so that catastrophic collapse requires depths of failure large enough for the gravitational stress to overcome the peak strength and these, in turn, are associated with unstable volumes greater than a threshold value.

Progressive cracking in rock is readily catalysed by water. Deep-seated movements are thus favoured by elevated water pore pressures. Catastrophic failure is preceded by slow, but accelerating movements as small cracks develop and unite into the major plane of failure. A new slow-cracking model has been developed and tested against observed accelerations in slope movement before the 1963 collapse of Mt Toc. The model shows excellent agreement with field data and has strong potential as a general tool for forecasting catastrophic collapse.

Reactivations of slower movements at the test sites are also favoured by elevated pore pressures. Stability analyses and new geotechnical data have identified the conditions most-likely to initiate new slope movements at Tessina, BdT and Bad Goisern. These have been combined with databases on precipitation, land-use, slope, and water accumulation (1) to assess the reliability of piezometric measurements for forecasting imminent reactivation, (2) to identify appropriate hazard-mitigation methods, and (3) to prepare maps of local landslide hazard.

*Monitoring unstable slopes (Chapters 6, 7, 9, 11, 12; work package 4)*

The unstable test sites have been monitored by a combination of conventional EDM and direct-sight measurements, new GPS methods, and back analyses of earlier data for assessing the long-term evolution of each area.

GPS ground-deformation networks have been established around the BdT and Tessina landslides. The new networks augmented small-scale EDM networks already established at the sites and have provided information on (1) ground deformation in a wide area around each site, and (2) the application of GPS to a small semi-permanent dynamic network. Each network was re-occupied twice to assess annual and bi-annual displacements. The results revealed two very different deformation rates. While the BdT remained inactive during the course of Project RUNOUT, the Tessina valley has been very active with as much as 9 m of deformation around the collapse scar. Both networks have shown the utility of establishing large-area monitoring systems around slope instabilities and provide a baseline from which future deformation may be measured.

The GPS stations were also used to precisely locate natural reference points within and around zones of landsliding. By identifying the natural markers on archive aerial and satellite images, it has been possible to trace the long-term evolution of the instabilities and so identify long-term trends in slope behaviour that would not have been evident from measurements taken only during the lifetime of the project. At Tessina, in particular, the back analyses have enhanced computer simulations of future events for hazard analyses.

*Mitigating landslide risk (Chapters 6, 8, 12-14; work packages 5, 6)*

The risk from landslides can be reduced by (1) imposing land-management policies that minimize the value of vulnerable districts, (2) raising the awareness of vulnerable populations of the hazards to which they are exposed, and (3) establishing effective defense measures (*e.g.*, barriers or evacuation procedures) in times of emergency. The first two options have been addressed by Project RUNOUT.

GIS-based land-use maps have been prepared for the Tessina and BdT landslides. Combined with other thematic maps (see next section), these have revealed the dependence of landsliding on recent land-use practices and provide a framework for designing medium-term strategies, such as revegetation or changed agricultural or urban development, for reducing landslide risk. For the Tessina and BdT sites, the land-use maps have been combined with geological, geomorphological and groundwater data (see next section) to prepare landslide hazard maps.

Surveys within the BdT highlighted an uneven level of landslide awareness among communities at risk. A key reason explaining why some groups do not perceive landsliding as a major hazard is that almost 40 years have passed since the last serious landslide reactivation in the area (the 1956 movements of the Rosiana landslide). As a result, two generations have grown up without any experience of significant mass movements. An illustrated pamphlet (see CD ROM) for raising public awareness of landslide hazards has been specially designed for the BdT. This will be distributed by the local authorities. Similar pamphlets are being designed for communities exposed to the Tessina and Bad Goisern test areas.

The full RUNOUT datasets, model results and methodologies are being integrated into an existing training package "Geographic Information Systems for Slope Instability Zonation" (GISSIZ). The result will be a multimedia, GIS-compatible package for training personnel about landslide hazards and their mitigation.

*Base mapping and the development of thematic GIS maps (Chapters 4, 6-9, 12; work packages 2, 3)*

Base mapping has been fundamental to implementing the preceding analyses. New geomorphological maps have been prepared at scales between 1:5,000 and 1:50,000 of the Vajont, Tessina, BdT and Bad Goisern test sites; existing geomorphological maps were used for the Köfels test site. These have been supported with the preparation of digital elevation maps and thematic GIS maps covering (1) slope distribution, curvature, elevation and orientation, (2) zones of water accumulation, (3) land use, and (4) geology. Sample outputs are provided in the report that follows. Full imagery, including the base maps, can be found on the accompanying CD ROM.

### *Key deliverables*

The key deliverables are

- a dynamic model that quantifies the control of sturzstrom volume on runout distance.
- algorithms for the 2D simulation of sturzstroms as granular flows.
- simulations of the Köfels sturzstrom.
- cellular automata simulations of the Tessina landslide.
- a new slow-cracking model for forecasting the approach to catastrophic slope failure.
- stability analyses and geotechnical data for the Tessina, BdT and Bad Goisern landslides.
- evaluation of piezometric data as a tool for forecasting landslide reactivations.
- installation of GPS and EDM networks for monitoring the Tessina and BdT landslides.
- critical evaluation of GPS and EDM geodetic methodologies.
- new geomorphological maps of the Vajont, Tessina, BdT and Bad Goisern test sites.
- thematic GIS maps:
  - Tessina*: slope angle, landslide activity, landslide phases, material, proximity to gullies and reservoirs, land use, geology.
  - BdT*: slope angle, landslide activity, landslide phases, material, proximity to gullies and reservoirs, land use.
  - Bad Goisern*: slope angle, distribution, curvature and orientation, zones of water accumulation, lithology, neotectonics and distributions of soil, vegetation and precipitation.
  - Köfels*: slope angle, distribution, curvature and orientation, zones of water accumulation.
- landslide hazard maps for Tessina and BdT.
- guidelines for raising public awareness of landslide hazards.
- preliminary integration of project results into a GIS-based package to assist training in landslide hazards and their mitigation.

**Table 1.** Implementation of Tasks

<i>Task</i>	<i>Status</i>	<i>Comments</i>	<i>Chapter</i>
<b>WP1. Sturzstrom Modelling</b>			
1. Regime scaling	OK		2
2. Simulation	OK	Full 3D version to be verified	3
3. Field data	OK	Vajont & Kofels	4, 5
<b>WP2. Slow Slope Instabilities</b>			
1. Precursors to catastrophic landslides	OK		1
2. Precursors to slow landslides	OK		6, 8, 9
3. Maps: geology & geomorphology:			
Tessina	OK		6
Bad Goisern	OK		8
Barranco de Tirajana	OK		9
Vajont	OK		4
Köfels	OK		5
4. Lab. tests (geotechnical, geochemical, granulometry)			
Tessina	OK		10
Bad Goisern	OK		10
Barranco de Tirajana	OK		9
5. Geodetic network			
Tessina	OK		7, 11
Barranco de Tirajana	OK		9, 11
6. Stability analyses	OK		10
<b>WP3. Environmental &amp; Human Impact on Slopes</b>			
Databases and land-use maps			
Tessina	OK		12
Bad Goisern	OK		8
Barranco de Tirajana	OK		12
<b>WP 4. Monitoring Strategies</b>			
1. EDM/GPS evaluations			
Tessina	OK		11
Barranco de Tirajana	OK		11
2. Alert systems	Delay	Resources redirected for monitoring new movements at Tessina.	
<b>WP5. Risk Mitigation</b>			
1. GIS thematic maps	OK		7, 8, 11
2. Awareness guidelines	OK	Barranco de Tirajana; others delayed	13
3. Cellular automata	OK	Tessina only	7
<b>WP6 Integration of WP1-5</b>	Delay	Partial implementation	14

**Table 2.** Chapters, work packages and lead partners.

<i>Chapter</i>	<i>Work Package</i>	<i>Lead Partners</i>
1	2	UCL, UOP
2	1	UCL, UNIFE, UNIVIE
3	1	UCL
4	1	UNIFE, UCL
5	1	UNIVIE, UCL
6	2	UNIFE
7	2, 5	UNIFE, UCL
8	2, 3, 5	UNIVIE, UOP, UCL
9	2	ULPGC, CGCHE
10	2, 5	UOP
11	2, 4	CGCHE, ULPGC, UNIFE
12	3	JRC, ULPGC, UNIFE
13	5	UCL
14	6	All

### **Information exchange, project meetings and field campaigns**

Information was exchanged among partners via a dedicated mailing list (managed by SA Sorensen, UCL) and numerous informal meetings of subgroups focusing on a particular test area or landslide process. These exchanges were supported by four formal project meetings as tabulated below.

<i>Event</i>	<i>Host</i>	<i>Field Visits (and Guides)</i>
March 1998 Meeting	JRC, Ispra, Italy	Vaiont, Tessina (UNIFE)
Summer 1998 Field Meeting	UNIVIE, Austria	Köfels, Bad Goisern (UNIVIE)
October 1998 Meeting	ULPGC, Gran Canaria, Spain	Baranco de Tirajana (ULPGC)
April 1999 Meeting	EGS 24th General Assembly	

### **Dissemination of results**

All partners contributed to the international meetings (a) Disaster Management and Information Technology, organised by S.A. Sørensen (UCL) and held at University College London in 1998, and (b) the 24th General Assembly of the European Geophysical Society (EGS), held at the Hague in 1999 and for which Cees van Westen (UCL) was a session convenor (Session NH2-02). Presentations published in the abstracts of the EGS meeting are given below; selected papers will appear as a thematic RUNOUT section in the International Journal of Applied Earth Observation and Geoinformation. A. Pasuto (UNIFE) has arranged for papers derived from this final report to form a special RUNOUT volume of the journal *Geomorphology*. Further RUNOUT presentations are scheduled for the 25th General Assembly of the EGS in Nice in 2000.

### **RUNOUT presentations at EGS 1999**

Avolio MV, Di Gregorio S, Mantovani F, Pasuto A, Rongo R, Silvano S, Spataro W (1999)

Cellular automata simulations for analysing the landslide risk for the Tessina area.

Hervás J, Barredo JJ, Lomoschitz A (1999) Use of Landsat TM imagery for investigation of

landslide hazard from human activities in the Barranco de Tirajana area, Gran Canaria Island.

Ho-Chee N, Sørensen SA (1999) On the dynamics of massive landslides.

- Mantovani F, Pasuto A, Silvano S (1999) Data collection aiming at the definition of future hazard scenarios of the Tessina landslide.
- Moss JL Using the Global Positioning System to monitor dynamic ground deformation networks on active landslides.
- Quintana A, Corominas J, Lomoschitz A (1999) Geological and geomorphological features of the Barranco de Tirajana Basin, Gran Canaria, as a natural depression with large landslides.
- Santana F, Martín J, Linares R, de Andrés, Lomoschitz A (1999) Surveying and geophysical methods applied to control the Rosiana landslide, Gran Canaria.
- Zanin A, Kilburn CRJ, Corominas J, Mantovani F (1999) Forecasting the runout length of landslides.

### **Other conference presentations**

- Avolio MV, Di Gregorio S, Rongo R, Sorriso-Valvo M, Spataro W (1998) Hexagonal cellular automata model for debris flow simulation. Proc IAMG'98, 183-188.
- Avolio MV, Di Gregorio S, Mantovani F, Pasuto A, Rongo R, Silvano S, Spataro W (1999) Hexagonal cellular automaton simulation of the 1992 Tessina landslide. Proc IAMG'99, 291-296.
- Barredo JI, Hervás J, Lomoschitz A, Benavides A, Van Westen CJ (1999). Landslide hazard assessment using GIS and multicriteria evaluation techniques in the Tirajana basin, Gran Canaria Island. Proc. 5<sup>th</sup> EC GIS Workshop, 1999. European Commission.
- Crisci GM, Di Gregorio S, Nicoletta FP, Rongo R, Spataro W (1998) Cellular automata approaches for simulating rheology of complex geological phenomena. ACRI'98 Proc 3rd Conf Cellular Automata Research Industry, 106-116.
- Kilburn CRJ (1999) The dynamics of sturzstroms. Anniversary Meeting for 70th Birthday of Ken Hsü, Beijing, China.
- Pasuto A, Silvano S (1999) Alert systems as a tool for landslide risk mitigation. Japan-Italy Conference, Tokyo-Kagoshima 1-4 Nov 1999.

### **Publications**

- Kilburn CRJ, Sørensen SA (1998) Runout lengths of sturzstroms: the control of initial conditions and of fragment dynamics. J Geophys Res, 103: 17,877-17,884.
- Lomoschitz A (1999) Old and recent landslides of the Barranco de Tirajana basin, Gran Canaria, Spain. In, Griffiths S, Stokes MR, Thomas RG (eds) Landslides. Proc 9th Int Conf Field Trip Landslides, Bristol UK, 5-16 Sept 1999, 89-95. Balkema, Rotterdam.
- Lomoschitz A (1999) La depresión del barranco de Tirajana, Gran Canaria. Cabildo de Gran Canaria, pp 199.
- Solana MC (2000) Los deslizamientos de ladera del Barranco de Tirajana (Landslide-hazard preparedness, Gran Canaria). Ayuntamientos de Santa Lucia y San Bartolomé, Gran Canaria.

### **Related publications**

*Application of slow-cracking model.*

- Kilburn CRJ, Voight B (1998) Slow rock fracture as eruption precursor at Soufriere Hills volcano, Montserrat. Geophys Res Letters, 25: 3665-3668.

**Media citations**

Articles on RUNOUT-related topics have appeared in regional and national newspapers, including *Canarias7* (Canary Islands) and *The Guardian* (UK).

**Future dissemination**

The final results of Project RUNOUT will appear on a newly-designed website at UCL (replacing the existing site at [www.ucl.ac.uk/geolsci/runout](http://www.ucl.ac.uk/geolsci/runout)). Proposals are also being considered for an international meeting in London in late 2001 or early 2002.

# 1. Forecasting giant, catastrophic slope collapse

## Abstract

Sturzstroms are giant landslides of shattered rock that can travel kilometres within minutes ( $\sim 10\text{-}30\text{ m s}^{-1}$ ). They are catastrophic events which follow the sudden collapse of unstable volumes of  $\sim 10^6\text{-}10^7\text{ m}^3$  or more. About 30 sturzstroms have been recorded across the world during the last 150 years, although the actual number of such events is probably much greater. The large size and speed of sturzstroms renders them unstoppable by current defensive techniques, so that evacuation remains the only viable procedure for protecting vulnerable communities. Evacuation alerts, in turn, require a reliable method for forecasting imminent slope failure. Giant, catastrophic collapse is here related to rock fracturing, a mechanism which not only explains the minimum volumes observed for sturzstroms, but also provides a method for forecasting the approach to wholesale slope failure.

## Conditions of slope collapse

Sturzstroms occur in all regions of high relief, from young mountain chains to recent volcanoes, and involve volumes from  $\sim 10^6\text{-}10^7\text{ m}^3$  to  $\sim 10\text{-}100\text{ km}^3$ . The mechanism driving collapse must thus operate independently from local geology and also be effective over volumes of deformation that vary by several orders of magnitude. Although some recorded events (Hadley 1978, McSaveney 1978, Plafker and Ericksen 1978) have clearly been triggered by large earthquakes (magnitudes greater than 6.5-7.0), most appear to have been the result of extended periods, from weeks to decades, of progressively accelerating creep (Voight 1978).

Slope collapse occurs when the gravitational stress  $\tau_g$  driving movement exceeds slope resistance, given by the Navier-Coulomb criterion as (Hoek & Bray 1997)

$$\tau_g = \tau_c + \mu \sigma' \quad (1)$$

where, along the future plane of failure,  $\tau_c$  is material cohesion,  $\mu$  is the coefficient of sliding friction, and  $\sigma'$  is the effective normal stress, given by  $\sigma - U$ , the difference between actual normal pressure  $\sigma$  and fluid pore pressure  $U$ .

Failure depths are typically measured in hundreds of metres (Voight 1978), corresponding to applied loads of 1-10 MPa. By virtue of their deep-seated nature, planes of failure normally develop within compacted clay or stronger rock. Such rocks under loads of 1-10 MPa approach failure in three-stages (Fig. 1; Hallbauer et al. 1973, Petley 1998): an instantaneous elastic deformation for applied shear stresses smaller than a critical peak value  $\tau_p$ , followed by continued deformation at  $\tau_p$  until, beyond a critical strain, the shear resistance of the strained material rapidly decreases to a residual value  $\tau_r$ . Since the applied shear stress remains at  $\tau_p$ , the sudden drop in resisting stress to  $\tau_r$  yields a stress imbalance  $\tau_p - \tau_r$ , whose associated force imbalance triggers a rapid acceleration in slope movement.

Equating sudden slope collapse with the rapid drop in resisting stress, time-dependent precursors to collapse must depend on processes operating while the shear stress remains at the peak value for material resistance. Thus the failure condition in Eq. (1) can be expressed as (Fig. 1)

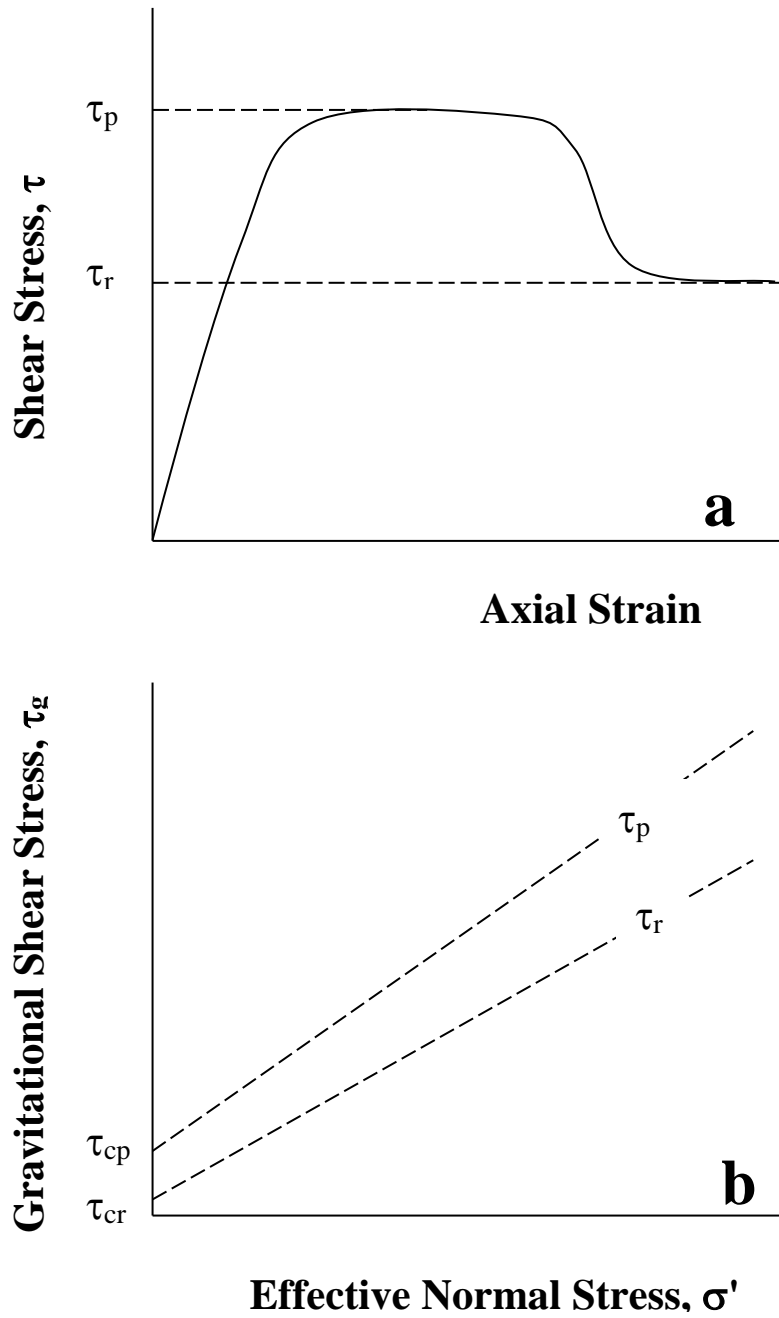


**Figure 1.** (a) Idealised deformation of rock under loads of 1-10 MPa. The rock initially deforms elastically for applied stresses smaller than  $\tau_p$ . It continues to deform at  $\tau_p$  as microcracks nucleate and grow. When the cracks link to form a major failure plane, the shear resistance of the rock rapidly decreases to  $\tau_r$ , the stress at which final collapse takes place. Conventional stress-strain diagrams plot deviatoric stress in place of shear stress, but the deformation curves remain qualitatively similar in both cases. (b) Navier-Coulomb failure envelopes for rocks with peak and residual shear resistance. At any given  $\sigma'$ , microcracking will commence when shear stresses reach the  $\tau_p$  envelope. At failure, the shear resistance drops to  $\tau_r$ . The stress difference  $\tau_p - \tau_r$  across the failure surface provides the necessary force for sudden slope collapse.

$$\tau_g = \tau_p = \tau_{cp} + \mu_p \sigma' \quad \text{for } t_0 \leq t < t_f \quad (2a)$$

$$\text{and } \tau_g = \tau_r + \rho h a = \tau_{cr} + \mu_r \sigma' + \rho h a \quad \text{for } t \leq t_f \quad (2b)$$

where  $t_0$  and  $t_f$  are the times when inelastic deformation commences and when bulk failure occurs,  $\rho$  and  $h$  are the mean density and thickness of the unstable volume, and  $a$  is slope acceleration after bulk failure; as before, the subscripts  $p$  and  $r$  denote peak and residual values of the quantities involved.

Experiments indicate microscopic cracking as the mechanism controlling inelastic deformation before bulk failure (Hallbauer et al. 1973, Main and Meredith 1991, Lockner, 1995, Petley 1998). Under conventional geological conditions, rocks can weaken and crack at constant stress as a result of stress corrosion (Anderson and Grew 1977; Atkinson 1984). Circulating fluids, especially water which readily corrodes silicate materials (Atkinson 1984), promote crack nucleation and growth by attacking molecular bonds around tiny material flaws (effectively crack nuclei) and at the tips of existing small cracks. As each molecular bond breaks, its neighbouring bonds relax, releasing elastic strain energy that becomes available to drive further growth or to open new cracks (Lawn 1993). New and growing cracks increase the bulk volume of rock under stress and, eventually, they coalesce to form a major plane of failure (Main and Meredith 1991, Lockner 1995, Kilburn and Voight 1998).

Although cracks both nucleate and grow throughout the period preceding bulk failure, laboratory data and thermodynamic models suggest that microcracking is dominated initially by the formation of new cracks and, shortly before complete crack interlinking, by crack growth (McGuire and Kilburn, 1997, Kilburn and Voight 1998). While rates of crack nucleation increase exponentially with time (Main and Meredith 1991), rates of crack extension increase exponentially with crack length (Main et al. 1993). Arithmetic manipulation shows that the condition for crack growth is equivalent to a linear decrease with time in the *inverse*-rate of cracking (McGuire and Kilburn, 1997, Kilburn and Voight 1998)

$$(dN/dt)^{-1} = C - \gamma t \quad (3)$$

where  $dN/dt$  is the rate of cracking at time  $t$ , and  $C$  and  $\gamma$  are constants that depend on material properties and the applied stress.

Following Main et al. (1993), Eq. (3) is expected to be valid both for a single crack and for a population of cracks with a fractal size-frequency distribution (McGuire and Kilburn 1997, Kilburn and Voight 1998). In the case of unstable slopes, cracking occurs due to the downslope stress acting on the deforming horizon. The opening and growth of a population of cracks will thus be recorded macroscopically by a combination of bulk dilation and of downslope displacement. Assuming that the bulk movements are proportional to the total rate of cracking, rates of downslope displacement ( $dx/dt$ ) shortly before wholesale collapse will be proportional to  $dN/dt$ , such that the inverse-deformation rates should also decrease linearly with time

$$(dx/dt)^{-1} = \psi (C - \gamma t) \quad (4)$$

where  $\psi$  is a constant of proportionality. Equating the time of failure with the condition that  $(dx/dt)^{-1}$  becomes zero (*i.e.*, rates of deformation become infinitely large), Eq. (4) can be used to forecast the onset of catastrophic collapse by linearly

extrapolating measured inverse-rate trends to the time axis (Voight 1988, Kilburn and Voight 1998).

### Applications of the slow-cracking model

Three implications of the slow-cracking model that can be verified against field data are (1) that slow failure begins at depths where the applied shear stress equals the peak strength of a rock (Eq. (2a)), (2) that collapse accelerations are controlled by the shear stress drop  $\tau_p - \tau_r$  (combining Eqs (2a) and (2b)), and (3) that, shortly before catastrophic collapse, the inverse-rates of slope displacement decrease linearly with time (Eq. (4)).

Setting  $\tau = \rho g h \sin \alpha$ , where  $\alpha$  is the mean angle of slope failure, and  $h = CV^{1/3}$ , Eq. (2a) yields for the onset of deformation

$$V = [\tau_p / (\rho g C \sin \alpha)]^3 \quad (5)$$

Subtracting Eq. (2a) from (2b) further gives for the mean acceleration during collapse

$$a = (\tau_p - \tau_r) / \rho h \quad (6)$$

From observation, typical ranges for  $\alpha$  and  $C$  are  $20^\circ - 40^\circ$  and 0.1-0.5. At confining pressures of 1-10 MPa,  $\tau_p \sim 1-2$  MPa for undrained clay (Petley 1998) and  $\sim 10-10^2$  MPa for crystalline rock; associated drops in shear stress are  $\sim 0.1-0.5$  MPa for undrained clay and  $\sim 10-10^2$  MPa for crystalline rock (Hanks 1977). Inserting these values into Eq. (5) yields minimum volumes at failure of about 5-10 million  $m^3$ , corresponding to minimum failure depths of  $\sim 10^2$  m.

Smaller failure depths normally involve movement along weaker rock types. Associating a minimum depth of  $10^2$  m with failure along compacted clay, Eq. (6) implies minimum accelerations of  $\sim 1$   $m\ s^{-2}$ . For very large collapses involving the failure of crystalline rock,  $h \sim 10^3$  m for which nominal collapse accelerations are 0.4g. Even with accelerations of  $1$   $m\ s^{-2}$ , a landslide could achieve sturzstrom velocities  $u$  of  $10-30$   $m\ s^{-1}$  within intervals ( $\sim u/a$ ) of only 10-30 s. Both the minimum sturzstrom volumes and short collapse times agree well with field data (Muller 1964, Hsü 1975).

Few precursory data are available for catastrophic slope collapses. A classic exception is the set of observations compiled for the Alpine Mt Toc which, after nearly three years of intermittent, slow deformation, collapsed catastrophically into Italy's Vajont reservoir on 09 October 1963, claiming more than 2,000 lives (Chapter 4; Muller 1964). Final failure occurred after more than two months of slowly accelerating slope movement (Fig. 2). When the inverse deformation rate during this interval is plotted against time (Fig. 2), a clearly linear decrease is observed, as expected from the slow-cracking model (Eq. (4)).

Mt Toc collapsed during filling of the then recently-completed Vajont reservoir, and it has long been acknowledged that instability was promoted by the resulting accumulation of meteoric water within the mountainside (Kiersch 1965, Hendron and Patton 1985, Semenza and Ghirotti 1998). In particular, analyses have focused on the role of water in increasing fluid pressure within the clay horizon along which movement was concentrated (Hendron and Patton 1985). Increasing fluid pressure ( $U$ ) destabilizes slopes by reducing  $\sigma'$  in Eqs (2). However, increases in pore pressure alone have been unable quantitatively to explain the two-month acceleration to

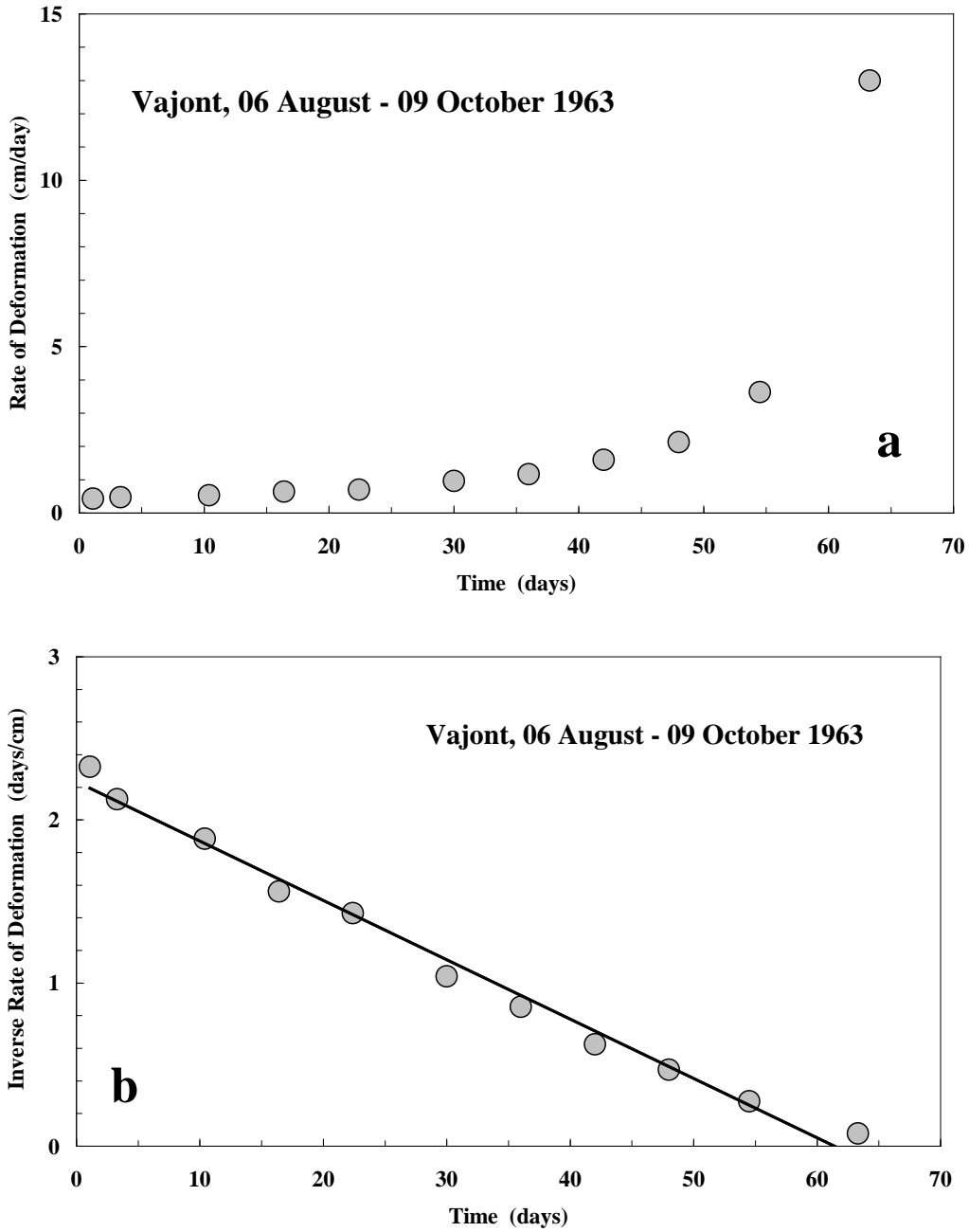


**Figure 2.** Rates of slope movement before the catastrophic collapse of Mt Toc into the Vajont reservoir on 09 October 1963. (a) Daily measurements show slow accelerations for 60 days from less than 1 cm day<sup>-1</sup> to 15 cm day<sup>-1</sup>. The monitored rates are associated with the growth of microcracks, and are small compared with mean collapse velocities of about 10 m s<sup>-1</sup> attained when the cracks linked to form a major failure plane and reduced the resisting stress from  $\tau_p$  to  $\tau_r$ . (b) The inverse-deformation rate decreases linearly with time, as expected from slow cracking dominated by crack growth. Linear regression gives an  $R^2$  correlation coefficient of 0.99. A linear trend would have been apparent at least by Day 35, yielding a minimum 25-day forecast for major collapse. Errors on measured rates are estimated to have been less than 5%, within the radius of the circles. Data from Muller (1964) and Voight (1988).

complete failure. Slow-cracking, in contrast, naturally accounts for the increases in deformation rate before collapse, suggesting that, at least for deep-seated landslides, the key role of accumulated water may be to promote the corrosive weakening of rock under stress.

### **Conclusions**

Catastrophic slope collapse after extended periods of slow, but accelerating deformation is the macroscopic result of a rock horizon, stressed to its peak value, undergoing sudden stress-weakening. Rates of deformation before collapse are controlled by the nucleation and growth of a population of microcracks. These cracks eventually link together to form a major plane of weakness, at which time the rock shear strength rapidly decreases from peak to residual values. Applied to giant slope failure, the slow cracking model accounts for the minimum volumes required for sudden collapse, the increases in rates of slope movement shortly before collapse, and the high accelerations obtained during collapse. The model also accounts for linear decreases with time in the inverse rate of precursory movements. Applied to the 1963 collapse of Mt Toc in northeastern Italy, the model reveals not only the potential to forecast collapse as much as weeks beforehand, but also highlights the importance of water in catalysing corrosive microcracking. Future studies may therefore reveal stress corrosion to be a key factor in producing deep-seated slope instabilities, especially in wet corrosive environments, such as those expected alongside reservoirs and around degassing volcanoes.

## References

- Anderson OL, Grew PC 1977. Stress corrosion theory of crack propagation with applications to geophysics. *Rev. Geophys. Space Science*, 15: 77-104.
- Atkinson BK 1984. Subcritical crack growth in geological materials. *J geophys Res* 89: 4077-4114.
- Hadley JB 1978. Madison Canyon rockslide, Montana, U.S.A. In Voight B (ed) *Rockslides and avalanches.1. Natural phenomena*, 167-180. Elsevier, Amsterdam.
- Hallbauer DK, Wager H, Cook NGW 1973. Some observations concerning the microscopic and mechanical behaviour of quartzite specimens in stiff, triaxial compression tests. *Int J Rock Mech Mining Sci*, 10: 713-726.
- Hanks TC 1977. Earthquake stress-drops, ambient tectonic stresses, and stresses that drive plates. *Pure Appl Geophys*, 115: 441-458.
- Hoek E, Bray JW 1997. *Rock slope engineering*, 3<sup>rd</sup> Edn (rev). IMM and E&FN Spon, London, pp 358.
- Hsü KJ 1975. On sturzstroms - catastrophic debris streams generated by rockfalls. *Geol Soc Am Bull* 86: 129-140.
- Kiersch GA 1965. The Vaiont reservoir disaster. *Mineral Information Service*, 18: 129-138.
- Kilburn CRJ, Voight B 1998. Slow rock fracture as eruption precursor at Soufriere Hills volcano, Montserrat. *Geophysical Research Letters*, 25: 3665-3668.
- Lawn B 1993. *Fracture of brittle solids*, 2nd Edn. Cambridge University Press, Cambridge, pp 378.
- Lockner DA 1995. Rock failure. In Ahrens TJ (ed) *Rock physics and phase relations. A handbook of physical constants*. AGU Ref Shelf 3, 127-147.
- Main IG, Meredith PG 1991. Stress corrosion constitutive laws as a possible mechanism of intermediate-term and short-term seismic event rates and b-values. *Geophys J Int*, 107: 363-372.
- Main IG, Sammonds PR, Meredith PG 1993. Application of a modified Griffith criterion to the evolution of fractal damage during compressional rock failure. *Geophys J Int*, 115: 367-380.
- McGuire WJ, Kilburn CRJ 1997. Forecasting volcanic events: some contemporary issues. *Geol Rundsch*, 86: 439-445.
- McSaveney MJ 1978. Sherman glacier rock avalanche, Alaska, U.S.A. In Voight B (ed) *Rockslides and avalanches.1. Natural phenomena*, 197-258. Elsevier, Amsterdam.
- Muller L 1964. The rock slide in the Vaiont valley. *Felsmech Ingenieurgeol* 2: 148-212.
- Petley DN 1998. Failure envelopes of mudrocks at high confining pressures.
- Plafker G, Ericksen GE 1978. Nevados Husacarán avalanches, Peru. In Voight B (ed) *Rockslides and avalanches.1. Natural phenomena*, 277-314. Elsevier, Amsterdam.
- Semenza E, Ghirotti M 1998. Vaiont-Longarone 34 anni dopo la catastrofe. *Ann Univ Ferrara*, 7: 63-94.
- Voight B 1978 (ed) *Rockslides and avalanches*, 1. Natural phenomena. Elsevier, Amsterdam, pp 833.
- Voight B 1988. A method for prediction of volcanic eruptions. *Nature* 332: 125-130.

## 2. The flow of giant rock landslides

### Abstract

Giant, rapid landslides, or sturzstroms, are among the most powerful natural hazards on Earth. They occur as whole mountainsides are displaced kilometres within minutes. Thirty years ago, popular explanations attributed high sturzstrom velocities to exotic mechanisms for reducing friction, notably the entrapment of cushions of air. Ken Hsü challenged this view in the 1970's, arguing that sturzstrom behaviour is a natural result of collections of rock fragments. Hsü's view today prevails, supported by advances in granular-flow dynamics. The latest modifications of Hsü's model assume that sturzstroms lose most of their energy by deformation in a basal boundary layer and, possibly, in narrow horizons within the body of the landslide. The favoured model views material in the boundary layer as a Bingham plastic which, for most of a sturzstrom's emplacement at high deformation rate, behaves approximately as a Newtonian fluid. This model provides a physical basis for forecasting the runout lengths of sturzstroms and for improving methods for assessing their hazard.

### Introduction

Sturzstroms are giant landslides of shattered rock that can travel kilometres within minutes. They occur when unstable volumes exceed  $\sim 10^6$ - $10^7$  m<sup>3</sup>, and their runout lengths tend to increase with initial volume (Fig. 1). Their speed, size and travel distance are often taken to imply that sturzstroms have an unusually high mobility compared to smaller landslides, and this has driven numerous investigations into how volume controls sturzstrom friction (Hsü 1975, Erismann 1979, Melosh 1987). Such studies have fallen into two classes: (1) those which invoke external mechanisms (*e.g.*, trapped air or rock melting) to enhance mobility, and (2) those which relate mobility to properties inherent to colliding rock masses. Hsü (1975) championed the latter approach which, although unfashionable at the time, has since come to prevail among sturzstrom models. Building on Hsü's approach, this paper argues that volume is important to sturzstrom behaviour because it controls the energy available for transport rather than the inherent mobility of a landslide.

### Sturzstrom characteristics

Sturzstrom volumes on Earth range from  $\sim 10^6$  m<sup>3</sup> to about 30 km<sup>3</sup> (Fig. 1). They occur in virtually all major rock types, from carbonates, through metamorphic rocks, to volcanic material. Their deposits consist of collections of fragments, from fine grains to blocks the size of a house. The fine material appears normally to be concentrated either within the lower layers of a deposit or along narrow horizons at different levels throughout its thickness (Fig. 2). The simplest interpretation is that deformation and the comminution of rock tends to be focused along a small number of horizons (Hendron and Patton, 1985; Hewitt, 1988; Kilburn and Sørensen, 1998).

Also consistent with focussed deformation is the tendency for sturzstrom deposits to preserve their large-scale, pre-failure stratigraphy, such that a pre-failure sequence of, say, carbonates over gneiss, would yield a sturzstrom deposit with disrupted carbonate levels sitting on broken gneiss. Indeed, the exposed upper portions of some giant sturzstrom deposits, such as at Köfels and Flims in the Alps, preserve fine structures at scales of 0.1-1.0 m (Erismann, 1979). These latter deposits are remarkable when seen in outcrop, in that they appear from a distance to consist of massive rock faces ( $\sim 10$ - $100$  m across), when they in fact consist of rock masses which have been shattered at the centimetre scale, but which have experienced no

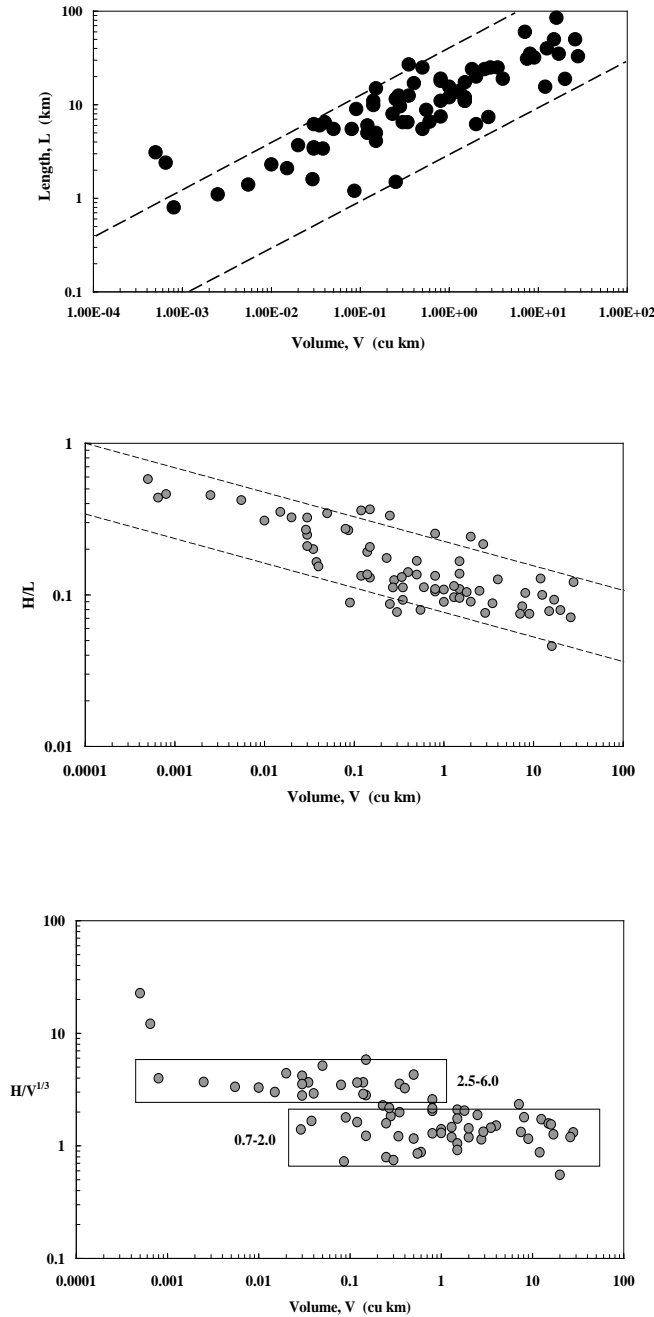


**Figure 1.** (a, top) The runout length of sturzstroms tends to increase with sturzstrom volume. Simple boundary-layer models (Eq. (20)) expect  $L$  to increase with the square root of volume. The dashed lines show the limits  $L = BV^{1/2}$ , where the upper and lower values of  $B$  are  $40 \text{ km}^{-1/2}$  and  $5.5 \text{ km}^{-1/2}$ . (b, middle) The ratio  $H/L$  of vertical drop height to runout length decreases as sturzstrom volume increases. Boundary-layer models (Eq. (15)) yield  $H/L = bV^{-1/6}$ , shown by the dashed lines with upper and lower values for  $b$  of  $0.22 \text{ km}^{-1/3}$  and  $0.075 \text{ km}^{-1/3}$ . (c, bottom) The ratio  $H/V^{1/3}$  for sturzstroms lies within two preferred ranges of values. Most data suggest  $H/V^{1/3} \sim 1$  (lower box; for which  $V > 0.02 \text{ km}^3$ ); these may correspond to when collapse occurs almost directly onto the runout surface ( $z/y \ll 1$  in Fig. 3). A second preferred range gives  $H/V^{1/3} \sim 4$  (upper box;  $0.0004 < V < 1 \text{ km}^3$ ) and this may reflect when collapse involves a significant vertical drop beyond the collapse scar ( $z/y \geq 1$  in Fig. 3).

*relative* deformation during emplacement. They are the equivalent of a three-dimensional jigsaw puzzle that has travelled several kilometres without any of the pieces becoming dislodged.

At the very largest scale, sturzstrom deposits appear as sheets, much wider than thick, whose periphery is often lobate or even divided into tongues following topographic depressions (Hsü, 1975, 1978). Such geometry is typically associated with fluid behaviour which, in the context of rock emplacement, can only be explained if the bulk shape of the rock mass is controlled by individual fragments (again from sand to the size of a house), each of which can move in response to local conditions, just as a fluid spreads according to the movement of its molecules.

Together, the basic features of sturzstrom deposits suggest that sturzstroms are emplaced as collections of fragments through which deformation is concentrated along their base and, possibly, also along narrow bands at higher levels. These essential elements were certainly recognised at least forty years ago. Uncertainty occurred when trying to explain why deformation was concentrated and why such such deformation could allow sturzstroms to travel great distances.

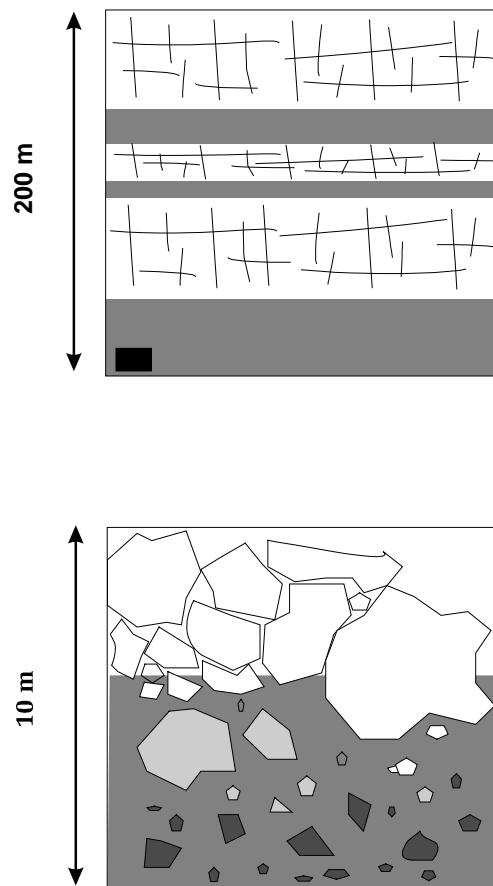


**Figure 2.** All sturzstrom deposits consist of broken rock. Near the source (*top*) heavily fractured hard rock (*white*) overlies a thinner base of gravel and small debris, possibly mixed with mud or clay (*stipple*), along which deformation is initially concentrated; secondary clay-rich layers within the body of the landslide may later develop as preferred horizons for deformation (Fig. 6). Away from the source (*bottom*), the whole sturzstrom has become much thinner and a larger basal fraction consists of a small debris supported by fine-grained matrix (*stipple with grey and black debris*). This layer is overlain by giant angular blocks (*white*). Notice the poor mixing between different stratigraphic horizons (*white, grey and black levels*). The black box in the top diagram shows the relative thickness of the lower section. Although idealised, these sections are based on observations at Vaiont, Italy (Hendron and Patton, 1985; *top*) and in the Karakoram Himalayas (Hewitt, 1988; *bottom*).

### **Sturzstrom volume and mobility**

Albert Heim pioneered the modern study of giant rock landslides following a series of landslide disasters in the Alps (Heim 1882, 1932; Hsü 1978). He noticed that, for a given vertical drop height  $H$ , a sturzstrom tended to travel a greater horizontal distance  $L$  as the pre-failure volume  $V$  became larger (Figs 1, 3 & 6). Applied to a sliding rigid block, the ratio  $H/L$  is simply related to the friction coefficient  $\mu$  along the sliding plane as (Hayashi & Self, 1992):

$$H/L = \mu \quad (1)$$

Equation (1) is important because it relates geometric features of sturzstrom travel ( $H/L$ ) to an effective roughness ( $\mu$ ) of the sliding surface, most of which happens to be the sturzstrom-ground contact. The effective roughness, in turn, depends on the interaction between uneven ground and the irregular base of the sturzstrom. The more frequently irregularities in the ground and the sturzstrom interact, the greater the value of  $\mu$  and hence of  $H/L$ . Applying Equation (1), therefore, the inverse relation between sturzstrom volume and  $H/L$  (Fig. 1) suggests that larger volumes can trigger mechanisms for reducing the effective interlocking between ground and sturzstrom.

An early lubricating model of enduring popularity proposed that sturzstroms are able to glide over cushions of trapped air (Shreve, 1968). Essential features for air entrapment are that: (1) topography must allow a sturzstrom to detach itself from the ground and fly for a short distance before crashing back down and compressing the air caught underneath; and (2) the compressed air must remain trapped for a time long enough to allow a significant runout for the landslide.

Although flying sturzstroms may seem unlikely, one such was observed near the Swiss village of Elm in 1881, when a block undercut by quarrying collapsed onto a ledge, was deflected into the air and returned to the ground a few hundred metres downslope (Hsü, 1975, 1978). Such circumstances are rare, however, and so cannot be considered essential for the emplacement of sturzstroms.

Even when air-launching does occur, air entrapment requires poor leakage from a landslide. For very wide landslides, it is plausible that lateral gas loss affects only the margins of the moving body (provided the velocity is not large enough to tear the slide apart (Erismann, 1979)) and, hence, that gas entrapment depends primarily on the upper levels of the landslide acting as an effective cap. Effective capping, in turn, is only feasible if the upper layers of a sturzstrom are virtually impermeable (Erismann, 1979), a condition that is unlikely to be satisfied by the shattered, fragmented nature of sturzstrom deposits.

The air-cushion hypothesis was further weakened by its inability to explain why larger sturzstroms have smaller apparent coefficients of sliding friction (Erismann, 1979), and by the discovery on the airless lunar surface of possible sturzstrom deposits (Howard, 1973). Alternative models therefore returned to processes operating within a landslide itself, since these would not rely on environmental controls (the entrapment of air) and might naturally explain the influence of landslide size on mobility.

Given the fragmental nature of sturzstrom deposits, the interaction between fragments is an obvious starting point to investigate sturzstrom dynamics. Hsü (1975) pursued this approach while air-cushioning was still the popular explanation for long sturzstrom runout. He reintroduced Albert Heim's studies of Alpine sturzstroms (Heim, 1882, 1932), whose results had laid dormant for over 40 years. Heim (1932) had postulated that collisional energy losses were important to the behaviour of

sturzstroms, but had lacked a theoretical support for the idea. Two decades later, Bagnold (1954) introduced the idea of grain-dispersive pressure among collections of moving fragments. He argued that, by colliding with each other, the grains in a granular mass can force themselves apart (the collisions producing the so-called grain-dispersive pressure), so helping faster grains to jump beyond their slower neighbours and reducing their frictional contact with respect to the static state (Bagnold, 1954).

Making a crucial connection between Heim's hypothesis and Bagnold's granular-flow model, Hsü (1975, 1978) conjectured that grain-dispersive pressures could explain why the apparent friction coefficients of sturzstroms are smaller than those typical of sliding rigid blocks. He formally proposed the name *sturzstrom* to avoid implying a sliding emplacement for giant landslides and cited the comminuted rock matrix as a principal source of dispersive pressures (Hsü, 1975). Although also proposed independently (Howard, 1973) and applied in the field (*e.g.*, McSaveney, 1978), the simple granular-flow model was challenged on the grounds that, while bulk friction may be reduced, the total rate of energy loss throughout a landslide would be too rapid to allow sturzstroms to travel the distances observed (Melosh, 1979, 1986, 1987). Modifications of Hsü's sturzstrom model have thus sought conditions that favour lower rates of collisional energy loss by some combination of (1) increasing the effective size of fragments, (2) introducing an interstitial fluid, and (3) reducing the proportion of the sturzstrom volume in which the most energetic collisions occur. The key ideas can be summarized as follows.

(1) *Increasing the effective size of fragments.* Fragments increase their effective size when, instead of bouncing as individuals, they move as groups of fragments, so that collisions within groups are minimized and most energy is lost by contact among the outer fragments of adjacent groups. Melosh (1979, 1986, 1987) suggested that such behaviour could be induced by the passage of sound (acoustic) waves through a landslide. Triggered by shaking during collapse, the acoustic waves could also temporarily reduce overpressures on fragments, especially along the lower layers of a sturzstrom, thereby further decreasing the effect of frictional contacts.

(2) *Introducing interstitial fluids.* Although mud may sometimes be available (Hsü, 1975), the granular nature of most sturzstrom matrices has been used to support models invoking a gaseous and pressurized interstitial fluid that gradually escapes during transport. Thus Kent (1966) proposed fluidisation by air entrapment, while others have appealed to frictional heating for vaporizing trapped groundwater (Habib, 1967; Goguel, 1978) or for dissociating carbonate rocks to yield CO<sub>2</sub> (Erismann, 1979). Erismann (1979) further considered frictional rock melting as a means of increasing landslide mobility.

(3) *Reducing the volume of energetic collisions.* As collisional energies increase, fragments not only move faster but also attempt to increase their mean separation. Using computer simulations (Campbell and Brennan, 1985; Straub, 1996), Campbell (1989) and Straub (1997) have argued that, under suitable conditions over rough ground, bouncing might be strong enough to carry a sturzstrom over a rarified layer containing a few, but rapidly colliding fragments. Although the collisions are energetic, the volume of the basal layer is small enough to ensure that the total rate of energy dissipation is much less than that expected from collisions throughout the landslide mass, thereby reducing the sturzstrom's bulk resistance.

All the above mechanisms are remarkable in their imagination and in their appeal to extreme conditions. Being extreme is not by itself a motive for exclusion, but it does imply unusual conditions that should be evaluated with caution. Thus, as for Shreve's air-cushion hypothesis (Shreve, 1968), the pressurized-gas models all suffer

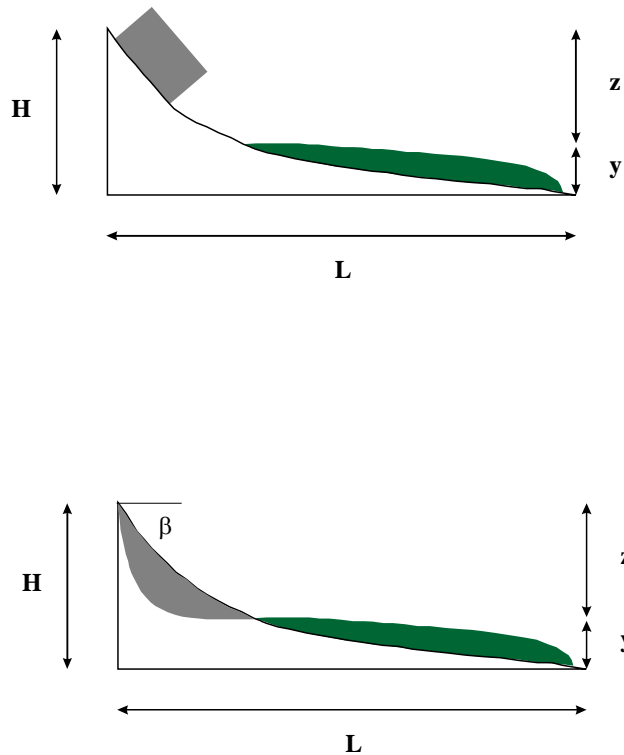


**Figure 3.** Definition sketch of key sturzstrom dimensions. The top figure shows a geometry commonly assumed in models, for which the source (*stipple*) is viewed as a block whose dimensions are independent of the drop height  $H$ . A more realistic situation (*bottom*) shows that slope failure often occurs near the runout slope and suggests that, by virtue of the stress field required to form a new failure surface, the drop height  $H$  may vary approximately with the cube root of sturzstrom volume (Fig. 1).

from the need for the upper layers of sturzstroms to be virtually impermeable, an unlikely condition for fragmental flow. The extreme of rock melting does occur (Erismann, 1979), but has been observed in only a handful of larger deposits, so that its general application is questionable (Melosh, 1987). For rarified basal layers to support a giant landslide, the impact velocity of basal fragments must exceed  $\sim 10 (gh)^{1/2}$  (Campbell, 1989), where  $h$  is landslide thickness and  $g$  is gravitational acceleration. For typical collapse thicknesses of sturzstroms, the minimum implied fragment velocities and impact pressures ( $\rho v^2$ , where  $\rho$  is fragment density) are  $\sim 140$ - $300 \text{ m s}^{-1}$  and  $\sim 10^8 \text{ Pa}$ . Even for the ideal (frictionless) conversion of potential to kinetic energy, such velocities imply (a) collapse heights of  $\sim 2$ - $10 \text{ km}$  (greater if friction is important), similar to and greater than the maximum values observed on Earth (Fig 6), and (b) impact pressures similar to the compressional strength of intact rock (Lockner, 1995), so it is unclear whether or not such fragments (which probably have lower strengths due to internal flaws) could sustain such collisions for any significant length of time before disintegrating.

Compared with the alternatives, only the acoustic model of Melosh (1979) appears as a plausible general mechanism for reducing sturzstrom friction. However, as with all the previous models, the acoustic fluidisation hypothesis cannot quantify the observed decrease in  $H/L$  with increasing sturzstrom volume. Indeed, to address this problem in particular, it is convenient to return to Hsü's starting point of using the

keestablished Bagnold model for concentrated granular flow (Bagnold, 1954; Hsü, 1975).

### Sturzstroms as granular flows

Energy is dissipated in granular flows by inelastic collisions between fragments, by friction (rolling and sliding) between fragments, and by the deformation of any fluid between the fragments. The relative importance of each factor depends on the volumetric concentration of fragments, the size distribution of fragments, the rheology of any interstitial fluid, and the velocity of deformation (Fig. 4).

Deformation rate is a crude measure of the energy available for motion. At low rates of deformation, fragments collide only weakly and most energy is lost either through frictional contact or by deforming an interstitial fluid. At high deformation rates, collisions occur so frequently that inelastic energy losses dominate granular-flow resistance. The values of transitional deformation rates between these extremes increase as the concentration of fragments becomes larger and the resistance of any interstitial fluid increases (Fig. 4).

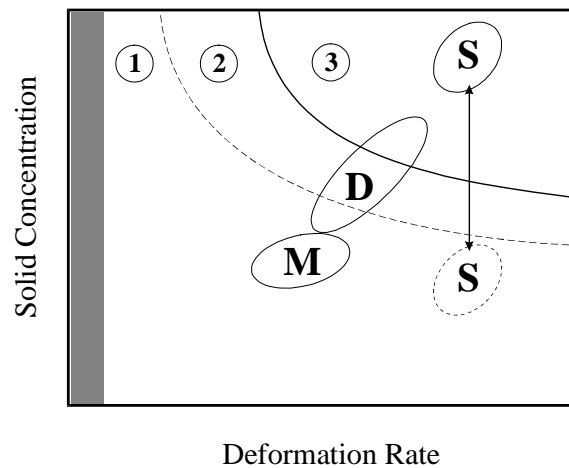


**Figure 4.** Landslide behaviour varies with the volume concentration of solid fragments and the rate of deformation. At small deformation rate or solid concentration (*Region 1*), most energy is dissipated by deforming material (typically mud) between larger fragments. At large deformation rate and solid concentration (*Region 3*), most energy is dissipated by collisions among large fragments. Between these extremes (*Region 2*) both collisions and fluid deformation are important. *M*, *D*, and *S*, refer to notional fields for mudflows, debris flows and sturzstroms. The relative positions of *M* and *D* illustrate the increasing importance of fragment collisions among debris flows. Two sturzstrom fields are shown: that in *Region 3* assumes all solid material loses most energy by collisions; that in *Region 1* considers fine solids to behave as an effective fluid, so that the effective solid concentration is that only of large fragments. The shaded border on the left corresponds to long term creep. The curves show the shapes of field boundaries expected from Bagnold's relation (Eq. (21)). For constant physical properties, the dashed and solid boundaries correspond to  $Ba \sim 40$  and  $Ba \sim 400$ ; when physical properties vary, the boundaries will move towards the top right as the matrix viscosity increases and as the mean size and density of colliding fragments decrease (Eq. (21)).

Applied to landslides, a range of dynamic behaviour can be expected according to the proportion of interstitial fluid and the rate of deformation. Since the typical interstitial fluid is mud, an immediate possibility is that sturzstroms form one end of a continuous spectrum of landslide types that grade, with increasing mud content, through debris flows into mudflows (Fig. 4; Pierson and Costa, 1987; Iverson 1997).

However, if the fragments in dry landslides consist of larger pieces within a matrix of very fine material, ambiguity arises as to what constitutes an interstitial fluid. Thus, while collisions control energy dissipation from the large fragments, frictional effects may determine energy losses from the matrix, so that the matrix behaves effectively as an interstitial fluid (Fig. 4).

Initial arguments that Bagnold flow dissipates energy too quickly to explain sturzstrom runout (Melosh, 1986, 1987) assumed that energy dissipation is dominated by collisions between fragments throughout the landslide. A complete analysis, however, must consider the potential influence (a) of boundary-layer flow and (b) of energy loss being controlled by fine material behaving as an interstitial fluid.

### **Boundary-layer flow in sturzstroms**

To explain the preservation of prefailure stratigraphy, deformation during transport must be restricted to narrow horizons within a sturzstrom; otherwise material from the prefailure ground level could be expected somewhere within the body of the final deposit (Erismann, 1979). Since deformation must occur between the moving sturzstrom and stationary ground, the simplest inference is that significant deformation, and hence loss of energy and momentum, occurs *at least* within a narrow boundary layer along the base of the landslide.

As a sturzstrom advances, its basal material is the first to be slowed by stationary ground. Owing to collisions between neighbouring fragments, retardation of the basal layer induces a deceleration in the layer of fragments immediately above. At a rate controlled by the ability of slow fragments to decelerate their overlying neighbours, the retarding effect of the ground is gradually felt through an increasing amount of the granular mass.

If  $t_e$  is the emplacement time of a sturzstrom and  $t_h$  is the time for the retarding effect to involve the whole landslide thickness  $h$ , then *boundary-layer flow* and *whole-body flow* can be distinguished according to whether  $t_h/t_e$  is much greater than or much smaller than unity. Thus (a) for  $t_h/t_e \gg 1$ , emplacement is complete before the retarding effect of the ground has penetrated deeply into the landslide, so that only collisions in a basal boundary layer actively contribute to energy dissipation (Fig. 5c), but (b) for  $t_h/t_e \ll 1$ , the whole landslide thickness is retarded by the ground soon after motion begins, so that collisions throughout the whole body contribute to energy loss during most of the sturzstrom's emplacement (Fig. 5a). Landslide heterogeneity may allow localised deformation to occur also along structural weaknesses before these are directly affected by a thickening basal boundary layer (Fig. 5c). The following analysis concentrates first on the influence of a basal layer; the influence of structural weaknesses are considered later.

Since dissipating collisions in boundary-layer flow are concentrated within only a small volume of the sturzstrom, the total rate of energy dissipation is less than it would have been if the whole body had been actively deforming. Correspondingly more time is thus required to dissipate the kinetic energy of the whole body, thereby favouring greater runout lengths for a given vertical descent and, hence, smaller values of  $H/L$ . The effect of such a boundary layer is easily seen from a bulk energy balance for sturzstrom emplacement. Sturzstrom energy is derived from the potential energy released during descent and is consumed by friction. Equating these energy terms yields (*e.g.*, Kilburn and Sørensen, 1998)

$$H/L \sim \tau A / \rho g V \quad (2)$$

where  $H$  and  $L$  are the vertical and horizontal distances between the top of the failure scar and the toe of the sturzstrom deposit, of volume  $V$  and bulk density  $\rho$ ,  $g$  is gravitational acceleration, and  $\tau$  is the mean basal stress acting over the mean basal area  $A$ .

The resisting stress  $\tau$  is equivalent to the energy dissipated per unit basal area per unit length of advance. For runout under gravity, a simple force balance also yields

$$\tau = \rho g h \sin \alpha \quad (3)$$

where  $h$  is the mean thickness of the landslide as it moves down a slope of angle  $\alpha$ .

The smaller the boundary layer, the smaller the energy dissipated and so, from Eq. (2), the smaller the value of  $H/L$ . Geometric similarity of sturzstrom deposits suggests that  $A = C_A V^{2/3}$  where the geometric ratio  $C_A \sim 100$  (a complete range of values is 20 to 300; Dade and Huppert, 1998; Iverson et al., 1998; Kilburn and Sørensen, 1998), so that Eq. (2) implies

$$H/L \propto \tau V^{-1/3} \quad (4)$$

from which the final variation of  $H/L$  with volume is seen to depend on any volumetric dependency of the basal shear stress.

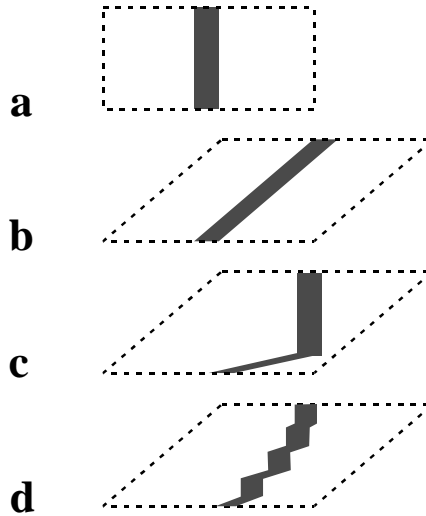


**Figure 5.** Styles of bulk deformation within sturzstroms. As a sturzstroms moves from its starting condition (*a*), it may deform significantly throughout its whole thickness (*b*, whole-body deformation) or along a restricted number of horizons (*c*, *d*, boundary-layer deformation). Ground resistance favours the growth of a basal boundary layer (*c*), while structural weaknesses may enable deformation also along narrow horizons within the body of the sturzstrom (*d*). If the boundary layers thicken with time, then stage *a* may pass through stages *c* or *d* towards stage *b*. In this case, the preferred deformation regime depends on whether the total runout time is much shorter or longer than the time for boundary-layer thickening to affect the whole sturzstrom (see text for discussion).

### Volumetric dependence of basal shear stress

Two broad approaches are available for analysing a sturzstrom's resistance to motion. The first seeks to apply simple rheological models to the bulk behaviour of a landslide. The second attempts to describe the local mechanisms of momentum loss and to integrate these over the entire landslide volume. By virtue of simplicity, bulk analyses will first be considered, leaving the integration of local analyses to a later section.

#### *Boundary layers and bulk deformation models*

Three simple models are immediately available to describe a large mass moving on a thin basal layer. The first follows traditional landslide studies and treats a landslide as a rigid block (Hoek and Bray, 1981), for which friction is determined by irregularities between the sturzstrom and the ground. In this case, basal friction can be described by the Coulomb relation for sliding:

$$\tau = \mu (\rho gh \cos \alpha - w) \quad (5)$$

where  $w$  is a fluid pressure. Since previous arguments have excluded fluid pressure as an essential feature of sturzstrom emplacement, geometric similarity and Eq. (5) imply  $\tau \propto h \propto V^{1/3}$ , from which Eq. (4) yields  $H/L$  as being independent of volume.

Alternative bulk models consider the basal layer as a fluid underlying a weakly-deforming sturzstrom mass. In this case, basal stress depends on the bulk rheology of the basal layer. At its simplest, the basal layer behaves as a viscous fluid, for which

$$\tau = \eta \, du/dy \quad (6)$$

where  $\eta$  is the viscosity of the material and the deformation rate  $du/dy$  is the change in forward velocity ( $du$ ) over a thickness  $dy$ .

Equation (6) implies that a sturzstrom will halt ( $du/dy = 0$ ) when the resisting stress and, hence, also the driving stress are zero. Unless contained by topography, the net stress on a viscous boundary layer approaches zero only when the layer becomes infinitesimally thin. Hence, either Eq. (6) holds until the basal layer is exhausted (*i.e.*, it has been left as a deposit trailing behind the main landslide), or the basal layer itself possesses a strength that must be exceeded for flow to continue. In the second case, the simplest bulk model is that for a Bingham fluid, which yields:

$$\tau = \tau_y + \eta \, du/dy \quad (7)$$

where  $\tau_y$  is the yield strength below which no motion can occur. An important feature of Equation (7) is that at sufficiently large deformation rates ( $du/dy$ ), the effect of the yield strength becomes negligible and Equation (7) approximates to Equation (6), but when  $du/dy$  becomes small sturzstrom resistance depends on the yield strength  $\tau_y$  alone.

At one extreme,  $du/dy$  may be small enough throughout emplacement for  $\tau \approx \tau_y$  (Dade and Huppert, 1998). Assuming constant rheological properties, the condition  $\tau = \tau_y$  yields from Eq. (4)

$$H/L \propto V^{-1/3} \quad (8)$$

From Eq. (3), however, a constant basal stress also implies that a sturzstrom's thickness  $h = \tau_y/(\rho g \sin \alpha)$ . A sturzstrom should thus become thicker as it moves onto shallower slopes, a condition clearly contrary to observation. Thus, while a yield strength might be important to halting a sturzstrom (discussed later), it cannot control runout without significantly decreasing in value with time.

When  $\tau_y$  is not important, Eqs (6) and (7) yield for constant rheology

$$\tau \propto du/dy \approx U/\delta \quad (9)$$

where  $\delta$  is the thickness of the boundary layer, over which velocity increases from zero at the ground to  $U$  at the top of the boundary layer.

The rapid velocities of sturzstroms are similar to those expected for an efficient conversion of potential to kinetic energy during collapse (Hsü, 1975; Kilburn and Sørensen, 1998) - that is, sturzstroms accelerate to velocities of  $\sim U$  during collapse and then decelerate during runout. To a first approximation, therefore,  $U \sim (gz)^{1/2}$ , where  $z$  is the vertical distance dropped during initial collapse (Fig. 3). The boundary layer may be constrained by landslide structure to a nearly constant thickness ( $\delta = \text{constant}$ ), or it may increase with time as a diffusive boundary layer (controlled by collisions between fragments), for which the mean boundary-layer thickness  $\delta$  increases with the square root of the emplacement time  $t_e$  (Kilburn and Sørensen, 1998). In the first case,

$$\tau \propto z^{1/2} \quad (10)$$

and, in the second,

$$\delta \propto t_e^{1/2} \propto (L/U)^{1/2} \propto (L/z^{1/2})^{1/2} \quad (11)$$

which, combined with Eq. (2) leads to

$$\tau \propto z^{3/4}/(H V^{1/6}) \quad (12)$$

Equations (10) and (12) show that, for the effective viscous deformation of a boundary layer, the volumetric control of basal stress depends on relations between sturzstrom volume and vertical collapse height,  $z$ , and vertical drop height,  $H$ . Conventional analyses assume  $H$  is independent of volume (Fig. 3), while geometric similarity suggests the approximation  $z \propto V^{1/3}$  (Fig. 3; Goguel, 1978; Kilburn and Sørensen, 1998). Applying these conditions,

$$\tau \propto V^{1/6} \quad H/L \propto V^{-1/6} \quad (13)$$

for a boundary layer of constant thickness (from Eqs (10) and (4)), and

$$\tau \propto V^{1/12} \quad H/L \propto V^{-1/4} \quad (14)$$

for a boundary layer thickening by diffusion (from Eqs (12) and (4)).

A feature neglected by conventional analyses is that sturzstroms tend to collapse directly onto gently inclined surfaces, so that  $H$  often happens to be similar to  $z$  (Figs

1 & 3). In this case, H as well as z will vary in proportion to  $V^{1/3}$  (Kilburn and Sørensen, 1998), so that Eqs (10) and (12) now yield

$$\tau \propto V^{1/6} \quad H/L \propto V^{-1/6} \quad (15)$$

for a boundary layer of constant thickness, and

$$\tau \propto V^{-1/4} \quad H/L \propto V^{-7/12} \quad (16)$$

for a boundary layer that thickens diffusively with time.

**Table 1.** Volumetric dependencies of bulk sturzstrom characteristics.

<i>Deformation Constraint</i>	$L \propto V^m, m =$	$H/L \propto V^n, n =$
<b>H independent of V</b>		
<b>Whole-body flow</b>	<b><i>1/2</i></b>	<b><i>-1/2</i></b>
<b>Boundary-layer flow:</b>		
<b>(a) thickness independent of V</b>	1/6	<b><i>-1/6</i></b>
<b>(b) thickness increases by diffusion</b>	1/4	-1/4
<b>Constant basal stress</b>	1/3	-1/3
<b>H proportional to <math>V^{1/3}</math></b>		
<b>Whole-body flow</b>	5/6	-1/2
<b>Boundary-layer flow:</b>		
<b>(a) thickness independent of V</b>	<b><i>1/2</i></b>	<b><i>-1/6</i></b>
<b>(b) thickness increases by diffusion</b>	11/12	-7/12
<b>Constant basal stress</b>	2/3	-1/3

Figures in bold italics follow observed trends. The only combination to describe *both* L-V and H/L-V trends corresponds to boundary-layer flow with (a) a volume-independent boundary-layer thickness and (b) a drop height proportional to the cube root of volume.

Table 1 summarizes the H/L-V relations implied by the rigid-block, constant-stress and two viscous boundary-layer models (for constant  $\delta$  and thickening  $\delta$ ). Observational data follow most closely the trend  $H/L \propto V^{-1/6}$  (Fig. 1), consistent with a viscous boundary layer whose thickness is independent of landslide volume (Eqs (13) and (15)). To distinguish the cases when H is volume independent (Eq. (13)) or proportional to  $V^{1/3}$  (Eq. (15)), the energy equation (Eq. (2)) can conveniently be rewritten as

$$L \sim \rho g H V / (\tau A) \quad (17)$$

which, for  $A \propto V^{2/3}$  and  $\tau \propto U \propto z^{1/2} \propto V^{1/6}$  reduces to

$$L \propto H V^{1/6} \quad (18)$$

Hence, Eq. (18) gives for H independent of volume

$$L \propto V^{1/6} \quad (19)$$

and for  $H \propto V^{1/3}$

$$L \propto V^{1/2} \quad (20)$$

As shown in Figure 1, the actual variation of runout length with volume closely follows an  $L-V^{1/2}$  trend. The bulk behaviour of sturzstroms is thus consistent with (1) emplacement on a viscous boundary layer whose thickness does not depend on landslide volume, and (2) collapse geometry which favours an approximate cube-root volumetric dependence of the vertical drop height (Fig. 1).

#### *Halting a sturzstrom*

As noted above (Eq. (6)), a true viscous boundary layer will stop only if it has been halted by an external barrier or has become infinitesimally thin. In the first case, runout lengths will be controlled by topographic irregularities, for which it is difficult to perceive why  $L$  should show any dependence on landslide volume. The second case assumes that the top of a boundary-layer is controlled by an horizon of material too strong to be deformed. Such a control would require restricted variations in the nature of the materials forming sturzstroms, a characteristic inconsistent with their formation in most common rock types.

Alternatively, the apparent viscous control may reflect rapid deformation of a Bingham fluid (Eq. (7)), for which the viscous stress ( $\eta \, du/dy$ ) dominates the yield strength ( $\tau_y$ ) for most of the landslide's emplacement. If so, a sturzstrom may suddenly come to rest once the viscous stress has decreased (as velocity decreases) below a critical fraction of  $\tau_y$ . Indeed, such behaviour is consistent with eye-witness accounts of the 1881 Elm sturzstrom which, having travelled some 2 km in less than one minute, halted within seconds of its arrival in Elm (Hsü, 1975, 1978).

#### *Boundary layers and local deformation models*

Concentrated granular flows behave as simple viscous materials when energy dissipation is controlled by frictional contact between fragments (Fig. 4). Bagnold (1954) described such behaviour as *macroviscous* deformation, and it is expected when the ratio of inertial to viscous stresses  $Ba$  (the Bagnold Number, or granular Reynolds Number) is smaller than a critical value.  $Ba$  is given by

$$Ba = [(D/S)^{1/2} \rho_f D^2 \, du/dy]/\eta_i \quad (21)$$

where  $D$  and  $S$  are the mean diameter of and spacing between colliding fragments (so that  $D/S$  increases with the volume concentration of fragments),  $\rho_f$  is the mean fragment density,  $du/dy$  is deformation rate, and  $\eta_i$  is the viscosity of interstitial fluid, considered to be a newtonian material. For  $Ba$  less than about 40, most energy is dissipated by deforming the interstitial fluid (liquid or fine grains) and deformation is macroviscous; for  $Ba$  greater than about 400, energy dissipation is determined by collisions between fragments (excluding fine material behaving as an effective interstitial fluid); and for  $Ba$  between 40 and 400, both dissipating mechanisms are important.

The viscous behaviour of sturzstrom boundary layers implied by bulk analyses is thus consistent with deformation in the macroviscous regime. However, of all the

terms in Eq. (21), only fragment density can be estimated with confidence, so it has not been possible to verify macroviscous behaviour using the Bagnold Number.

An alternative to macroviscous deformation, Kilburn and Sørensen (1998) considered collisional energy dissipation from a boundary layer, for which Bagnold's model yields for basal stress

$$\tau \propto (\Delta/D) (D/S)^2 \rho_f U^2 \quad (22)$$

where  $\Delta$  is the thickness of the boundary layer.

As with the preceding analyses, Kilburn and Sørensen (1998) assumed  $A \propto V^{2/3}$ ,  $U \propto (gH)^{1/2}$ , and  $H \propto z \propto V^{1/3}$ . They also assumed that the energy for fragmentation during collapse is proportional to the potential energy released, from which  $(D/S) \propto z^{1/2} \propto V^{-1/6}$ . With these assumptions, the collisional model yielded the observed trends  $H/L \propto V^{-1/6}$  and  $L \propto V^{1/2}$  (Fig. 1) only for a boundary layer thickening diffusively with time ( $\Delta \propto t_e^{1/2}$ ). Indeed, for this condition in particular, the indirect volumetric dependences of  $\Delta$  and of  $D/S$  counterbalance to give, from Eq. (22),  $\tau \propto U$ , equivalent to that expected from a viscous boundary layer whose thickness does not depend on landslide volume. The thickening collisional boundary layer thus *appears* to behave as a macroviscous boundary layer of fixed thickness and so, without independent testing of the assumptions concerning initial fragmentation and boundary-layer thickening (discussed later), it remains uncertain as to whether the collisional or macroviscous interpretation is the more realistic.

### Whole-body deformation of sturzstroms

Computer simulations of collapsing granular masses (Campbell et al., 1995) show that the key structural features of sturzstroms can be preserved even if the entire mass is actively involved in deformation. However, for deformation beyond a boundary layer to be significant to runout lengths, it must control the net rate of energy dissipation from the landslide. The analyses of whole-body deformation are similar to those above for boundary-layer flow, with the exception that the deforming thickness is now that of the whole landslide ( $h$ ) rather than that of the boundary layer ( $\delta$ ).

Given that  $h \propto V^{1/3}$ , Kilburn and Sørensen (1998) showed that the implied  $H/L$ - $V$  and  $L$ - $V$  relations for whole-body deformation in the collisional regime are not consistent with observation. For macroviscous flow, substitution of  $h$  for  $\delta$  yields  $\tau \propto V^{-1/6}$  (Eq. (9)),  $H/L \propto V^{-1/2}$  (Eq. (4)), and  $L \propto V^{1/2}$  for  $H$  independent of landslide volume, and  $L \propto V^{5/6}$  for  $H \propto V^{1/3}$  (Eq. (17)). Although the first lengthening trend agrees with observation, the required  $H/L$ - $V$  relation is not reasonable. Boundary layers are thus better candidates for controlling rates of energy loss from sturzstroms.

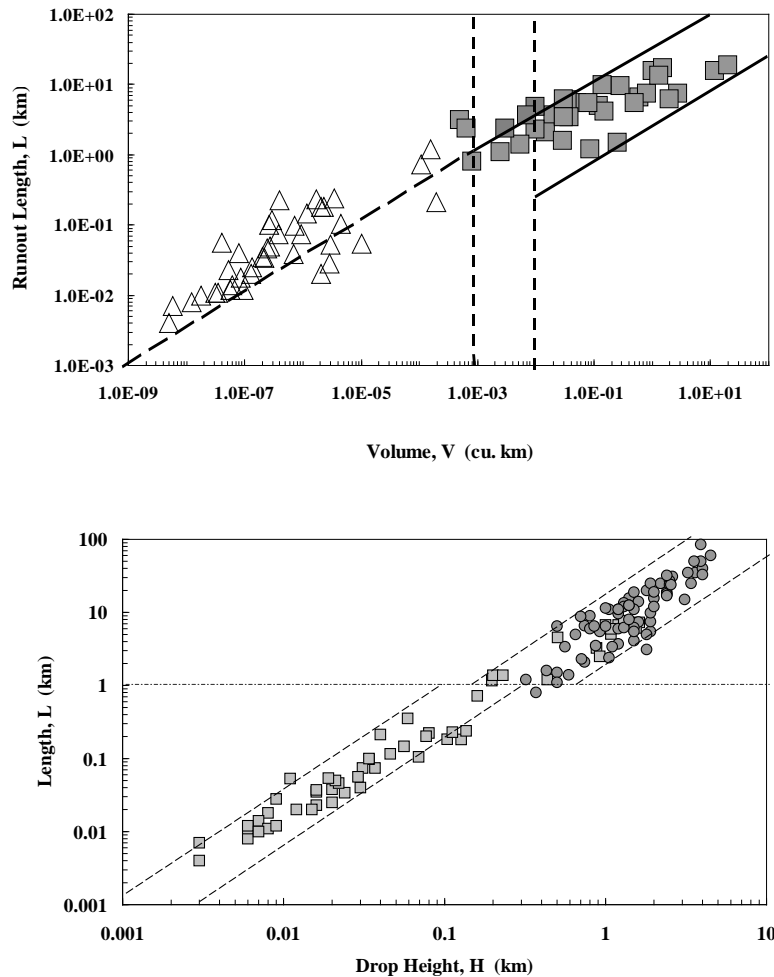


**Figure 6.** Assessing sturzstrom hazard. Limits from the boundary-layer models (Eqs (20) and (24)) link potential runout length to (a) landslide volume and (b) drop height. Estimates of either  $V$  or  $H$  before collapse provide forecasts of the probable distance that a landslide will travel. Note (1) that small landslides and sturzstroms follow parallel trends, with jumps at volumes of about  $10^6 \text{ m}^3$  and corresponding runout lengths of about 1 km, and (2) that backward extrapolation of the sturzstrom trend would tend to *underestimate* the distance actually travelled by small landslides (see text for discussion).

## Discussion

The primary volumetric dependencies of  $H/L$  and of sturzstrom runout can be explained most easily if a landslide loses energy at a rate controlled by an effectively viscous boundary-layer. Sudden halting can then be attributed to a boundary-layer yield strength which only becomes significant once the applied basal stress becomes sufficiently small. Melosh (1986, 1987) argued that acoustic fluidisation could induce apparent plasticity (strictly pseudoplastic behaviour) in a granular mass. It is thus possible that such fluidisation might contribute to sturzstrom behaviour, but it is not necessarily an *essential* feature of sturzstroms.

Hsü (1975) interpreted sudden halting in terms of a time-dependent increase in landslide resistance. The Bingham interpretation, in contrast, appeals to a stress dependence on resistance: above a threshold applied stress, the landslide boundary layer behaves as a viscous fluid; below the threshold, it behaves as a more resistant plastic. Since sturzstroms spread and become thinner with time, it is difficult from field observation to distinguish (a) an increase in resistance due to decreasing stress from (b) an increase in resistance due to the time for which the boundary layer has been deforming. The Bingham interpretation is preferred here by virtue of simplicity.

#### *The number and thickening of boundary layers.*

Although attention has been focused on a basal boundary layer, similar H/L-V and L-V relations are expected if deformation also occurs along additional narrow horizons within a sturzstrom. In this case, the bulk rheological properties and effective boundary-layer thickness will represent an average rheology and thickness for all deforming horizons. Deformation bands within sturzstroms (Figs. 2a and 5d) are thus consistent with the boundary-layer hypothesis.

The two boundary layer models for an effective viscous response assume either macroviscous flow ( $Ba \leq 40$ ) with an effective boundary layer whose thickness is independent of volume, or collisional flow ( $Ba \geq 400$ ) with an effective boundary layer that thickens diffusively with time (Kilburn and Sørensen, 1998). While diffusive thickening is plausible, its effect may be counterbalanced by the general thinning of a sturzstrom as it spreads during emplacement. It is common for sturzstroms to thin to about one-tenth to one-twentieth of their starting values. Assuming that thinning occurs uniformly, then boundary layer thickening will only be important if the ratio of final to initial boundary layer thicknesses is much greater than 10-20. Taking a ratio of 100, the minimum emplacement time becomes about  $100^2$  times the time for the initial boundary layer to develop. Since giant slope collapse occurs on the order of seconds, the *minimum* implied emplacement time is  $\sim 10^4$  s, or about half an hour, much longer than the few minutes observed. Thus the importance of diffusive thickening remains debatable, so favouring the macroviscous boundary-layer model.

#### *Boundary layers and the minimum volume for sturzstroms.*

If it is better to interpret sturzstrom behaviour in terms of boundary-layer deformation rather than sliding, the same question can be posed for landslides in general (Kilburn et al., 1999). Figure 6 extends the length-volume behaviour of landslides from sturzstrom volumes to values as small as  $10 \text{ m}^3$ . The data show that, as for sturzstroms, small landslides also follow an  $L-V^{1/2}$  trend. However, backward extrapolation of the sturzstrom trend underestimates the potential runout distance of landslides smaller than  $\sim 10^6 \text{ m}^3$ . As discussed by Kilburn et al. (1999), the form of the small-landslide trend is consistent with viscous boundary-layer deformation, while the jump in trends at  $\sim 10^6$ - $10^7 \text{ m}^3$  implies a major change in emplacement conditions. Assuming that boundary-layer deformation is common among all landslides, the change in trends most likely reflects a change in the rheology of the deforming medium. Small landslides typically consist of solids within a clay or mud matrix (Iverson, 1997), while sturzstroms tend to have finely granular matrices. The change in behaviour at  $\sim 10^6$ - $10^7 \text{ m}^3$  may thus correspond to the need for most rapid giant landslides to crumble rock before they can form: large volumes need deep failure horizons to initiate collapse and, in general, any failure deeper than  $\sim 10 \text{ m}$  is likely to involve the fracturing of intact crust. The threshold volume for sturzstroms can thus be linked to the typical structure of mountainsides on Earth (Kilburn et al., 1999).

#### *Interpreting the ratio H/L.*

The original interpretation of H/L as a friction coefficient assumed that landslides behave as rigid blocks and that their vertical drop heights are independent of landslide volume. Neither assumption is reasonable. As soon as sturzstroms are considered to deform on viscous boundary layers and to have drop heights that vary with the cube root of their volume, then (a) frictional losses will depend on both boundary-layer

rheology *and* deformation rate, and (b) landslide velocity (and, hence, deformation rate) will increase with volume through its dependence on drop height ( $U \propto H^{1/2} \propto V^{1/6}$ ). The new assumptions also yield that the emplacement time  $t_e \sim L/U$  increases with  $V^{1/3}$ . Hence large sturzstroms travel further than smaller ones because they normally have higher velocities as well as longer times available to lose energy through a boundary layer. Expressing H/L as

$$H/L = \tau A / (\rho g V) = \text{Mean rate of momentum loss per unit weight} \quad (23)$$

it emerges that the inverse volumetric dependence of H/L occurs not because the inherent resistance of landslide material decreases, but because (1) H/L reflects momentum loss per unit weight of the *whole* sturzstrom and (2) the frictional losses are concentrated within only a portion (the boundary layer) of the sturzstrom and these increase with  $V^{5/6}$  rather than with the total landslide volume. Thus, as sturzstroms become larger, an increasing proportion of their volume contributes to the momentum and energy available for transport without also contributing to frictional loss.

#### *Reducing the risk from sturzstroms.*

Since sturzstroms are highly destructive and emplaced within minutes, it is virtually impossible at present to conceive of defence measures involving protective barriers or bunkers. The most efficient strategies are to evacuate exposed populations before slope collapse or to prevent inhabitation of vulnerable districts. In either case, it is essential reliably to estimate the potential runout length of a sturzstrom.

By quantifying the trend between runout length and volume, Eq. (20) provides a physical justification for constraining observational data between the limits shown in Figure 1. Thus, once the volume of an unstable mass has been estimated, the L-V limits can be used to identify zones at risk. If the unstable volume is unknown, Eqs (15) and (20) can be combined to yield (Fig. 6)

$$L \propto H^{3/2} \quad (24)$$

from which potential runout lengths can be estimated using topographic constraints on drop height.

A drawback of using the L-V and L-H trends in Figures (1) and (6) is that the limits embrace a considerable scatter about mean trends. Most of the scatter can be attributed to variations in collapse and sturzstrom geometry (for linking H, z, A and h to V), boundary layer dimensions ( $\delta$ ) and rheology ( $\eta$ ), and the effects of topography for either blocking or channelling a landslide (Kilburn and Sørensen, 1998). Improving measurements to reduce the scatter is a major goal for future studies.

#### **Conclusions**

The essential features of sturzstrom emplacement can be explained if they lose kinetic energy through viscous deformation in one or more boundary layers. The boundary layers consist of rock fragments in a fine grained rock matrix. The matrix may behave as a fluid with a yield strength that brings sturzstroms to a rapid halt once driving stresses in the boundary layer become smaller than a critical value. These interpretations justify Hsü's postulate that sturzstroms behave as fragmental masses (Hsü, 1975), a model which, after nearly a quarter-century of alternatives seeking

exotic mechanisms for sturzstrom transport, has reemerged as the one yielding the most reasonable results.

## References

- Bagnold RA 1954. Experiments on a gravity free dispersion of large solid particles in a Newtonian fluid under shear. *Proc Royal Soc London A*, 225: 49-63.
- Campbell CS 1989. Self lubrication for long runout landslides. *J Geol*, 97: 653-665.
- Campbell CS, Brennan CE 1985. Computer simulation of granular shear flows. *J Fluid Mech*, 151: 167-188.
- Campbell CS, Cleary PW, Hopkins M 1995. Large-scale landslide simulations, global deformation, velocities and basal friction. *J Geophys Res*, 100: 8267-8283.
- Dade WB, Huppert HE 1998. Long-runout rockfalls. *Geology*, 26: 803-806.
- Erismann TH 1979. Mechanisms of large landslides. *Rock Mech*, 12: 15-46.
- Goguel J 1978. Scale-dependent rockslide mechanisms, with emphasis on the role of pore fluid vaporization. In *Rockslides and Avalanches 1. Natural Phenomena* (ed. Voight B), 693-708. Elsevier, New York.
- Habib P 1967. Sur un mode de glissement des massifs rocheaux. *CR Acad Sci*, 264: 151-153.
- Hayashi JN, Self S 1992. A comparison of pyroclastic flows and debris avalanche mobility. *J Geophys Res*, 97: 9063-9071.
- Heim A 1882. *Der Bergsturz von Elm*. *Deutsch. Geol. Gesell. Zeitschr.*, 34: 74-115.
- Heim A 1932. *Bergsturz und Menschenleben*. 218 pp. Fretz und Wasmuth, Zurich.
- Hendron AJ, Patton FD 1985. The Vaiont slide, a geotechnical analysis based on new geologic observations of the failure surface, Vol. 1. Tech Rept GL-85-5, US Army Corps of Engineers, Washington DC.
- Hewitt K 1988. Catastrophic landslide deposits in the Karakoram Himalaya. *Science*, 242: 64-67.
- Hoek E, Bray JW 1981. *Rock Slope Engineering* (3<sup>rd</sup> Edn, Rev.). 358 pp. E&FN Spon, London.
- Howard KE 1973. Avalanche mode of motion, implication from lunar examples. *Science*, 180: 1052-1055.
- Hsü KJ 1975. On sturzstroms - catastrophic debris streams generated by rockfalls. *Geol Soc Am Bull*, 86: 129-140.
- Hsü KJ 1978. Albert Heim: Observations on landslides and relevance to modern interpretations. In *Rockslides and Avalanches 1. Natural Phenomena* (ed. Voight B), 71-93. Elsevier, New York.
- Iverson RM 1997. The physics of debris flows. *Rev Geophysics*, 35: 245-296.
- Iverson RM, Schilling SP, Vallance JW 1998. Objective delineation of lahar-inundation hazard zones. *Geol Soc Am Bull*, 110: 972-984.
- Kent PE 1966. The transport mechanism in catastrophic rockfalls. *J Geol*, 74: 79-83.
- Kilburn CRJ, Sørensen SA 1998. Runout lengths of sturzstroms: the control of initial conditions and of fragment dynamics. *J Geophys Res*, 103: 17877-17884.
- Kilburn CRJ, Zanin A, Solana MC, Mantovani F, Corominas J 1999. The volumetric control on sturzstrom formation.
- Lockner DA 1995. Rock failure. In *Rock physics and phase relations, a handbook of physical constants*, AGU Ref Shelf 3 (ed. Ahrens, TJ), 127-147.
- McSaveney MS 1978. Sherman glacier rock avalanche, Alaska, USA. In *Rockslides and Avalanches 1. Natural Phenomena* (ed. Voight B), 197-258. Elsevier, New York.
- Melosh HJ 1979. Acoustic fluidization: a new geologic process? *J Geophys Res*, 87: 7513-7520.
- Melosh HJ 1986. The physics of very large landslides. *Acta Mech*, 64: 89-99.

- Melosh HJ 1987. The mechanics of large rock avalanches. *Rev Eng Geol* VII, 41-49.
- Pierson TC, Costa JE 1987. A rheological classification of subaerial sediment-water flows. *Geol Soc Am, Rev Eng Geol*, 7: 1-12.
- Shreve RL 1968. The Blackhawk landslide. *Spec Paper Geol Soc Am*, 108: 1-47.
- Straub S 1996. Self-organization in the rapid flow of granular material, evidence for a major flow mechanism. *Geol Rundsch*, 85: 85-91.
- Straub S 1997. Predictability of long runout landslide motion: implications from granular flow mechanics. *Geol Rundsch*, 86: 415-425.

### **3. Modelling fragment interaction within sturzstroms**

#### **Introduction**

Analytical studies in Chapter 2 have shown that the bulk dynamic features of sturzstroms can be explained in terms of conventional fragmental flow models. These studies, however, have not investigated the detailed nature of potential interactions among fragments. Detailed analyses are required not only to test key assumptions of the analytical models, but also to develop the capability of realistically simulating the dynamics of giant, catastrophic landslides.

This chapter describes the principles underlying a new three-dimensional simulation of sturzstroms, using the contact force paradigm introduced by Cundall and Strack (1979). Implications for understanding sturzstrom emplacement are discussed in Chapter 5 in relation to the K fels landslide. The simulation generalises the Cundall-Strack method to three dimensions and introduces the interaction sphere, a generic object that replaces simple spherical particles. This change has supplied a platform on which to create additional interaction scenarios. Two such scenarios employing stochastic collisions have been implemented. The application also introduces the concept of neighbourhoods and uses this concept both to improve performance and to parallelise the problem to allow the use of modern, distributed, multiprocessor systems. The work on parallel processing is still at the testing stage and it is too early to tell how well the problem scales.

#### **The model**

The distinct element method uses discs or spheres to model granular systems. The momentum exchange between colliding particles is accomplished through the introduction of a contact force proportional to the distortion of participating particles (in reality the overlap of the spheres). This divides the problem into two separate tasks: (1) solving Newton's second law, and (2) calculating the forces acting on individual particles.

The first task is identical to that encountered in collisionless models and existing numerical methods can easily be applied. The difference between the task facing us here and classical implementations like models of planetary systems, galaxies or star clusters is the severe restriction the contact forces place on the time step. The numerical integration will typically use time steps that are several orders of magnitude smaller than those used when collisionless models are evaluated. The resulting increase in processing time is exacerbated by the need to re-evaluate the forces acting on every particle during each time step. As this evaluation can be extremely time consuming, it is important that care is taken to perform the task efficiently.

#### **Newton's second law**

Cundall and Strack's physical model approximates the particles in a granular material - complex multifaceted bodies - with smooth uniform spheres. This simplifies the task of calculating contact forces but is at the same time restricting the range of interaction scenarios that can be considered. To overcome this problem, we introduce the concept of an interaction sphere. The centre of this sphere coincides with the centre of mass of a granular particle and its radius marks the boundary of the particle's physical extend. The interaction sphere is not itself associated with the calculation of contact forces. Rather, it is a generic object that indicates where such forces can arise.

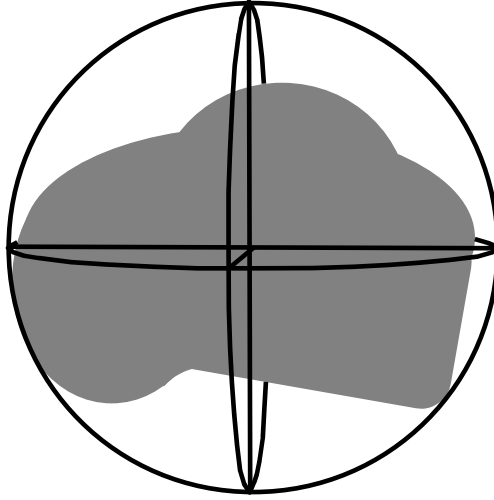


**Figure 1.** Rock with associated interaction sphere

From a dynamic perspective the spheres are Newtonian particles with mass  $M$ , linear momentum  $\vec{P} = (Mv_x, Mv_y, Mv_z)$  and angular momentum  $\vec{L} = (I_x \omega_x, I_y \omega_y, I_z \omega_z)$ , where  $(I_x, I_y, I_z)$  are the principal moments of inertia. The spheres move independently of each other guided only by Newton's second law and the forces, including contact forces, which act on them. The progress of the interaction spheres is calculated using standard numerical techniques. Here we have employed a fourth-order step-by-step difference scheme developed by R. de Vogelaere (1955) to integrate the second order differential equation

$$m \frac{d^2 x_i}{dt^2} = F_i \quad (1)$$

While a first order scheme is used to integrate the angular momentum equation

$$\frac{d^2 L_i}{dt^2} = M_i \quad (2)$$

where  $M$  is the torque about the centre of mass resulting from shear stresses.

The Newton solver thus perform the integration using the following scheme:

$$x_1 = x_0 + hv_0 + \frac{h^2}{6}(-f_{-1} + 4f_0) \quad (3)$$

$$L_1 = L_0 + hM_0 \quad (4)$$

$$f_1 = F(x_1, t_1) \quad (5)$$

$$x_2 = x_0 + 2hv_0 + \frac{h^2}{3}(2f_0 + 4f_1) \quad (6)$$

$$L_2 = L_1 + hM_1 \quad (7)$$

$$f_2 = F(x_2, t_2) \quad (8)$$

$$v_2 = v_0 + \frac{h}{3}(f_0 + 4f_1 + f_2) \quad (9)$$

where  $h$  is the time step.

### Contact forces

The interaction sphere forms a generic base class common to all interaction scenarios. It contains only the particle variables and the methods associated with the integration scheme. From this class we use inheritance to add interaction information and create specific granular particle classes. Three such classes have so far been developed. One is the traditional interaction model where rocks are represented by smooth spheres. In the other two, some of the interaction variables are assumed to be stochastic variables rather than constants.

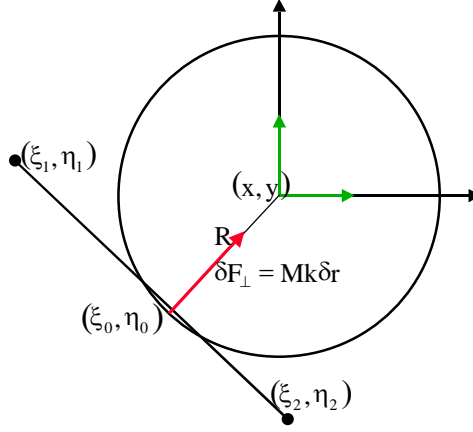


**Figure 2.** Normal force and contact forces during particle-wall encounter

The calculation consists of two distinct classes: Granular particles and walls. Contact forces may arise either when two interaction spheres overlap or when a wall intersects a sphere. The value of these contact forces depends on the exact particle class being used. Examples of the three interaction types are given below. All examples are limited to two dimensions because three-dimensional illustrations tend to be confusing and expansion from two to three dimensions is largely trivial.

### Uniform spheres

An example of a particle-wall collision is shown in Figure . The particle is situated in  $(x, y)$  and the wall extends from  $(\xi_1, \eta_1)$  to  $(\xi_2, \eta_2)$ . A vector through  $(x, y)$ , perpendicular to the wall will intersect the wall at  $(\zeta_0, \eta_0)$ . If the point is part of the line segment  $((\xi_1 \leq \xi_0 \leq \xi_2) \wedge (\eta_2 \leq \eta_0 \leq \eta_1))$  and the distance  $R_0 = \sqrt{(x - \xi_0)^2 + (y - \eta_0)^2}$  is smaller than the particle radius, contact forces will arise. The force perpendicular to the wall is  $\delta F_{\perp} = Mk\delta r$  where  $\delta r$  is the overlap and  $k$  is the normal stiffness. Figure shows the forces along the plane where we assume Coulomb-type friction. As long as the relative velocity between particle and wall  $v_R = v_{\parallel} - \omega R \neq 0$ , the particle will be skidding along the wall and we will have a force  $\delta F_{\parallel} = \mu\delta F_{\perp}$  acting on the particle, where  $\mu$  is the coefficient of friction. The force acts on the linear momentum  $Mv_{\parallel}$  and introduces a torque  $R\delta F_{\parallel}$  that in turn change the angular momentum.

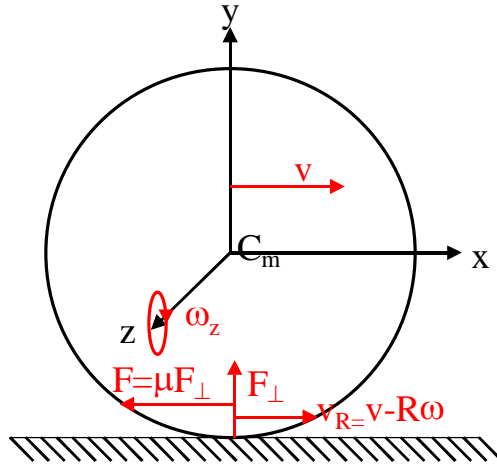


**Figure 3.** Shear forces during particle-wall encounter.

If  $(\xi_0, \eta_0)$  does not form part of the wall but is within a distance  $R$  from one of the end points, the connection line will no longer be perpendicular to the wall and the vectors  $\delta F_{\parallel}$  and  $v_{\parallel}$  are now perpendicular to the connection line rather than parallel to the plane. Particle-particle collisions are treated in the same way as particle-wall encounters except that both particles are subjected to identical but opposite forces.

The system allows for normal damping during a collision by using different stiffness factors when the particles are approaching and when they are receding. In this case the particle will not regain all the lost momentum. A damping factor of zero will correspond to momentum conservation while a collision with a factor of one is inelastic.

### Stochastic spheres

This class is similar to the classical spheres outlined above except that the impact no longer is calculated purely from the geometric values. The absolute value of the normal force is the same but it is no longer assumed to be normal. Instead it is twisted by an angle  $\alpha$ . The angle is constant throughout an encounter but between collisions it is considered a stochastic parameter with a normal distribution around zero. The distribution has a low standard deviation and is truncated so that values with a z-score above 3 are prohibited. The forces are imposed on the centre of the sphere and will therefore only impact directly on the linear forces although the friction force will be changed because the normal force is decreased. The reason for introducing this class is to take into account the surface structure of the particle. The actual shape of a particle should not be taken into account, as that would limit the validity of an experiment to a very specific set of initial conditions. With the introduction of a stochastic element to collisions, the assumption of uniform spheres has been broken and the experiments made more general.

### Fully stochastic particles

The stochastic interaction class is an extension of the stochastic spheres. Here all the contact related parameters are assumed to have a stochastic contribution. As with the class above, the evaluation of the stochastic contribution is not performed at every force evaluation but fixed through each encounter.

## Fragmentation

One of the areas under investigation is the impact of particle fragmentation. Fragmentation takes place when the energy imposed on a particle by the contact forces exceeds a given threshold. The particles are then replaced by a number of smaller particles as seen in Figure 4. The fragments all have non-overlapping interaction spheres that do not extend outside the boundaries of the original sphere and the force balance is therefore left undisturbed.

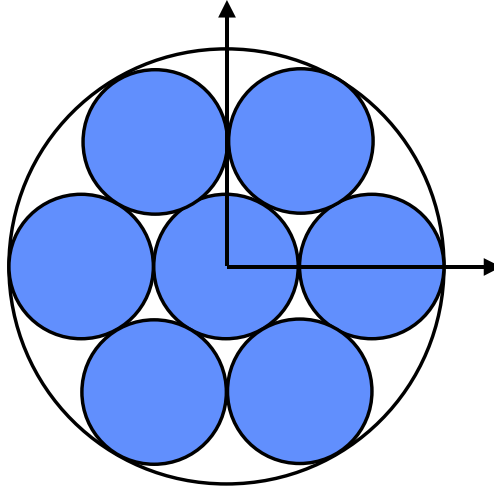


**Figure 4.** Particle fragmentation into seven objects.

Each of the  $n$  fragments contains the mass  $M/n$  and the linear momentum  $\vec{P} = \left( Mv_x/n, Mv_y/n, Mv_z/n \right)$ . In the current implementation, angular momentum is not transferred to the fragments, nor is the angular momentum of the original particle assumed to influence the linear momentum of the fragments. The fragmentation process is hierarchical and will continue until the resulting particles have exceeded a lower limit imposed on the model.

## Performance issues

As mentioned above, the most costly part of the evaluation is the calculation of contact forces. From a performance viewpoint, the problem can be divided into two separate tasks. One involves the search for overlapping spheres while the other involves the contact forces calculation that must be performed when an overlap is detected. The latter task is fairly straightforward. The only major performance enhancement comes from the fact that the load presented by the preparatory processing is a significant part of the total processing load for this task. It is therefore important that contact forces are calculated for both the particles in a collision whenever possible.

## Particle families

A more important problem is the search for overlapping spheres. For systems involving only a small number of particles it may be possible to go through every pair and check for overlap. For a system containing  $N$  particles, this will require  $N^2/2$  comparisons, and most of these will be wasted as a particle only has the potential of

interacting with a very small number of particles in its direct neighbourhood. There is consequently scope for wasting a lot of processing effort, even though the amount of processing per pair is small.

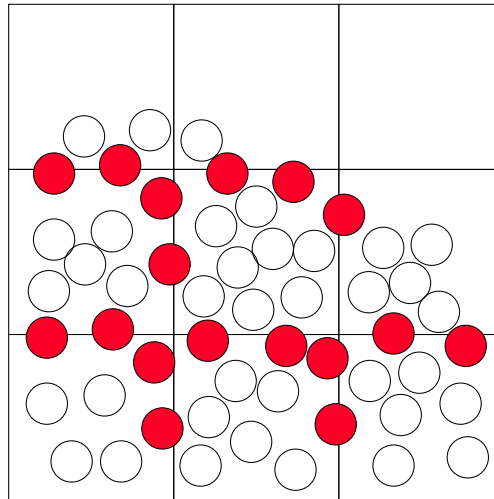


**Figure 5.** Neighbourhood grid with puritans (white) and tarts (dark).

Performance can be improved considerably if the search for overlaps is reduced to the immediate neighbourhood. To accomplish this, we take the volume that initially bounds the particles forming the slide and divides it into a grid of smaller cells. An example of such a grid is shown in Figure 5. Each cell in this grid is rectangular with sides parallel to the co-ordinate axes. The smallest dimension of a cell must be at least twice the diameter of the largest interaction sphere, although they tend to be significantly larger in practice. The cells divide the granular material into neighbourhoods and thus reduce the search for overlapping pairs. The gain depends on gridsize and particle distribution but is typically two to three orders of magnitude.

Spheres belong to a neighbourhood when their centres are inside the defining volume. A neighbourhood contains two types of members: puritans and tarts. A puritan particle is completely embedded in the volume defining its neighbourhood and it is therefore only necessary to compare it against puritans in the same area. Tarts on the other hand have part of their sphere in more than one neighbourhood and consequently have to be compared to all of these. The division into two types is essential because the contact forces are calculated simultaneously for both particles involved in an overlap. It is therefore crucial to avoid considering the same pair twice as that would cause the force field to be distorted.

Walls can also belong to neighbourhoods although this has not been implemented in the current version. The reason is that we in the current study have considered fairly simple landscape shapes and consequently only employed a limited number of wall elements.

The procedure of forming neighbourhood families consists of two checks. One is to establish which neighbourhood a particle belongs to and the other to establish whether the particle is a puritan or a tart. Both checks are simple and require very limited processing. With respect to the grid itself, we are faced with two options. One is to use a fixed grid throughout the simulation and the other to implement a dynamic grid. Currently we are using the dynamic option where only active cells are represented. Although there appear to be a potential performance problem with the management of such a scheme, the overhead is limited because the configuration

change very slowly and grid reconfigurations are therefore rare. Parallel processing considerations may indeed tilt the argument further in favour of a dynamic grid as discussed below.

### **Parallel processing**

The introduction of particle types and a neighbourhood grid is the first step towards a distributed processing environment. The approach we have taken is to use the grid as the basis for a coarse grain, processing model. Only limited restructuring is needed in order to implement this change. The main change is to distribute the neighbourhood cells among the available processors. In addition, we have introduced a mechanism for transferring tart-information from processor to processor. This breaks the principle that each pair of spheres only can be evaluated once, but as the evaluation is done in parallel on separate processors the overhead is limited.

Where the parallel processing environment has the highest impact on the processing speed is in securing that the loading of individual processors is balanced. Here the advantage of dynamic grid management becomes clear. Where a fixed grid configuration makes it difficult to optimise the load, a dynamic scheme allows volumes to be reshuffled for better performance. How well this will scale is still an open question. If the load sharing can be performed efficiently, the problem should in theory scale perfectly. At present we have only performed experiments on an eight-processor Beowulf. For a machine of that size, the load sharing can to a certain degree be performed manually based on the user's knowledge of the models involved. We have so far not invested any effort in developing a generic version of the balancing tool and it is still unclear whether the general scaling problem can be solved.

### **Testing**

The system was initially tested using smooth spherical rocks with conservation of linear momentum. The test environment used was the "billiard table" with perfect cushions. The models used periodic orbits involving both particle-particle and particle-wall collisions. This the model accuracy to be tested simply by monitoring the changes in energy during the tests. Tests involving the stochastic interaction model will also conserve energy if damping is disabled. They will, however, not support periodic orbits and it was therefore only possible to perform testing with energy and momentum conservation tests. The software was also tested against appropriate model results published by Cleary and Campbell and found to be in good agreement. Implications for the model applied to real data are discussed in Chapter 5.

### **References**

- Cundall, PA, Strack, ODI 1979. *Geotechnique*, 29: 47.  
de Vogelaere, RJ 1955. *Res. Nat. B. Stan.*, 54: 119.

## 4. The Vajont landslide, Italy

### Introduction

The Vajont reservoir in Italy's northeastern Alps is located along the lower reaches of the Vajont river, close to its confluence with the River Piave. Some 100 km NNW of Venice, the reservoir was created artificially in 1960 after the Vajont river was dammed as part of a regional expansion in hydroelectric-power generation. The dam, 265 m high and 160 m across its top, was at the time of construction the highest and one of the most advanced double-arched dams in the world. Filling of the reservoir destabilised its southern margin, Mt Toc which, after nearly three years of intermittent creeping, catastrophically collapsed at 22.39 on 09 October 1963. Within 30-40 seconds, some 270 million m<sup>3</sup> had crashed into the reservoir (Fig. 1), expelling the water with a wave about 100-150 m over the dam. The wave crashed through the town of Longarone and neighbouring villages, claiming more than 2,000 victims.

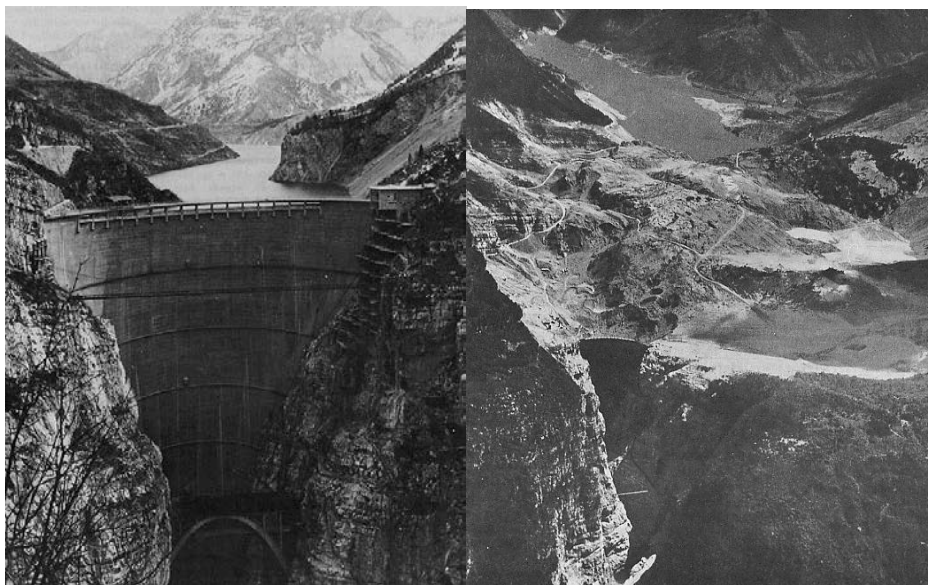


**Figure 1.** The Vajont dam before (*left*) and after (*right*) the 1963 collapse of Mt Toc

Mt Toc was more vulnerable to instability than expected since its outer flanks consisted of an ancient landslide deposit and not bedrock as initially inferred. Giudici & Semenza (1960) first proposed that Mt Toc was covered by an ancient landslide, citing a mylonitic belt and the remains of a slide with an abnormal attitude on the opposing north side of the valley, isolated by the gorge cut by the Vajont river. They also identified another massive ancient landslide, La Pineda landslide, upstream from the Vajont collapse, which had previously dammed the Vajont river to produce a natural lake.

The geomorphology and structure of the Vajont landslide and surrounding district has been completely remapped at a scale of 1:5,000 (see accompanying CD ROM). The results not only identify zones of potential future instability, but also provide a framework for interpreting the mechanisms leading to sudden catastrophic collapse (Chapter 1).

### Geomorphology

The report by Semenza & Giudici (1965) has been taken as the starting reference for geomorphological evaluations of the Vajont area. These authors suggested that during the last deglaciation the lower reaches of the Vajont river were completely truncated by a northeast directed landslide. The river subsequently cut a new path through the easily erodable landslide deposit, producing the deep and narrow Vajont gorge that today decreases over a vertical drop of 240 m

from widths of 150 m to 20 m. The current E-W trend of the valley follows that of its pre-glacial, predecessor, determined in turn by a regional tectonic trend. The topography of the area changed enormously following the 1963 collapse, especially infilling of the gorge with loose landslide material consisting of morainic deposits, ancient alluvial deposits (fluvial and torrential), sometimes cemented, and slope debris, all of Quaternary age.

### *Geomorphological map*

In the Vajont valley and the adjacent mountain group formation, outcrops range in age from the Upper Trias (Dolomia Principale) to Middle Eocene (Flysch). During the Lower Lias the area was part of a basin in which cherty micrites with pelagic fauna accumulated. Interbedded are calcarenites and oolitic or bioclastic calcirudites that were driven into the basin by gravity currents from platforms around the basin margins. Indeed, most of the characteristic differences between formations reflects variations in the material being derived from the marinal platforms. The following sections describe the geological and geomorphological units distinguished on the map. For simplicity, these units have been grouped as (1) bedrock, (2) the 1963 landslide and (3) glacial and periglacial deposits.

### *Bedrock*

- **FLYSCH** (Eocene; > 200 m thick) A succession of turbiditic arenites intercalated with mudstones. The arenitic fraction is represented by calcarenites passing to grey or yellow litharenites; the mudstones are formed by marls and grey marly clays.
- **MARLS OF ERTO** (Paleocene; 100-150 m thick) This informal unit represents the transition between the Scaglia Rossa and the Flysch and is formed by marls and subordinate grey marly limestones, intensely bioturbated, containing rare thin layers of calcarenites and litharenites.
- **SCAGLIA ROSSA** (Upper Cretaceous; ~300 m thick) Monotonous succession of marls and red marly limestones, completely lacking of gravity resediments in the typical facies of Scaglia. This formation equalized the pre-existing topography because it lays evenly the whole of the area.
- **SOCCHER LIMESTONE** (Lower-Upper Cretaceous; 150 m thick) An alternation of microcrystalline limestones, calcarenites and bioclastic-intraclastic calcirudites coming from the Friuli platform. The fine component is represented by decimetric layers of micrites, marly micrites and marls, that can be grey, red or greenish with nodules and beds of chert. Some micrites belong to the Rosso Ammonitico facies. There are numerous intraformational discordances interpreted as slump scars. The coarser components of the slump material can be further subdivided into bioclastic calcarenites and conglomerates-and-breccias that are sometimes associated with stratigraphic unconformities. The breccias and conglomerates are characterized by great lateral continuity and are visible in the mass which slid from Mt Toc.
- **ROSSO AMMONITICO** (Kimmeridgian Tortonian; 5-15 m thick) Nodular reddish and grey micrites with ammonites, occurring as massive units or as layers of more than 1 m thick that differ only in colour from the classic facies outcropping in the Veneto area.
- **FONZASO FORMATION** (Oxfordian; 10-40 m thick) The complex succession of levels between the Vajont Limestone and the Scaglia Rossa have been attributed to the Socchèr Limestone. In the stratigraphic interval corresponding to this formation it is nevertheless possible to distinguish lithologies that are easily attributable to the classic formations that in the Veneto area are called Fonzaso Formation, Rosso Ammonitico and Biancone. For this reason it is better to save such denominations and only use the formational term of Socchèr limestone exclusively for the Cretaceous succession corresponding elsewhere to the Biancone. The Fonzaso Formation is formed by finely graded biocalcarenes and chert-rich, brown micritic limestone in beds 5-20 cm thick with parallel and oblique laminae. Interbedded layers of green

claystone (5-10 cm thick) are of particular interest because of their role in the movement of the Vajont landslide.

- **VAJONT LIMESTONE** (Dogger; 450 m thick) Hazelnut oolitic calcarenites, massive or layered in thick beds, intercalated with decimetric layers of brown basal micrites and intraformational breccias (clasts formed from the erosion of the micrites); the latter are more frequent in the upper part of the formation. Nodules and beds of brown chert can be locally present. Sedimentary structures are represented by graded beds with parallel or oblique laminae.

#### *The Vajont landslide*

The Vajont landslide deposits can be divided into three kinematic subunits, following the order of events during the 1963 collapse.

*Subunit A* describes the northernmost part of the landslide which, now infilling the valley, was the originally at the toe of the unstable slope and represents the material that displaced water from the Vajont reservoir. It consists of a single mass of layers strongly deformed during collapse. All prefailure vegetation has been removed. However, it has been possible map the principal surface fractures and prefailure surface material which survived the return water wave after collapse (ancient collapse and glacial deposits). These features are interspersed with zones of fragment accumulation – the fragments being poorly-sorted mixtures ranging in size from gravel to blocks – produced during deposition from the return wave. Depressions are also visible along its western margin, above the dam.

*Subunit B.* Intermediate unit between the present failure scarp (at higher elevation) and subunit A below. Prefailure vegetation is visible, trees showing classic landslide deformation marks along their trunks. There is no evidence of significant interaction between this unit and waves produced by the collapse – consistent with a second-stage collapse shortly after displacement of subunit A.

*Subunit C.* The portion of the landslide directly against the dam, south of state road 251 (Val Cellina-Val di Zoldo) and north of subunit A. The surface is lower than that of subunit A and consists mainly of sand and gravel. The loose surface material completely covers the originally displaced slope (which underneath may be continuous with the adjacent subunit A) and appears to have been derived from fragments washed back onto the landslide by the return wave immediately after collapse.

#### *Glacial and periglacial deposits*

Glacial and periglacial deposits are distributed across the study area and can be related to the activity of three interconnected glaciers in the Vajont valley, the Lagaria valley and the Mesazzo valley. The Vajont deposits outcrop at Moliesa (800 m asl) and the 1963 collapse deposits. The Lagaria deposits can be found in the Case Liron district at the confluence of the Lagaria and Mesazzo rivers, within the Lagaria valley and near Marzana (650-700 m asl). The Mesazzo deposits occur within the Mesazzo valley at the level of Casera Costa Ortiche. The nature of the deposits are described below.

#### *The Vajont glacier*

- *Moliesa outcrops.* Diamaceous deposit of material derived from the surrounding Scaglia Rossa, Fonzaaso and Vajont Limestone units. The deposits consists of subrounded to angular clasts in a sandy matrix. Despite a low degree of weathering, primary sedimentary structures cannot be distinguished. They overlie cemented conglomerates showing the typical foreset and topset structures of deltas. The foreset dips 35° southeast; the topset is subhorizontal.
- **1963 collapse outcrops.** Unlike the Moliesa deposits, glacial material carried down from Mt Toc by the 1963 landslide contain well-rounded clasts of metamorphic rock which cannot have had a local origin. The simplest interpretation is that during the Wurm period by a major glacier along the Piave valley managing to branch some distance up the Vajont valley, leaving behind fragments gathered from further north.

### *The Lagaria glacier*

- *Lagaria valley outcrops*. Deposits with a very fine matrix supporting a wide variation in the proportion of clasts (from matrix-supported to clast-supported volumes). The locally-derived clasts (gravel-to-pebble sizes) are rounded, striated and unaltered. Given their position relative to the glacial cirque, these materials appear to be glacial till.
- *Case Liron outcrops*. Sandy diamaceous deposits containing unaltered subangular-to-subrounded clasts. The deposits show no stratification and the clasts are locally-derived: both these features suggest that the deposits were parts of lateral or terminal moraines.
- *Lagaria-Mesazzo confluence outcrops*. Intercalated clay and sand horizons without an organic component. While the finer material is white, the coarser sand has a pale hazelnut colour. The sequence shows a rhythmic lamination and includes drop stones, both features typical of a glacial lake environment beyond the front of a glacier. The deposits lie on erosive contacts above cemented conglomerates with subangular-to-rounded clasts, as well as foresets dipping 30° north and subhorizontal topsets. The sequence is interpreted as a deposit from glacial streams.
- *Marzana outcrops*. Rhythmic layering of clay-sand deposits to total thicknesses of as much as 15 m, indicating a deepening of glacial lake deposits to the east. The units are overlain by glacial stream gravels and till deposits.

### *The Mesazzo glacier*

Sandy diatomaceous deposits with predominantly subangular to subrounded clasts of calcareous gravel and pebbles. The material is clast-supported and appears to have been deposited as a moraine by a retreating glacier.

### **Summary**

Oriented along a regional structural trend, the Vajont gorge is a deep glaciated valley that was subject to landsliding after glacial retreat. The Vajont river eroded a new path through the weak landslide deposits, creating its modern morphology. Instability induced by filling the Vajont reservoir between 1960 and 1963 led to the massive collapse of Mt Toc, on the south side of the valley, in at least two sections. The first section expelled from the reservoir the water that erased Longarone. Water waves rebounding within the reservoir deposited sand and gravel over the lowermost landslide unit, but appears to have little effect on the displaced mass some 200 m above the original reservoir level. The 1963 collapse occurred within an earlier landslide deposit, itself dominated by limestone with clay horizons. The 1:5,000 geomorphological map is provided on the accompanying CD ROM. Implications of reservoir filling for forecasting catastrophic slope failure are discussed in Chapter 1.

## 5. The Köfels sturzstrom, Ötz valley, Austria

### Introduction

The Köfels sturzstrom is the largest landslide in the crystalline Alps (Figs 1 and 2). Failure occurred along a 4-km stretch of the Fundus crest (the western ridge of the Ötz valley), inferred to have risen before slope collapse to 2,500 m above sea level, some 400 m higher than present. Moving along a 20°-30° detachment plane in the gneiss bedrock, the sturzstrom struck the opposite side of the valley, dividing into two units (Fig. 3). The shattered lower unit remained in the valley, while the upper section continued into the Horlach valley. The surface separating the two units is exceptional for the development of glass and pumice textures, indicating rock melting along the contact at temperatures reaching magmatic values. The landslide covers some 13 km<sup>2</sup> and has a volume estimated at 3 km<sup>3</sup>. Emplacement took about 1-3 minutes, during which time the centre of mass moved horizontally and vertically some 2,500 m and 750 m, respectively. The landslide dammed both the Ötz and Horlach valleys, producing lakes whose deposits reach thicknesses of at least 90 m. Since then, the middle reaches of the landslide have been dissected in the Ötz valley after downcutting by the River Öztaler Ache.

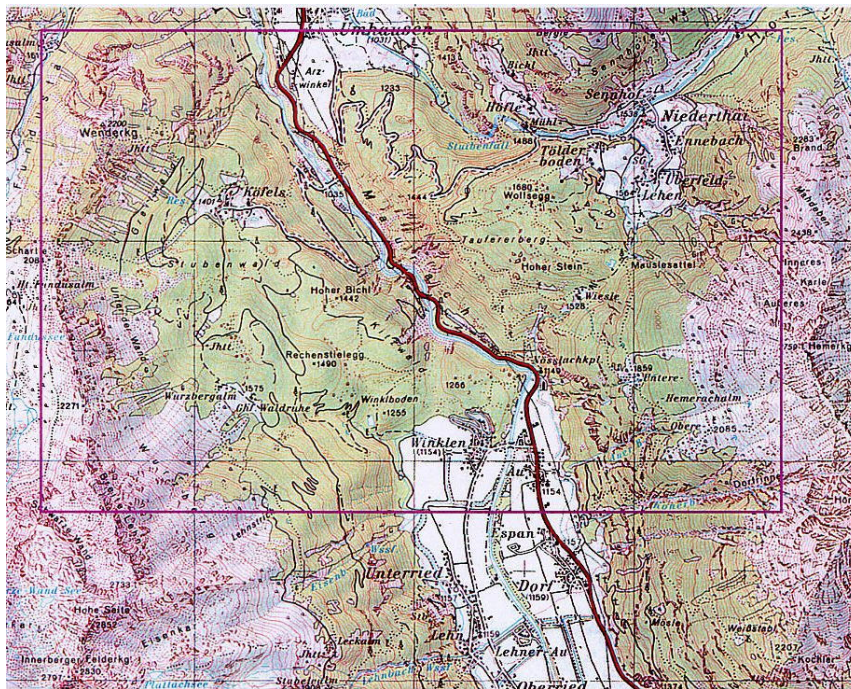


**Figure 1.** Location map of the Köfels landslide in the Ötz valley. North is to the top. The grid squares are 2 km apart.

Due to the modest 20° mean angle of sliding beyond the headwall, large parts of the landslide deposits appear from a distance as coherent rock and were mapped as bedrock during early geological surveys. At close hand, however, the apparently continuous rock is seen to be intensely dissected by hairline cracks separated at the centimetre scale. A tunnel built for hydrogeological purposes in 1951 at 1200 m asl on the western slope of the Ötz valley confirmed the nature of the sturzstrom by revealing the contact between "real" bedrock (paragneiss) and the fractured landslide deposits (augengneiss). It also revealed the pre-existing (now buried) gorge of the Horlach valley. The Horlach river was deflected to the north by the landslide and

today plunges 150 m over a rock cliff. This waterfall is called Stuiben fall and has eroded 6-8 m into bedrock, providing a good marker horizon.



**Figure 2.** Aerial (postcard) view of the Köfels landslide. West is to the left. Note the downcutting by the Ötz river through the middle part of the deposit.

### Age of the sturzstrom

Stratigraphic dating of the Köfels landslide has been complicated by the fact that while glacial deposits are abundant on the eastern side of the Ötz valley (around the toe of the landslide), they are completely absent from the landslide source region along the opposite wall of the valley. In other words, the stratigraphy in the source area suggests a preglacial collapse, while that by the toe of the landslide is consistent with a postglacial event. One resolution of this paradox, due to Heuberger (1975) and Heuberger et al. (1984), is that the event was indeed postglacial, the landslide itself transporting to the west residual surface glacial deposits from the eastern side of the valley. Supporting geomorphological evidence is that the contact between the scarp and the head of the landslide deposits (the 'knick point') is still angular, a feature that is unlikely to have survived glacial action.

Confirmation of post-glacial collapse was obtained from radiocarbon dating of strongly deformed wood found in shattered landslide sediment from the 1951 tunnel borings. Determined to be  $8,710 \pm 150$  BP, the age of the wood not only constrains the date of collapse, but also yields a mean rate of erosion along the Horlach river of about 1 m every 1,000 years.

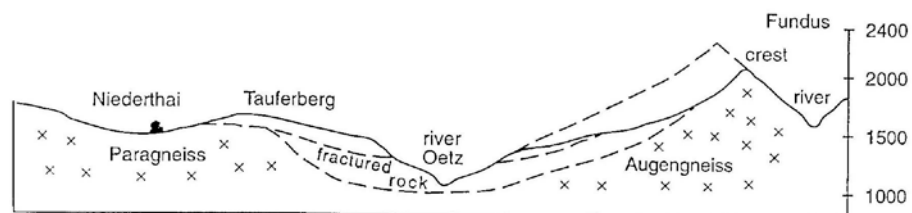


**Figure 3.** Simplified geological cross-section through the Köfels landslide. West is to the left. No vertical exaggeration.

## Geomorphology

The Köfels area has been remapped geomorphologically and the results are currently being integrated into a dedicated GIS (described below). The rocky headscarp is very steep, locally reaching slope angles of 40°-50° along trails from Köfels to the Fundus crest. At the foot of the head wall the slide surface disappears below the landslide deposits. Pumice outcrops have not been found at the primary sliding surface but close to the secondary sliding surface north of Köfels. The slope flattens markedly upon reaching the head of the landslide deposit east of Greitwald. In this small flat area lies the hamlet of Köfels (consisting of just a few farmsteads and two inns) at 1400 m asl. Shallow surface slopes continue southwest from Hoher Bichl to Rechenstielegg, where the slope steepens again, descending to the present Ötz river at 1030 m asl.

The landslide material varies from partly pulverised horizons to blocks exceeding 10 m in diameter. Due to the low sliding angle across the valley floor, large parts of the landslide have remained more or less coherent and look like bedrock. The Ötz river has cut into the landslide, but has not yet reached its former, pre-collapse river bed. The resulting Maurach gorge has caused very dangerous situations during flooding of the Ötz.

On the east bank of the Ötz, the Tauferer Berg (Figs 1 and 4) is the prominent sturzstrom deposit which blocked the original course of the river and ran up a depression in the eastern valley side into the Niederthai basin (Fig. 4). It reaches an elevation of 1600-1700 m and has an undulating and typically toma landscape. After damming of the Ötz river, a lake developed to the south of the landslide deposit in the Längenfeld area. The basin of Längenfeld has a very flat floor reflecting the deposition of lake sediments. Silt and claybeds produced marshes that still existed up to a few hundred years ago. The lake surface reached only to about 1200 m asl, owing to seepage of water through the loose landslide deposits. When the river finally broke through the landslide, a large alluvial cone was built on its northern side, extending from Arzwinkel via Umhausen to Farchat. Today the eastern part of this large cone is covered by much younger and steeper debris flow cones from the eastern mountain flank of the Ötz valley (the Horlach valley, Murbach, Graues Bachle and Farst).



**Figure 4.** View looking East from the upper Hörlach valley. The rise in the middle left of the picture is the Tauferer Berg, which comprises the toe of the Köfels landslide. The depression in the mountain range behind marks the collapse site from the Fundus crest on the opposite side of the Ötz valley

The Tauferer Berg consists of fragmental deposits of augeneiss derived from the Fundus crest. The fragments range in size from grains to blocks tens of metres across (Fig. 5). The largest blocks occur at the eastern toe of the slide; some are intact while others are broken along joints. Ancient Ötz river gravel and morainic material can be found on top of the blocks and between joints. Since the Ötz river has never flowed at such high elevation, the gravel must have been scraped out of the riverbed (together with material from moraines covering river terraces) by the landslide and deposited on top of and between its constituent blocks.

Crescentic gouges on augeneiss blocks resting on top of the sturzstrom deposits at Tauferer Berg indicate the movement of overlying ice. Since glaciers had retreated from the Ötz valley before the landslide occurred, these marks must have been produced when the rock surface was still *in-situ* high up on the ice-covered levels of the Fundus crest. The crescentic gouges indicate ice movement in the direction opposite from that of the main glacial direction, suggesting that the gneiss block must have been rotated through 180° during transport on top of the sturzstrom.



**Figure 5.** Adjacent blocks in the toe of the Köfels deposit can be connected as if part of a three-dimensional jigsaw puzzle. Although apparently coherent, the blocks are fractured at the centimetre scale.

Sediments within the Niederthai basin itself consist of silt, coarse sand and river gravel, all of which were laid down by the dammed Horlach river. These sediments partially covered the toe of the landslide and today outliers of landslide material (including transported moraines) form conical peaks about 10 m high.

Elsewhere, moraines of the Ötz glacier intermingle with the landslide mass in numerous places. They are most evident on the rock terrace of Wiesle at the southern edge of the landslide mass. This terrace marks the remnants of the former eastern flank of the Ötz valley at approximately the elevation of the Niederthai basin. All the glacial features (*e.g.*, moraines and kettle holes) disappear beneath the slide material and must therefore be older (late Wurm glacier) than the landslide. Heuberger (1966) also mentioned well-developed morainic features at Mauslajöchel which are at the same elevation. The little lake seems to be a dead ice feature. The lithological material is easily distinguished from the adjacent landslide because it contains biotite-gneiss, amphibolite, and garnet schist, all of which are derived from the upper watershed of the Ötz glacier.

The former Ötz valley rock terrace can also be seen north of Tauferer Berg as an area of rounded and polished rock surfaces near Höfle. The river Horlach has cut into

this rock surface about 6-8 m before it becomes the Stuiben waterfall and plunges into the Ötz valley. This is the new riverbed of the Horlach river. Since it took the river about 8 000 years to cut some 8 m into rock, the mean rate of fluvial erosion can be estimated at about 1 mm per year. A prominent rock terrace along Höfle-Bichl, to the northwest of the Stuiben waterfall, marks at 1600 m asl the highest lateral moraine of this section of the Ötz valley.

### **The Köfels pumice**

The Köfels event became famous when in 1863 veins of pumice and fused rock (centimetres to metres thick) were found at the site, both near the headwall and in the middle reaches of the deposit along the apparent contact between the upper and lower units of the landslide. This raised the question of the source of the energy that would be required to produce such a rock structure. Initial hypotheses attributed the pumice to volcanic activity or to meteoritic impact. In neither case could relevant sources be found (*i.e.*, a volcanic centre or impact ring structure), nor was the mineralogy of the pumice consistent with volcanic or impact material Preuss (1971). The energy for rock melting and vesiculation must therefore have come from the landslide itself.

The material producing the pumice was a gneiss containing water-rich amphiboles and biotite, as well as quartz and feldspar. Most of the amphibole and biotite were consumed during melting, thereby yielding a source of volatiles for degassing. Experiments by Erismann (1977) confirmed that the gneiss could produce pumice upon heating and inferred potential temperatures of 1,700 °C. Such temperatures, however, are far in excess of magmatic values and, indeed, by analogy with acidic magmas of similar bulk composition to the gneiss, melting and degassing can be anticipated after heating by some 1,000 °C. Erismann (1977) proposed that rock melting was important for reducing friction along the failure plane and so permitting rapid emplacement. As discussed in Chapter 2, however, this interpretation is *not* essential for explaining sturzstrom features. Indeed, as shown below, rock melting and degassing can simply be viewed as a natural *consequence* of rapid emplacement.

### **Landslide collapse and rock heating**

A simple first-order model (Chapter 1) provides the basis for quantifying conditions at collapse, the rate of emplacement and potential heating effects. Assuming a mean rock density  $\rho$  of 2,500 kg m<sup>-3</sup>, a mean collapse thickness  $h$  of 250 m and a mean collapse angle  $\alpha$  of 28° (Fig. 3), the failure shear stress  $\tau$  for the Köfels collapse can be estimated from

$$\tau = \rho g h \sin \alpha \quad (1)$$

which yields  $\tau \sim 3$ MPa. The associated load due to the weight of overlying rock ( $\rho g h \cos \alpha$ ) is  $\sim 5$ MPa.

The failure shear stress is smaller than the typical peak failure stresses expected for crystalline rock (Chapter 1), suggesting that failure must have occurred either along a weakened surface or as a result of seismic activity (an earthquake with a Richter magnitude greater than 6.5; Chapter 1). Current earthquake activity in the Ötz-valley district is insufficient to provide the necessary seismic energy. Unless elevated seismicity was more common some 9,000 years ago, failure must have occurred along a weakened gneiss horizon.

For a failure stress of 3 MPa, the associated drop in shear stress between the onset of failure and final collapse is expected to have been in the range 0.1-1 MPa. If  $a$  is the mean acceleration during collapse, then from Chapter 1

$$a = (\text{Shear stress drop})/\rho h \quad (2)$$

which gives notional accelerations of 0.16-1.6 m s<sup>-2</sup>. It is important to recall here that Eq. (2) assumes simple frictional sliding along the detachment plane (Chapter 1), *without invoking special mechanisms for reducing frictional resistance*.

Movement displaced the centre of mass of the landslide by some 2.6 km downslope (Fig. 3). If  $s$  is the displacement distance, the emplacement time  $t$  is approximately

$$t = (2s/a)^{1/2} \quad (3)$$

yielding values of 1-3 minutes, with corresponding mean velocities of 43-14 m s<sup>-1</sup>.

Assuming most of the kinetic energy of the landslide was dissipated as heat along the detachment surface of the landslide, the increase in temperature  $\Delta\theta$  is given by (ignoring latent heat to a first approximation)

$$\Delta\theta = 0.5 (u^2/c_p) (h/\delta) \quad (4)$$

where  $u$  is the mean velocity,  $c_p$  is the specific heat capacity of the heated rock (~1,000 J kg<sup>-1</sup> K<sup>-1</sup> for gneiss), and  $\delta$  is the thickness of rock heated adjacent to the detachment plane.

For the Köfels detachment plane, therefore, Eq. (4) yields

$$\Delta\theta \sim (24.5 \text{ to } 231)/\delta \quad (5)$$

for  $\Delta\theta$  in °C (or K) and  $\delta$  in metres.

For the observed thicknesses of centimetres to decimetres for glassy and pumice veins in the landslide deposit, the associated temperature increases are ~100-1,000 °C for  $u = 14$  m s<sup>-1</sup> and 1,000-10,000 °C for  $u = 43$  m s<sup>-1</sup>. The extreme values are clearly unrealistic, yielding best solutions of temperature increases of ~1,000 °C over thicknesses of centimetres for  $u = 14$  m s<sup>-1</sup> or decimetres  $u = 43$  m s<sup>-1</sup>, consistent with field observation.

It is feasible, therefore, that the Köfels collapse was the result of progressive failure, perhaps induced by percolating water seeping into the rock from the base of an overlying glacier. Emplacement times of a few minutes are consistent with velocities high enough to induce localised frictional melting and rock degassing. Importantly, velocities were estimated assuming that motion occurred against simple sliding friction along the detachment plane. Thus the speed of emplacement can be explained without invoking reduced friction due to melting. Indeed, melting and degassing can be seen simply as a consequence of catastrophic collapse.

### **Discrete-element modelling of the Köfels sturzstrom**

The preceding analysis demonstrates that the collapse, rapid transport and heating of the Köfels landslide can be explained without recourse to exotic emplacement mechanisms. The detailed mechanisms of energy loss, however, remain to be

determined. The fragmental nature of the landslide suggests that interaction among fragments was the principal mode of energy loss. Fragment interactions lose energy through inelastic collisions (including fragmentation) and friction. For a dense mass of material, frictional effects are anticipated to dominate collisional losses. To examine the nature of these effects in more detail, the discrete-element model for the flow of a collection of fragments (Chapter 3) has been utilised to explore conditions during emplacement of the Köfels landslide.

For initial testing of the discrete-element model, two aspects of the Köfels landslide have a special importance. The first is the presence of boulders on the top of the slide between Hoher Stein and Wolfsegg. These boulders are large with dimensions measuring tens of meters and very sharp edges. They are furthermore forming what appears to be a slightly disturbed jigsaw puzzle, suggesting that they were only slightly disturbed during transport across the Ötz valley (Fig. 5). Although larger slabs were broken into fragments, the buffeting between fragments must have been minimal. The shape and position of the boulders also eliminate the possibility that they were rolling during the transfer. This impression is further enhanced at the head of the slide where we find overlapping boulders reminiscent of falling dominoes. Here, the direction of the slabs indicates that the head of the slide decelerated and was overtaken.

The second aspect of note is the shape of the Taufererberg, deep towards the head of the slide and tapering off towards the tail. This again seems to indicate that the slide ran out of steam before reaching the steeper mountain slopes. Unfortunately, the river Ötz now flows very close to the slopes below the Fundus crest and it is difficult to determine the shape of the slide near the origin with any accuracy.

#### *Experiments investigating frictional effects*

The first set of experiments investigated the 2-dimensional flow down a uniform slope of the starting configuration is shown in Figure 6. The key objective was to investigate the effect on bulk landslide morphology of the dominant mode of fictional energy loss. Animated versions of the simulations are given on the accompanying CD ROM.

The starting condition consists of a block containing 900 boulders placed on a 30° slope. The slope extends into a flat section and ends in a wall. The experiments were aimed at understanding the general behaviour of rock avalanches and obtain some understanding of the impact energy dissipation has on the dynamics of the slide. Based on evidence from Köfels that rotation only plays an insignificant role, we have in these models disregarded the effect of angular momentum.

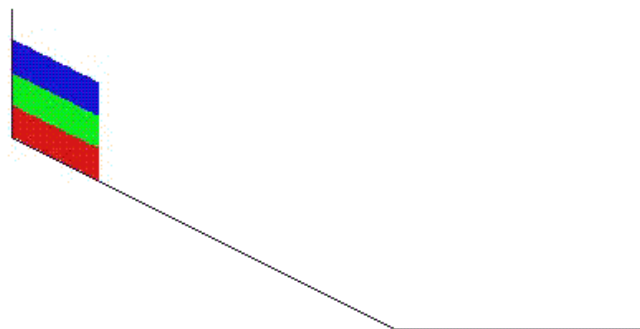


**Figure 6.** Starting configuration for initial experiment.

The first effect to be investigated was momentum loss during collisions. If only two particles are involved, the classical Huygens' model determines the momentum transfer. If two spheres have the velocities  $u_1$  and  $u_2$  (along their common axis) before a collision, their velocities ( $v_1, v_2$ ) after the collision are given by

$$v_1 = \frac{m_1 u_1 + m_2 u_2}{m_1 + m_2} + \alpha \frac{m_2 (u_2 - u_1)}{m_1 + m_2} \quad (6)$$

$$v_2 = \frac{m_1 u_1 + m_2 u_2}{m_1 + m_2} + \alpha \frac{m_1 (u_1 - u_2)}{m_1 + m_2} \quad (7)$$

where  $\alpha=1$  represents a perfect, elastic collision while  $\alpha=0$  corresponds to an inelastic collision after which the two rocks move in unison. Experiments were performed with the value of the damping coefficient ( $\alpha$ ) ranging from 0 to 1 in steps of 0.05.

The slides can also suffer from momentum loss through friction. The type of friction initially investigated was of the Coulomb-type where the friction force is proportional to the normal force. Again this was investigated by this series of experiments.



**Figure 7.** Pressure wave at the back of slide during initial state.

The experiments showed that the damping coefficient ( $\alpha$ ) had little effect on either the shape or the energy of the slide. As for the shape, all experiments started as a rectangular block. Sometimes this block was released as a horizontal rectangle while at other times it was allowed to rest on the slope. The starting configuration turned out to have only minimal effect on the outcome. In all cases the block was deformed into a triangular shape reminiscent of a pile of sand. The shape is created as the block collapses and spread out the lowest layers of particles. At the rear of the slide the material that forms the upper back part of the original block meets this movement. This material cannot escape because of the solid wall and will therefore collide with the expansion.

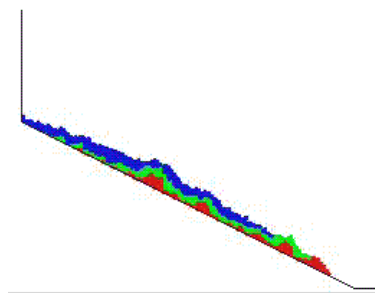


**Figure 8.** Slide with high damping. Red layer is seen forming nodes.

As shown in Figure 7, the result is a pressure wave forming roughly along the diagonal leading from the upper front to the lower back of the slide. The pressure wave accelerates the front of the slide and ejects the rear end of the slide, forming a front pile with some debris behind. As the slide progresses, the damping will encourage areas of relaxation where frequent encounters remove energy faster than in other places. This is seen in Figure 8 as a series of nodes forming along the slide. If friction is included the pile tends to develop more slowly but the basic scenario does not change.

*Analysis of the Köfels landslide morphology*

In a second set of experiments, the basic shape of the Köfels slide was used to study the front of the slide. A block of 900 particles, each with a interaction radius of 5 meters are stacked loosely on a 60° slope. The slope originates at 1000 meters above the valley floor, falling to ground level and raising again as a 30° slope to a vertical wall starting at 1,000 meters altitude. Based on field evidence from the Köfels landslide that there is no rotation involved, exchange of angular momentum has been disregarded in these models. Two scenarios have been considered for low and high friction.

(1) *Low-friction emplacement.* Figure 8 shows the loss in total energy during the first 25 seconds for a low friction model with  $\alpha$  in the range 0.1 (red) to 0.7 (blue). Notice the three separate sectors. First a gently loss as the slide descends the slope. Then a massive decline as the slide collides with the valley floor, followed by another gentle decrease as the slope traverses the valley and climbs the shallower slope. While the impact with the valley floor is clearly marked, the impact of the raising slope is hidden in the noise.

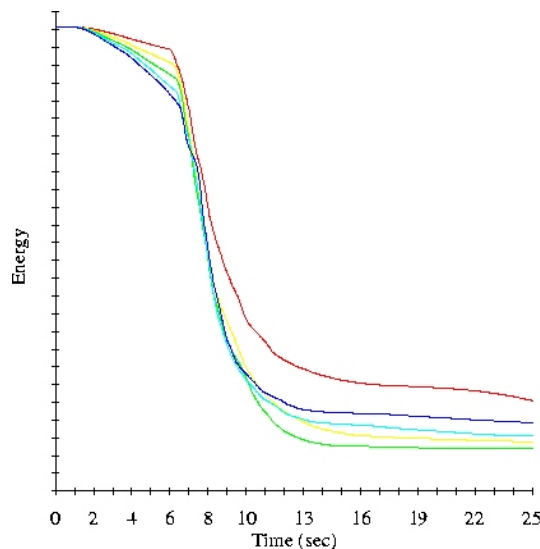


**Figure 8.** Energy loss in model with low friction.

The purpose of introducing the slowly-rising floor was to halt the flow and to find the parameters leading to the top-heavy shape we observe at Köfels. The experiments clearly showed that standard Coulomb friction could not alone be responsible for said formation. The Coulomb friction favours the areas with large normal forces and it is therefore most effective near the middle of the slide where the pressure from the thick

layers of rock maximises the gravitational pull. The front of the slide will therefore tend to run away from the rest when Coulomb-type friction is used. This is also true for slides where the particles are of a large range of sizes. Notice that no energetic layer is formed by migration of smaller particles through the flow. The migration is in reality found to be rather slow compared to the downslope speed of the flow. Consequently, mixing is minimal by the time the flow has stopped, in agreement with field observation.

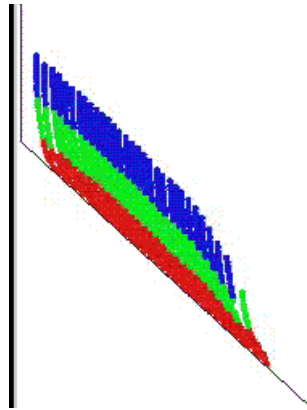


**Figure 9.** Block behaviour in high friction slide.

(2) *High-friction emplacement.* Models with high friction are expected to display signs of block movement, as the individual particles would be inhibited in their relative motion. The effect is seen in Figure 9, where the slide is seen fragmenting into a series of columns. Each column clearly shows the effect of particle-particle friction, but the block does not move as a unit. The reason is that individual columns are formed by stacks of rocks but because there are no forces binding the columns together, they appear to evolve as discrete columns. Had the blocks been stacked with overlaps in a manner similar to the bricks in a wall, a more natural 'clumping' movement of the material would have been observed. The effect shows the shortcomings of the spherical-particle assumption, a drawback which is currently being investigated.

Applied to the Köfels sturzstroms, the simulations demonstrate that fragmental-flow mechanics can account for the long runout and final upslope advance of the landslide. The results show, however, that simple Coulomb friction between fragments cannot account for the observed variations in bulk landslide morphology. As suggested in Chapter 2, an effective-fluid friction (*e.g.*, for a viscous or Bingham liquid) may be more appropriate. The simulations also show that collections of small fragments can behave as coherent blocks during transport, provided inter-fragment friction is sufficiently large. Additional simulations are in progress that will evaluate the effects of non-Coulomb friction laws and of non-spherical fragments, using the results from analytical models (Chapter 2) for boundary constraints.

### **GIS development**

A Digital Elevation Map (DEM) has been prepared of the Köfels landslide at a scale of 1:50,000 (Fig. 10). The DEM provides the basis for a dedicated GIS analysis. The essential features of the GIS are described in Chapter 8. Figures 10 and 11 provide samples of shaded relief maps and automatic profiling across the Ötz valley.

Additional sample thematic maps of slope distribution, curvature, elevation and orientation, as well of zones of water accumulation are given on the image files of the accompanying CD ROM.

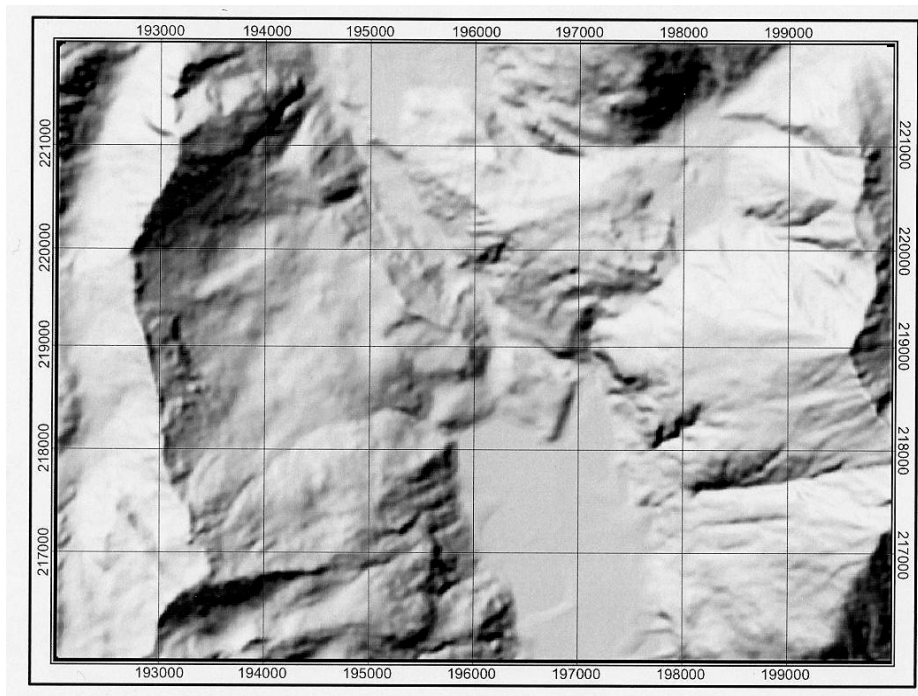


**Figure 10.** Shaded relief map from GIS enhancement of a 1:50,000 DEM of the Köfels landslide. West is to the left. Compare with Figure 2.

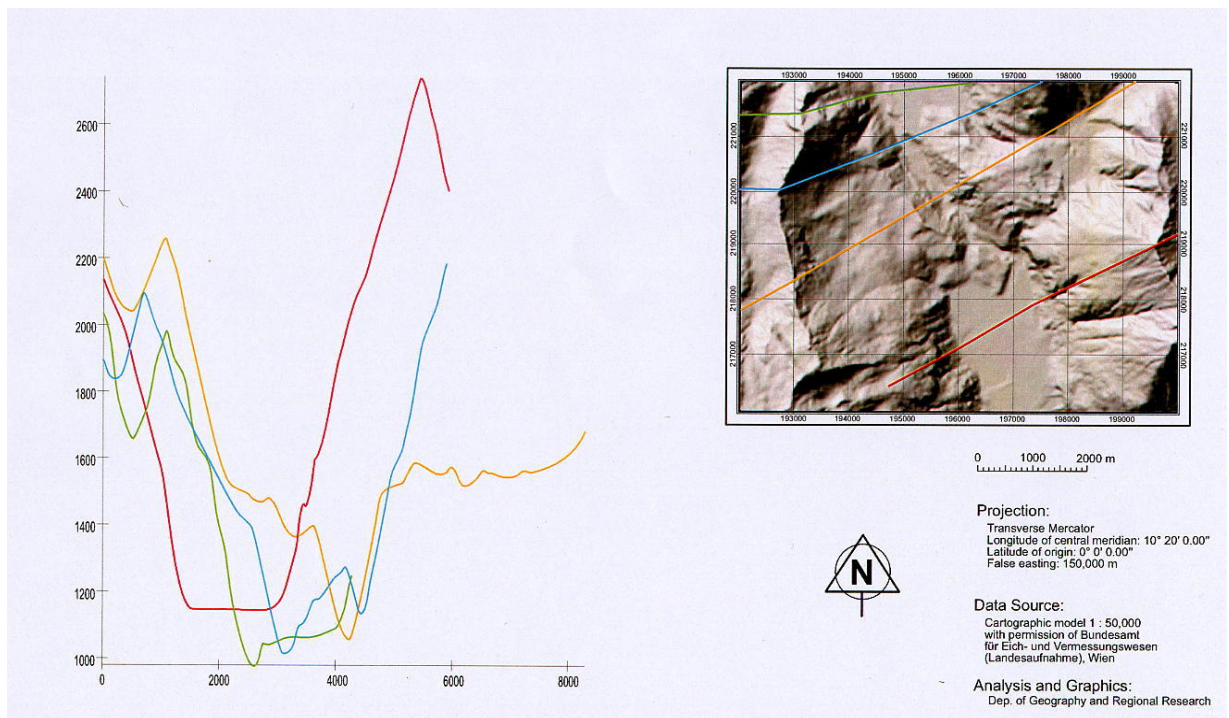


**Figure 11.** Sample profiles across the Ötz valley obtained from GIS analysis.

## References

- Erismann, T 1977. Der bimstein von Köfels, impactit oder frictionit? Material und Technik, 77.
- Heuberger, H 1975. Das Öztal, bergstürze und alte gletscherstände. Innsbrucker Geographische Studien, 2.
- Heuberger, H, Masch L, Preuss E, Schöcker A 1984. Quaternary landslides and rock fusion in Central Nepal and in the Tyrolean Alps. Mountain Research and Development, 4.
- Preuss, E 1971. Über den bimstein von Köfels, Tirol. Fortschritte der Mineralogie, 49 (1): 70.

## 6. Monitoring and hazard analysis at the Tessina landslide, Italy

The Tessina landslide is a complex gravitational movement, affecting the Tertiary Flysch Formation, located on the southern slope of Mt. Teverone, in the eastern part of the Alpi valley in the Province of Belluno, Northeastern Italy (Fig. 1). The particular urban development of the area has required in-depth studies and the planning and installation of a monitoring system which is still active for the safeguard of the population. The area has also been the object of particular attention for the definition of a civil defence plan which, for the first time in Italy, was tested by means of drills and simulations involving the whole population.

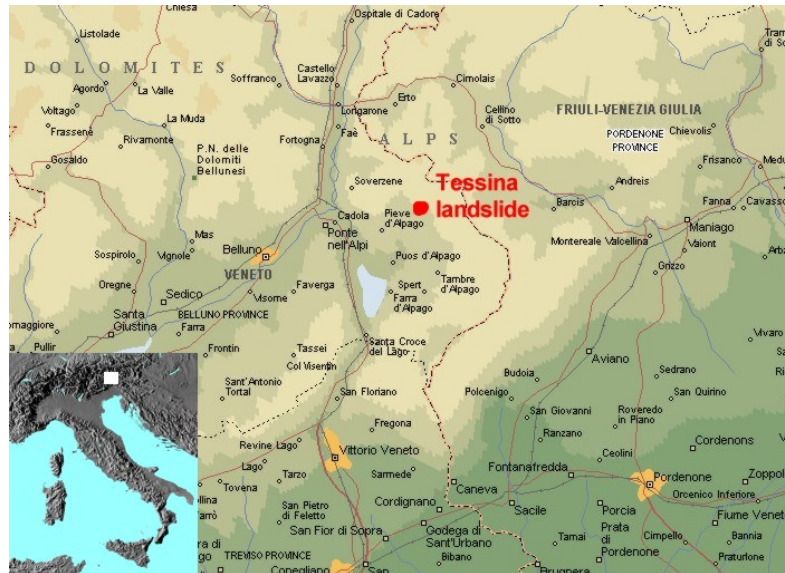


Figure 1. Location map of Tessina landslide.

### Geological and morphological setting

From the structural standpoint, the slope portion affected by the landslide belongs to the northern flank of the asymmetrical brachysyncline of the Alpi catchment basin (Mantovani et al., 1976). The material involved in the slope movement belongs to the Flysch Formation (Eocene). It is made up of a rhythmic sequence of marlstones, clay shales and calcarenite layers up to 1 m thick. This formation is particularly permeable owing to a high degree of fissures mainly resulting from tectonic stresses. Its attitude is generally dip-upstream, with overturned strata in correspondence with the main scarp and the upper landslide portion. More down the slope the attitude is south-dipping, dip-downstream with low angle. Quaternary deposits crop out with continuity from the foot of the Mt. Teverone slopes, covering with variable thicknesses the underlying formations. Apart from vast detrital covers found at the foot of Mt. Teverone, moraine deposits from the River Piave glacier and other local glaciers are found.

From the morphological viewpoint the Tessina landslide stretches from 1200 m to 640 m a.s.l. The landslide is classified as a complex movement including a rotational slide in its upper part and a mudflow in its mid-lower part. On the basis of its morphological and dynamic characteristics, it has been divided into four morphodynamic units: i) the detaching zone (1200-1000 m a.s.l.), which consists of a highly fractured crown beyond the main scarp and the active scarp itself; ii) the upper accumulation zone (1000 to 975 m a.s.l.), identified in a sub-horizontal embayment, 500 m across and 350 m downslope, within which newly-collapsed material can be accumulated before being eventually transported onto a secondary scarp at about 975 m a.s.l.; iii) the connection canal zone (975 to 900 m a.s.l.), corresponding to the steep scarp (ca. 30° slope)

immediately below the upper accumulation zone which funnels landslide material with the highest acceleration into the main valley below; iv) the lower accumulation zone (below 900 m a.s.l.) in which the landslide material, remobilised as a mudflow, fills the existing valley. The latter now extends for about 1.5 km from 900 to 610 m a.s.l. and collects the material threatening the villages of Funes and Lamosano.

The landslide's evolution is still in progress and has led to a constant widening of the source area, which from the original 300,000 m<sup>2</sup> of material is now about 500,000 m<sup>2</sup>. The total displaceable volume has been assessed as about 7 million m<sup>3</sup>. The velocity of the movement seems to vary considerably according to the episodes and sections considered. The maximum velocities attained were recorded uphill of Lamosano in May 1992, with displacements of the most fluid part of the main flow of 70 to 100 m/day. In the same period, velocities of about 25 to 30 m/day were recorded in proximity of Funes.

### **Tectonics**

The area affected by the landslide is part of the northern flank of the Alpage brachysyncline. The axis of this structure, which stretches roughly in a NW-SE direction, is mildly arcuate with a SE facing concavity. It is located at the boundary between the Belluno Southern Alps to the west, which have undergone small compressional strains with a ENE-WSW Val Sugana-style deformation, and the Carnia Southern Alps to the east. The latter show a higher degree of compressional strains with a greater influence of the Dinaric component of the Alpine deformation, thus conferring a WNW-ESE trend to the main lineaments.

The structural and tectonic arrangement of the Alpage region is also conditioned by its location in a transition area between a brittle block to the south, corresponding to the highly uplifted Cansiglio massif (a fragment of the Friuli shelf), and a ductile block to the west, corresponding to the Belluno basin, where folds and fold-faults prevail, and from which the Alpage region is separated by a south-trending group of faults which bound the Lapisino Graben.

The southern slope of Mt. Teverone, corresponding to the northern flank of the brachysyncline, is characterised by nearly vertical strata and is affected by an important NW-SE displacement, i.e. the transpressive oblique ramp of the Belluno overthrust. In this sector the fault has a rather high angle and the prevalently marly rock masses show a ductile behaviour in response to the lateral stresses of the brittle carbonate blocks. This fault is basically a south-verging overthrust, with the calcareous members ("Calcere del Fadalto" and "Scaglia Rossa" *sensu lato*) overriding the Eocene members (Flysch dell'Alpage). Furthermore, the Scaglia Rossa Formation is extremely thinned up owing to its considerable tectonic reduction.

The southern flank of Mt. Teverone is crossed over by NE-SW trending transversal discontinuities. Of these, the major ones favoured the emplacement of the Venal di Funes and Montanes structures; they are high-angle reverse faults with sinistral transcurrent component linked to the Belluno overthrust.

The element of novelty resulting from field surveys carried out within the framework of this project, is the presence of at least one low-angle fault, identified on the basis of attitude and morphological considerations; this structure is vicarial from the main overthrust. Its presence seems to be confirmed by the Flysch changes of attitude, with sudden dip changes (from 20°÷40° in the northern sector to 70°÷80° in the southern one) and by eastward widening of the area involved in the landslide which since 1992 has assumed an elliptical shape, with E-W trending main axis. This vicarial lineation, which seems to be found in correspondence with the area characterised by attitude changes, is also recognisable in the easternmost sector, outside the area investigated. Therefore, this structure bounds an embriated south-verging tectonic "scaglia", inside which low-angle, north-dipping overturned strata are visible.

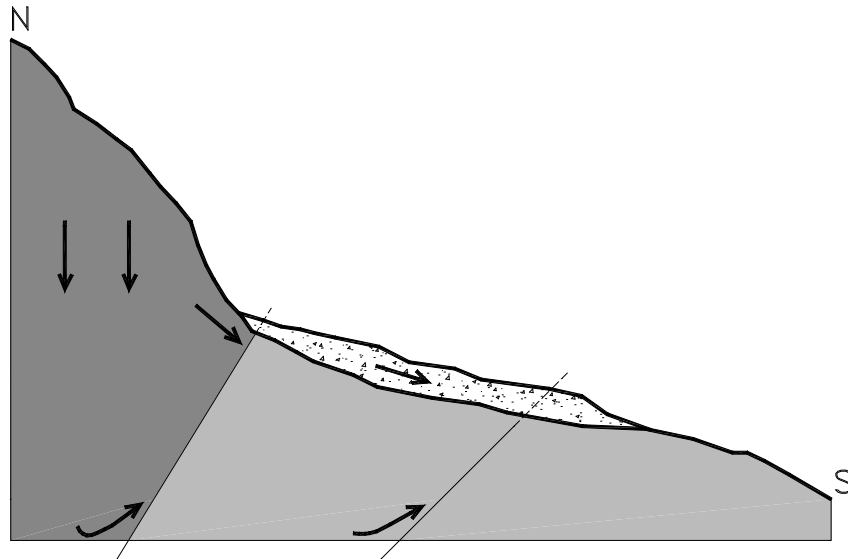


**Figure 2.** Schematic sections of hydrological conditions.

This tectonic attitude, as illustrated in the geological section of the map enclosed, plays a considerable role in the groundwater flow pattern. The presence of numerous springs, some of which are perennial with practically unchanged water regimes since the draining tunnel was dug, could be related to these tectonic discontinuities, which could act as preferential flow paths toward the surface. Fig. 2 shows a schematic section in which the carbonate formations corresponding to the main aquifer are represented by the dark colour, whereas the more impervious Tertiary formations affected by the main discontinuities are represented by the lighter colour.

According to this flow pattern, precipitation water (rain and snowfall) would first percolate into the carbonate Mt. Teverone massif and later would come back to surface in the landslide area along these tectonic lineations. The latter would also induce a secondary permeability due to fracturing in the Flysch Formation, thus favouring the presence of springs with a perennial water regime. The lowering of the water table inside the carbonate massif, caused by the digging of the draining tunnel, would only regulate the springs' flow rates by reducing their peaks, but it would not eliminate completely the presence of water in the landslide area.

### **Current monitoring of the landslide**

Several measuring instruments have been installed within the landslide body and surrounding areas (see also Chapter 11); at the same time, investigations have been started in order to constantly monitor the mass movement evolution and predict possible evolution models. These systems generally record measurements of surface and in-depth displacements, piezometer fluctuations and meteorological data. Furthermore, flow rate measurements carried out in the draining tunnel, have allowed the influence of precipitations and its relationships with piezometer changes measured inside the landslide area to be verified. The results of the investigations carried out in 1998-1999 are described in the following chapters, with particular attention given to their possible correlations during the various reactivation phases of this gravitational process.

### ***Shallow displacements***

Shallow displacements have been measured by means of both standard topographic techniques and satellite-based systems (GPS = Global Positioning System). On the basis of the kinematic landslide characteristics, two different investigation areas have been identified. The first area coincides with the source area (crown and main scarp) and the accumulation upper part, whereas

the second one coincides with the flow, uphill and downhill of Funes, where some benchmarks have been installed in order to verify and confirm the assumption that some displacements were caused only by sudden overloading due to new flows overlapping the older, already stabilised flows.

#### *Automated topographic system*

The displacements of about 30 benchmarks, some of which had been installed in 1992 and others in 1998 and 1999 have been measured (Fig. 3). The sampling frequency was, usually, every 4 hours, with changes from 6 to 2 hours according to the various activity states of the landslide and climate conditions. The graphs of displacements (Figs. 4) emphasize a marked difference of values between the benchmarks located near the landslide crown and scarps (Fig. 4 a, b, c) and those located in the upper accumulation zone (Fig. 4 d). This is because the upper accumulation zone is characterised by “pulsing” movements, with minimum displacements during the dormancy periods and considerable movements (up to over 1 m/day) during the reactivation phases, whereas the more elevated area shows a greater uniformity of displacements.

The trend of displacements, measured in the 1997-1999 period, has allowed a landslide zonation into four areas with different kinematic characteristics (Fig. 5):

1. the upper accumulation zone with annual average displacements exceeding 1 m.
2. the crown zone with annual average displacements of 30 cm to 1 m;
3. the zone uphill of the main scarp with annual average displacements of 15 to 30 cm;
4. the left hydrographic side between Roncadin and Pian de Cice, with annual displacements lower than 15 cm;

On the basis of GPS measurements carried out on the right hydrographic side of the valley, also a fifth unstable zone has been identified. This area shows annual average displacements exceeding 20 cm, with considerable amount of activity resumed during seismic shocks.

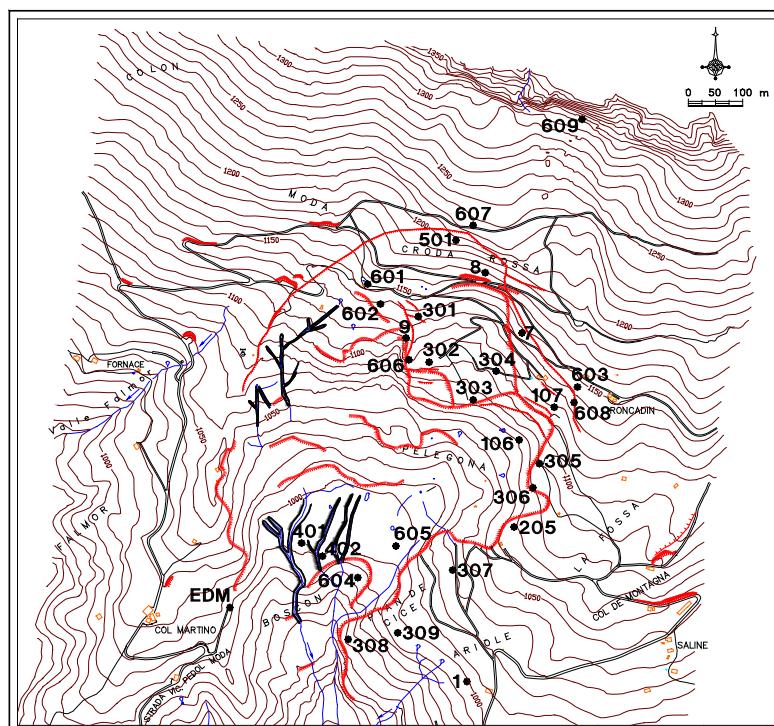


**Figure 3.** Benchmark location for the automate topographic system.

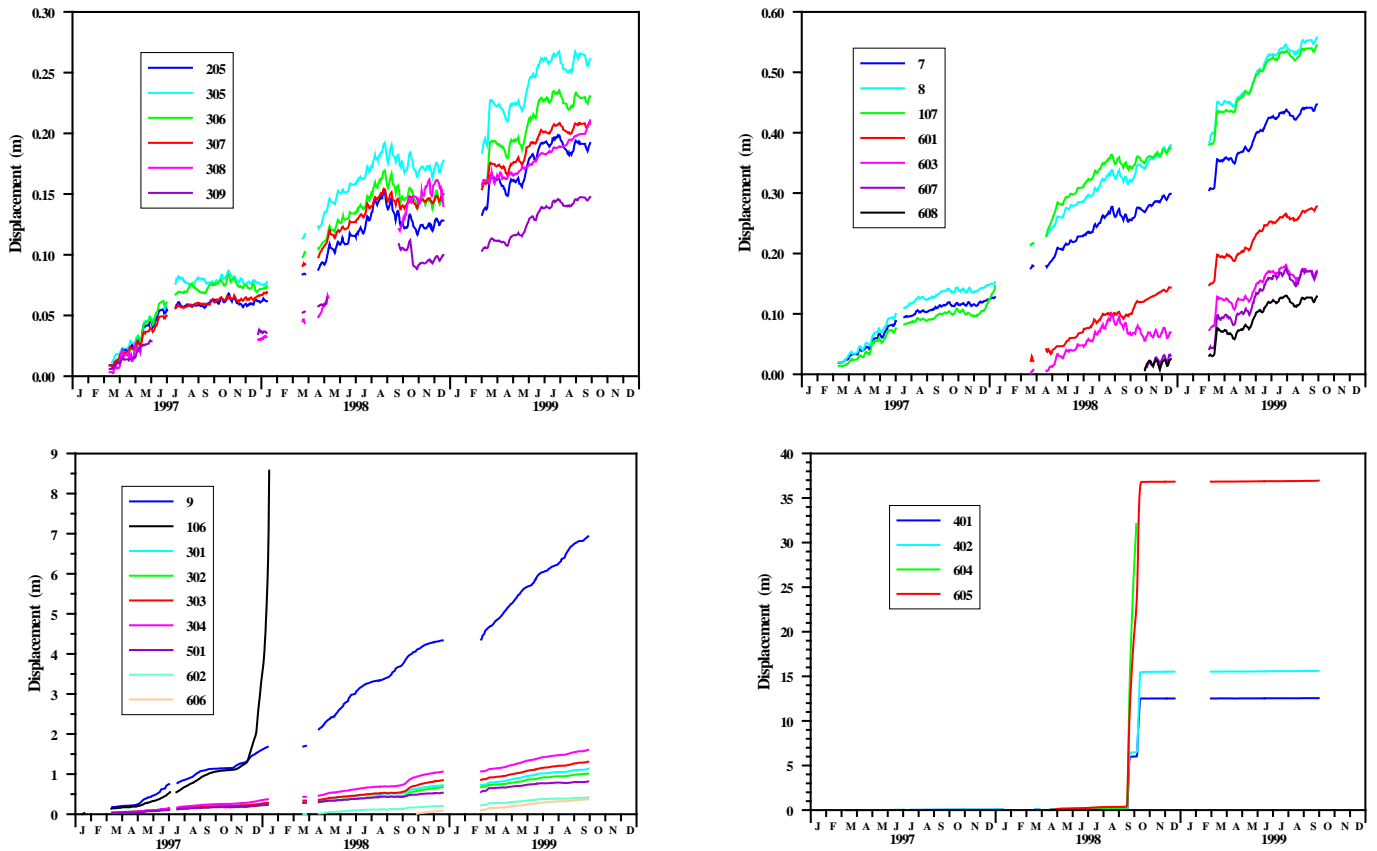


**Figure 4.** (a, top left) Benchmarks with displacements lower than 15 cm/year. (b, top right) Benchmarks with displacements between 15 and 30 cm/year. (c, bottom left) Benchmarks with displacements exceeding 30 cm/year. (d, bottom right) Benchmarks with displacements exceeding 1 m/year.

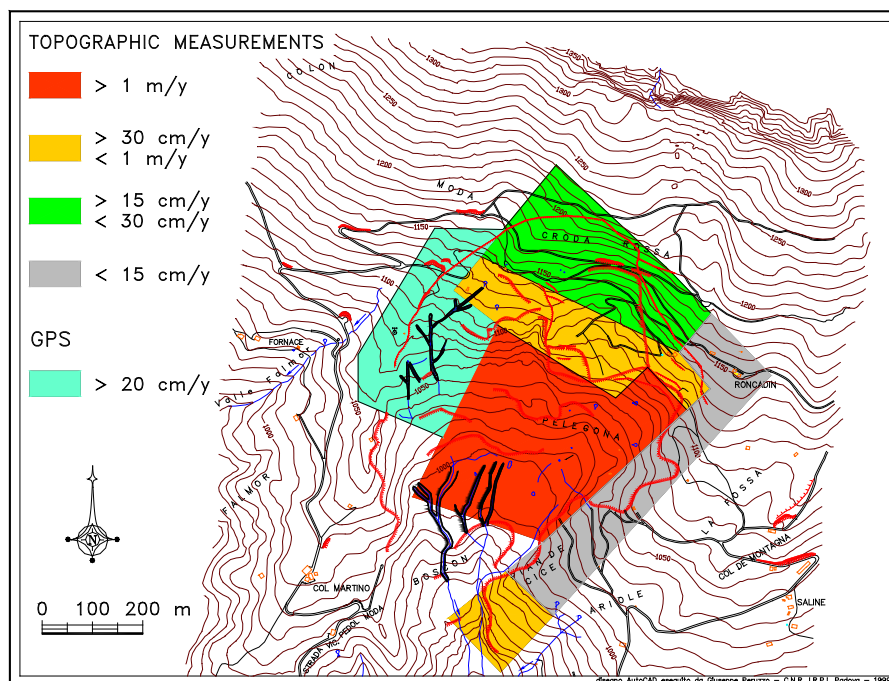


**Figure 5.** Areas with different kinematic characteristics.

### GPS measurements

A GPS monitoring network, made up of about 25 points prevalently located uphill of the main scarp and on the crown, was installed. Three measurement sessions were carried out in July 1998, July 1999 and November 1999, respectively (Fig. 6). These GPS measurements allowed a vast area to be analysed, monitoring also those areas which were not directly visible or reachable by automatic topographic positioning (see also Chapter 11).

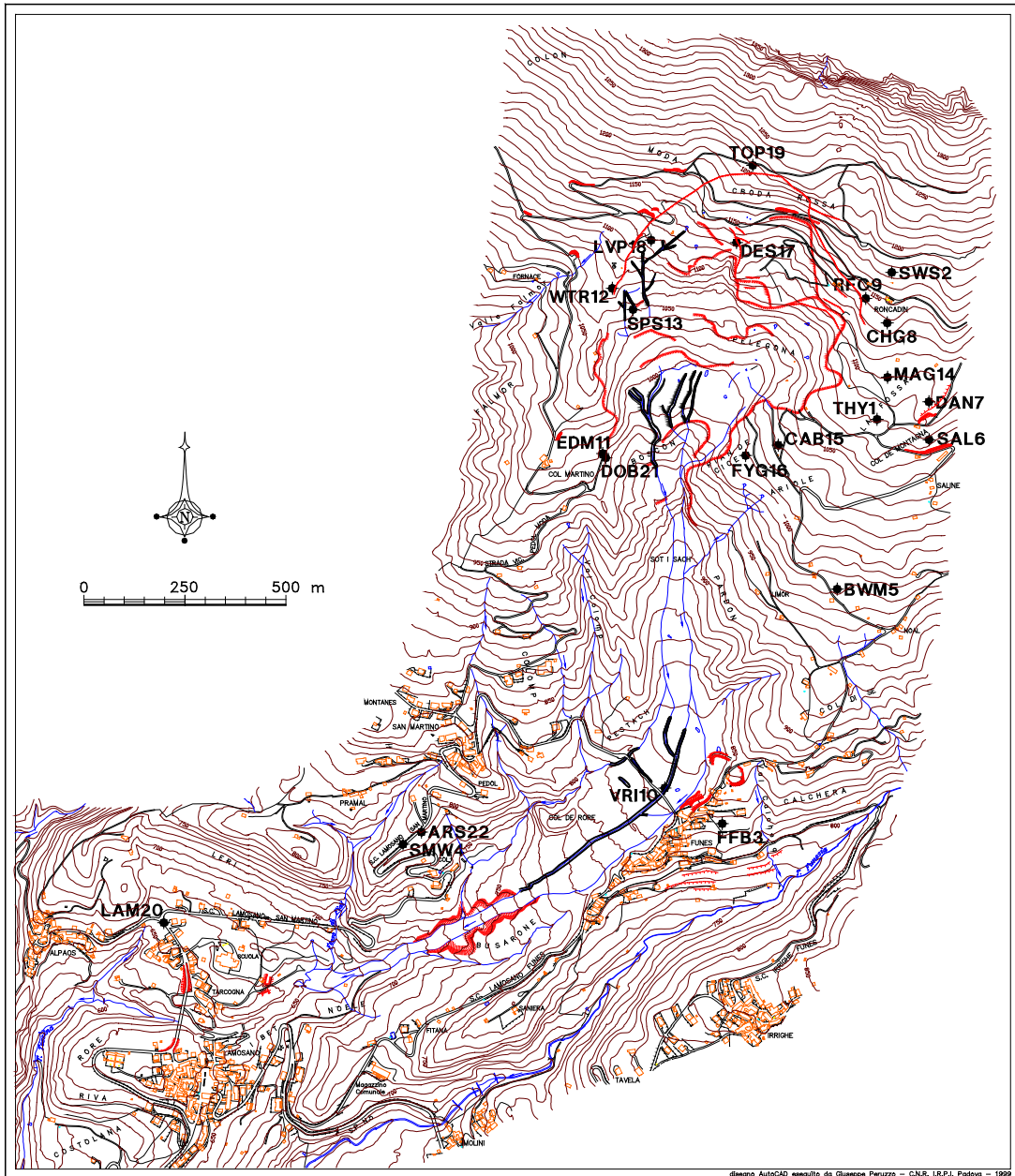
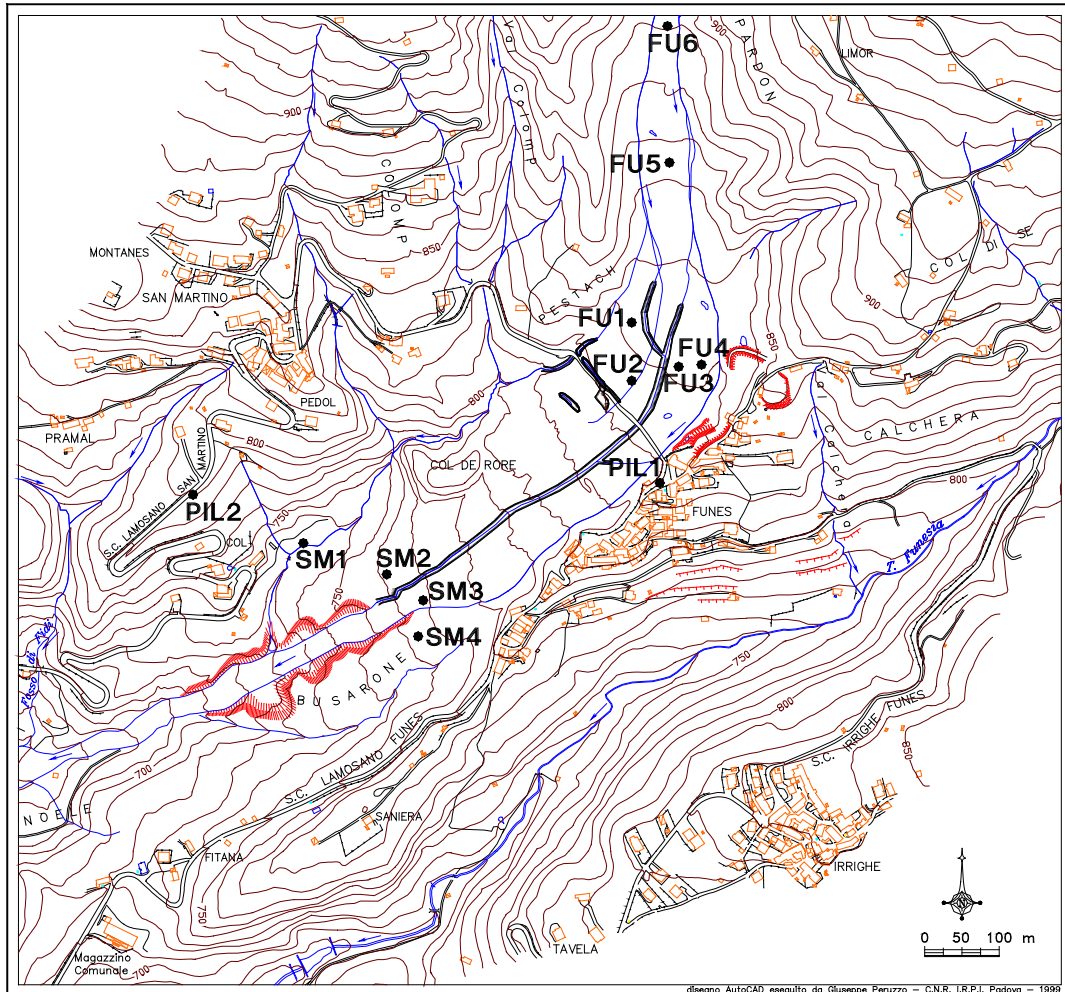


Figure 6. Location of GPS survey station.

Measurements sessions were carried out by means of rapid static technique with a double frequency measuring equipment. The results thus obtained pinpoint displacements of varying amount in the whole area; nevertheless, displacements around 1-2 cm may be due to instrumental errors and should therefore be checked during further measurement sessions (Chapter 11).

### *Manual topography*

Manual topographic measurements (Fig. 7) have been carried out in order to verify whether movements could take place in the flow body without the presence of sudden overloading due to the formation of new flows overlapping those already stabilised. Measurements have confirmed that during a 20-month observation period, prior to the 1998 event, displacements were not recorded.



**Figure 7.** Location of the benchmarks for manual topographic measurements.

### *Deep displacements*

Displacement measurements at depth were carried out by means of the following (Figs 8 a, b):

- i) inclinometer measurements (T1, T2, S1 and S2 borings);
- ii) TDR cable measurements (T1 boring).

In order to identify the presence and depth of potential slip surfaces, the proper functioning of over 20 well pipes installed between 1992 and 1995 were tested. The well pipes and boreholes dug upstream of the main landslide scarp were mostly broken at depths of 20 to 68 m.

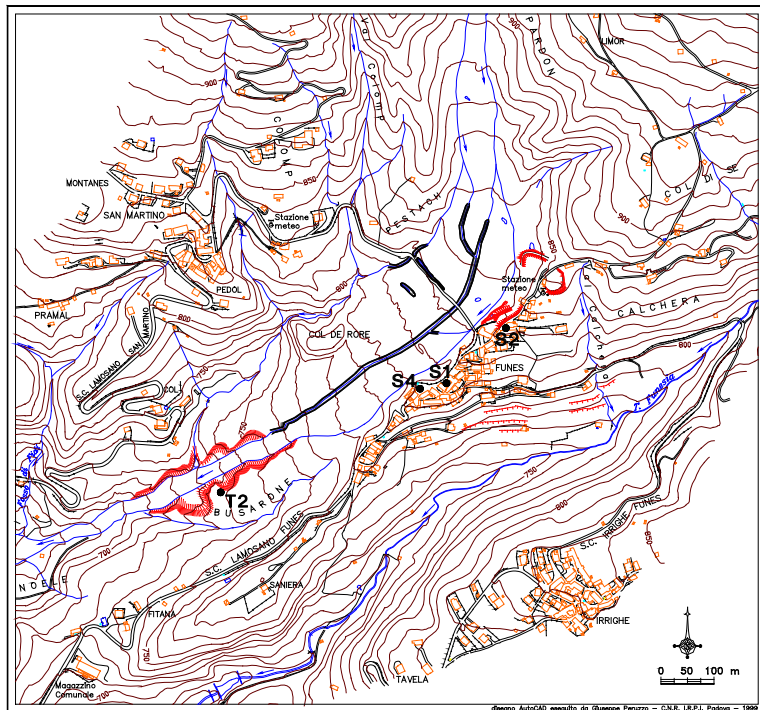
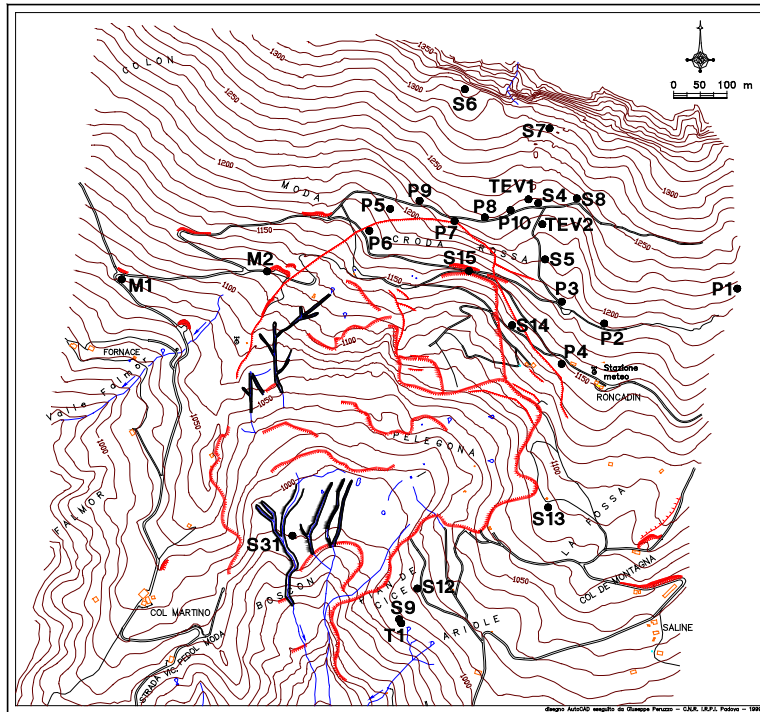


**Figure 8. (a, top)** Inclinoetric tubes, TDR cables and piezometers in the source area.  
**(b, bottom)** Inclinoetric tubes installed in the Funes area.

The presence of a considerably thick debris cover with a surface of rupture at a depth ranging between -50 and -60 m was identified on the left side of the source area thanks to this analysis and the interpretation of stratigraphic logs, as shown by the failure of well pipes P7, P8, P9, P10, S4, S5, TEV1 and TEV2. This fact confirms the presence of noticeable amounts of debris deposits, probably accumulations of ancient landslides whose existence has been inferred by means of aerial photo-interpretation.

*Inclinometer measurements*

Inclinometer measurements were carried out in four boreholes T1, T2, S1, S2 (Figs 8). Measurements of S1, S2 and T2 show no displacements (Figs 9b-d). Borehole T1 pinpoints the continuous displacement of the area known as Pian de Cice with a slip surface at the depth of about 26 m (Fig. 9a).

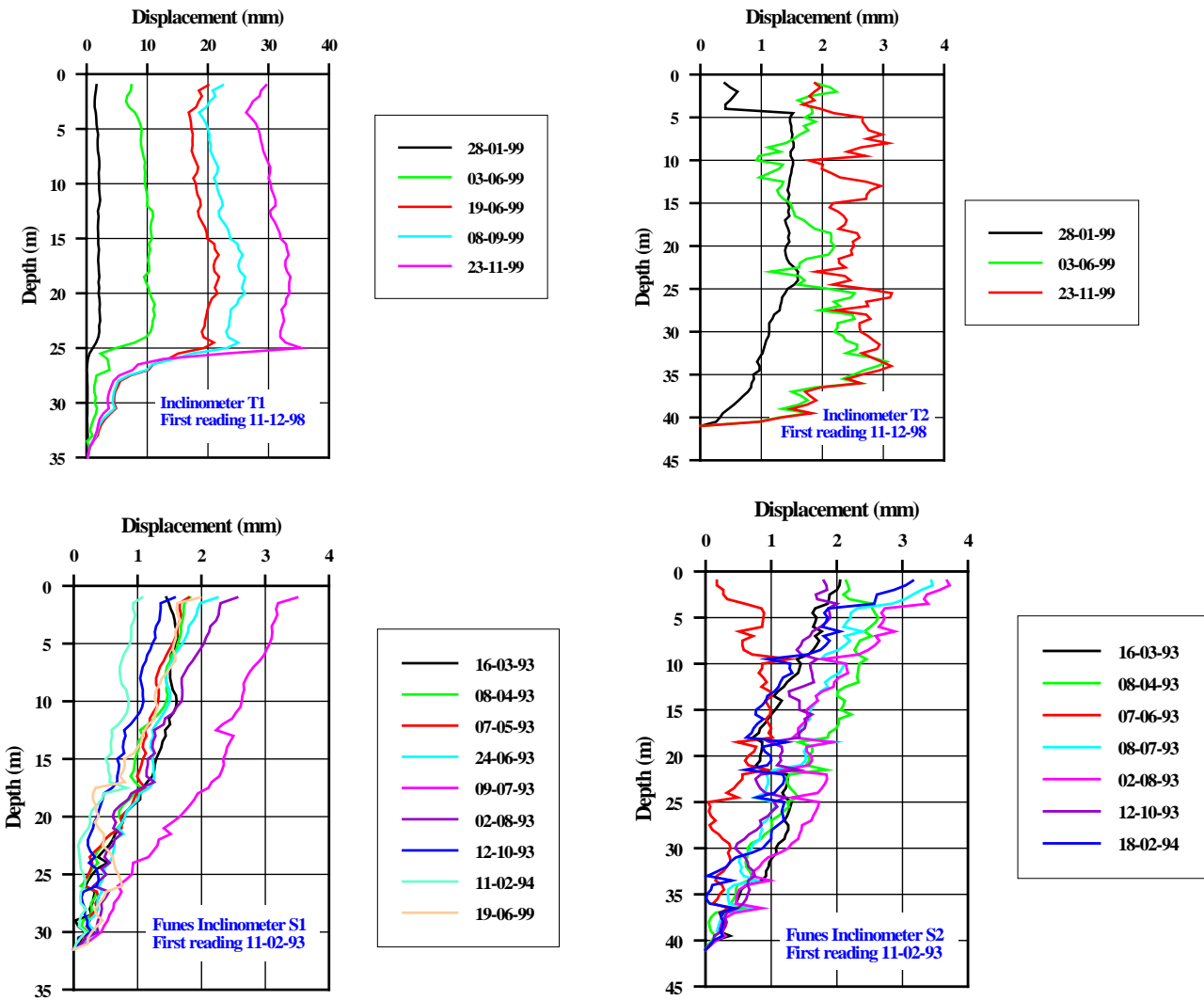


**Figure 9 (a, top left).** Inclinometer T1. **(b, top right).** Inclinometer T2. **(c, bottom left)** Inclinometer S1. **(d, bottom right)** Inclinometer S2.

### *TDR Measurements*

At Pian de Cice, near borehole T1, a twin hole equipped with TDR cables was dug out. TDR (Time Domain Reflectometry) technology allows changes in the shape and section of a coaxial cable to be identified by means of an electromagnetic impulse generated by an oscilloscope (O'Connor & Dowding, 1999). The TDR system also permits multiple failure surfaces to be identified and, with respect to the inclinometer system, has the advantage of a longer durability, although it may show a delay in the response to displacements when installed in non-rigid rock masses.

Two coaxial cables (7/8" and 1"5/8 thick) were installed and 4 measurements were carried out in November 1998, January 1999, June 1999 and December 1999, respectively. The comparison with subsequent measurements (Fig. 10) seems to point out some displacements at a depth of 24 to 28 m in the 7/8" cable, whereas displacements in the 1"5/8 cable were recorded between 10 and 15 m, and at 24.4 m and 31.6 m, partially corresponding to the data recorded in the nearby T1 inclinometer.

The picture emerging from the measurements of surface and at depth displacements, confirmed also by geomorphological evidence, highlights the constant retrogradation of the main scarp and the progressive enlargement of the unstable area. Furthermore, it shows a worrying general increase of the displacement velocity which will have to be carefully assessed and monitored also in the years to come. The perimetral fissure is in fact quite close to the slope of Mt. Teverone; this retrogradation is probably linked to the reactivation of previous landslide deposits which in the past affected the Roncadin area. Indeed, just in this sector the depth of the slip surface, which is probably placed at the boundary between debris materials and sound rock, increases considerably up to 65 m.

Also the secondary scarp, which bounds downstream the upper accumulation zone, is subject to retrogression. This is causing a hazardous approach of the secondary scarp to the main one. The connection between these two important morphological elements would cause quite a dangerous situation since in this way a single large scarp, some hundred metres high, would be formed, impending over the mudflow lower part. This would in turn decrease drastically the time interval between the flow activation and the moment when the displaced material would presumably reach the proximity of Funes, with evident negative repercussions on its risk conditions. Significant movements have also been recorded in the Pian de Cice area which is of strategic importance for the stability of the whole upper accumulation. Along the discharge canal a well-defined surface is visible, pinpointed by continuous water percolation. This surface corresponds to an important discontinuity whose presence and activity is also confirmed by inclinometer data. The disarrangement of this sector would induce serious negative changes on the stability of the upper area. Finally, the different evolution of this process recorded in the past few years, consisting in the mobilisation of all the unstable area, as resulting also from the September 1998 event, is of some concern. In that occasion an acceleration of the movement was recorded in all topographic points; this was confirmed also by morphological evidence observed directly in the field, such as a fracture which continually separates the upper accumulation zone from the main scarp.

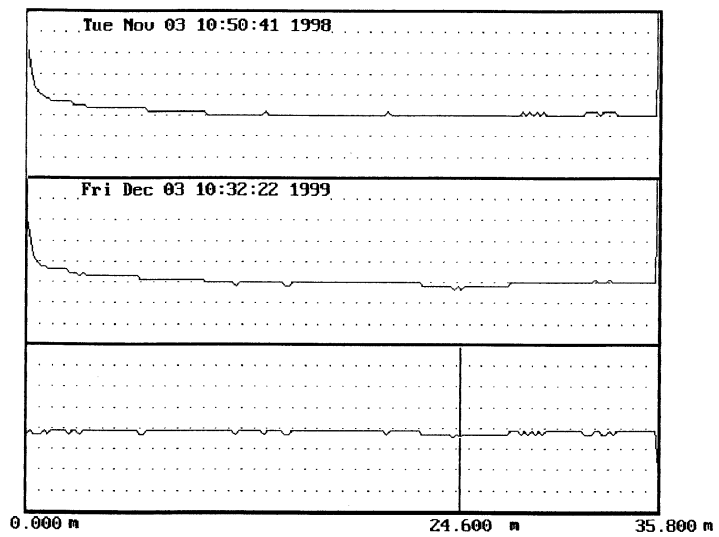
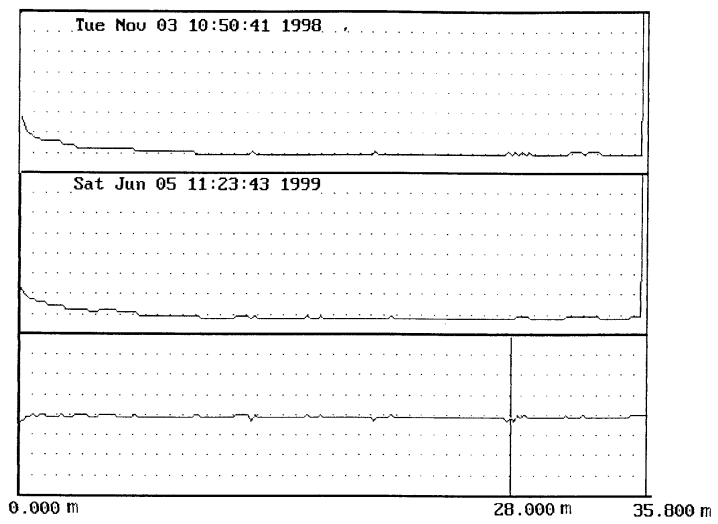
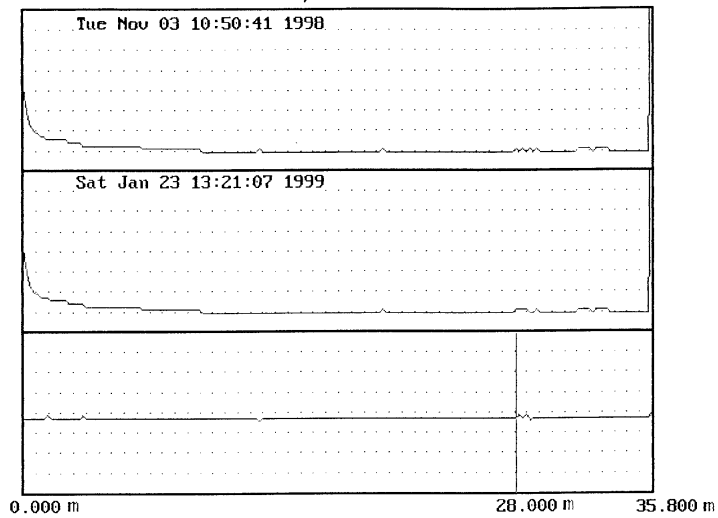
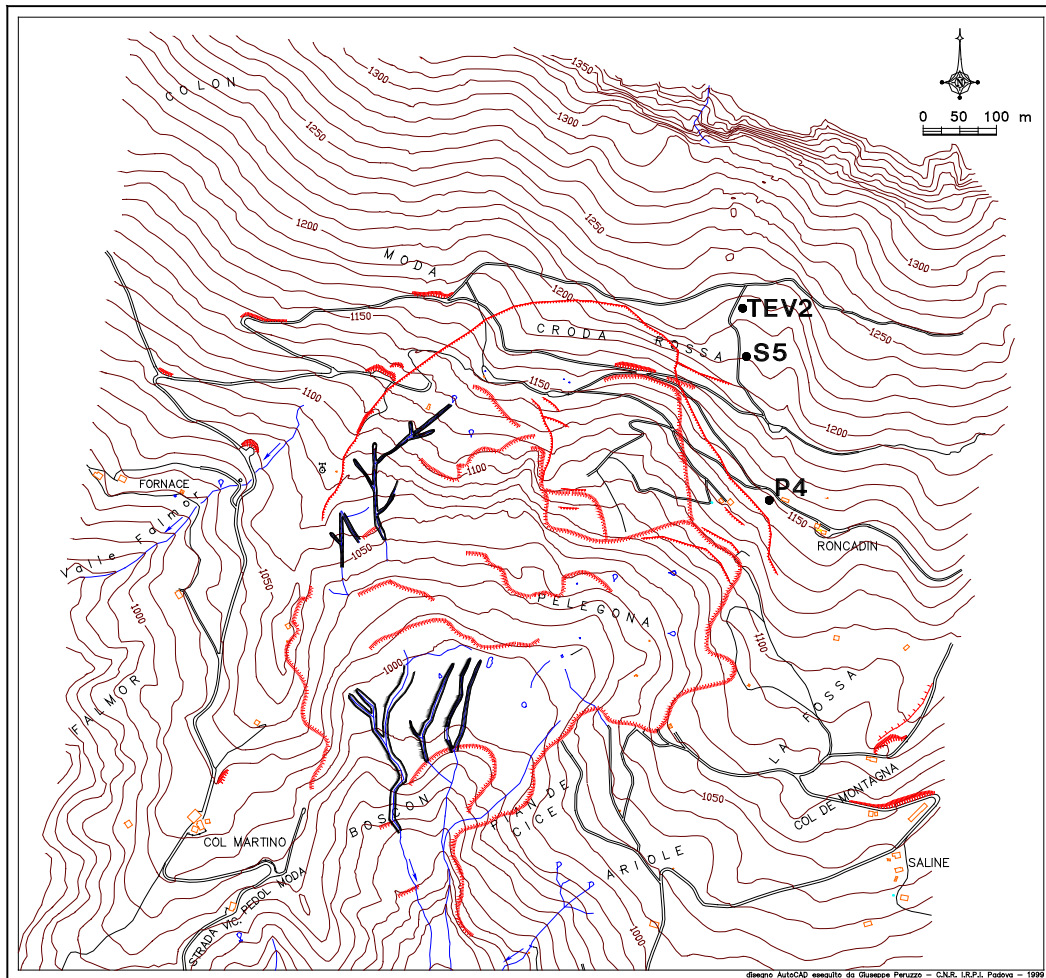


Figure 10. TDR cable (7/8"). Comparison among 2,3,4 and 1 readings.

### **Measurements of piezometric levels**

Measurements of piezometer levels, which have been continually recorded by means of pressure transducers and data logger, have concerned the only wells still explorable around the source area (Fig. 11).



**Figure 11.** Automated water table recording.

Fig. 12 shows the trend of the piezometric level in well S5 starting from 1992. Until 1996, measurements were carried out manually nearly every day whereas subsequent measurements were recorded automatically. It is important to note how the trend of piezometric levels, in particular of the maximum values, does not show substantial changes between the 1992-1994 and 1998-1999 periods. On the contrary, definitely lower values were recorded in the 1994-1997 period, which mostly coincides with the excavation of the draining tunnel. This might mean that the tunnel has at first developed an effective draining action on both the Mt. Teverone massif and on the landslide accumulation. In the latter a return to the pre-tunnel hydrological conditions was probably developed once that draining conditions were stabilised owing to the presence of different and deeper hydrogeological circuits.

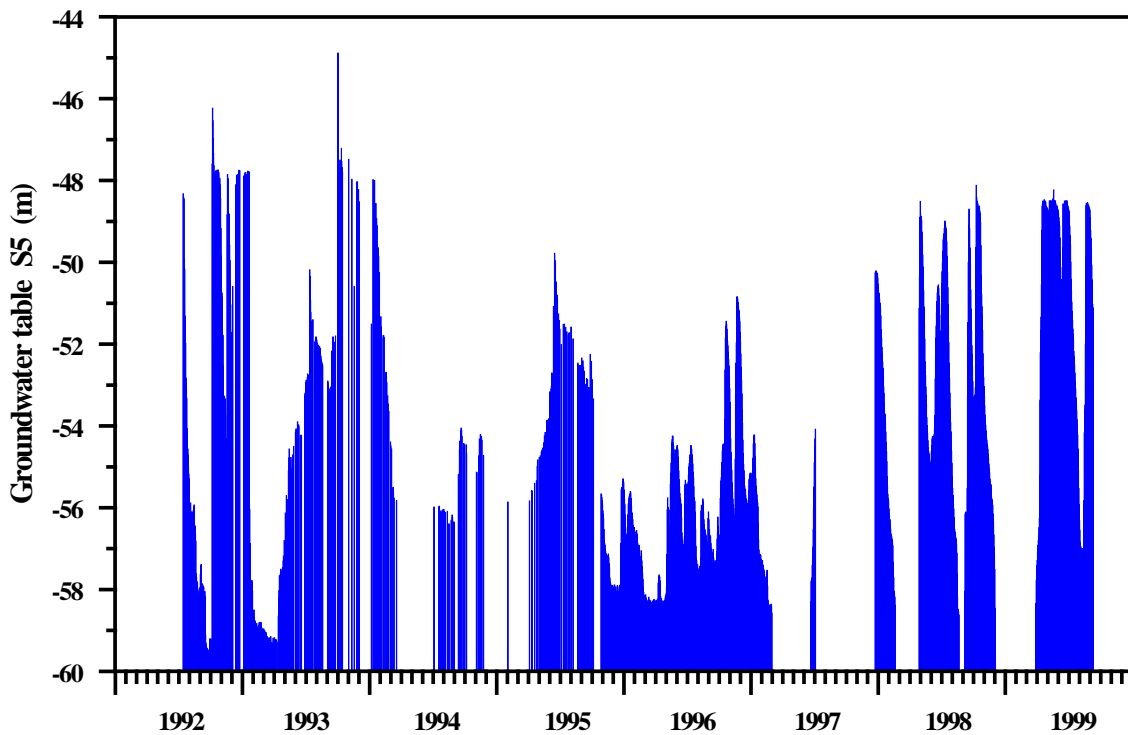


Figure 12. Groundwater table fluctuation in S5 borehole (1992-1999).

***Precipitation measurements***

Figs 13 and 14 show the trend of precipitation and the 12-month cumulated values recorded at the San Martino d’Alpago meteorological station in the Veneto Region. Nevertheless, the analysis of precipitation data has not allowed clear and univocal relationships with the trend of displacements to be identified. As a consequence, it was not possible to define rainfall thresholds for the triggering of landslide events, both for the 1950-1999 period (Fig. 15) and the 1997-1999 period. Fig. 16 shows some rainfall cumulated histograms concerning both the September 1998 event and other situations during which increases of landslide activity were not recorded. The latter also show similar or sometimes higher values in both intensity and time length.

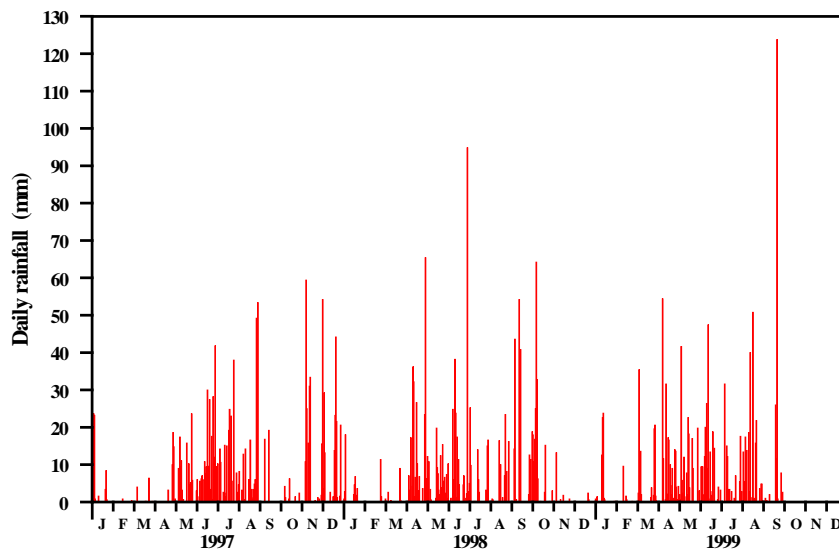


Figure 13. Daily rainfall at S. Martino d’Alpago station.

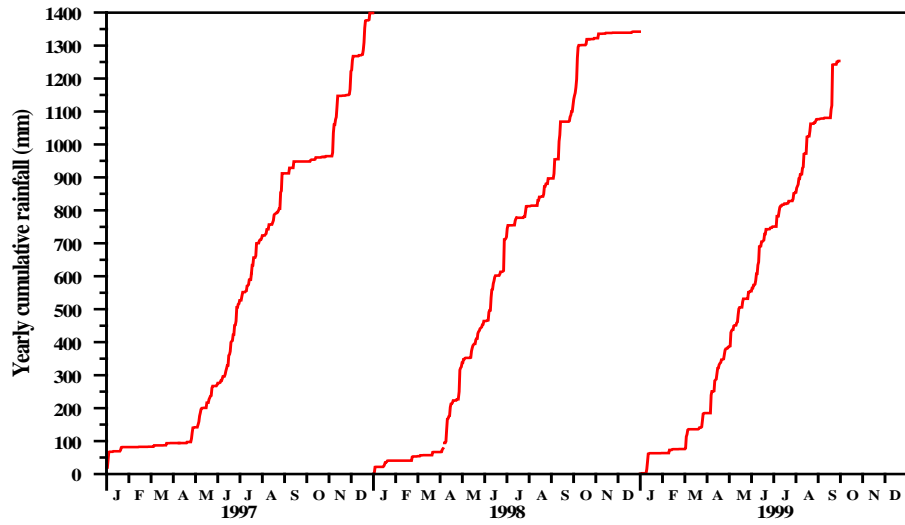


Figure 14. Yearly rainfall cumulate at S. Martino d'Alpago station.

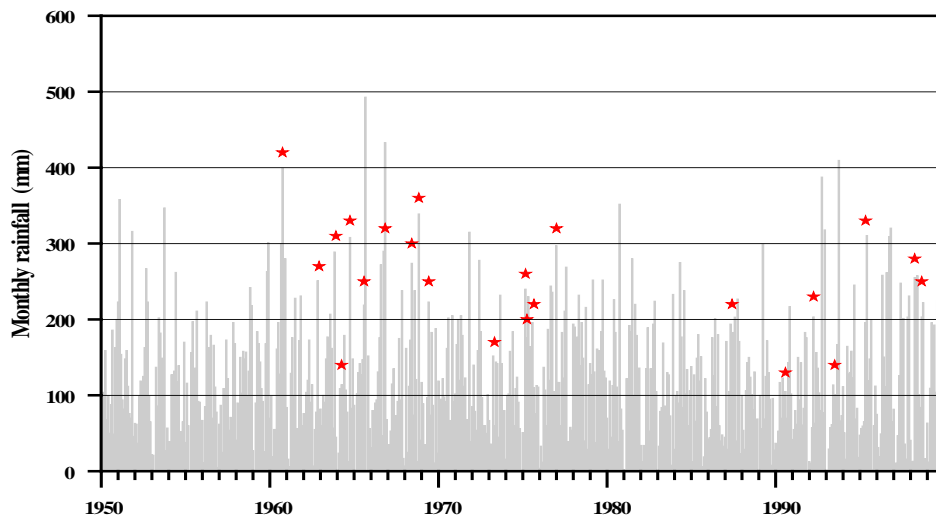


Figure15. Comparison between monthly rainfall cumulates and triggering events.

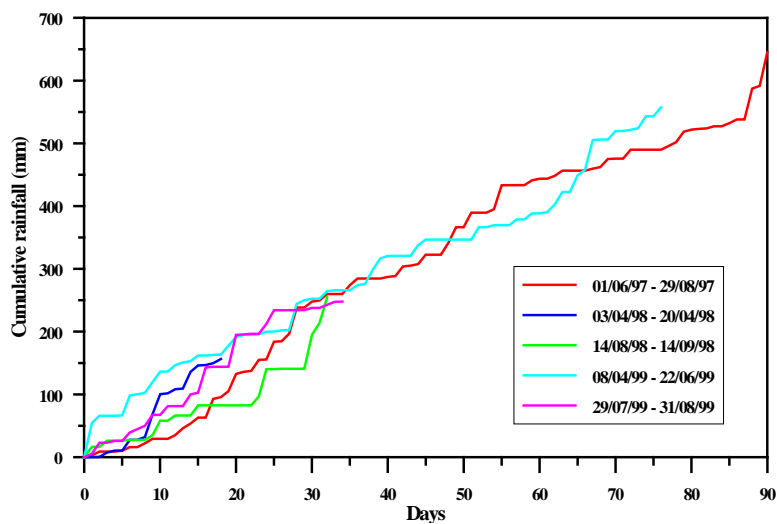
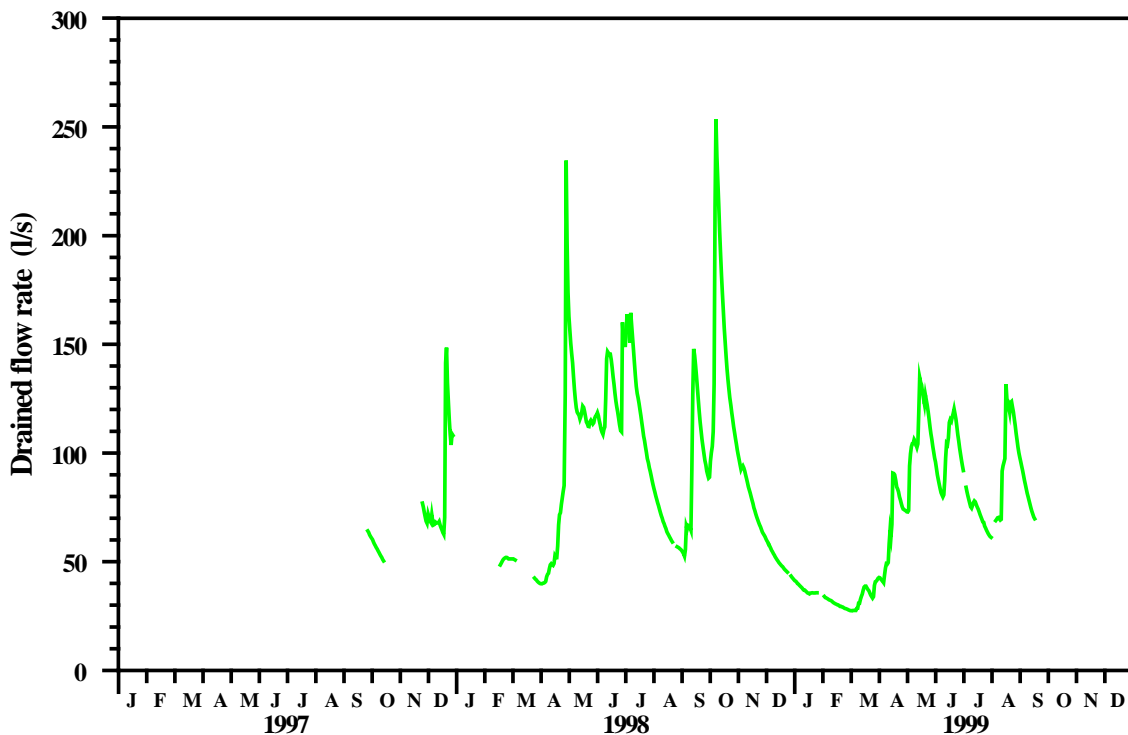


Figure 16. Cumulated rainfall during 1997-1999 for major pluviometric events. The green line shows the rainfall cumulate in September 1998.

### ***Flow rate measurements in the tunnel***

Fig. 17 shows flow rate valued recorded in the tunnel starting from the installation of the automatic measurement system (September 1997). A continuous, constant flow rate of about 30÷40 l/s is present, with increases, changes and daily peaks which have sometimes attained 250 l/s. The trend of flow rates shows the good performance of the draining tunnel and its immediate response, with practically instantaneous increase of the flow rate with respect to precipitation (Fig. 18); this fact demonstrates the presence of a particularly active groundwater circulation due to fracturing.



**Figure 17.** Drained flow rate in the tunnel.

### ***Correlations between precipitation, water table and drained flow rate in the tunnel***

Figs 18 and 19 show the trends of precipitation, water table fluctuations in TEV2 and S5 and the flow rate of the draining tunnel in order to better identify their reciprocal correlations. Comparison of Figs. 18 and 19 highlights an adequate draining response of the tunnel on the Mt. Teverone massif, with maximum flow rates sometimes exceeding 200 l/s and confirms, although still approximately, a close correlation between water table fluctuations and trend of drained flow rates in the tunnel, with responses which are immediate and practically similar to the trend of precipitation. In the March-August 1999 period a considerable difference between the water table level and the flow rate of the draining tunnel was recorded in piezometer S5, compared with what had occurred in the previous periods. In fact, flow rates show relatively low values with respect to the water table levels measured.

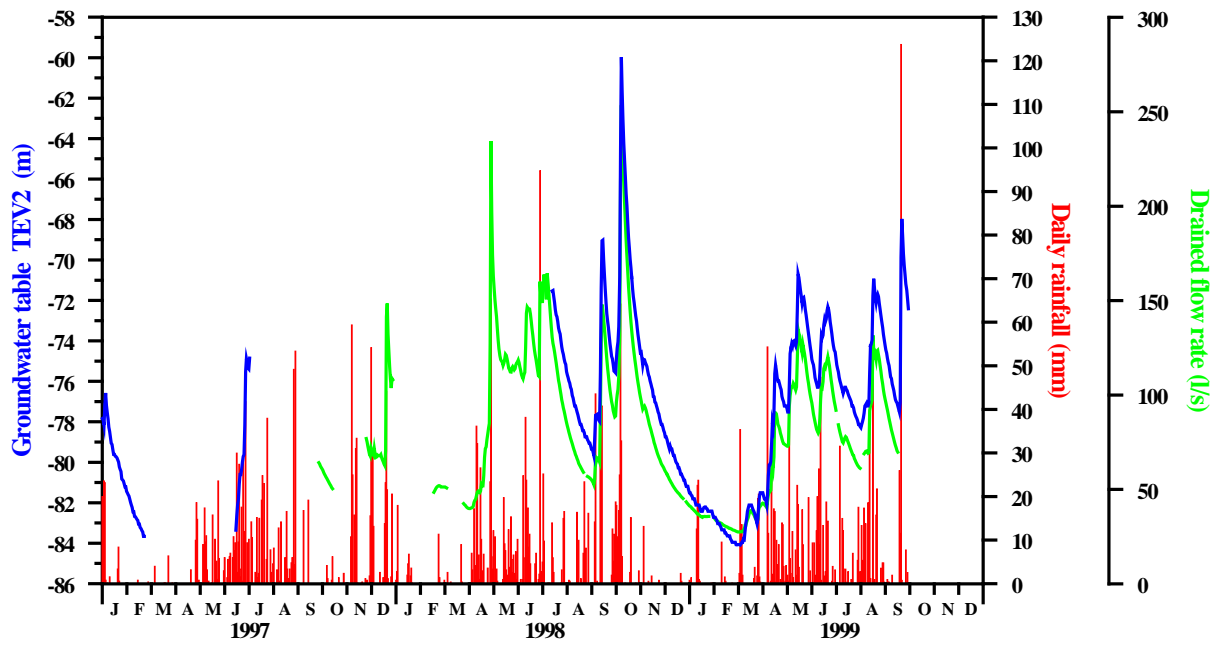


Figure 18. Comparison among daily rainfall, groundwater table (TEV2) and flow rate of the draining tunnel.

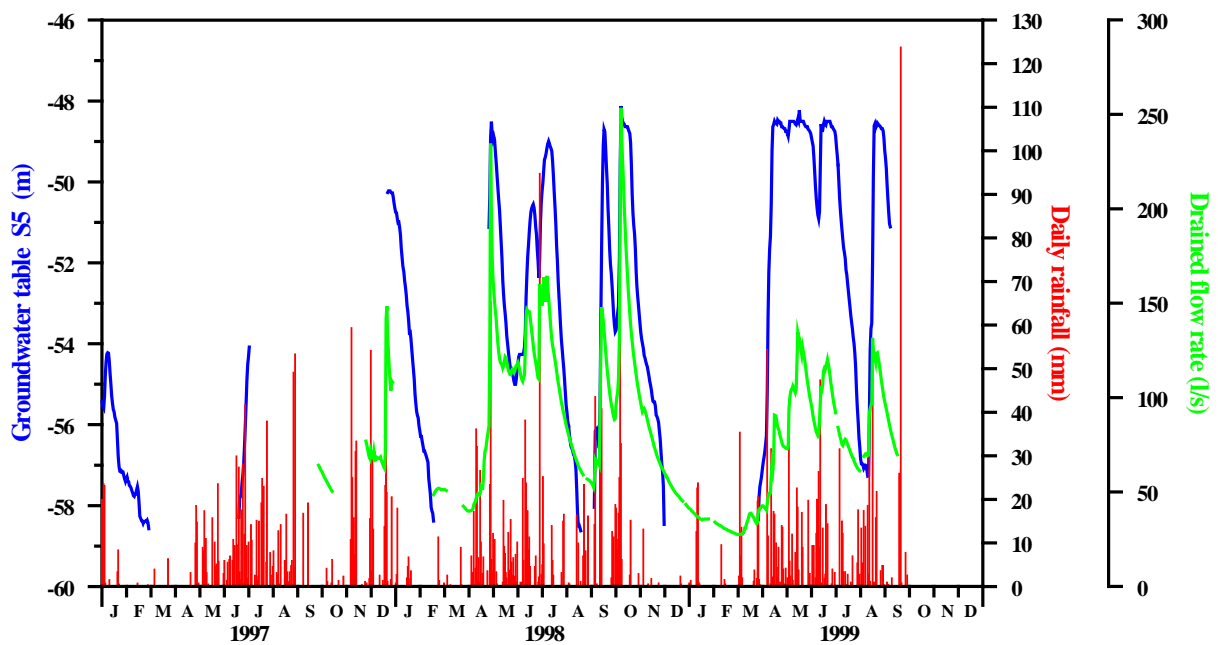


Figure 19. Comparison among daily rainfall, groundwater table (S5) and flow rate of the draining tunnel.

Hydrological analysis has proven a delay of about 6 hours between the beginning of precipitation and flow rate increase in the tunnel and a delay of 9 and 12 hours between the beginning of precipitation and the increase of water table levels in boreholes TEV2 and S5, respectively (Table 1). Such a quick response from both the draining tunnel and piezometric surface reveals a particularly active water circulation inside the rock mass, due to the numerous fractures present in the whole area.

**Table 1.** Time lags between onset of precipitation and response at recording stations

<i>Date</i>	<i>Time lag (h)</i>			<i>Rainfall</i>		
	Q tunnel	GWT S5	GWT TEV2	Period		Cumulate (mm)
10-12 June 98	8	17	-	10/06/1998	12/06/1998	63.2
28 June 98	3	7	-	27/06/1998	28/06/1998	97.8
5 September 98	8	11	9	04/09/1998	05/09/1998	57.8
11-13 September 98	5	11	6	11/09/1998	14/09/1998	113.8
4-5 October 98	8	25	17	30/09/1998	07/10/1998	192.2
7-8 April 99	9	12	12	07/04/1999	08/04/1999	65.6
4-5 May 99	7	13	9	30/04/1999	07/05/1999	57.4
14-15 May 99	3	12	9	12/05/1999	15/05/1999	50.8
13 June 99	4	8	5	04/06/1999	13/06/1999	126.4
12-13 August 99	6	11	8	10/08/1999	13/08/1999	61.4
AVERAGE	6.1	12.7	9.4			

Nevertheless, in the March-August 1999 period the amount of flow rate in the draining tunnel shows a considerably lower value with respect to what one would expect from the comparison with the respective piezometric levels. This fact, associated to the presence of active water emergences inside the landslide body also in the driest periods, has been interpreted as a draining action exerted by the tunnel only on the outermost part of Mt. Teverone; in any case, the existence of a much deeper hydrogeological circuit not directly depending on Mt. Teverone massif seems to be very likely.

Indeed, according to the previously discussed data, Mt. Teverone's southern slope is affected by tectonic lineations which put in straight contact the Fadalto Limestones with the Alpage Flysch. These north-dipping structures seem to isolate large tectonic slivers and offer groundwater preferential flow paths which feed the springs existing along the main scarp. Therefore, according to this flow pattern, water is conveyed into the landslide area not just by groundwater overflowing from the aquifer present inside Mt. Teverone — which would be highly influenced by the action of the draining tunnel — but by a deeper circuit not intercepted by the tunnel itself.

### **Stability analyses**

The results of some stability analyses carried out both in the source area and on the mudflow are here after reported in order to define possible evolution scenarios.

#### *Source area*

In order to define the conditions which led to the development of the Tessina landslide and forecast its possible evolution in time, stability analyses have been carried out along both the slope lower portion, in the area known as Pelegona, and the left hydrographic profile passing through the Pian de Cice (Fig. 20) area.

Investigations have been carried out along two profiles by using the UDEC computation code with distinct elements (ITASCA, 1993) which allows mobilised shear strengths, displacement rates and distribution inside the rock mass to be assessed. This programme simulate the mechanical behaviour of the rock mass represented as a set of discrete blocks subject to both static and dynamic load.

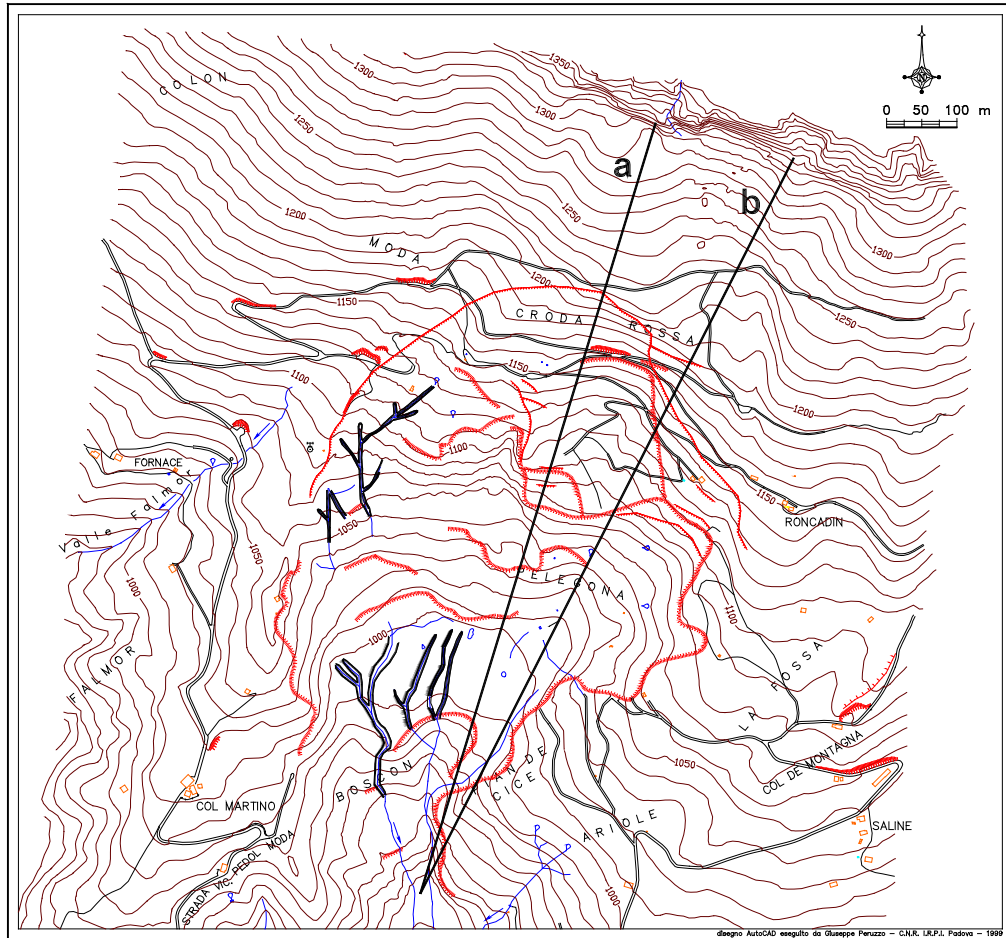


**Figure 20.** Stability analyses cross sections.

The main characteristics of the computation code are the following:

- discontinuities are treated as boundaries between blocks; finite displacements along discontinuities and rotations between blocks are permitted;
- blocks may be either rigid or deformable; contacts are always deformable;
- the programme recognises new contacts which are developed with the proceeding of the computation;
- various behaviour models are available which follow linear and non-linear laws, both for discontinuities and blocks;
- the programme can simulate a steady-state or transient flow through a discontinuity.

*Profile a: Slope and material modelling*

The slope modelling was elaborated on the basis of morphological features and attitude of the main discontinuity systems observed just before the 1998 collapse. The mesh adopted is shown in Fig. 21.

Job Title : Tessina - profilo a  
From File : dati\dfranal1.sav

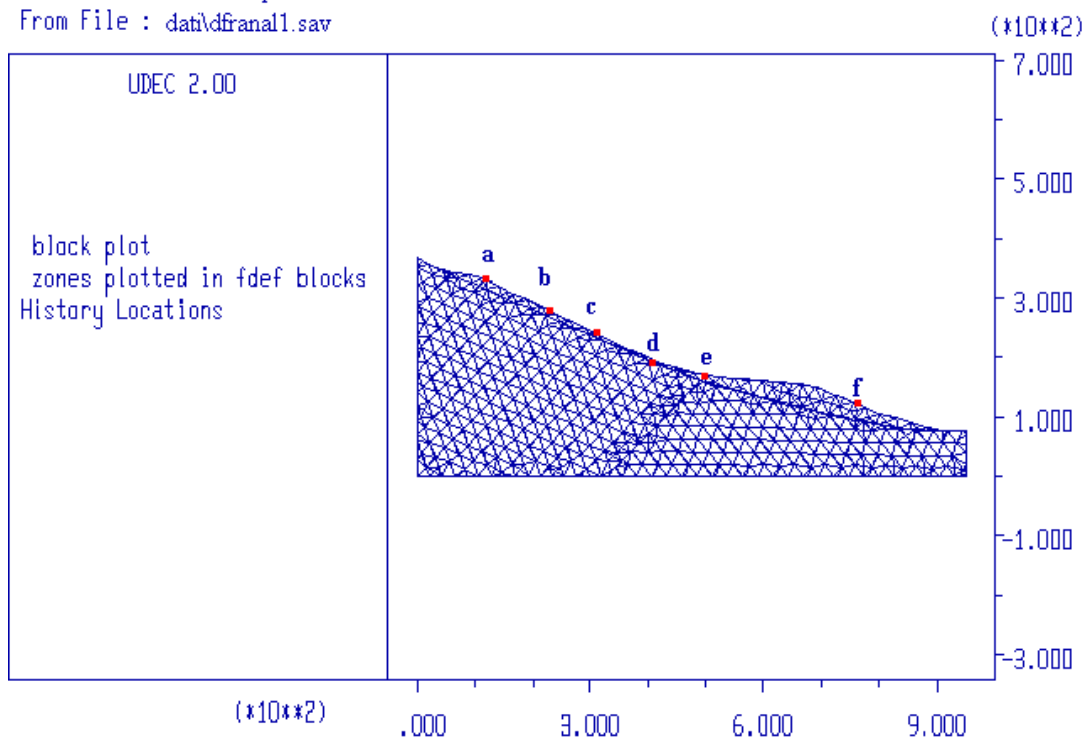


**Figure 21.** Discretised net of the analysed slope. a-f displacements monitored points.

The bedrock (made up of flysch), the landslide debris in the slope lower portion and the overhanging talus fan (between 1040 and 1200 m a.s.l.), have been considered as completely deformable blocks and therefore discretised into triangular elements of different dimensions; the model of mechanical behaviour assigned to both the three rock types and discontinuities is an elastic perfectly plastic model (Mohr-Coulomb). Fig. 22 shows the geological model of the analysed section.

On the basis of data acquired by field surveying (in particular a perennial spring was recognised at the altitude of 1130 m a.s.l.), the presence of groundwater contained inside the debris and confined by the underlying flysch has been inferred. By considering slope inclination and the hydraulic characteristics of the talus fan, the piezometric level was located at about 6÷10 m from ground level, whereas the slope lower portion, made up of landslide debris, has been considered as completely saturated.

Job Title : Tessina - profilo a  
 From File : dati\dfanal4.sav

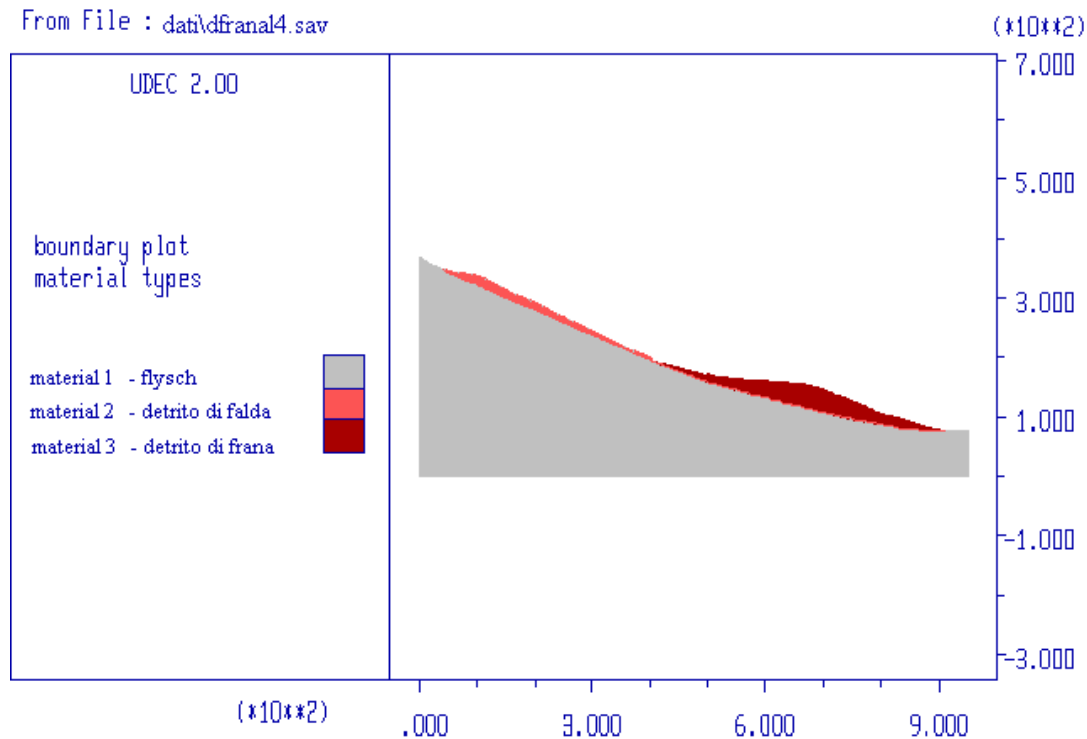


**Figure 22.** Geological model of the analysed section (material 1: flysch; material 2: talus; material 3: landslide debris).

The values of the materials' geotechnical and geomechanical parameters utilised for the stability analyses have been determined by means of laboratory tests (Table 2; see also Chapter 10).

**Table 2.** Geotechnical parameters and constitutive models used in computations.

<i>Material</i>	$\gamma$	$c$	$\phi_{cv}$	$K$	$G$	$JK_n$	$JK_s$	<i>Model</i>
Flysch	24	$3 \times 10^4 - 1 \times 10^4$	30-24	$8 \times 10^9$	$4 \times 10^9$	-	-	MC
Talus	21	$1 \times 10^4 - 0$	32-27	$9 \times 10^8$	$4 \times 10^8$	-	-	MC
Landslide debris	19	0	26-20	$7 \times 10^8$	$7 \times 10^7$	-	-	MC
Joints	-	0	26-20	-	-	$9 \times 10^7$	$9 \times 10^7$	CY

The characteristics attributed to the flysch correspond to the peak shear strength conditions of remoulded material (constant volume parameters or critical state values); this choice was made in order to consider the weathering and softening processes affecting the most superficial flysch level. On the other hand, residual shear strength parameters have been ascribed to the discontinuity joints present in the flysch, owing to the chaotically arranged attitude of this formation. The properties of the talus fan have been determined on the basis of grain-size and undisturbed characteristics which show the presence of a weak cementing bond.

## Results

After having determined the materials' stress state, a flow pattern for the groundwater percolating inside the slope was elaborated. Afterwards, a combined flow-deformation analysis was carried out. Since the UDEC code does not provide a direct calculation of the factor of safety, the stability conditions are described by the trend of horizontal displacements of the points monitored.

The geometrical and mechanical characteristics imposed to the slope point to instability conditions for its lower portion; the analysis of horizontal deformations (Fig. 6.42) shows in fact that the landslide body is subject to displacements exceeding 10 m up to a depth of 20÷30 m (displacements are function of the number of calculation cycles) whereas at altitudes over 950 m a.s.l. displacements less than 5 m are recorded.

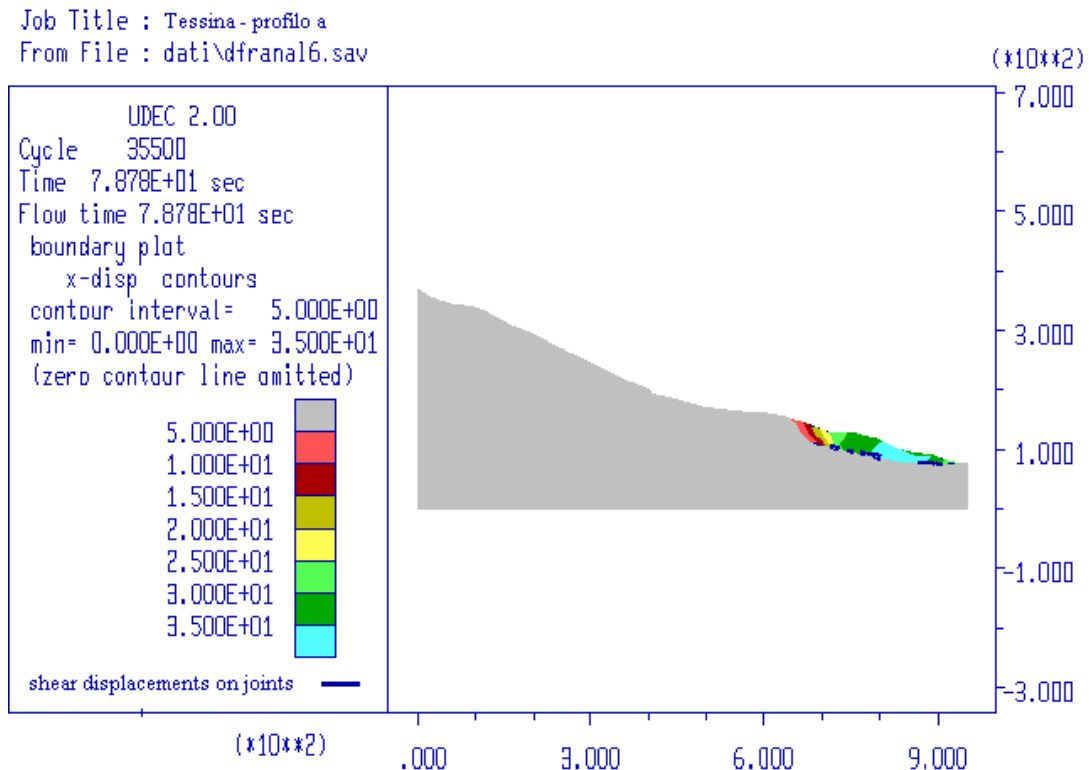


**Figure 23.** Horizontal displacements contours at calculation cycle n. 35,500.

Such are the characteristics of the landslide materials that in the slope lower portion the highest deformation values are recorded; this hinders the development of analyses in the slope upper portion, as shown by the diagrams of horizontal deformations which were monitored at points a, b, c, d and e, located in the slope upper part (Fig. 24). The diagram of horizontal deformations of the lowermost monitored point (f) does not show the attainment of equilibrium conditions and the displacement values depend therefore only on the number of calculation cycles.

Job Title :  
 From File : dati\dfranal6.sav

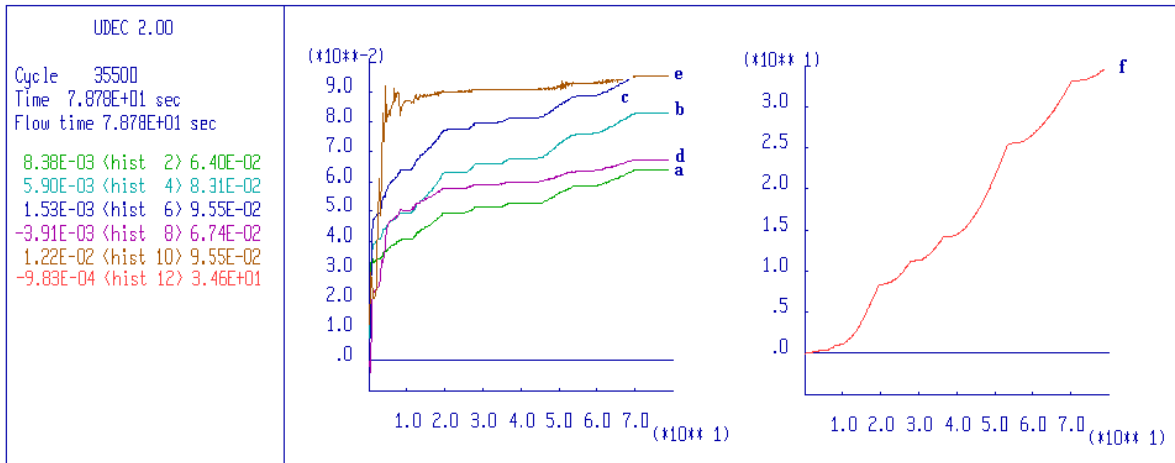


**Figure 24.** Horizontal displacements at the monitored points a-f as a function of calculation time.

With the proceeding of analyses, i.e. with the number of calculation cycles, instability conditions are propagated uphill (Fig. 25), with regressive kinematic mechanism, as shown by the diagram of displacement vectors (Fig. 26 a cycles: 35,500; b cycles 55,500); the basal surface of rupture is therefore located at an approximate depth of 30÷40 m, at the boundary between flysch and landslide debris.

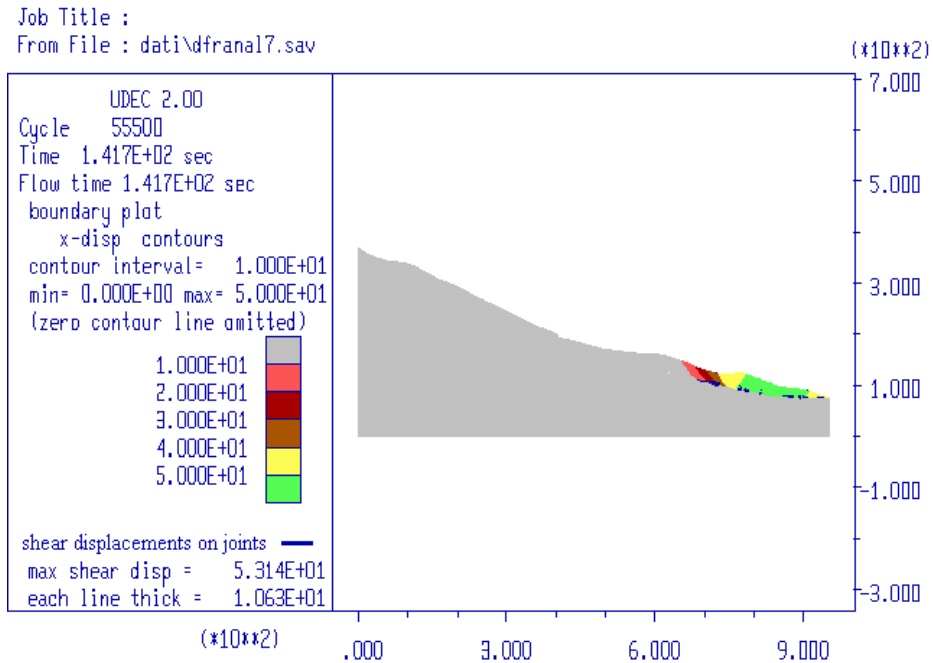


**Figure 25.** Horizontal displacements contours at calculation cycle n. 55,500.

The evolution of the landslide process as results from analysis results is quite similar to what actually occurred in the Pelegona area.

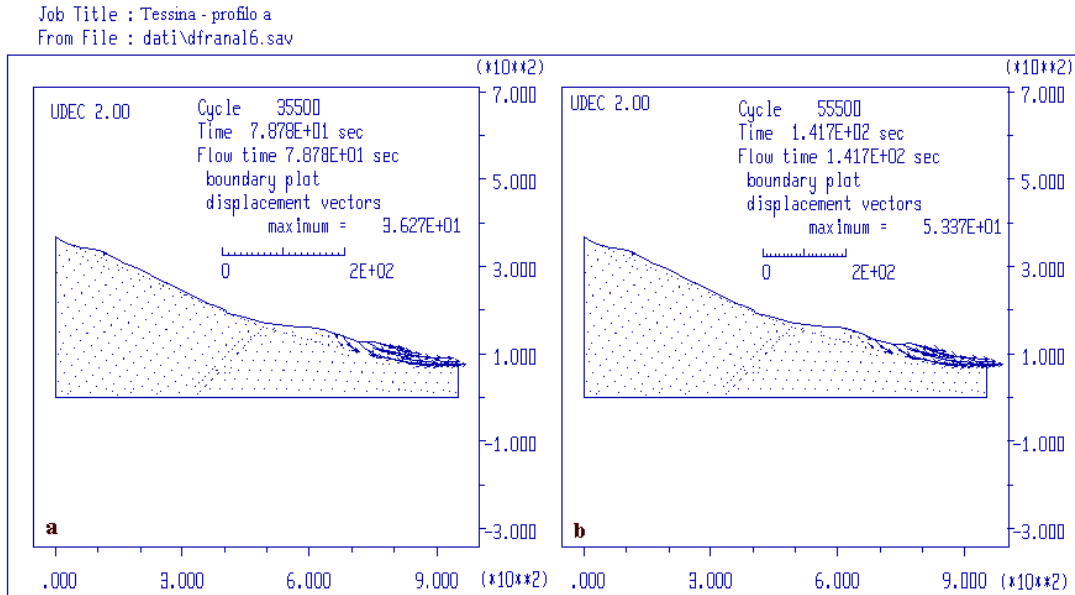


**Figure 26.** Displacement vectors.

Fig. 27 shows the displacement affecting the mesh in the slope lower portion.

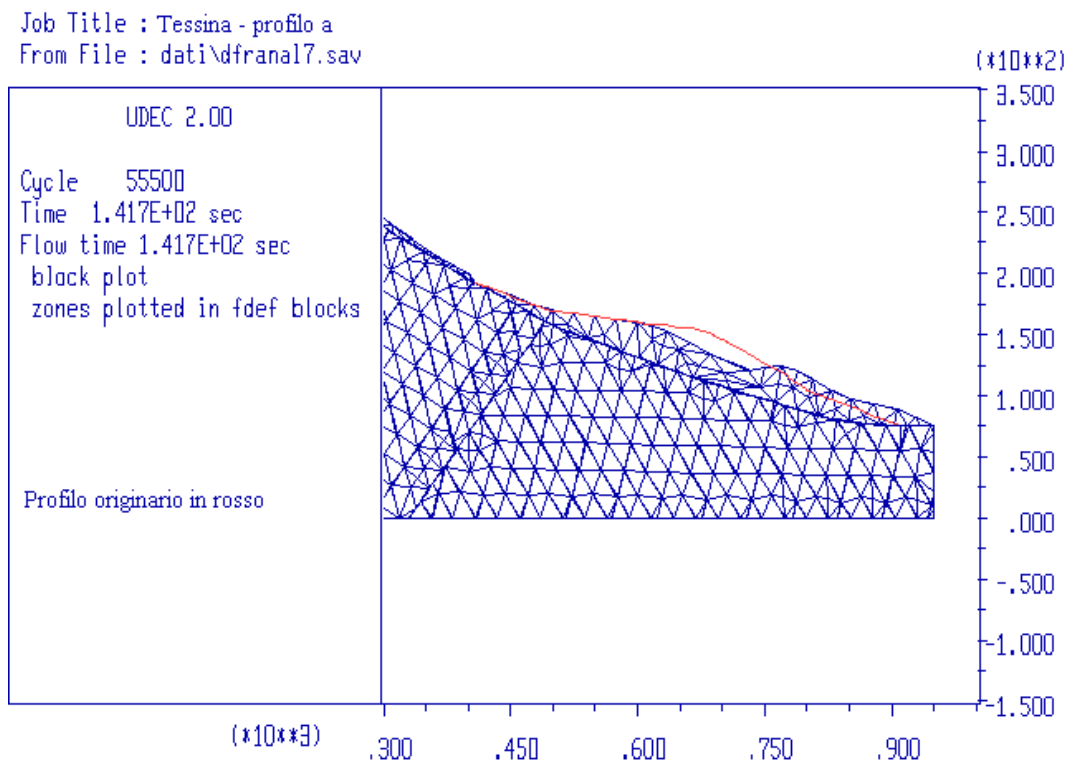


**Figure 27.** Deformation of the net at cycle n. 55,500 (the red line represents the original profile).

The fact that stability analyses show a non-equilibrium situation, i.e. the full development of a landslide process — whereas in reality a new collapse of the landslide debris has not yet taken place in the slope portion downhill of the approximate elevation of 1020 m a.s.l. — means that the shear strengths actually involved have not yet declined to the values corresponding to the critical state, i.e. constant volume conditions. Nevertheless, the presence of extension cracks, ground swelling and other geomorphological evidence clearly shows that the slope is progressively subject to deformations; in time the rate of displacement will be such that the available shear strength will reach its minimum value, thus triggering a slope movement with characteristics similar to those shown by the stability analyses.

*Profile b: Slope and material modelling*

A stability analysis was carried out also on the profile passing through the Pian de Cice area, which was topographically surveyed in May 1999. The adopted mesh is shown in Fig. 28.

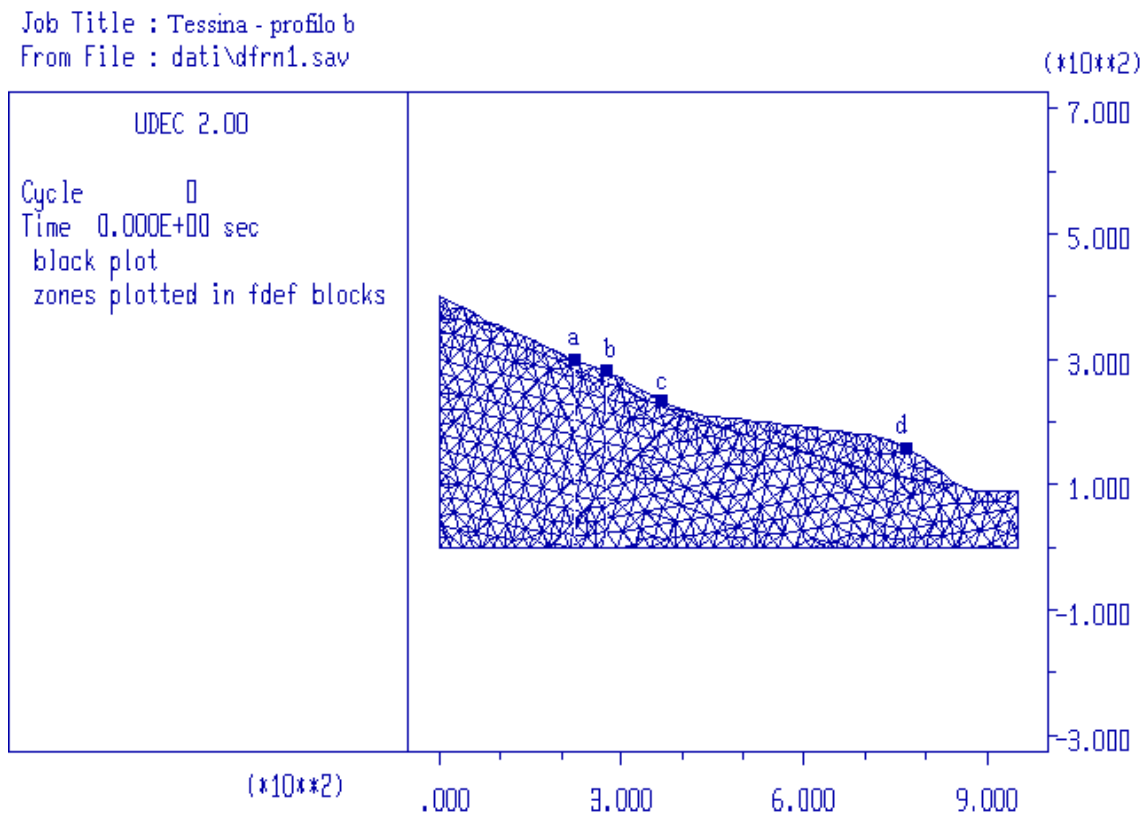


**Figure 28.** Discretised mesh of the analysed slope. a-d: displacements monitored points.

As in section a, the flysch bedrock, the landslide debris in the slope lower part and the talus fan in the slope upper part have been considered as completely deformable blocks and therefore discretised in triangular elements with different dimensions; the model of mechanical behaviour assigned to both the three rock types and discontinuities is of the elastic perfectly plastic type (Mohr-Coulomb).

Fig. 29 shows the schematic geological model of the section analysed.

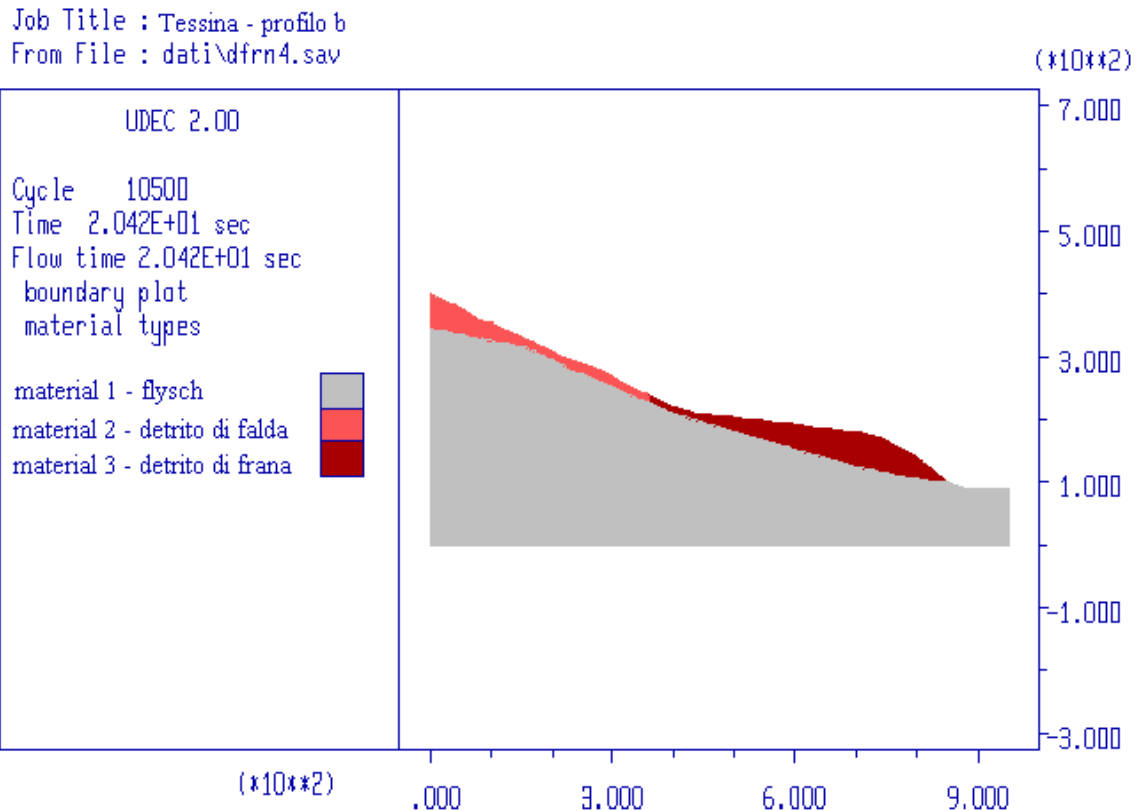


**Figure 29.** Geological model of the analysed slope (material 1: flysch; material 2: talus; material 3: landslide debris).

The position of the groundwater contained within the debris and confined by the underlying flysch was determined on the basis of piezometer data. By considering the slope inclination and the debris hydraulic characteristics, the water table would coincide with the ground level. The geotechnical and geomechanical parameters of the materials involved in the process studied are the same as those utilised for the analysis of section a (see Table 2).

#### *Final results*

As previously discussed, the stability conditions are described by the trend of horizontal displacements in the points monitored. The geometrical and mechanical characteristics chosen lead to instability conditions both in the slope upper part, where the water table coincides with the ground level, and in correspondence with the front of the landslide debris, owing to the high slope inclination. The analysis of horizontal displacements (Fig. 30) shows that the talus fan, which is subject to displacements exceeding 80 m (as a function of the calculation cycles) up to a depth of about 20÷30 m, advances downstream with a translational-type movement (Fig. 31); in this way considerable stresses are transmitted to the landslide body which resumes movement in its frontal part, whereas the central portion seems to be stable at the moment. The basal surface of rupture is located at an approximate depth of 30÷40 m, at the boundary between landslide debris and flysch, both in the unstable uphill sector and in the downhill one.

Job Title : Tessina - profilo b  
From File : dati\dfnrn5.sav

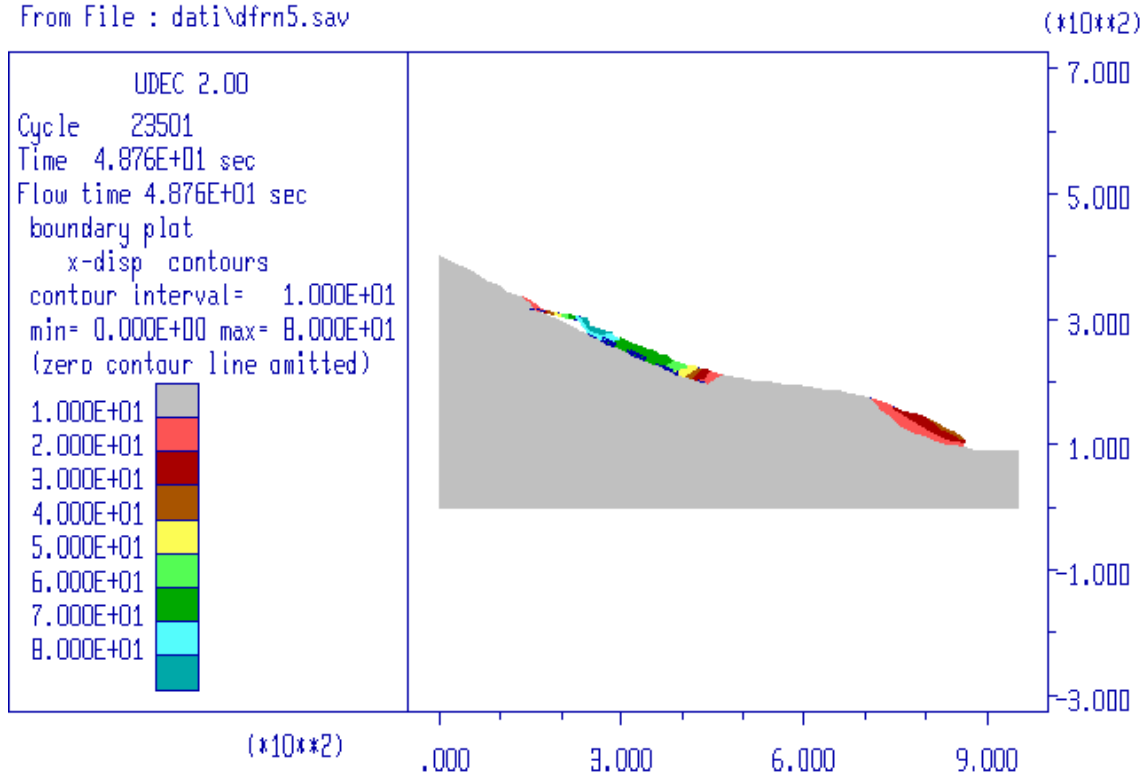


**Figure 30.** Horizontal displacements contours at computation cycle n. 23,501.

The diagram of horizontal displacements of the monitored points a, b, c and d (Fig. 32) points out that the highest deformations are developed in the slope upper part. The analysis therefore shows that equilibrium conditions have not been attained and values of displacements depend only on the number of calculation cycles.

Job Title : Tessina - profilo b  
 From File : dati\dfn5.sav

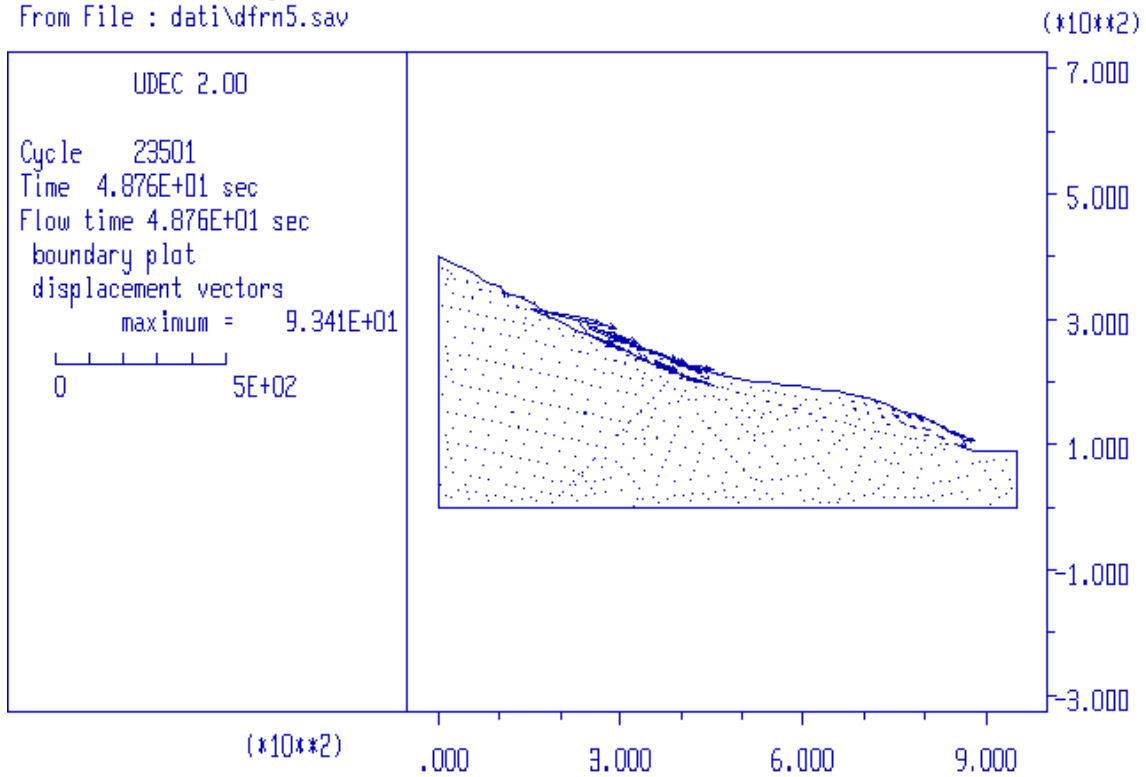


**Figure 31.** Displacement vectors.

Job Title : Tessina - profilo b  
 From File : dati\dfn5.sav

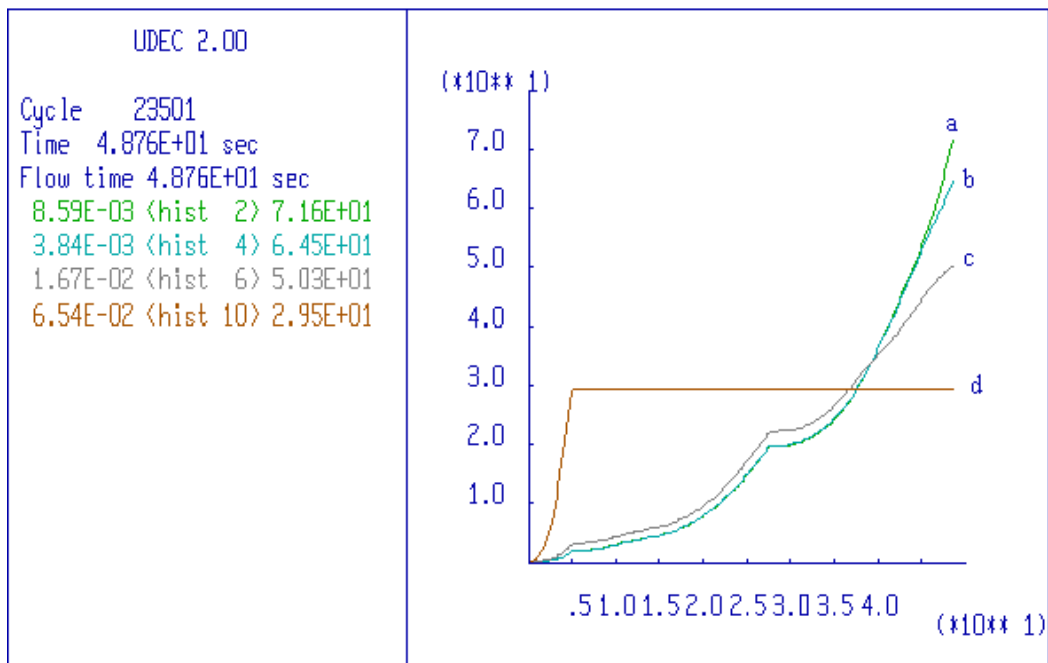


**Figure 32.** Horizontal displacements at the monitored points a-d as a function of calculation time.

## **The mudflow**

As regards the mudflow area, an effort was made in order to identify the reactivation possibility for the existent accumulation materials, also as an overlapping effect of new flows. The extent of the mudflow along the Torrent Tessina valley has reached in time a length of about 2000 m, a width up to 300 m and a thickness of about 60 m.

The material is a mixture of pebbles, gravel, coarse to fine sand in a clayey matrix. From the particle-size analysis high values of material passing through no. 40 sieve are obtained (mesh size 0.42 mm): from a minimum of 55% to a maximum of 61%. Also the amount of material passing through no. 200 sieve (mesh size 0.074 mm) attains considerable values: from a minimum of 53% to a maximum of 58%. These percentages refer to the weight of the material, whereas the volume ratios obviously show very different values and the finest fraction totally fills up the voids of the coarser material.

The coarse material is therefore totally surrounded by the silty-clayey matrix, with hardly any contact between the various elements. As a consequence, the overall material's behaviour is exclusively constrained by the physical and mechanical characteristics of its finest fraction. Direct shear strength tests repeated on the same sample, made up of material passing through no. 40 sieve, have provided values of the drained residual strength angle approaching 30°.

Since present-day inclinations of the mudflow upstream and downstream of the village of Funes are on average 5.7° e 8.7° respectively, the slope is considered "stable". It could approximately be stated that with shear strength angles of 30°, the equilibrium inclination angle of these materials is around 15°. In fact, stability analyses carried out by applying the formula of unlimited slope with water table next and parallel to ground level, have found values of  $F_s = 2.7$  for the slope upstream of Funes and  $F_s = 1.79$  for the slope downstream (Skempton & DeLory, 1957). Therefore the two values define stability conditions for the whole mudflow, providing additional loads are not imposed, even in the most unfavourable situation with water table next to the ground level.

In any case, the results thus obtained apply only to materials which have undergone a complete and "normal" consolidation process, such as the one taken into account for the flow. Indeed, the frequency of flows from 1960 to the present, and therefore the time interval between major events, may be considered sufficiently long to allow dissipation of extra pore water pressures, still maintaining the material saturated.

This is also confirmed by direct observations: in the months following the 1992 events the mudflow topographic level has subsided some metres, without macroscopic evidence of horizontal displacements. The material's high water content, initially at the fluid state, has progressively decreased owing to geostatic load at various depths, thus causing a progressive reduction of the mudflow volume.

### *Sudden load tests*

Other material's collapses in the source area or in the upper accumulation zone might create new flows which would overlap those already stabilised. This produces the "undrained load" phenomenon (Hutchinson & Bhandari, 1971) on the older flow material, inducing in it stresses due to the sudden load. Moreover, new collapses usually take place during intense and prolonged precipitations or following snow melt; these conditions cause a rise of the water table within the landslide body, up to the ground level.

The new sudden load, due to the material coming from the unstable upper area, would therefore be entirely supported by the pore water saturating the in-place material, thus causing an increase of pore water pressure and, in mathematical terms, a decrease of the factor of safety. It is in fact well known that whereas in an equilibrium situation at a certain depth below the water table the load is supported both by the material's solid particles and pore water, in a low-permeability soil all the load is in the short term entirely supported by the pore water that cannot be drained. Therefore, the stability analysis of a slope affected by a flow and subject to a sudden

load, as in the case of the Tessina landslide, should be carried out by assessing the amount of new material that might overlies the stabilised one and the time necessary for the occurrence of this overload (see also Chapter 10).

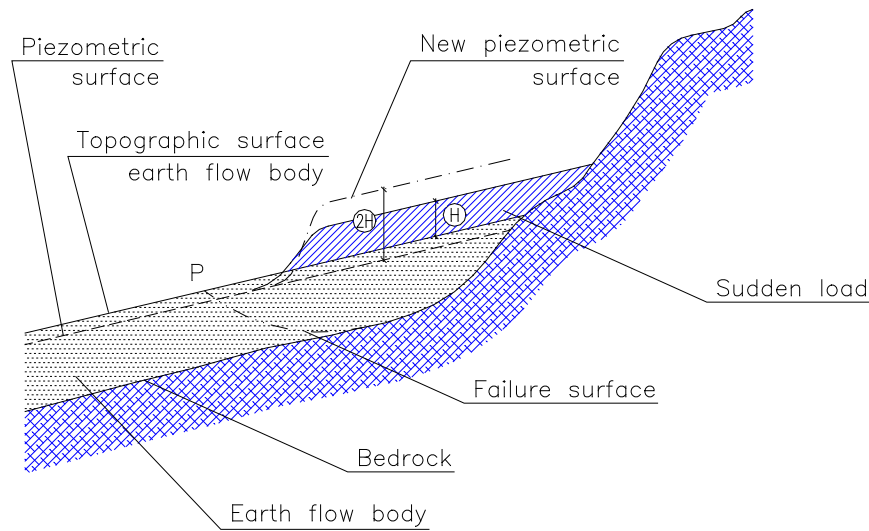


**Figure 33.** Piezometric fluctuations due to a sudden load.

The conceptual bases of the theory explaining the phenomenon are shown in Fig. 33, where the change of the piezometric surface due to the application of a sudden load is schematically shown. If the thickness of the new material is  $H$ , considering that the material's bulk unit weight is twice the water unit weight, the increase induced by the piezometric level is about  $2H$ .

Furthermore, the changes of the slope's geometrical characteristics, due to the accumulation of new material, further reduce the stability conditions. The system's variables may therefore be synthesized as overload height  $H$  and velocity of overload application.

By considering the flow's velocity and the low permeability of the material involved, the problem may be simplified by neglecting the velocity of overload application and taking into account the overload height only.

The attainment of instability conditions, induced by the undrained sudden load, as observed also during field surveys, does not imply the material's liquefaction but rather the rupture of the already stabilised landslide body along a surface which will crop out downstream of the overloaded foot (point  $P$  in Fig. 33): this new displaced material will burden the mudflow portion located immediately downstream of point  $P$ . This process may continue downhill, thus contributing to the further evolution of the movement.

Nevertheless, it should be noted that a single sudden overload event could not determine the general collapse of the landslide body: the new mudflow parts affected by the overload would contrast rupture until the depletion of the overload effect, thus reaching new equilibrium conditions.

Instead, the periodical occurrence of sudden overload events proceeding from upper landslide accumulation area and the mudflow could determine a progression of instability conditions until the whole landslide body is affected. Furthermore, the material thus remoulded would progressively increase its water content up to attaining or overcoming the liquid limit. The problem may be solved by calculating the following parameters (Fig. 34): i) sudden *instantaneous* overload height " $H$ " which leads to  $F_s = 1$  for a given water table depth; ii) value of inclination " $\alpha$ " as a function of the rock mass hydraulic conductivity, rock mass thickness (dissipation along vertical lines) and area occupied.

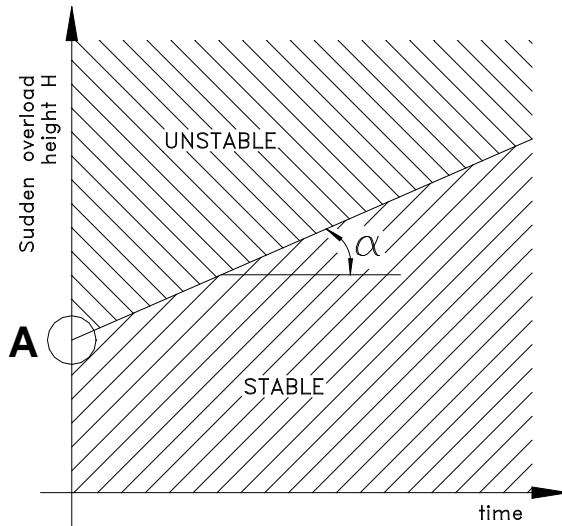


**Figure 34.** Sudden overload height  $H$  as a function of time. Straight line indicates the points at  $F_s=1$ .

The investigations and analyses carried out have allowed the initial water table depth/material thickness ratios to be defined as a function of the  $F_s$  values of the stabilised mudflow.

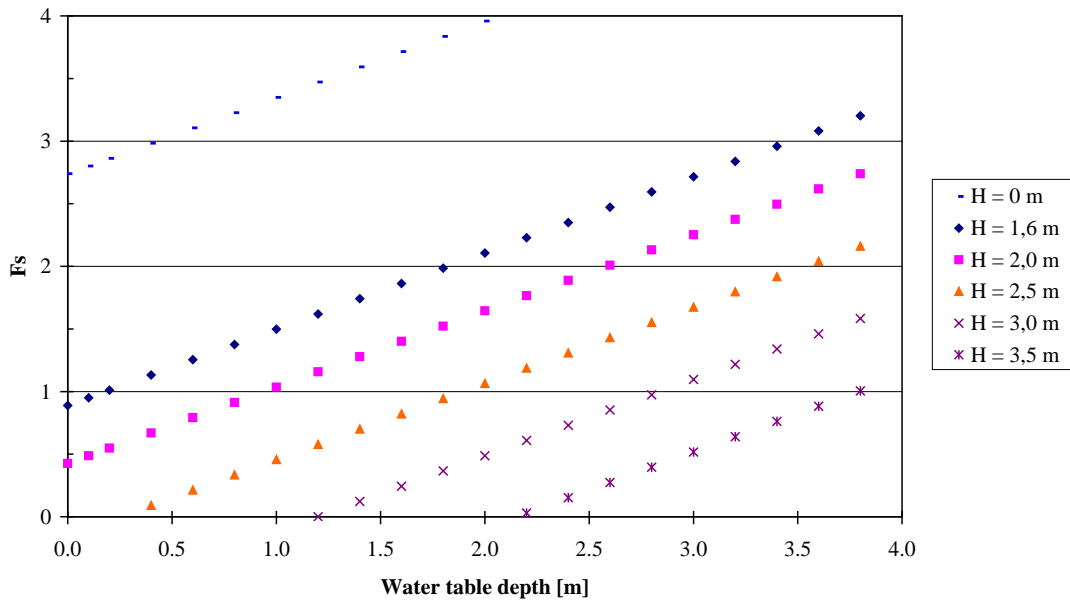


**Figure 35.** Safety factor  $F_s$  variation within the earth flow along a possible failure surface 5 m depth for an infinite slope as a function of sudden overload thickness and water table depth.

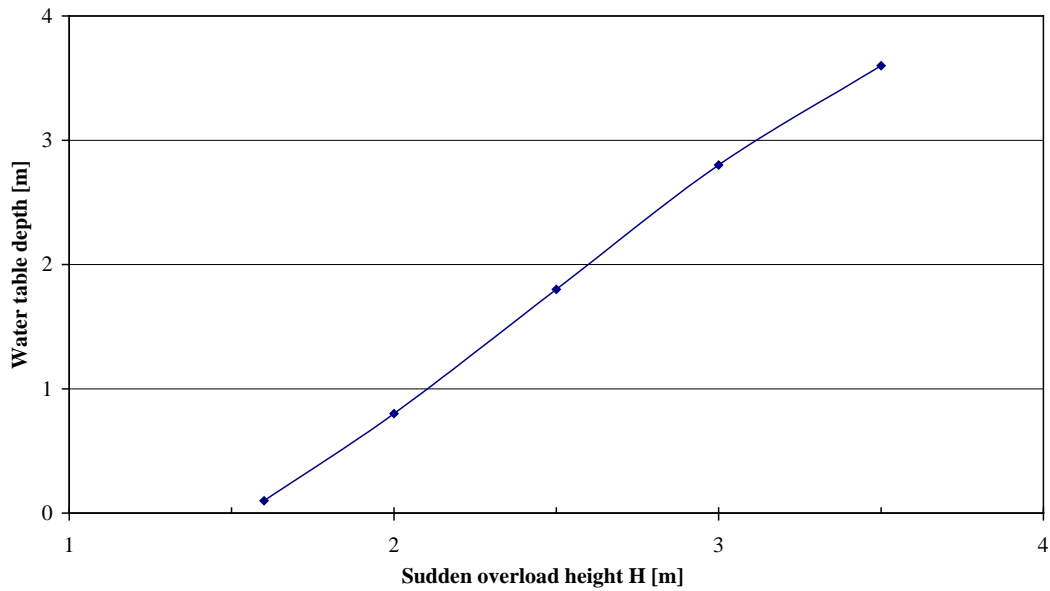


**Figure 36.** Water table depth as a function of a sudden overload for safety factor  $F_s=1$  of the earth-flow along a possible failure surface 5 m depth, for an infinite slope.

**Table 3.** Safety factor  $F_s$  variation for different thicknesses of sudden overload and water table depth for the Lamosano earth-flow along a possible failure surface 5 m depth for an infinite slope.

Water table depth (m)	$H = 0$	$H = 1.6$	$H = 2$	$H = 2.5$	$H = 3$	$H = 3,5$		
0.0	2.740	0.889	0.426				Failure surface depth	5 m
0.1	2.801	0.950	0.487				gamma	1.9 t/mc
0.2	2.862	1.011	0.548				beta	5.7 deg
0.4	2.983	1.133	0.670				Fire 1	30 deg
0.6	3.105	1.254	0.792	0.213				
0.8	3.227	1.376	0.913	0.335			For F = 1	
1.0	3.349	1.498	1.035	0.457			Sudden overload height	Water table depth
1.2	3.471	1.620	1.157	0.578			1.6	0.1
1.4	3.592	1.741	1.279	0.700	0.122		2	0.8
1.6	3.714	1.863	1.400	0.822	0.244		2.5	1.8
1.8	3.836	1.985	1.522	0.944	0.365		3	2.8
2.0	3.958	2.107	1.644	1.066	0.487		3.5	3.6
2.2	4.079	2.228	1.766	1.187	0.609			
2.4	4.201	2.350	1.888	1.309	0.731	0.152		
2.6	4.323	2.472	2.009	1.431	0.852	0.274		
2.8	4.445	2.594	2.131	1.553	0.974	0.396		
3.0	4.567	2.716	2.253	1.674	1.096	0.518		
3.2	4.688	2.837	2.375	1.796	1.218	0.639		
3.4	4.810	2.959	2.496	1.918	1.340	0.761		
3.6	4.932	3.081	2.618	2.040	1.461	0.883		
3.8	5.054	3.203	2.740	2.162	1.583	1.005		

Figs 33 and 36 and Table 3 show the stability conditions for the stabilised mudflow accumulation; they are relative to sudden material supply with thickness up to 3.5 m and initial water table depth of 0 to 4 m.

**Event scenarios**

The evolution patterns of the mudflow depend on various variable parameters, among which the volume of the collapsed soil mass, the volume flowing through the connection canal between the source area and the flow itself in time and, finally, its water content should be mentioned. Moreover, its movement is strictly depending on the characteristics of the new material flowing in from the upper unstable area without which the mudflow would soon come to a complete stop. The combination of these factors can therefore originate quite different events, especially with respect to the distance that the material can run and therefore to the mudflow point of depletion. As a consequence different risk situations are developed for the villages of Funes and Lamosano, respectively.

Mathematical simulation models have been developed in co-operation with the Universities of Calabria (Department of Mathematics) and Venice (Department of Environmental Sciences) by utilising a SCIDDICA programme based on the theory of parallel calculation of Cellular Automates. This programme, used for describing landslides taking place in debris materials with the local interaction of their constituent parts (Avolio et al., 1999), has allowed possible evolution scenarios of this landslide to be properly understood.

These simulations have considered various different scenarios, by changing the volume and point of depletion of the landslide and without taking into account the soil conservation structures already present. Of these, the three most significant simulations, in relation with possible risk conditions for the inhabitants of Funes and Lamosano, are here below described.

The first scenario contemplates a 0.5 million m<sup>3</sup> of material, with depletion of the mudflow in proximity of Funes; this condition has already occurred in the past. In this case, part of the village of Funes (the area around the church and the ex-restaurant) would be involved in the flow which would also spread over the underlying Funesia valley (Fig. 37).

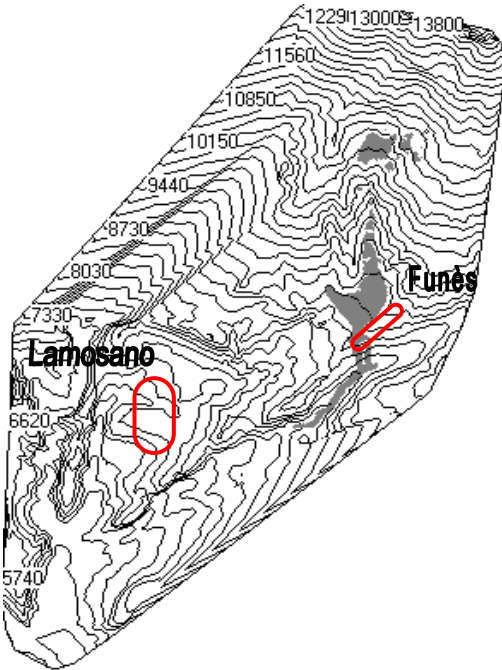


**Figure 37.** Simulation of a 500,000 m<sup>3</sup> event.

The second scenario infers that 1 million m<sup>3</sup> of material has been mobilised with depletion of the flow in proximity of Lamosano, therefore considering that the mudflow would show such kinematic conditions and volume/velocity ratio that its development would take place all over the valley. In this case the village of Funes would only be marginally affected by the flow passage, since the material would continue its downstream movement as far as the valley floor, whereas Lamosano would be overflowed in the part including the parish church and the town hall, mainly because of a decrease of the slope inclination and the sudden narrowing of the valley in proximity of this village (Fig. 38).

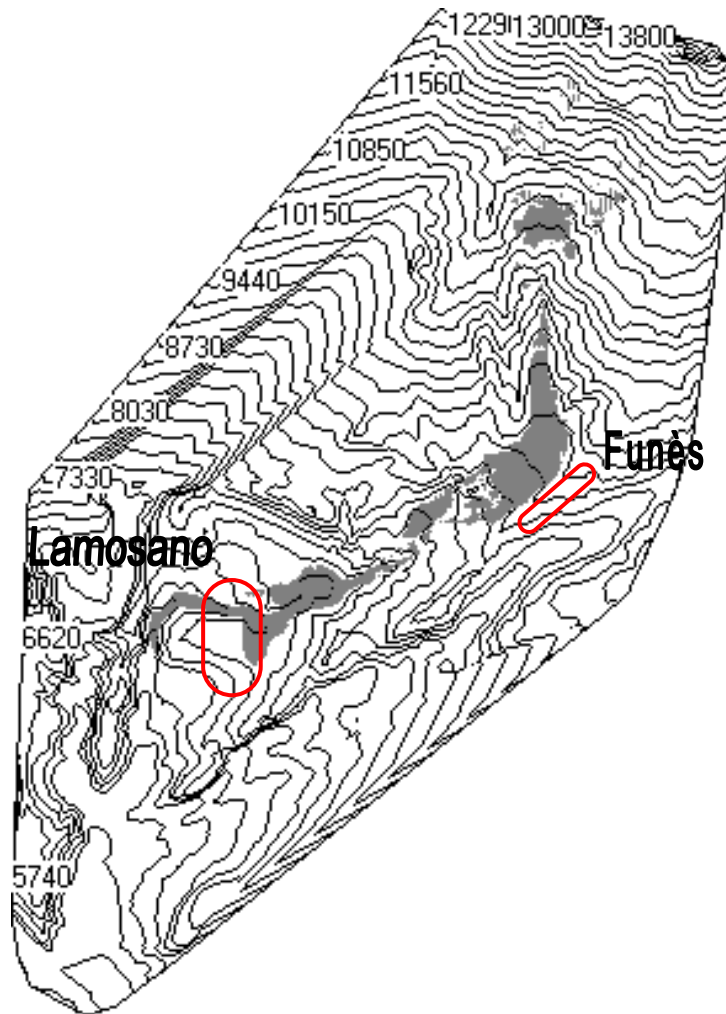


**Figure 38.** Simulation of a 1,000,000 m<sup>3</sup> event.

In the third scenario a collapse of about 5 million m<sup>3</sup> of material with depletion of the mudflow in proximity of Lamosano has been hypothesized. In this case the villages of Funes, Lamosano and Tarcogna would be affected (Fig. 39).

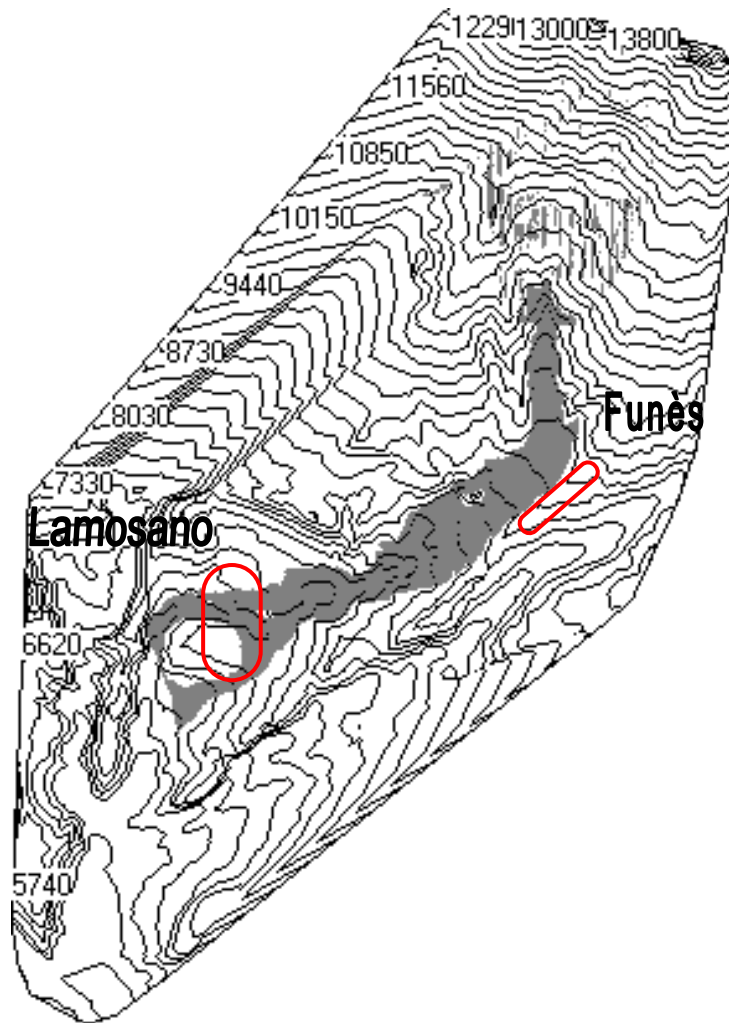


**Figure 39.** Simulation of a 5,000,000 m<sup>3</sup> event.

Notwithstanding the limits of these elaborations and the uncertainties of the morphological conditions which can change considerably at each mobilisation event and the possible evolution of the unstable area and mudflow, the scenarios proposed have emphasized that:

- the risk conditions for the two inhabited centres do not depend directly on the material volumes which could be mobilised; in fact, a succession of mudflows, even if modest in size, could result more serious for the village of Funes since these movements could cause a dangerous rising of the valley floor as far as the village boundary, whereas the most serious risk conditions for the village of Lamosano seem to be due to mudflows which, by taking place in longer time intervals, could eventually reach the inhabited area;
- the collapse of only 0.5 million m<sup>3</sup> of material could cause a partial overflowing affecting the village of Funes;
- the collapse of 1 million m<sup>3</sup> of material could already cause damage in parts of Lamosano and Tarcogna.

On the basis of the scenarios identified by means of mathematical modelling, it has been possible to identify the elements subject to the highest risk for the villages of Lamosano, Funes and Tarcogna. Figs40 and 41 show in colour red the elements subject to high risk, whereas colour blue corresponds to average risk and colour green to low or negligible risk.

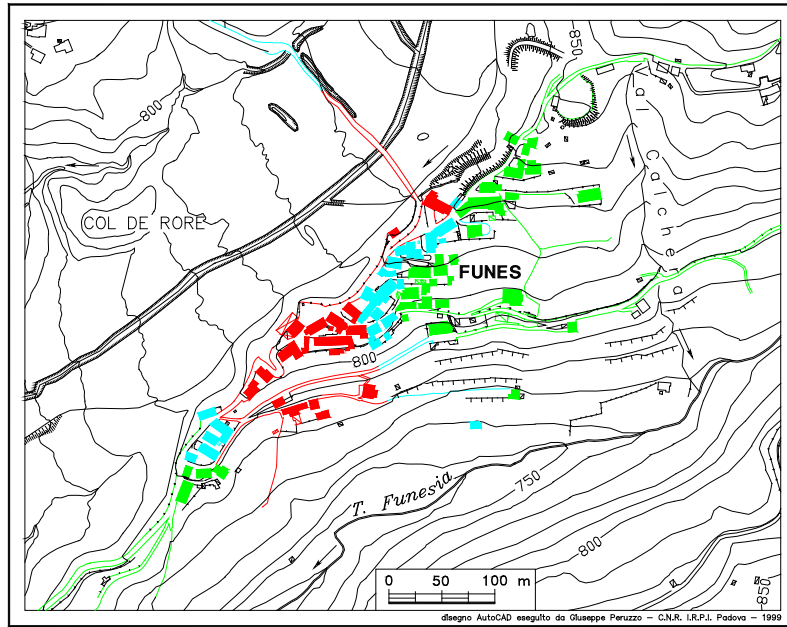


**Figure 40.** Zonation of Funes village in case of new landslide events: high risk in red; medium risk in blue; low risk in green.

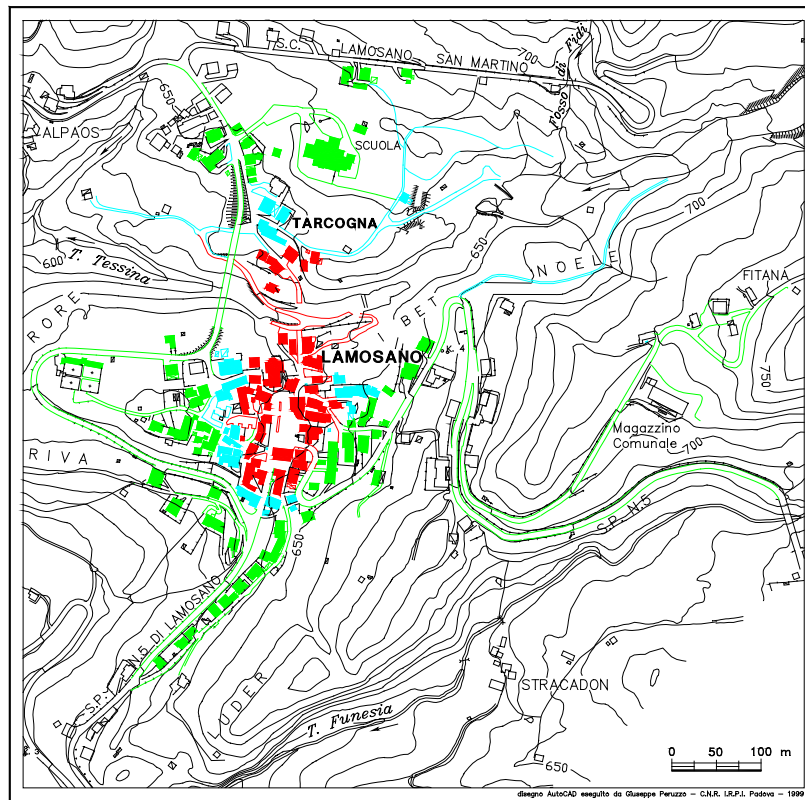


**Figure 41.** Zonation for Lamosano and Tarcogna villages in case of new landslide events: : high risk in red; medium risk in blue; low risk in green.

### **Remedial measures**

The studies carried out during the convention period have allowed the continuous activity of the Tessina landslide to be documented and its possible evolution to be forecast, both in terms of mobilised volumes of material and possible evolution scenarios.

The 1960 mass movement caused in a short time the filling of the valley floor with amounts of landslide debris up to 50 m thick, with a total displaced volume exceeding 5 million m<sup>3</sup>. The comparison between Figs 42 and 43 highlight the different situation between 1960 and today for the portion of valley on which the village of Funes lies.

The investigations carried out in the 1997-1999 period have pointed out a constant widening and a progressive retrogression of the unstable area, which now stretches as far as the foot of Mt. Teverone. At present the surface involved in the landslide is over 500,000 m<sup>2</sup>, to which an estimated volume of 5 million m<sup>3</sup> corresponds. Moreover, the tendency is toward a widening of the source area, with other areas at present stable which will be eventually affected, such as the area uphill of Pian de Cice. Also an increase of the displacement velocity is to be expected, as already confirmed by topographic measurements taken in the past two years.



**Figure 42.** The picture taken in 1960 shows the condition of the valley below Funes village just after the first Tessina landslide event (photo, G. Zanon).



**Figure 43.** Landslide situation on December 1999: a comparison with the previous picture shows the filling of the valley due to the earth-flow.

On the basis of what has been previously discussed, it is possible to hypothesize a series of structural and non-structural interventions suitable for the mitigation of risk in the inhabited centres, starting from the assumption that it will hardly be possible to stop completely the landslide process. The types of possible interventions may be either active, on the landslide body itself, or passive to safeguard public safety.

With respect to the present evolution stage of this mass movement, interventions based on slope reprofiling aiming to lower the inclination angle or to fill the cracks should be excluded. Also surface draining systems installed on the landslide body would be mostly ineffective, owing to the depth of the surface of rupture, the kind of hydraulic circuit (probably rather deep) feeding the springs and, finally, the difficulty to guarantee the effective functioning of works constructed on the landslide body.

As regards possible structural interventions, a new draining tunnel dug underneath the upper accumulation zone, inside the flysch materials, could attain satisfactory results in draining the unstable soil mass. Nevertheless, even a work of this kind, apart from its high costs, could not guarantee *a priori* any substantial effectiveness, considering the evolution state of this process. Therefore, the only intervention that could be reasonably planned is the programmed removal of the mudflow material as it advances on top of the stabilised landslide body.

This remedial measure would achieve the aim to:

- create a defined volume for constraining new landslide events and, at the same time, reduce in time risk situations for the villages of Funes and Lamosano;
- allow the valley environmental reclamation by following a precise territorial planning imposed by the need to guarantee the global stability of the area of intervention, according to the exigencies of local administration boards.

Since the removed material has particular chemical and physical characteristics, it could be utilised as raw material for the production of cement (in its natural state) and high-quality bricks (by using its finest component). The material's removal, which should be planned and carried out in a relatively short time in order to maintain safety conditions especially for the village of Funes, will have to proceed from the slope upper part towards its bottom, starting from the accumulation zone located between the deposit and the Funes-San Martino road. In this way an

earth collecting basin capable of confining the arrival of fresh material will be created; otherwise further landslide movements might directly affect Funes.

Moreover, the intervention procedures will have to be carefully planned in order to avoid local instability conditions due to the materials' low hydraulic conductivity and poor shear strength. An effective drainage system for the collection of surface water will have to be planned and installed by keeping water courses as far as possible from the excavation areas and by constructing the draining canals at an adequate depth in order to guarantee both the drainage of the soil mass and the stability of the canal banks.

As regards passive countermeasures, the only possible intervention seems to be monitoring, finalised to both movements' control and alert for the inhabitants. This remedial measure should in any case be activated and maintained apart from the implementation of any other type of intervention, either active or passive. First of all, it would be particularly useful to monitor surface displacements on all the upper unstable area and deep displacements in the Pian de Cice area, which seems to play a crucial role for the stability of the entire area.

As for the alert system, by considering the dynamics of the landslide resulting from the investigations carried out since 1992, it might not be indispensable; nevertheless it would exert a psychologically positive function for the inhabitants of the areas at risk as well as being a useful instrument for their safeguard.

Finally, owing to the difficulties inherent to the definite stabilisation of the area and the possible evolution scenarios of the landslide process, also the possible abandonment of part of the inhabited centres of Funes, Tarcogna and Lamosano and their reconstruction in safer areas should be seriously considered.

## References

- Avolio, A.V., Di Gregorio, S., Mantovani, F., Pasuto, A., Rongo, R., Silvano, S., Spataro, W., 1999. *Hexagonal cellular automaton simulation of the 1992 Tessina landslide*. In: S.J. Lippard, A. Naes, R. Sinding-Larsen (eds.), Proc. IAMG '99, Trondheim, Norway, 6-11 August 1999, pp. 291-296.
- Fell, R., 1994. *Landslide risk assessment and acceptable risk*. Can. Geotech. J., 31, pp.261-272.
- Hutchinson, J.N., Bhandari, R.H., 1971. *Undrained loading, a fundamental mechanism of mudflows and other mass movements*. Géotechnique, 21, London, pp. 353-358.
- ITASCA, 1993. UDEC: *Universal Distinct Element Code*. Version 2.0 ITASCA, Consulting Group Inc., Minneapolis.
- O'Connor, K.M., Dowding, C.H., 1999. *GeoMeasurements by Pulsing TDR Cables and Probes*. CRC Press, Boca Raton, 402 pp.
- Skempton A.W., De Lory, F.A., 1957. *Stability of natural slopes in London Clay*. Proc. 4th ICSMFE, London, 2, pp. 378-381.
- Varnes, D.J., 1984. *Landslide hazard zonation: a review of principles and practice*. Unesco, Paris, 48 pp.
- Whitman, R.V., 1984. *Evaluating calculated risk in geotechnical engineering*. ASCE Journal of Geotechnical Engineering, 110, 2, pp. 145-188.

## 7. The long-term evolution of the Tessina landslide

### Introduction

This report deals with a qualitative analysis of the evolution of the Tessina landslide from 1954 to the present, using multi temporal maps. These multi temporal maps were produced through the interpretation of multi-temporal aerial photographs and direct field-mapping of the 1998 and 1999 landslide situation using topographic maps. The interpretation results were converted to large scale multi-temporal topographical maps, and were digitized. This resulted in detailed geomorphological maps of the Tessina landslide for the following periods: 1954, 1961, 1969, 1980, 1991, 1998 and 1999.

Each of these unique ID polygon maps had its own attribute table, with data related to the landslide type and activity. Each polygon of the map linked to the attribute table by identifier domain but the columns in the table has there owned class domain. From these attribute tables it is possible to retrieve different maps according to the column of the table. Since the column activity in the table explains the reactivation or recent development of the Tessina landslide and each map has the same size, the comparison of the attribute maps, displaying the activity, allow us to show how the Tessina landslide changed in the period between 1954 and 1999. The class "very active" in the attribute maps indicates where new reactivation has occurred since the last period.

For a better understanding of the landslide advancement the maps are displayed together in one map, in which for each period the new active landslide area is shown in a different colour.

### Location



Figure 1. Location map of Tessina landslide

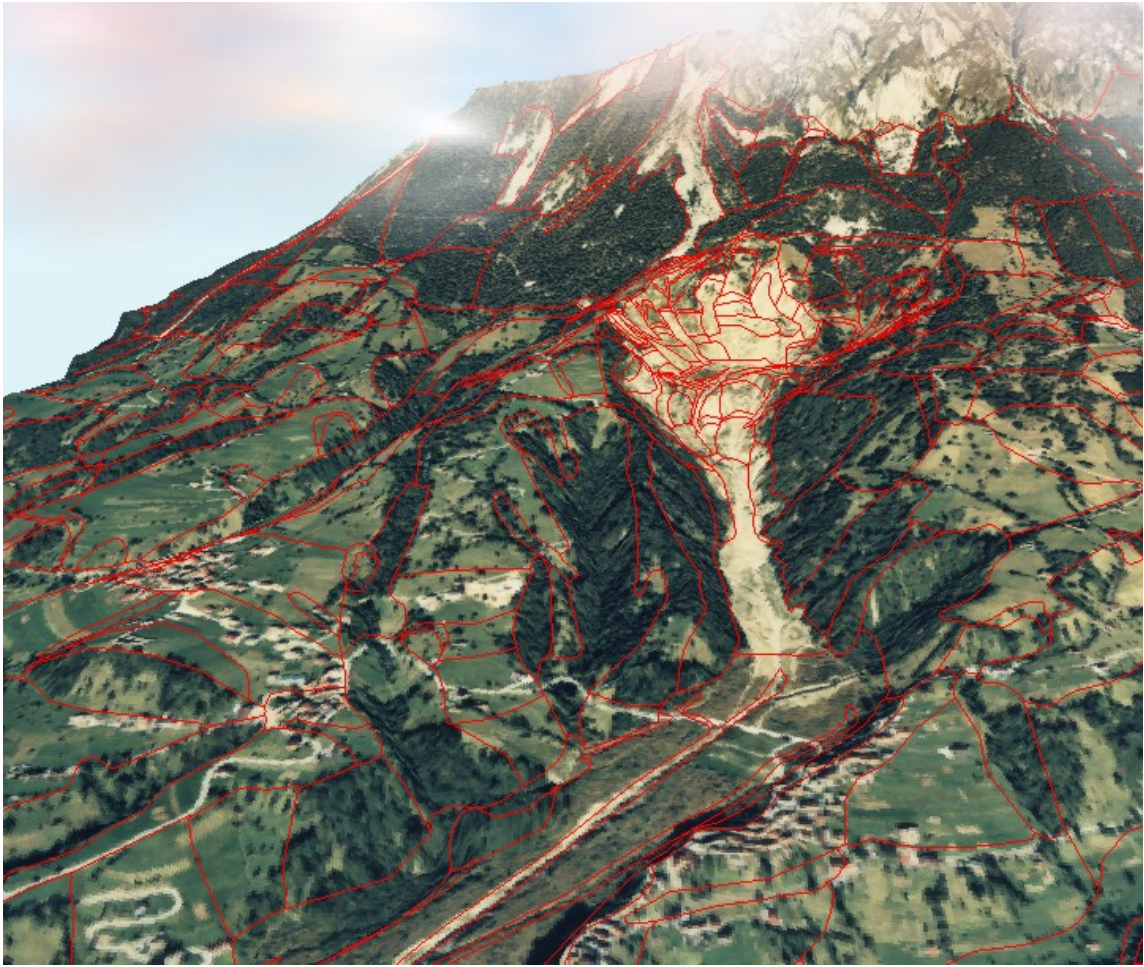


**Figure 2.** Three dimensional view of the Tessina landslide, generated using an orthophoto and a Digital Elevation Model. The red lines indicate the geomorphological units of the area.



**Figure 3.** Top part of the Tessina landslide

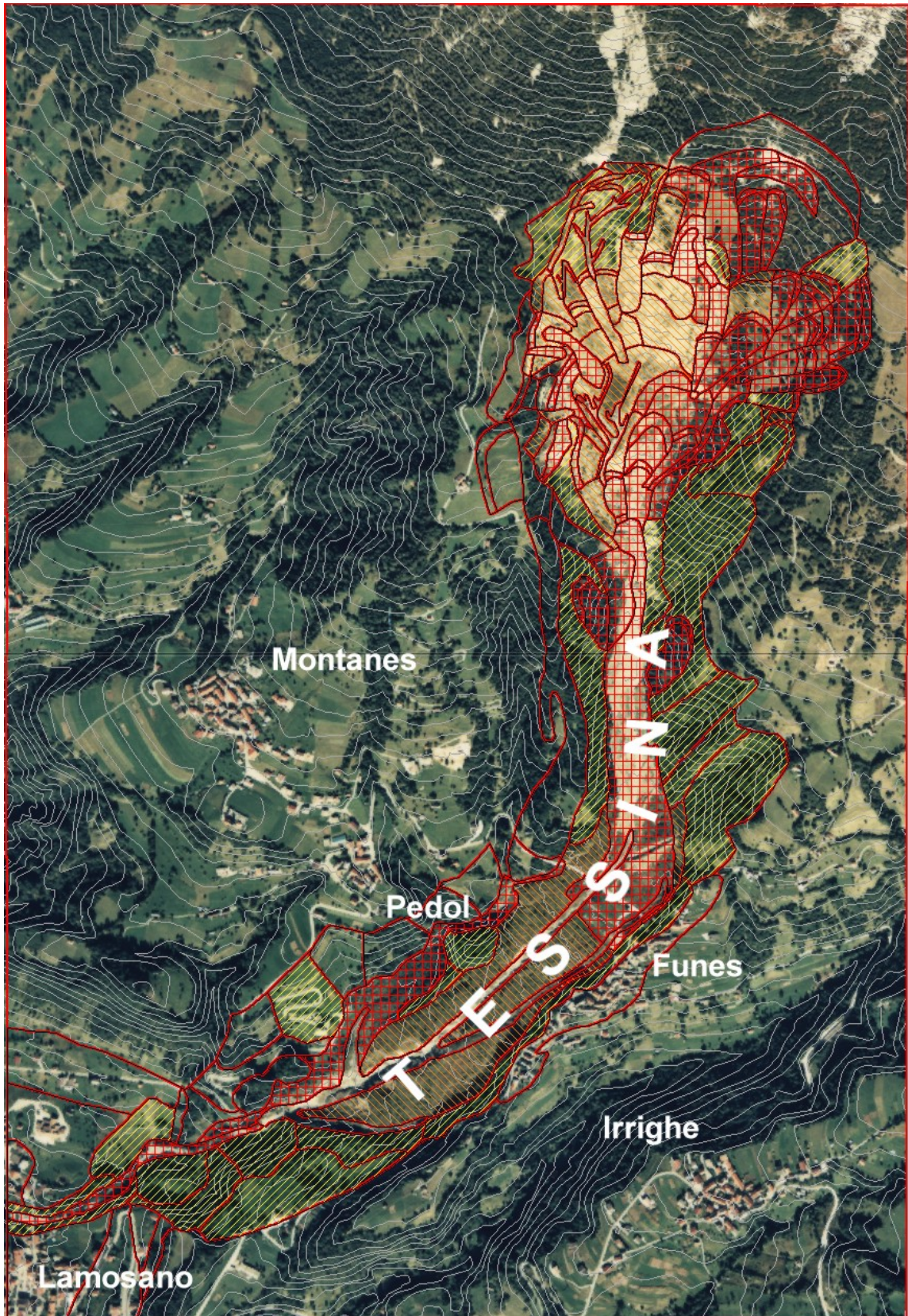


**Figure 4.** Orthophoto of the Tessina landslide area

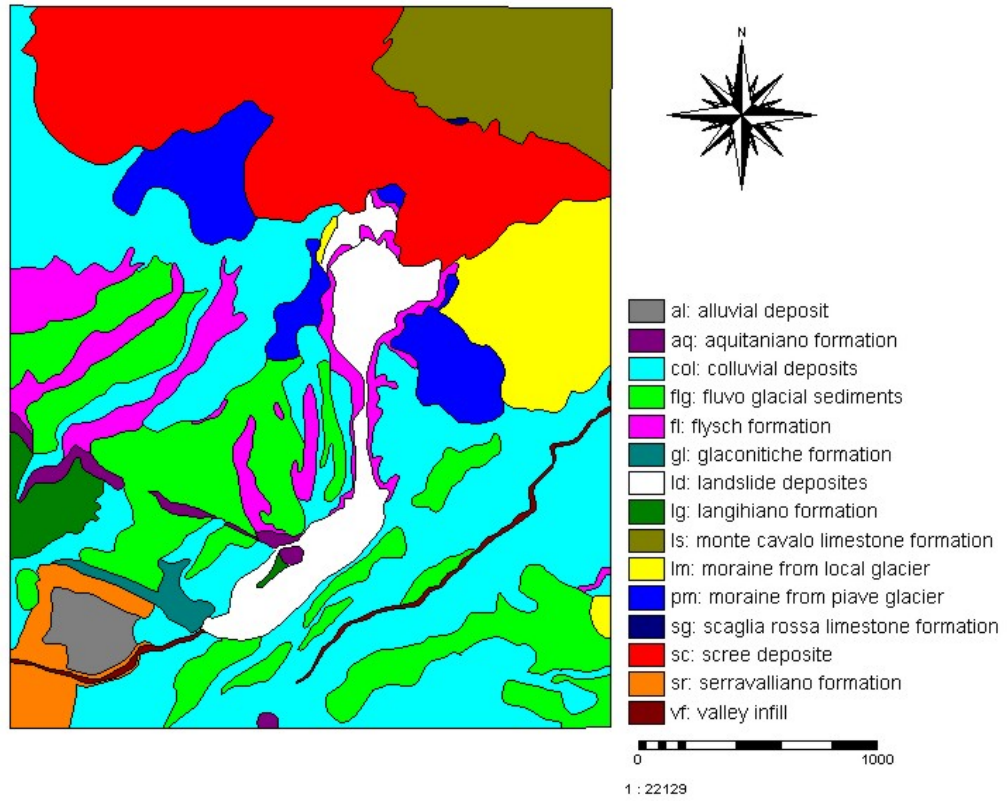


**Figure 5.** Geological map of the Tessina landslide

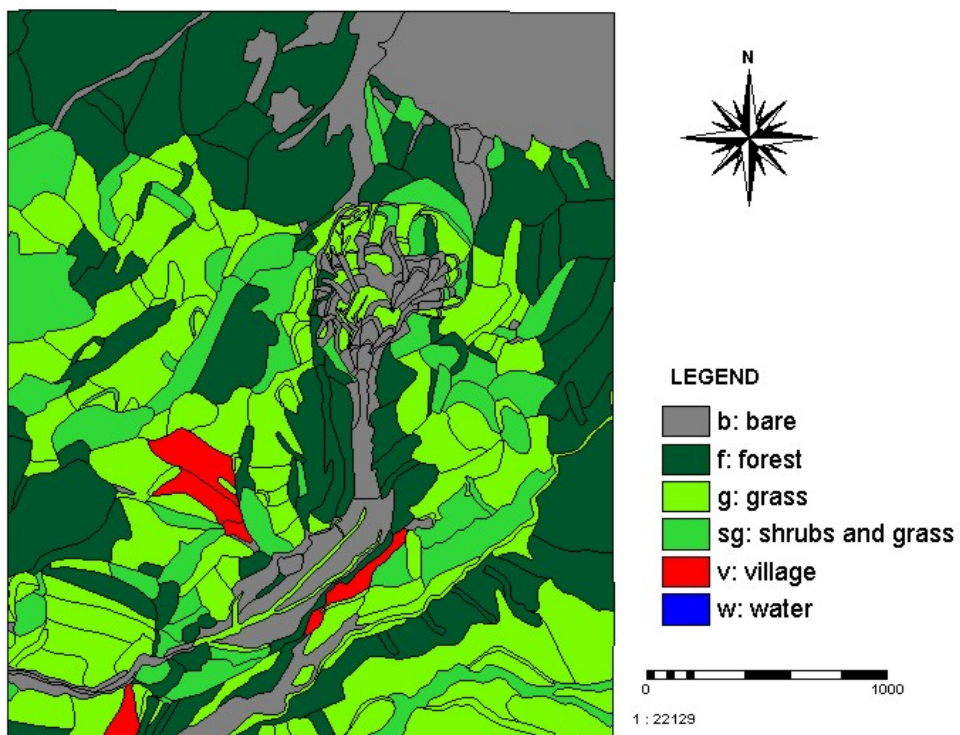


**Figure 6.** Land use map of the Tessina landslide



- |   |   |  |
|---|---|--|
| <ul style="list-style-type: none"> <li>1: Landslide</li> <li>11: Landslide excluding tessina landslide</li> <li>111: rotational</li> <li>1111: Rotational scarp</li> <li>11111: Rotational right lateral scarp</li> <li>11112: Rotational left lateral scarp</li> <li>11113: Rotational head scarp</li> <li>1112: Rotational body</li> <li>11121: Rotational body flow</li> <li>11122: Rotational body moved block</li> <li>11123: Rotational body slide material</li> <li>11124: Rotational intermediate scarp on the body of the landslide</li> <li>112: Complex</li> <li>1121: Complex_scarp</li> <li>11211: Complex right lateral scarp</li> <li>11212: Complex left lateral scarp</li> <li>11213: Complex head scarp</li> <li>1122: Complex body</li> <li>11221: Complex body flow</li> <li>11222: Complex body moved block</li> <li>11223: Complex body Slide material</li> <li>11224: Complex body intermediate scarp on the body of landslide</li> <li>113: debris slide</li> <li>1131: debris slide scarp</li> <li>1132: debris slide body</li> <li>12: Tessina land slide</li> <li>121: Pre 1960</li> <li>1211: Pre 1960 rotational scarp</li> <li>12111: Pre 1960 rotational head scarp</li> <li>12112: Pre 1960 rotational right lateral scarp</li> <li>12113: Pre 1960 rotational left lateral scarp</li> <li>1212: Pre 1960 rotational body</li> <li>12121: Pre 1960 rotational landslide material</li> <li>12122: Pre 1960 rotational moved block</li> <li>12123: Pre 1960 rotational flow</li> <li>12124: Pre 1960 rotational intermediate scarp on the body of the landslide</li> <li>122: post 1960</li> <li>12211: post 1960 landslide body with limited displacement</li> <li>1221: post 1960 upper main scarp</li> <li>122111: post 1960 landslide body with limited displacement with cracks</li> <li>122112: post 1960 landslide body with limited displacement without cracks</li> <li>12212: post 1960 initiating landslide</li> <li>122121: post 1960 initiating landslide with cracks</li> <li>122122: post 1960 initiating landslide without cracks</li> <li>1222: Post 1960 main scarp</li> <li>12221: post 1960 main head scarp</li> <li>12222: Post 1960 minor head scarp</li> <li>1223: Post 1960 right lateral main scarp</li> </ul> | <ul style="list-style-type: none"> <li>12231: Post 1960 right lateral minor scarp</li> <li>12232: Post 1960 left lateral scarp</li> <li>1224: Post 1960 right lateral scarp</li> <li>12241: Post 1960 left lateral main scarp</li> <li>12242: Post 1960 left lateral minor scarp</li> <li>1225: Post 1960 body of landslides</li> <li>12251: Post 1960 body of landslides flow</li> <li>122511: Post 1960 body of landslides single flow with cracks</li> <li>122512: Post 1960 body of landslides single flow without cracks</li> <li>122513: Post 1960 body of landslides combined flow with cracks</li> <li>122514: Post 1960 body of landslides combined flow without cracks</li> <li>12252: Post 1960 body of landslides slide turning into flow</li> <li>12253: Post 1960 body of landslides slide material</li> <li>12254: Post 1960 body of landslides debris flow accumulation</li> <li>122541: Post 1960 body of landslide debris flow accumulation levelled</li> <li>122542: Post 1960 body of landslides debris flow accumulation moderately steep slope</li> <li>122543: Post 1960 body of landslides debris flow accumulation gentle slope</li> <li>12255: Post 1960 body of landslides main flow</li> <li>122551: Post 1960 body of landslides main flow narrow</li> <li>122552: Post 1960 body of landslides main flow wide</li> <li>1226: pond</li> <li>2: Denudational landform</li> <li>21: Denudational valley</li> <li>211: Denudational valley Wide</li> <li>2111: Denudational valley Wide with landslide and gully</li> <li>21111: Denudational valley Wide with landslide and gully deep</li> <li>21112: Denudational valley Wide with landslide and gully shallow</li> <li>2112: Denudational valley Wide without landslide and gully</li> <li>21121: Denudational valley Wide without landslide and gully deep</li> <li>21122: Denudational valley Wide without landslide and gully shallow</li> <li>212: Denudational valley Narrow</li> <li>2121: Denudational valley Narrow with landslide and gully</li> <li>21211: Denudational valley Narrow with landslide and gully deep</li> <li>21212: Denudational valley Narrow with landslide and gully shallow</li> <li>2122: Denudational valley Narrow without landslide and gully</li> <li>21221: Denudational valley Narrow without landslide and gully deep</li> <li>21222: Denudational valley Narrow without landslide and gully shallow</li> <li>213: Denudational valley side with landslide and gully</li> <li>2131: Denudational valley side with landslide and gully gentle slope</li> <li>2132: Denudational valley side with landslide and gully moderately steep slope</li> <li>2133: Denudational valley side with landslide and gully steep slope</li> <li>214: Denudational valley side without landslide and gulleys</li> <li>2141: Denudational valley side without landslide and gulleys gentle slope</li> <li>2142: Denudational valley side without landslide and gulleys moderately steep</li> <li>2143: Denudational valley side without landslide and gulleys steep slope</li> <li>215: valley bottom</li> <li>22: Denudational hill</li> <li>221: Denudational hill gentle slope</li> </ul> | <ul style="list-style-type: none"> <li>222: Denudational hill moderately steep slope</li> <li>223: Denudational hill steep slope</li> <li>224: Denudational hill top</li> <li>23: Denudational slope</li> <li>231: Denudational colluvial slope</li> <li>232: Denudational scree slope</li> <li>2321: active denudational scree slope</li> <li>2322: Denudational scree slope affected by land slide</li> <li>2323: Denudational scree slope not affected by land slide</li> <li>233: Denudational scree fan</li> <li>234: Denudational rock fall</li> <li>24: Denudational Remnant ridge(hill)</li> <li>241: Denudational Remnant ridge(hill) top</li> <li>242: Denudational Remnant ridge(hill)gentle side slope</li> <li>243: Denudational Remnant ridge(hill)moderately steep slope</li> <li>3: Structural valley controlled landform</li> <li>31: Structural valley controlled landform dip slope</li> <li>32: Structural valley controlled landform face slope</li> <li>33: Structural valley controlled landform near vertical dip slope in limestone</li> <li>4: landform due to lithological difference</li> <li>41: landform due to lithological difference plain</li> <li>42: landform due to lithological difference steep slope</li> <li>43: landform due to lithological difference hill top</li> <li>44: landform due to lithological difference gentle slope</li> <li>6: landforms remodified by glacial process</li> <li>51: glacially eroded level</li> <li>52: glacially eroded slope</li> <li>53: fluvoglacial terraces</li> <li>54: shallow fluvoglacial valley</li> <li>55: moranic ridge</li> <li>551: moranic ridge gentle side slope</li> <li>552: moranic ridge moderately steep side slope</li> <li>56: ice marginal related to the maximum extent of local glacier</li> <li>561: ice marginal related to the maximum extent of local glacier level</li> <li>562: ice marginal related to the maximum extent of local glacier erosion</li> <li>57: ice marginal related to the maximum extent of plave glacial</li> <li>571: ice marginal related to the maximum extent of plave glacial level</li> <li>572: ice marginal related to the maximum extent of plave glacial level</li> <li>58: glacially eroded valley side</li> <li>581: glacially eroded valley side gentle</li> <li>582: glacially eroded valley side moderately steep</li> <li>6: Anthropogenic landform</li> <li>61: ditch</li> <li>62: quarry</li> <li>63: pits</li> <li>64: plain due to road construction</li> </ul> |
|---|---|--|

Figure 7. Geomorphological map of the Tessina landslide area

## **Multi-temporal geomorphological analysis**

This section uses multi-temporal landslide maps to investigate in detail how the morphology of the Tessina landslide has been changing in space and time. The time aspect refers to year of reactivation and the spatial aspect refers to the area that has been reactivated.

### **1954: Old landslide**

Although the actual Tessina landslide started in the sixties, we still refer to the previous situation as the "old landslide". This is because the Tessina landslide is in fact a reactivation of an old landslide complex, that is clearly recognizable in the old photos. The pre-1954 Tessina landslide covered almost the same area as the present landslides. Since there are no aerial photographs prior to 1954 the qualitative analysis of the landslide starts with the situation in 1954.

After the pre 1954 landslides there have been a series of landslides that occurred in the last 4 decades. From the multi-temporal aerial photograph interpretation one can observe that the present landslide morphology is following the morphology of the pre 1954 landslides. So the present landslide is simply the reactivation of the previous landslides.

As can be observed from the 1954 photographs the reactivation started in the center of the present landslide body. This place previously was a shallow narrow valley. The small landslides visible on the 1954 photos were interpreted as being of the "complex" type. The slide started as rotational on the scarp and further downslope changed into a flow. The flow went a relatively short distance inside the valley (Fig 8).

The landslides occurred on the debris accumulation of the previous landslide events. Apart from the few small active new landslide (indicated in red in Figure 8), a large number of old landslide masses can be observed in the 1954 airphotos. The age of these landslides could not be established, since the 1954 photos were the oldest ones available. What can be observed is a number of rotational slide masses, reaching upslope till the vertical limestone cliffs. The scree slope underneath the cliff shows a slight inclination in the direction towards the cliffs, opposite to what would be expected from a normal scree slope. On the Eastern part of the landslide a clear scarp can be observed reaching from the scree slope to to upper right sector of the present landslide. From these evidences it was concluded that the old Tessina landslide had reached all the way up till the limestone cliffs, still considerably larger than the current 1999 extension. The western part of the old landslide is now buried underneath a large scree fan, which does not show clear evidences of displacements. From this it can be concluded that the pre-1954 Tessina landslide is probably quite old, from early Holocene times, before the main production of scree deposits covered it.

### **1961: First reactivation**

On the airphotos from the year 1961 some important reactivations of the old Tessina landslide can be observed. The reactivations started in the lower part of landslide and advanced more towards the present left lateral scarps. The slide type is complex which started as rotational on the scarps and as flow on the body. Both the head and side scarps almost exactly fit with the 1954 landslide events, which are interpreted, as multiple rotational landslides. The landslides were triggered on 30<sup>th</sup> October 1960 after a period of particularly heavy rainfall in which 398.7mm of rain in 30 days were recorded. From this landslide an enormous amount of material was taken away from the scarp.

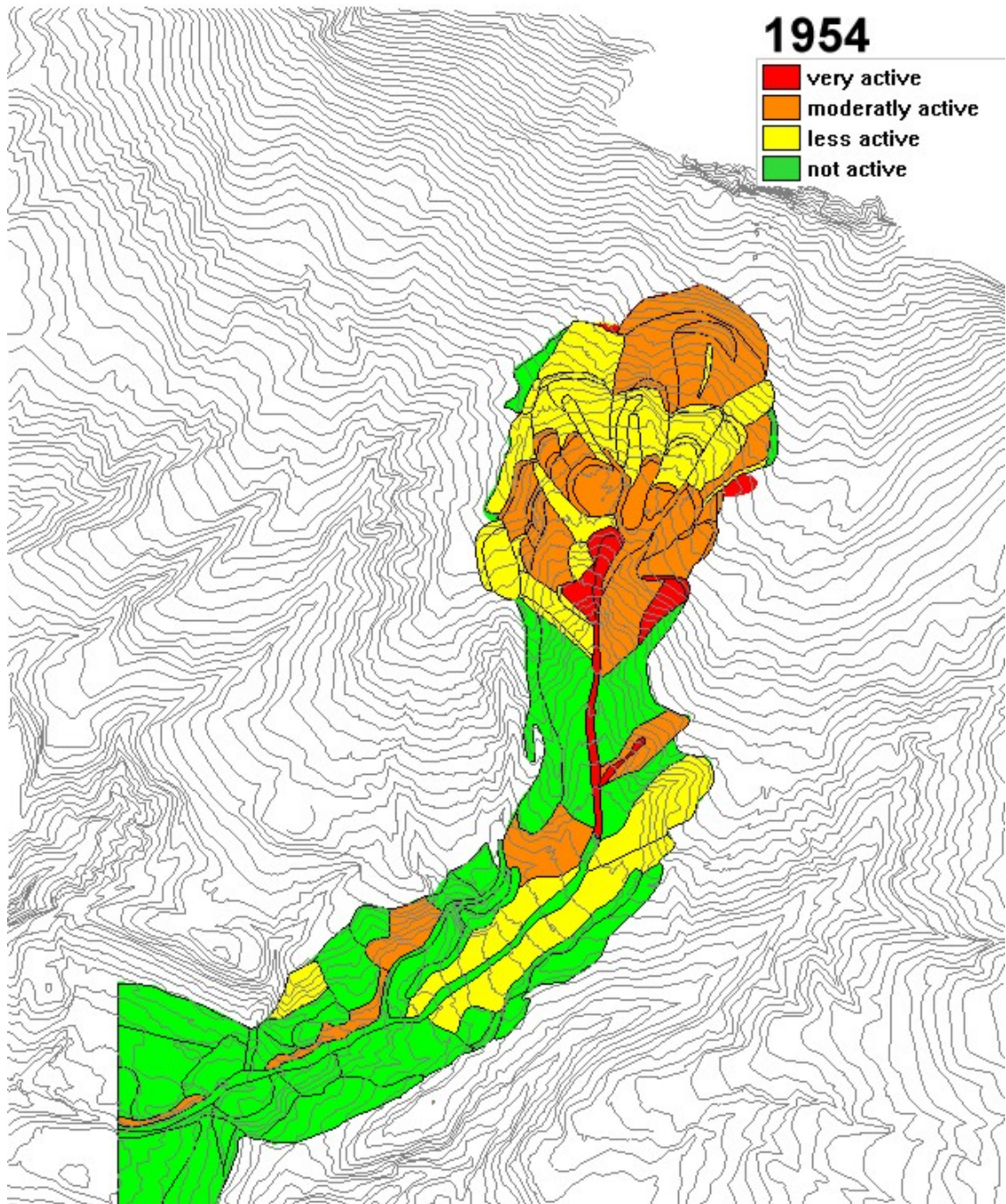


**Figure 8.** The 1954 Tessina landslide activity map

Therefore these rainwater saturated loose materials turned into a large mudflow that extended down to the valley along the village Funes (Figure 9). The mudflow filled-up the pre-existing fluvial valley to a considerable height.

During this reactivation the morphology of the left lateral scarp considerably changed. The narrow valley in the center of the landslide widened, a block of landslide materials was removed and the scarp moved upslope. The valley bottom widened because of the accumulation of landslide materials.

The reactivated Tessina landslide had a different movement mechanism than the old one. The old landslide moved as a number of clearly recognizable slump blocks, without transforming into flows as is the case with the recent reactivations. This is probably due to the fact the landslide occurred in less weathered Flysch deposits, overlain by scree and

moraine. As a result of the mechanical disintegration caused by the old landslide, the weathering of the Flysch materials was high, also because it is located in an area with a lot of water-supply, coming through the karstified limestone masses upslope. As a consequence, the reactivation of the landslide took place in very weathered Flysch materials, and the movement is basically of the flow type.

This reactivation advanced half way on both left and right lateral scarps and on the valley sides of Tessina landslide. The materials involved in these landslides are mainly the Flysch formation. In addition the pre 1954 minor head scarp on the scree slope also reactivated but there is not considerable geomorphological change.

The left lateral active scarp follows exactly the road, which was damaged during this landslide. This implies that besides other triggering factors, the construction of the roads played an active role for the reactivation of the landslide.

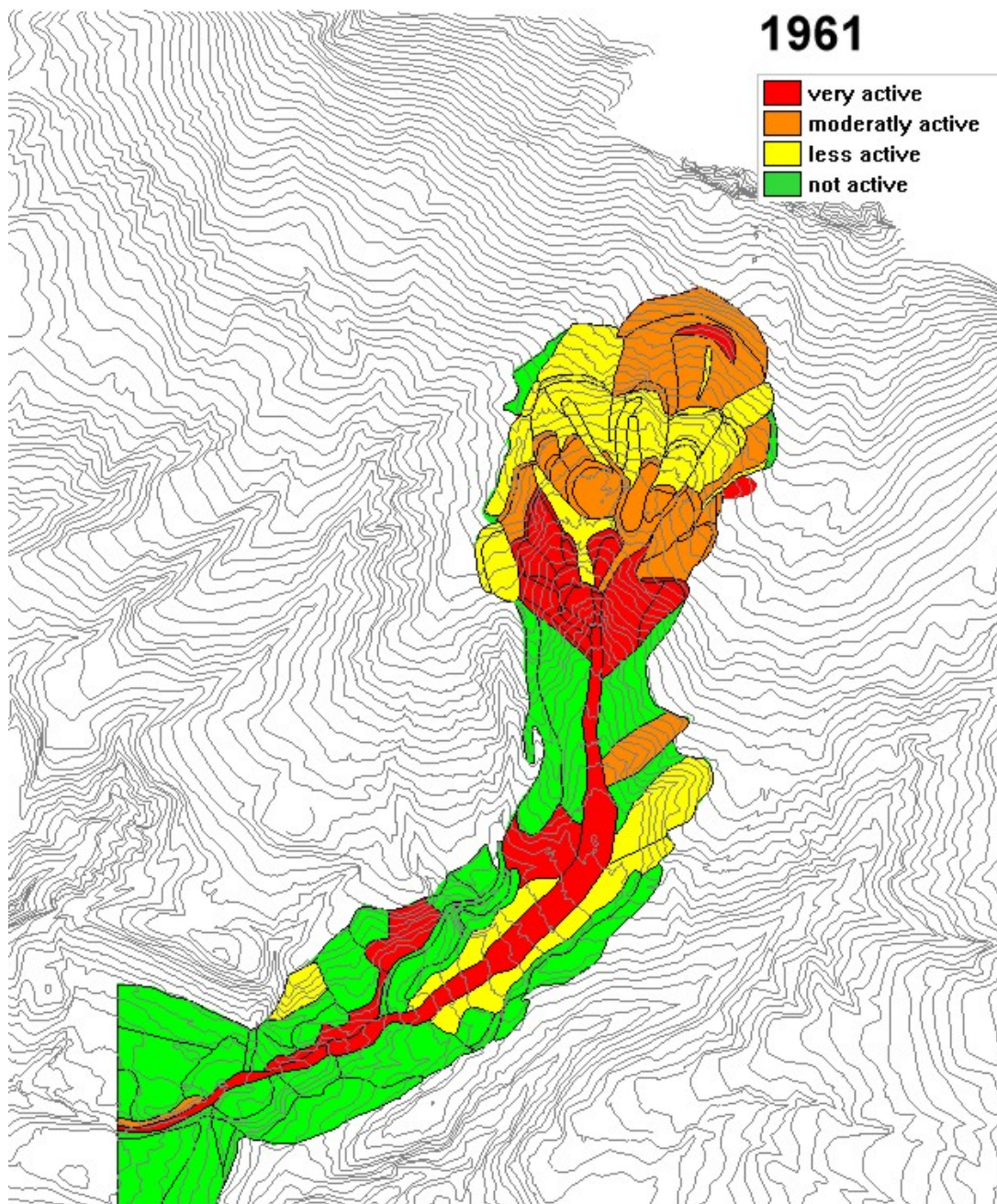


**Figure 9.** The 1961 Tessina landslide activity map

### **1969: Full development of the landslide**

In the airphotos from 1969 a large new area of reactivated can be observed, which is almost double in size as compared to the situation in 1961. The reactivation was especially important in the right lateral scarp, on the left lateral scarp and on the main head scarp. In the lower reaches the Tessina landslide had reactivated to the extension of the old landslide complex (Figure 10).

The head-, right lateral and left lateral scarps are generally characterized by multiple rotational, complex, single as well as multiple landslide types. However the rotational landslides changed into flow. This is due to the following reasons:

- the high degree of weathering of the Flysch materials;
- the high content of marly clays in the Flysch.;
- the availability of loose moraine and scree deposits;
- the reworked debris accumulation was saturated with rainwater and groundwater, especially in the centre of the landslide body, where the slides can be characterized as "flowslides".

In fact in each scarp flow-types and slide-types of landslides existed simultaneously. In addition to that the flows observed at the base of each landslide combined into a large flow. Again these combined flows merged into the main flow which flows in the valley along Funes. They now flowed along both sides of a higher part in the valley, leaving this area standing as an island within the mudflow masses. The height of the mudflow was also sufficiently high to endanger the village of Funes, located on the waterdivide, on the left flank of the valley.

In this landslide not only the main landslide areas reactivated but also the right side of the valley near to the village of Funes. Unlike the 1961 landslide event the local moraine, the Piave moraine, the scree deposits, the flysch and the debris materials were involved in the landslide.

After this landslide event the morphology of the valley along Funes dramatically changed. The road, which connects the village of Pedol to Funes, was totally destroyed by the flow. This large volume of flow extended towards the town of Lamosano. The flow was larger in size along the town of Funes and narrowed near the town of Lamosano towards the mouth of the Tessina valley. This is caused by the differences in width of the pre-existing fluvial valley, which is wider in the region of Funes, and narrow near Lamosano. Which, in turn, is due to the variation of resistance of the materials along the valley sides, with less resistant material along the town of Funes and more resistant rocks towards the SW.

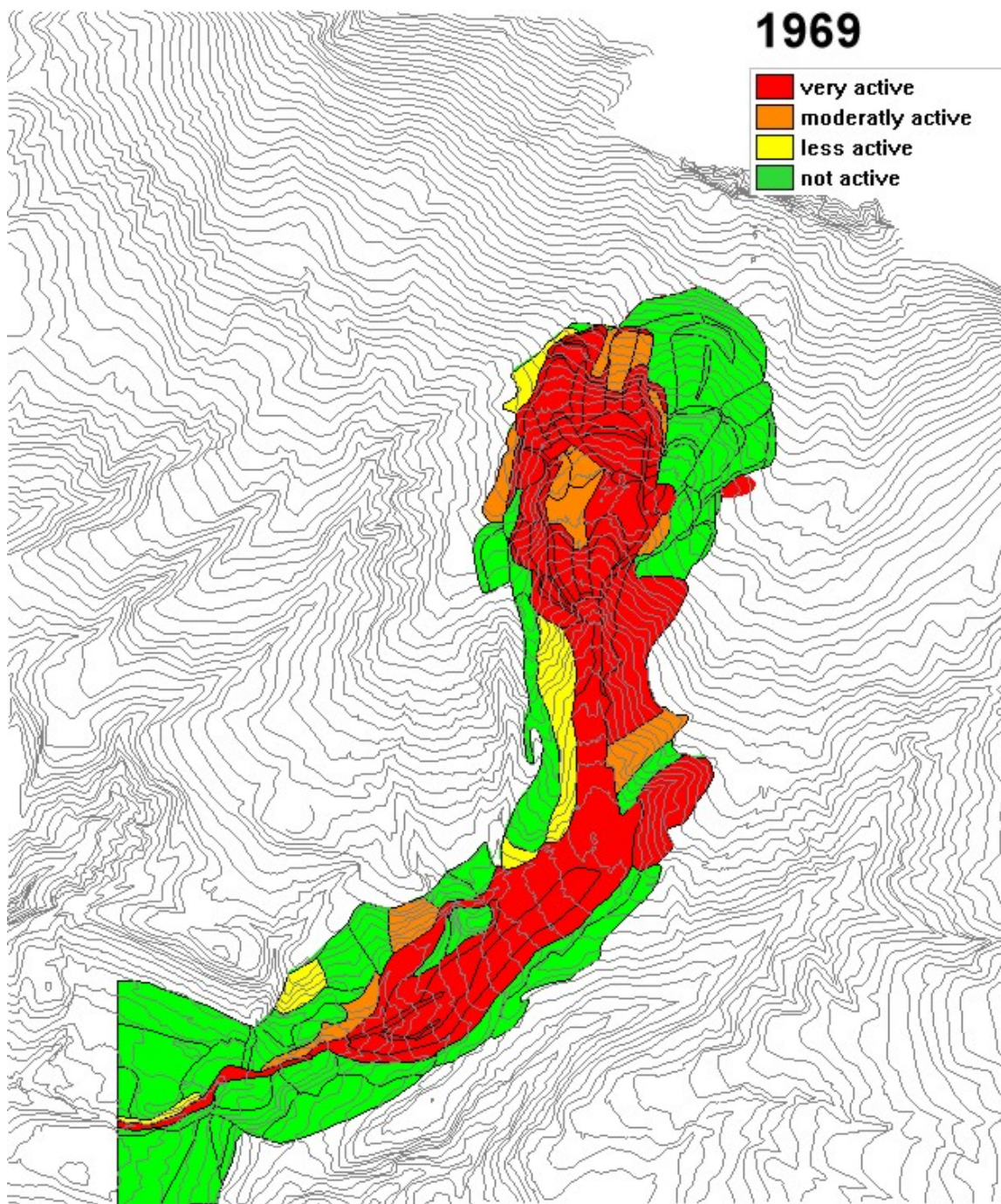


**Figure 10.** The 1969 Tessina landslide activity map

### **1980: New phases of activity**

The next set of airphotos available was from 1980. From these photos no major morphological change as compared with the 1969 situation could be observed, except for some minor changes in activity (Fig 11). In 1980 all the 1969 landslides were still active, as evidenced by the lack of vegetation. The right lateral, left lateral and head scarps of Tessina landslide had been reactivated slightly. But not large volume of materials was taken away.

The landslide bodies in the depletion zone were reactivated as flows. In the center of the landslide a large volume of material, coming from the slide masses above was present in a temporary storage area, bounded downslope by a secondary scarp from which the various flows merged into the main mudflow in the valley downstream. The slide mechanism is almost the same as the previous years. However during this reactivation most of the removed material was not derived from the upper scarp areas, but from the temporary landslide masses in the center of the landslide. A considerable amount of material from the debris accumulation in the upper accumulation zone was taken away as flow slide.

As can be observed from the 1980 airphotos, prior to 1980 a number of artificial drainage channels were constructed on the main flowmass. The objective of these was to drain off surficial runoff in an attempt to dry out the flow. The main flow extends down to the reconstructed road, which connects Funes and Pedol, and cause relatively small damage to it. The old flow between this road and Lamozano doesn't show signs of activity.

### **1991: More stabilized**

The next set of airphotos available were from 1991. From the interpretation of these photos only a slight reactivation of the previous landslides can be observed, and the rest of the area was hardly changed (Fig 12). The landslide accumulation was reactivated as flowslide and the new flow stops before the road, which connects Funes and Pedol.

Both the depletion zone and accumulation zone are relatively more vegetated than in the previous set of photos from 1980. The valley sides of the Tessina landslide are also more vegetated by grasses and shrubs. However the grass cover does not mean that it gives strength to the instability for there might be circular cracks in the grasses which will give rise to potential collapse of materials in the depletion zone.

### **1998: During the fieldwork**

Even though there were no new aerial photographs available after 1991, it was known that the landslide had an important reactivation in 1992. Therefore the features related to this 1992 reactivation were mapped using direct mapping, conducted in a fieldwork in 1998, using a 1:5000 scale contour map (Fig 13). A very large reactivation of the landslide was observed on the right lateral flank of the landslide. Here the landslide advanced towards the pre 1954 right lateral scarp and minor headscarp. There was no major change observed on the left lateral scarp. The small building that was still on top of the scarp, as interpreted from the 1991 airphotos, was now partly destroyed.

The 1998 Geomorphological map of the Tessina landslide shows how the landforms changed in the period from 1991 till the fieldwork was conducted in 1998.

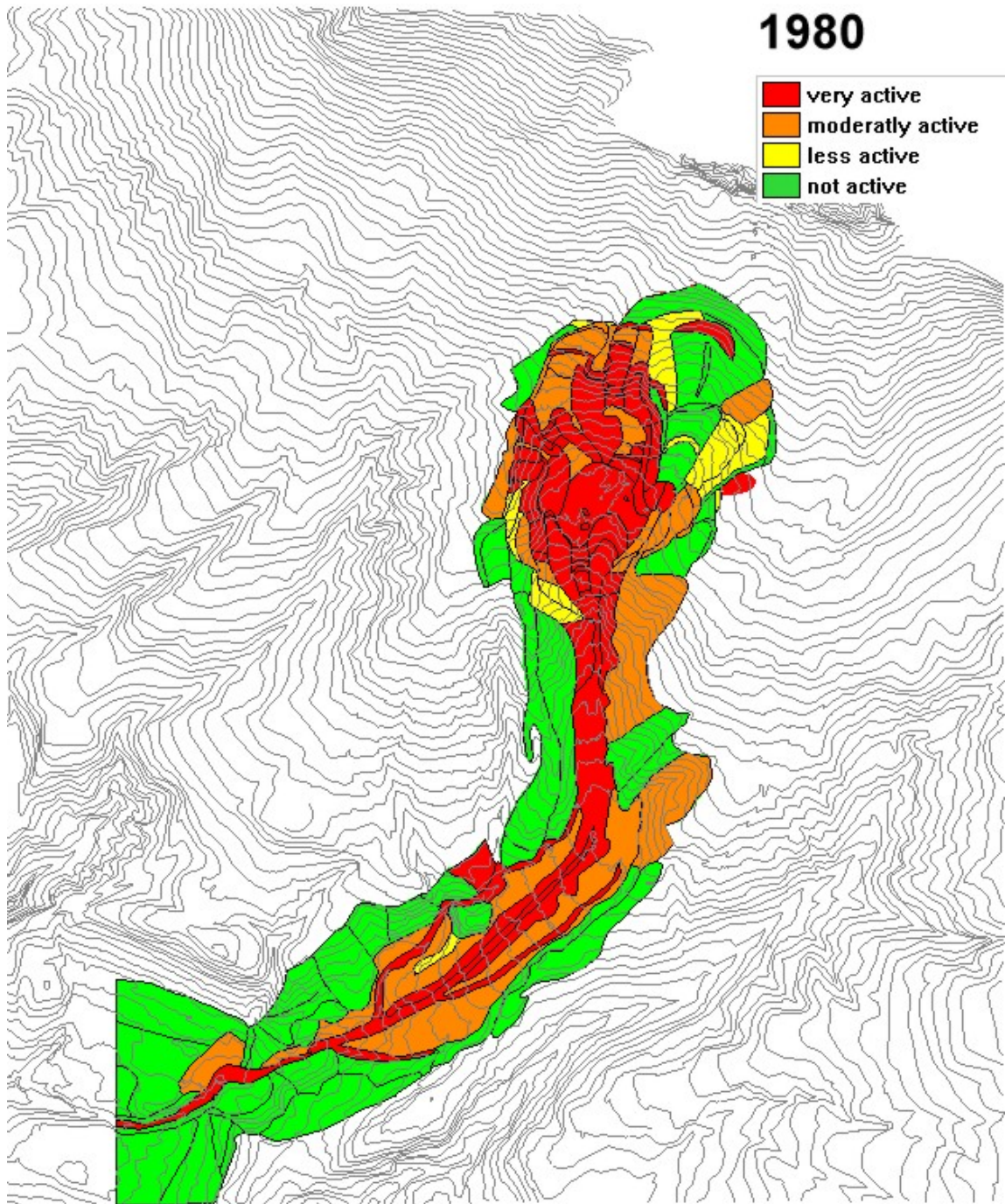


**Figure 11.** The 1980 Tessina landslide activity map

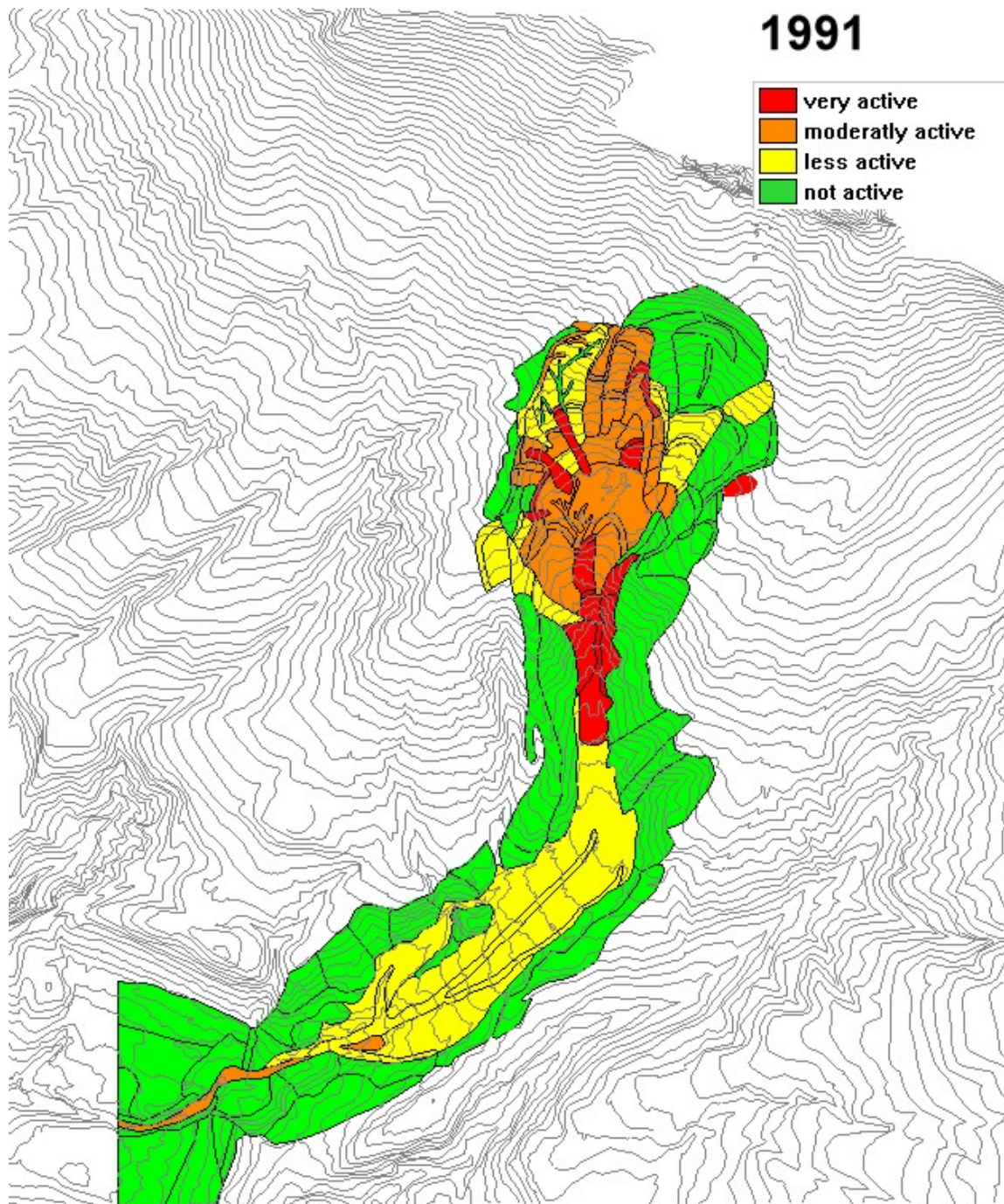


**Figure 12.:** The 1991 Tessina landslide activity map

As explained in the previous chapters, the reactivation by the 1992 landslide event mainly occurred in the areas which were previously covered by vegetation, and which were not yet reactivated before after the starting of the landslide reactivation in 1961. This huge reactivation almost doubled the size of the depletion area. In the grass covered areas above the landslide reactivation a number of circular cracks in the morainic deposit can be observed. Since almost every landslide event in the Tessina area was triggered after heavy rainfall, these cracks facilitated the infiltration of rain water in the landslide mass. This infiltrated water saturated the morainic deposits above the impermeable clay in the weathered Flysch formation. In the Tessina area, the Flysch

formation consists mostly of marly clay, with minor inclusions of highly fractured sandstone. Therefore the marly clay saturated with water and swelled, leading to a reactivation of the old, pre-1954 landslide masses. It is interesting to note that the reactivations from 1992 more or less coincided with landslide blocks that were previously observed in the 1954 photos.

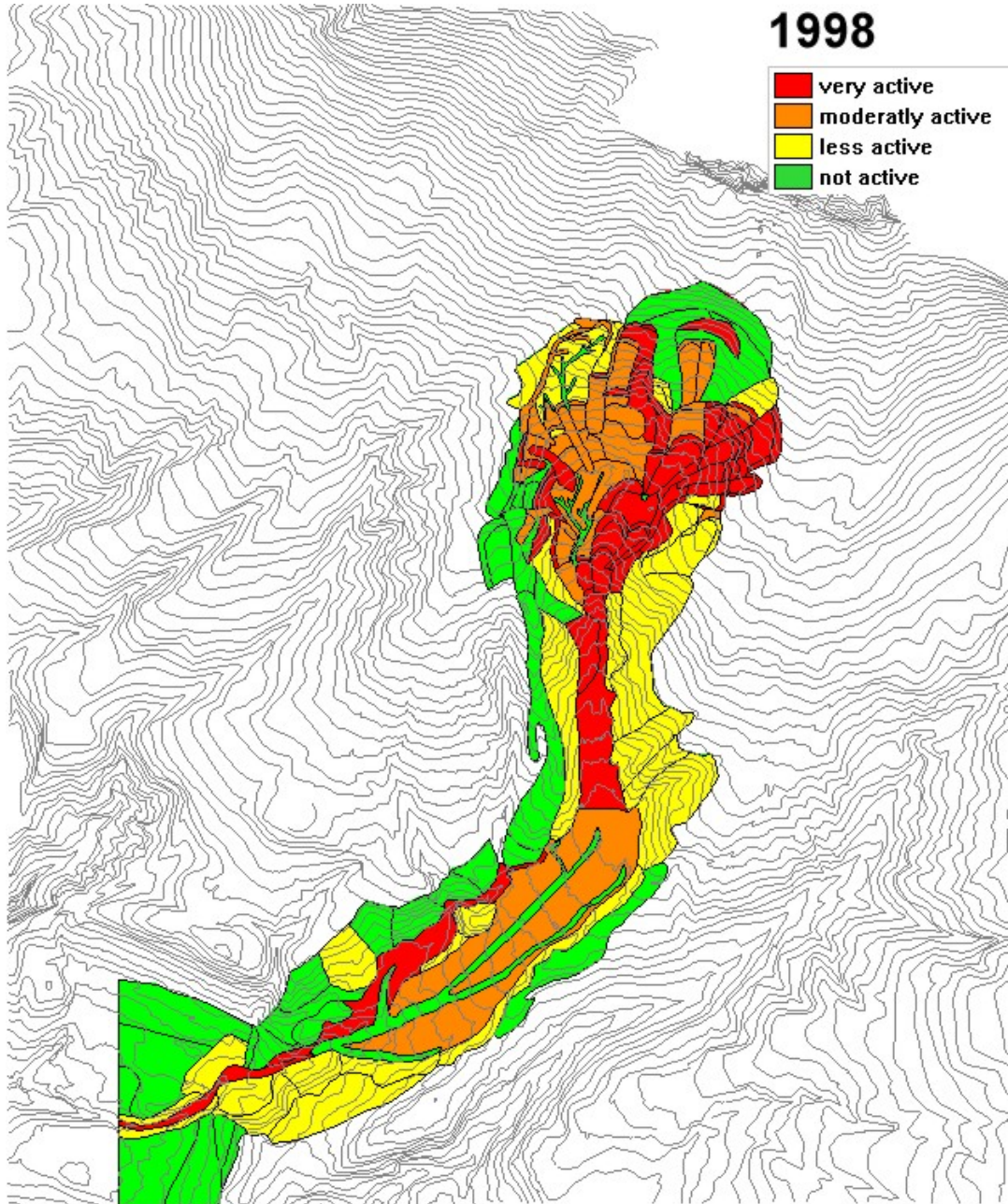


**Figure 13.** Attribute map of the 1998 Tessina landslide geomorphological map (left) and activity map (right)

The 1992 landslide was triggered by heavy rainfall (160mm in 15 days) on 17<sup>th</sup> of April 1992. The type of this landslide is a multiple rotational landslide, which affects the local moraine and the Flysch substratum. At the base of the scarps the slide turned into flow. These flows from each rotational slide combined together in a temporary storage area, below which they flowed down to the valley joining into the main flow. In just five days (22<sup>nd</sup> April) this flow had reached the road connecting to Funes to Montanes. Here a

channel was constructed across the road in order to allow the more fluid part of the flow to discharge. This mass which was about 5m wide and 1m thick moved at an approximate speed of 10m per hour whereas the main slide was moving at the speed of about 15m per day.

The 1992 reactivation caused an emergency situation in the villages of Funes and Lamozano, where people had to be evacuated given the danger of mudflow inundation. After the event a landslide monitoring and warning system for the Tessina area was set-up, with a measuring hut along the left lateral scarp, and a number of measuring points located all over the upper landslide area, using an automatic theodolite, extensimeters, piezometers, flow sensors, video cameras etc. The control center was set-up in the townhall of Lamozano. A concrete channel was constructed in Lamozano, equipped with water supply under pressure, intended to saturate the flow, so that it would not accumulate and endanger the town of Lamozano.

Also a large drainage gallery was constructed through the Monte Cavallo Limestone formation to the North of the landslide area. This drainage gallery, with a length of several kilometres, and with quite a large average discharge drains towards the East in a side valley. It was constructed in order to drain the groundwaterflow through the limestone, which was believed to have a major influence on the saturation of the Tessina landslide mass. However, up till now, no significant decrease in the activity of the landslide could be observed. On the contrary, in 1998 and 1999 some very important reactivations occurred.

During the fieldwork in October 1998 a new reactivation occurred. After 4 days (from 5<sup>th</sup> October 1998 to 8<sup>th</sup> October 1998) of less intense but long duration rainfall the right lateral scarp near to the mouth of the valley and the debris accumulation of the landslide were reactivated as flowslides. The scarp on the debris accumulation advanced inwards approximately 4m to 5m whereas on the valley sides, the flow passed rapidly through a smooth channel, along which slickensides were observed. Also the existing flow was saturated by the rainfall reactivated again. During this internal movement of the flow the road connecting Funes to Montanes started to fracture and on the next day one side of the road was pushed forward by the flow. Afterwards a new drainage channel had to be constructed across the road in order to allow the more fluid part of the flow to discharge.

### **1999: Latest reactivation**

The latest phase that was mapped represents the situation in the spring of 1999. A team of the University of Ferrara did this mapping. In 1999 the landslide advanced further in a NE direction, reactivating the minor head scarp of pre-1954 and the right valley side near to the mouth of the Tessina valley. On the pre-1954 minor headscarp rotational cracks developed whereas on the later the landslide itself reactivated.

At this moment the active part of the Tessina landslide is almost back to its pre-1954 extensions, especially in the lower part of the depletion area. The reactivation also starts in the forested area above the landslide, covered by scree deposits. It is expected that the landslide will continue to grow in a northern direction towards limestone cliffs, until it will finally have reached its pre-1954 boundaries..

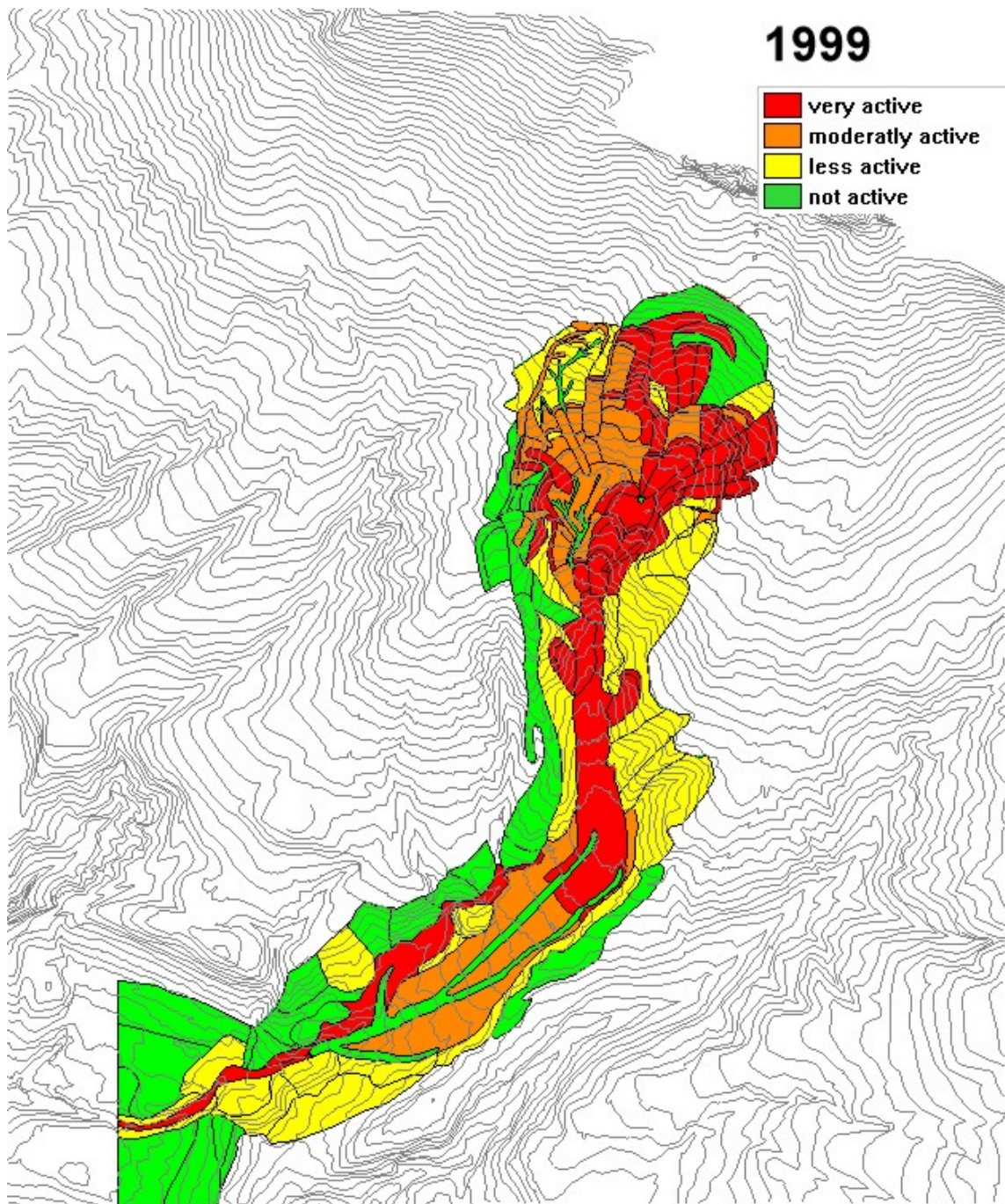


**Figure 14.** The 1999 Tessina landslide activity map

### **Description of the main causal factors for the landslide**

To determine the causes of the landslide detailed geomorphological, geological and hydrogeological surveying have been conducted. In this section a number of possible causes for the Tessina landslide will be discussed, based on the existing literature, the general geomorphological map, the multi temporal evolution map of the Tessina landslide and the geological and hydrogeological characteristics of the study area.

#### ***The pre 1954 land slide event***

From the general geomorphological map and the multi-temporal Tessina landslide evolution map one can observe that the landslide retrogressively advanced towards the margins of the pre 1954 landslide event. So the landslide is really a reactivation of an existing landslide. Before this research was carried out, the extension of the pre-1954 landslide was not established in the literature. Only after some long discussions and fieldvisits, the Italian counterparts could be convinced of the existence of a pre-1954 landslide mass, reaching all the way up to the limestone cliffs. Thus the above mentioned maps are one evidence which shows the current landslide map so far fully follows the previous pre 1954 landslide morphology.

#### ***The geology and geological structure***

The types of lithology and their structural setting are also supporting evidence for the occurrence of the Tessina landslide. Within the study area from the lithological observation especially the youngest top cover quaternary deposits and the moraine deposits are loose. In addition to this the lower substratum of Flysch is highly weathered and the sand stone highly fractured. This is due to the fact that these materials are in fact part of old landslide blocks. This lithological characteristics causes instability in combination with other landslide triggering factors.

From a structural point of view, the fault contact of the Flysch and the Monte Cavalo limestone and the bedding of the Flysch formation, might also support the occurrence of the landslide in combination with the other triggering factors.

Especially the lower older substratum, where the clay and sandstone layers are dipping steeply. This in turn causes instability from the hydrological point of view.

#### ***Hydrogeological characteristics***

The hydrogeological characteristics of the area relatively depend on the lithological type and structure. Both the youngest deposits, the quaternary and the moraine, have high permeability characteristics. In contrary to this the Flysch is relatively impermeable. However due to dipping contact of the Flysch with the overlain permeable lithologies the former absorbs the ground water. The clay in the flysch has swelling characteristics (Katerina Michaelides, 1995). Therefore these hydrological characteristics of the flysch and the above quaternary and moraine may cause instability in the landslide area.

Another important hydrogeological factor is the large inflow of groundwater from the limestone massif upslope. This inflow has not substantially decreased after the constructing of the large drainage gallery.

### Quantitative analysis of the Tessina landslide

This section deals with a quantitative analysis of the following aspects for each reactivation phase:

- The areas reactivated by the landslide
- The volume of materials removed from the depletion zone, and
- The volume of materials deposited in the accumulation zone.
- 

The calculations were performed using the ILWIS GIS package, with the following input data:

- Multi-temporal activity maps made by photo-interpretation and fieldwork for 7 different periods (1954, 1961, 1969, 1980, 1991, 1998 and 1999).
- Multi-temporal Digital Elevation Models derived from contour maps. For the Tessina area digital topographic maps (in AutoCad format) were obtained from CNR in Italy for the following years: 1948, 1964, 1980, 1992 and 1993. After converting these maps from AutoCad to ILWIS, the contourlines were separated from the rest of the topographic data. After that they had to be coded, since the contourlines were not coded according to the elevation. Finally the contourlines were rasterized, using a pixelsize of 5 meters, and interpolated into a DEM.
- Multi-temporal Digital Elevation Models derived directly from aerial photographs using scanned aerial photographs from 1954, 1969, 1980 and 1991. They provided 4 point files in ILWIS, which were converted into rastermaps.

The analysis was carried out in two ways: (1) by calculating the area and volume from the histogram of elevation difference maps made from multi-temporal DEM's; and (2) by first overlaying the elevation difference map with the landslide activity, and calculating the area and volume only for the class "very active" in the activity map. The area of expansion of the landslide in different years was directly calculated from the histogram of the activity raster maps.

### Area expansion of the Tessina landslide from 1954 till 1999

The area expansion of the Tessina landslide increases through time following the pre-1954 landslide, as explained in the previous chapter. In this section the area expansion of the following landslide events will be quantified: 1954,1961,1969,1980,1991, 1998 and 1999 . The area expansions were calculated from the histogram of the raster maps using the ILWIS 2.2 software, using the following equation:

$$A_i = TA_i - \sum_{n-1}^1 A + UA \quad (1)$$

where  $A_i$  represents the new area expansion during a certain reactivation period (e.g. 1980),  $TA_i$  represents the total area of the map from which the expansion  $A_i$  is calculated,  $\sum_{n-1}^1 A$  - represents the sum of the area expansions of the previous years ( e.g. the sum for 1954, 1961 and 1969),  $UA_i$  represents the area where no reactivation took place as compared to the previous period, and  $i = 1 \dots n$  represents raster maps fact1954 ,facv1,facv2, facv3,facv4,facv5 and facv respectively

The entire pre-1954 Tessina landslide covers an area of about 1,212,800 square meters. Out these about 681,250 square meters are areas reactivated during the various reactivation periods from 1954 to 1999 including the depletion and accumulation zone of

the landslide. Therefore about 56% of the pre-1954 landslide area is reactivated now. The area expansions during the different years is shown below in Table 1 and Figure 15.

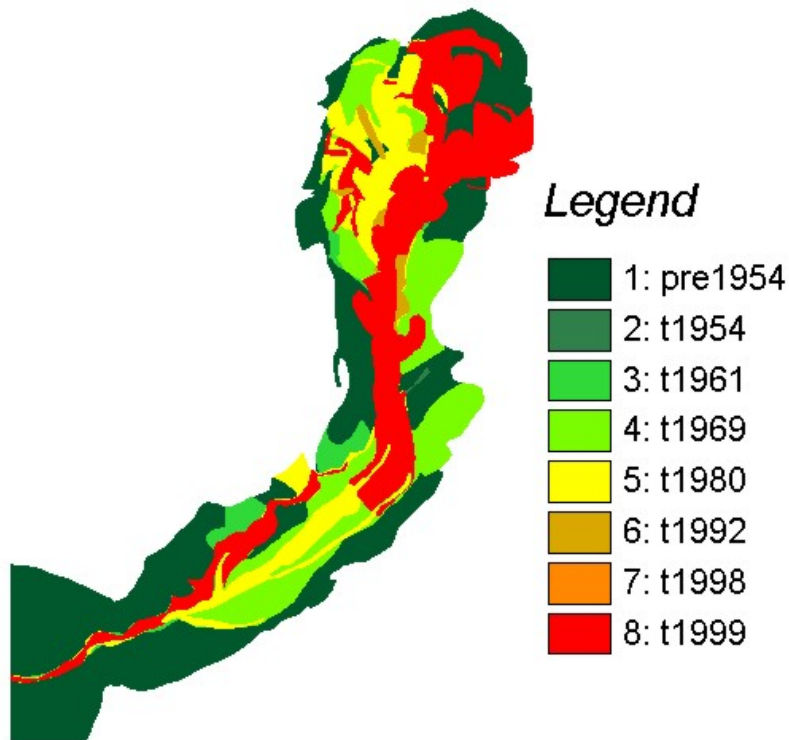


**Figure 15.** Map showing the area expansion of the Tessina landslide in different years between 1954 and 1999.

**Table 1.** The area expansion of the Tessina landslide for different periods.

<i>Year of Reactivation</i>	<i>Newly Damaged Area (m<sup>2</sup>)</i>
1954	37275
1961	204425
1969	309310
1980	33590
1992	675
1998	63125
1999	32850
Total Area Damaged	681250

Since 1998, however, the area of the landslide has almost doubled compared with its size in 1991 (Fig. 16; Table 2). Most expansion has occurred along the right lateral scarp (looking upslope). In comparison, the left scarp has appeared to be much more stable and runs close to the limits of the pre-1954 landslide (Fig. 17). In the short-to-medium term, therefore, it is expected that the Tessina landslide will continue to expand along its right margin until this too approaches the limit of the previous landslide.

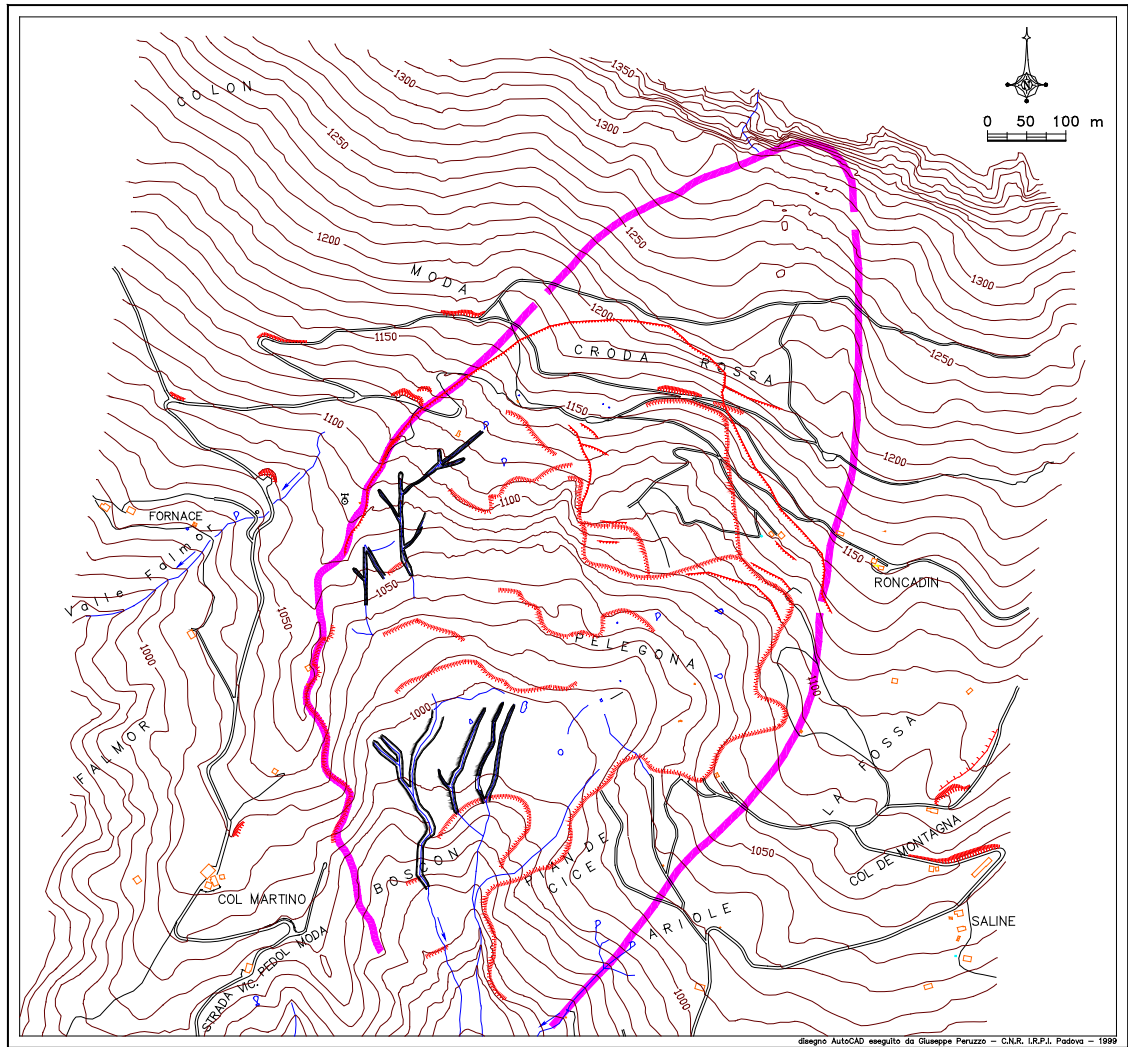


**Figure 16.** Boundary of unstable area in 1999.

**Table 2.** Widening of the unstable area

<i>Year</i>	<i>Landslide area (m<sup>2</sup>) (source area)</i>	<i>Landslide area (m<sup>2</sup>) (source area+mudflow)</i>
1965	115.000	351.250
1970	148.000	413.000
1980	156.000	443.750

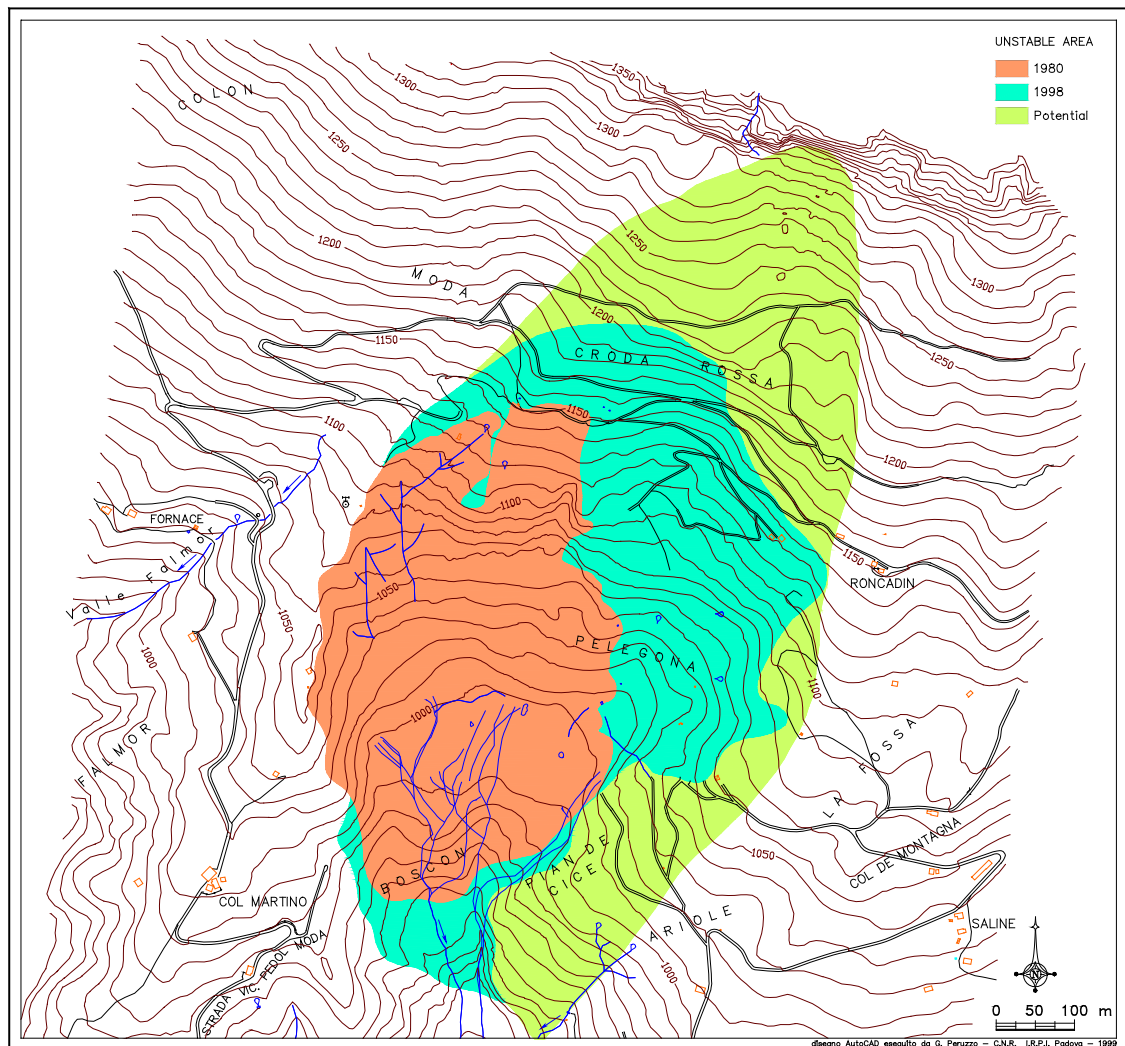


**Figure 17.** Expansion of the source area from 1980 to 1999.

### **Summary of the evolution of the Tessina landslide**

The Tessina landslide has evolved following the morphology of a pre-1954 landslide. Reactivation started in the centre of the earlier depletion between 1954 and 1961. Afterwards full-scale development of the landslide can be observed on the 1969 and 1980 aerial photographs, enlargement being very small between 1991 and 1998. Since 1998, however, the area of the landslide has almost doubled compared to its size in 1991. Most expansion has occurred along the right lateral scarp (looking upslope). In comparison, the left scarp has appeared to be much more stable and runs close to the limits of the pre-1954 landslide. In the short-to-medium term, therefore, it is expected that Tessina will continue to expand along its right margin until this too approaches the limit of the previous landslide.

## 8. Bad Goisern, Stambach Valley, Austria: The Zwerchwand rockfall/topple and Stambach mud slide

### Introduction

About forty-five km east of Salzburg, Stambach valley in the Austrian Alps is situated at the southern part of a giant anticlinal system undergoing tectonic uplift (Fig. 1). The anticline consists of rocks of the Hallstädter nappe (Triassic limestones, dolomites and halites-evaporites) with a thickness of about 2000 m. Along the southern wing of the anticline the strongly deformed and easily soluble “Haselgebirge” reaches the surface. This characteristic formation (consisting of a series of lower Mesozoic halites, shales, anhydrites and other evaporites) when in contact with water becomes highly unstable (owing to increased pore pressure and to weathering) and induces deformation in the overlying carbonate blocks (upper Triassic). Uplift has strongly fractured the Triassic units, promoting easy access of meteoric water to the Haselgebirge Formation, which continues gradually to steepen its surface angle of slope.

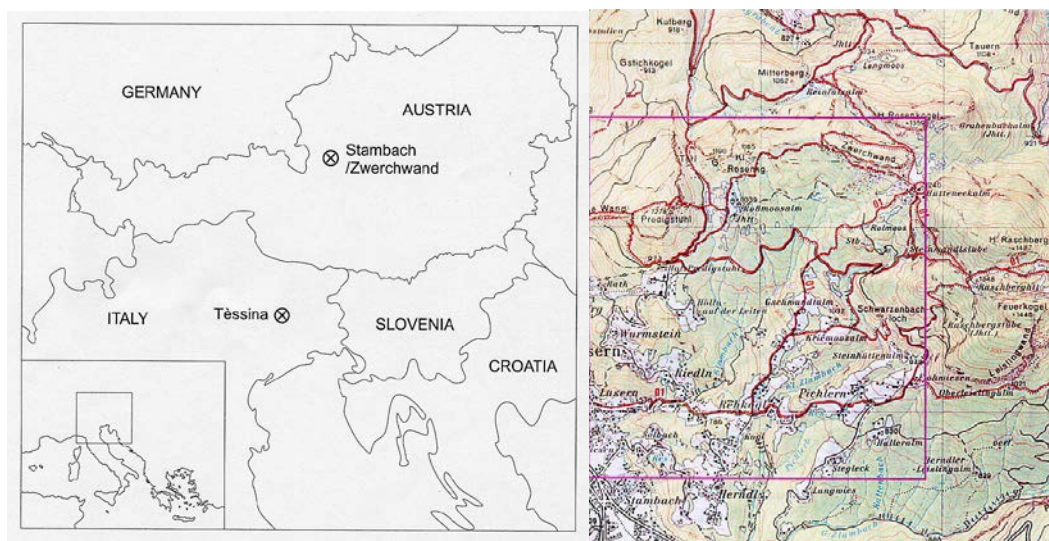


**Figure 1.** (Left) Location of the Stambach-Zwerchwand landslide above Bad Goisern in Austria. (Right) Bad Goisern district. Grid squares are 2 km across.

Dated landslides have occurred for at least 17,000 years, following deglaciation of the Traun valley. Since 1978, displacement of the Haselgebirge Formation has destabilized more than 10 million m<sup>3</sup> of rock and generated about 300,000 m<sup>3</sup> of slow mudslides, some advancing over 100 m a day. Detected slide planes in the source area lie about 40 m below the surface. More than 60,000 m<sup>2</sup> of primary forest has already been destroyed and further movement will threaten villages along the valley floor (Figs 2 & 4). Movement has created a complex landslide (Varnes, 1978, EPOCH 1993) consisting of three sub-components (Fig. 3): the head of the landslide is dominated by rockfalls at the crown, which deposits rocks onto the upper reaches of a *debris* flow that itself grades downslope into an earthflow as a result of particle sorting.

Hydrological measurements indicate that the water table is rising by 0.5-1.5 m a year and seismic refraction studies have confirmed a corresponding weakening of the water-laden horizons. Preventive measures taken against new mudslides include artificial drainage of the sliding area and the planting of light trees and bushes with strong roots (e.g. willow and alder). These measures alone are expected only to slow the rate of slope movement, rather than to arrest motion completely.

### Geology and geomorphology

Some 3.3 km long, the Stambach landslide (47° 38' N, 13° 37' E) is composed of a reworked clay matrix, with a limestone massif forming a 50 m high cliff above the head of the slide, along the Zwerchwand at the top of the Stambach valley (Fig. 3). Upper Jurassic limestones overlie Permian salt clay (Haselgebirge) and Liassic speckled marl. The Haselgebirge formation is a mixture of halite, shale and evaporites. Due to diapirism these permian saltclays have uplifted the overlying sediments. These sediments are strongly fractured and allow a high infiltration of water which leads to continued fracturing. Typical joint and fracture orientations show a clear association with regional structural trends, indicating a tectonic control on scarp formation and instability. Visible results of the instability are rockfalls from the limestone, which have loaded the debris flow derived from the Haselgebirge and Liassic speckled marl.

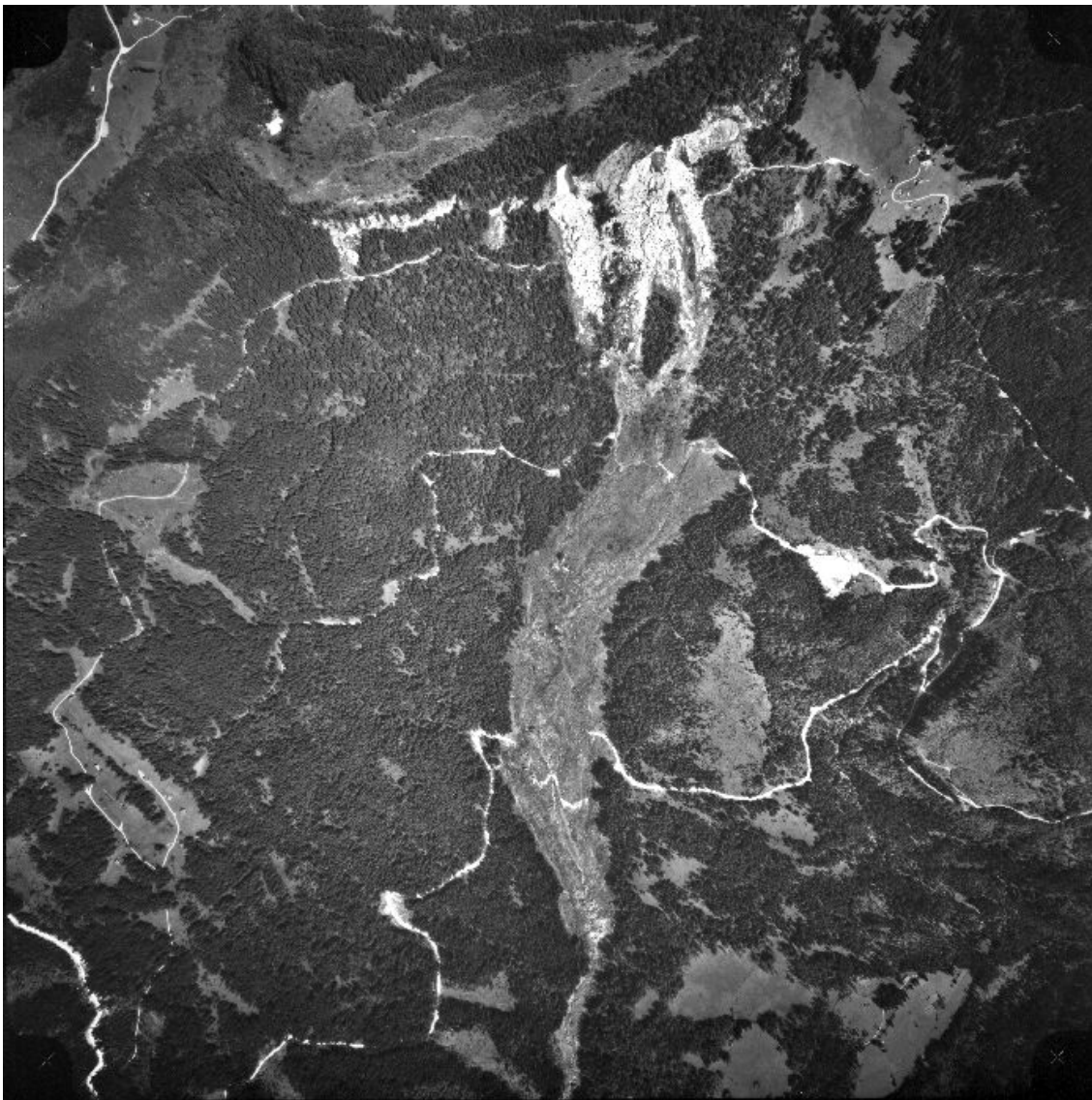


**Figure 2.** The Stambach landslide. Topples from the unstable Zwerchwand cliff (*top, white*) episodically reactivate the mobile lower reaches of the landslide (*middle, grey*), whose toe (*bottom*) lies just above the town of Bad Goisern (*out of picture, to bottom*).



**Figure 3.** The Zwerchwand headwall. Lighter areas reveal recent shear planes.

The limestones which form the crown of this complex landslide are grey-white, medium grained, fresh, very strong to extremely strong limestones (Fig. 3). The rock mass shows a low fracture frequency, and the orientation of those fractures are not favourably orientated for large scale slope failure. Rock mass rating values can be estimated as good-very good rock (Bieniawski, 1974). This allows an estimate of rock mass cohesion ( $c'$ ) and friction angle ( $\phi$ ) of 284 kPa and  $45^\circ$  respectively. Underlying this rock mass is a salt clay called the Haselgebirge. This is a dark grey, fine grained, laminated, weathered, weak mudstone. As this material weathers the strength of the rock changes from that of a weak rock to that of a soil mass.

The dynamic history of the landslide is unusual. Normally the movement of a debris flow consequent to undrained loading is relatively short. However, in this case there are two significant gaps between pillar collapse and the re-activation of the debris flow (Fig. 4). Thus, some six months elapsed between the pillar collapse of February 1980 and the reactivation of the debris flow in August of the same year, while a 10-month gap occurred between the pillar collapse of the 09 March 1981 and reactivation of the debris flow on 26 January 1982 (Fig. 4). Reasons for delayed reactivation will be addressed further below.

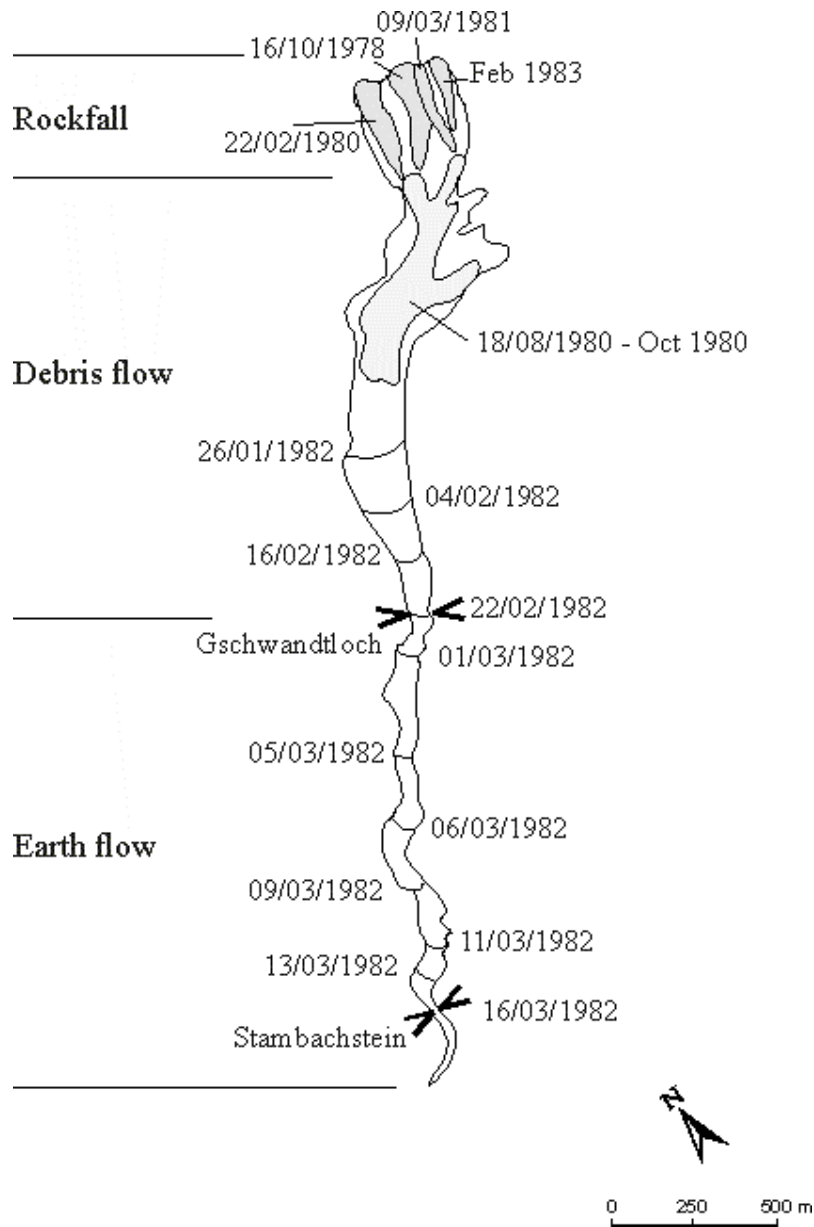


**Figure 4.** Evolution of the Stambach landslide, also showing the downslope change in primary style of deformation from rockfalls to earthflow.

Geomorphologically, the landslide can be subdivided into three major sections, corresponding to the style of deformation (Fig. 5): the headwall from which rockfalls occur, the upper slide zone (mud and debris flow), and the distal zone, about 1 km long, of the most recent mud and earth flow. The most prominent movements along the whole landslide have occurred since 1978. During this period, the upper mudflows have advanced about 380 m, while the lower earth flows have extended by only 180 m. Part of this difference is due to downslope decelerations in rates of advances, and also to landslide accumulation behind a tectonically aligned escarpment that has contained the toe of the landslide. Seismic sounding has located the base of the slide at depths between 30 and 45 m.

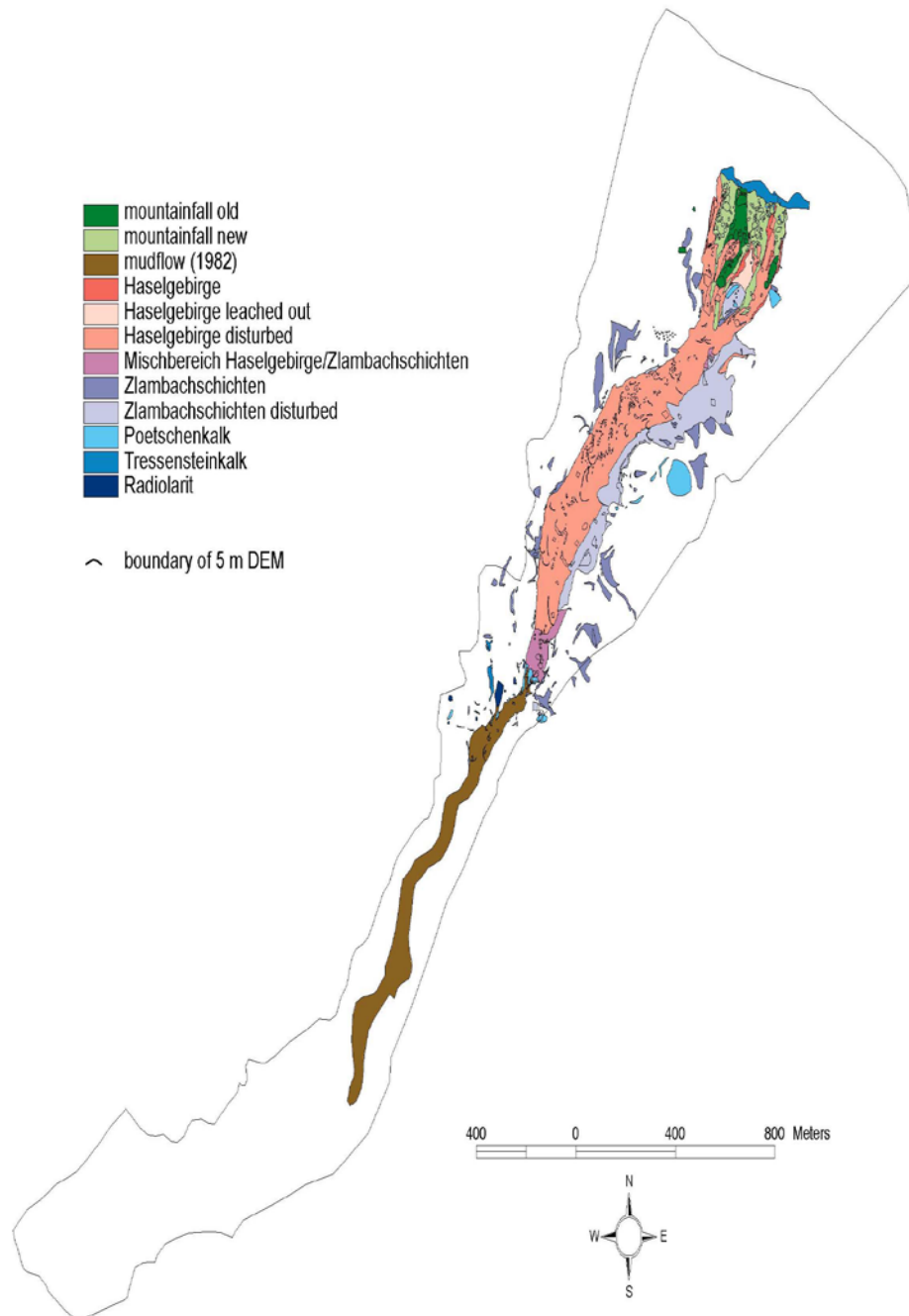


**Figure 5.** Geomorphological units along the Stambach landslide. A clear correlation exists between geomorphology and age of each unit (compare Fig. 4).

### Geotechnical analyses

The geotechnical characteristics of the Stambach landslide are summarised in Table 1. The materials have a small average cohesion of 14.16 kPa, suggesting that the measured strength reflects residual values available after the large degree of strain undergone by the landslide mass. It is thus reasonable to consider the *residual strength* of the soils when evaluating the stability of the slopes in question, using the Navier-Coulomb failure relation

$$\tau = c' + \sigma \tan \phi \quad (1)$$

where  $c'$  is cohesion,  $\phi$  is angle of friction, and  $\tau$  and  $\sigma$  are the applied shear and normal stresses at failure. For stresses in kPa, Eq. (1) becomes for the Stambach material

$$\tau = 14.16 + 0.33 \sigma \quad (2)$$

**Table 1.** Geotechnical features of Stambach landslide material

Sample	Cohesion $c'$ (kPa)	Friction Angle $\phi$	Unit Weight $\gamma$ ( $kN m^{-2}$ )	Plastic Limit (%)	Liquid Limit (%)	Plasticity Index (%)	Activity Index	Moisture Content (%)
<b>Mean</b>	14.16	18.12	19.52	21.40	48.20	26.40	0.73	37.34
<b>standard deviation</b>	10.75	1.89	0.08	1.95	10.83	10.16	0.24	8.09
<b>Minimum</b>	5.3	15.6	19.4	20	35	35	0.35	18.1
<b>Maximum</b>	31.9	20.2	19.6	24	62	62	0.97	49.7

The landslide material contains particles from 0.001 to 40 mm, some 60% being smaller than 0.06 mm (Fig. 6). Clay fractions constitute some 20-30% of each sample, the content increasing with downslope distance along the landslide. The high proportion of fine material suggests that a significant component of bulk strength will be derived from cohesive, rather than frictional components, while the downslope increase in clay content corresponds with an increase in plasticity index as the landslide evolves from a mudflow to an earth flow.

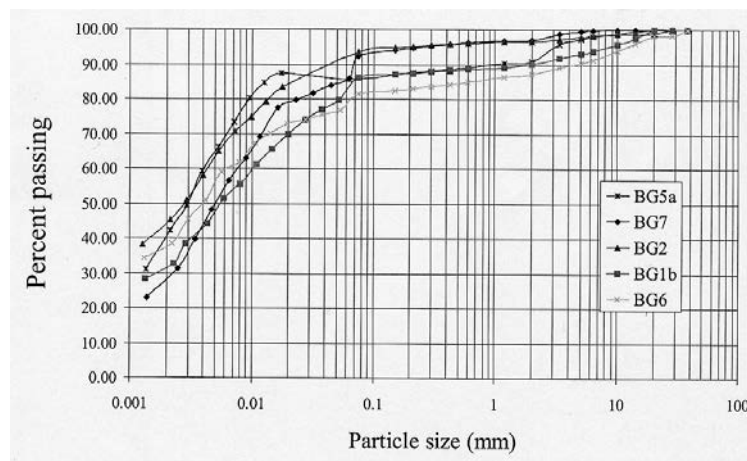


**Figure 6.** Particle size distributions for Stambach landslide material. Samples further downslope have larger clay contents, consistent with the apparent downslope increase in material plasticity. Note that for all the samples, some 60% consists of material smaller than 0.06 mm.

## Hydrology

Most of the landslide material is fractured and porous and so is readily infiltrated by meteoric water. Measured infiltration rates vary from 0.005 to 0.02  $m s^{-1}$ , implying mean infiltration volumes for the whole landslide (300,000  $m^2$ ) on the order of 300,000  $m^3$  per year. Such a water flux persistently weakens the landslide material, seismic surveys during 1982-1984 registering a lowering by some 10-15 m of a degraded horizon.

## Landslide mechanics

The 45° friction angle of the limestone along the Zwerchwand scarp favour slope stability under normal conditions. Intermittent collapse must therefore be the result of progressive weakening. Field observation suggests that such weakening is limited within the limestone itself. However, the salt clay levels within the underlying Haselgebirge formation are readily altered by meteoric water.

It is suggested that weathering of the Haselgebirge clay reduces the compressive strength of the mudstone units exposed at the base of the limestone scarp. The clay compresses, allowing the blocks of the overlying limestone to tilt outwards. As the weathering front advances into the clay, the base of the limestone block becomes increasingly unstable until toppling occurs (Fig. 7).

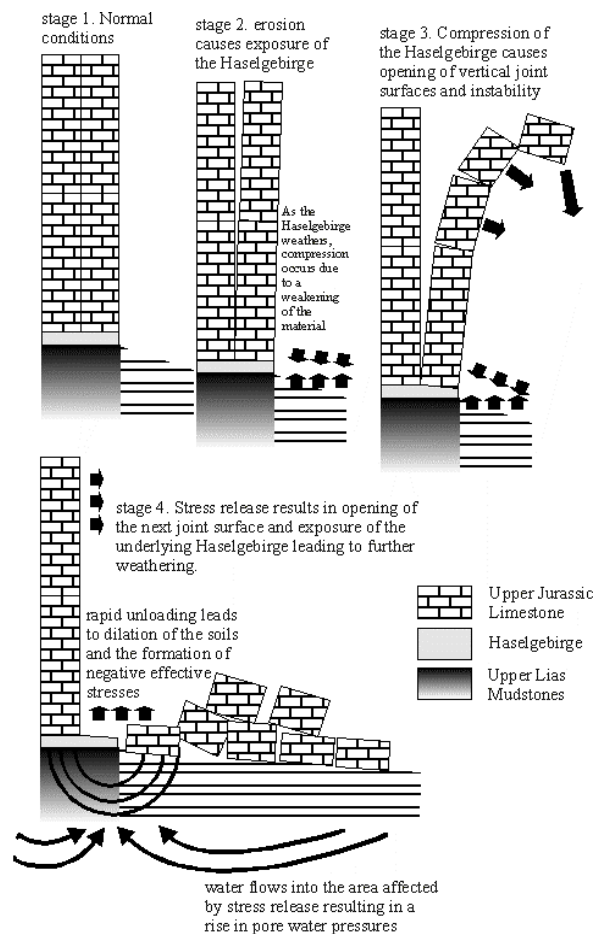


**Figure 7.** Model for episodic headwall collapse and delayed reactivation of landslide.

Toppling is the first stage in the movement of the main body of the landslide. Landslide movement is episodic, partly a result of intermittent pillar collapse, but also because of processes delaying the dynamic response of the landslide to such collapse. Collapsed pillars apply an undrained head load to the debris-flow section of the landslide. Such undrained loading would normally reactivate the landslide immediately, as a result of increases in the effective stresses acting on the shear plane (Hutchinson & Bhandari, 1971). To account for the delay by several months between pillar collapse and landslide reactivation, it is proposed that the sudden increase in total normal stress associated with pillar collapse induces negative *effective* stresses within the impacted debris-flow material. Such negative stresses (suction) would favour the debris flow remaining in place until the suction is dissipated by the equalisation of pore water pressures (Fig.

7). The monthly timescale of the delay is consistent with that observed generally for subsidence induced by the porous flow of water. Following pillar collapse, stress relief allows joints to open within the limestone rock mass, increasing its permeability and exposing more of the underlying mudstones to weathering, so establishing the conditions necessary for the next cycle of collapse and of landslide reactivation.

### **Corrective measures**

A slope-stability analysis of the Stambach landslide (Chapter 10) suggests slide reactivation is unlikely without pillar collapse. Appropriate hazard-mitigation procedures include (1) securing the pillars at the top of limestone escarpment by rock anchors, or (2) using a geomembrane to reduce the rates of weathering of the Haselgebirge units beneath the limestone pillars. In combination with current drainage measures being applied to the toe of of the landslide (Fig. 8), such engineering solutions could be undertaken without significant environmental impact.



**Figure 8.** Alder trees have been planted along the lower reaches of the landslide to aid removal of meteoric water from the active earth flow. The difference in vegetation clearly outlines the active landslide.

One further complication of the Stambach/Zwerchwand Landslide site can be considered and that is the triggering of the block failure itself. If block toppling occurs due to deformation of the Haselgebirge which weakens due to weathering and salt solution from the matrix, then the rate of weathering will control the pillar collapse rather than the slope morphology. This would mean that future landslide hazard models should be based on estimates of the weathering of the Haselgebirge, as opposed to standard slope stability model. Such hazard assessments would be further complicated by the problems outlined about how the fallen limestone blocks actually trigger the debris flow re-activation.

### **GIS analysis**

Topographic, photographic, geological and geomorphological data were combined at scales from 1:1,000 to 1:50,000 to provide a basic Geographical Information System (GIS) for the Stambach landslide (Fig 9).

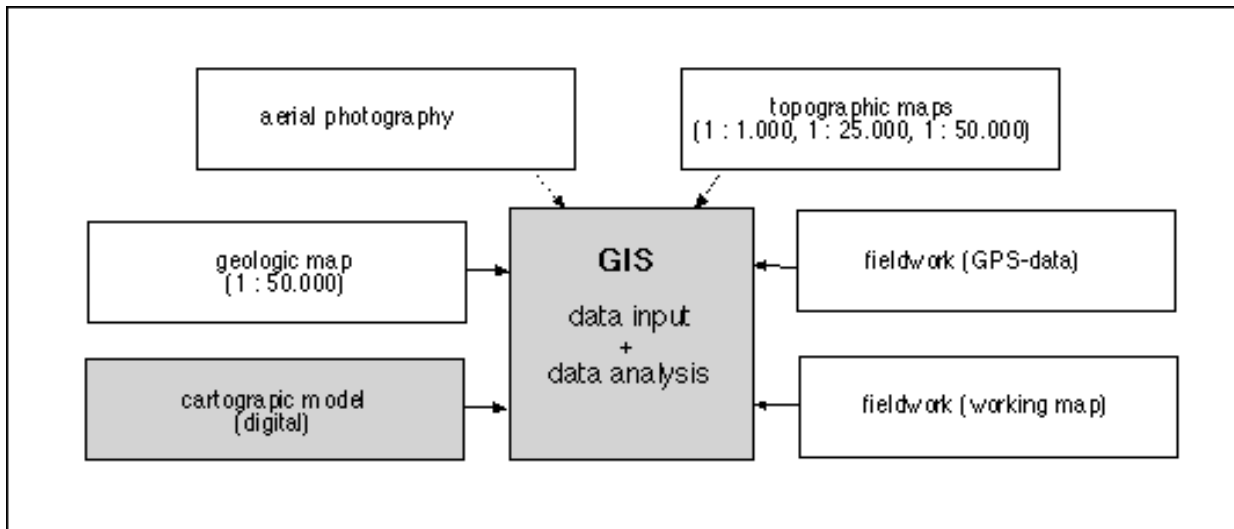


**Figure 9.** Outline of data input for dedicated GIS

A digital elevation model (DEM) was first created from conventional topographic maps model. The morphometric aspects of a geomorphologic research can be supported efficiently with the help of an optimised, true-scale DEM. The quality of the DEM is therefore of crucial importance. With the right choice of resolution and some additional structural steps during the DEM production, the output quality can be significantly increased. As it was impossible to gain a resolution better than 10-15 m from standard 1:50,000 cartographic maps, additional original data were sought at higher resolution. The best additional data were found from a 1:1,000 topographic map specially commissioned after the 1982 reactivation of the landslide. After manual digitization, it was possible to create a DEM at resolutions of 3-5 m.

Figures 10 and 11 illustrate sample outputs of shaded relief maps and automatic topographic profiles. Additional outputs include maps of slope distribution, curvature and orientation, zones of water accumulation, lithology, neotectonics, and distributions of soil, vegetation and rainfall. Sample sheets are provided on the accompanying CD ROM. These data have been combined to generate maps of relative landslide hazard over an area of 50 km<sup>2</sup> centered around the Stambach landslide.

The hazard maps were generated using the “map algebra” facility of Grid Analyst in Intergraph. A three-step “decision tree” was used to weight different categories and subcategories (*e.g.*, topography, lithology and environmental factors). Thus the probability of landsliding was viewed as a function of slope angle, rock-and-soil type, vegetation cover, and annual precipitation. The resulting hazard factors were then attributed relative values between zero and one (from least to greatest hazard). Thematic maps illustrating the transformation of raw data to hazard maps are provided on the accompanying CD ROM.

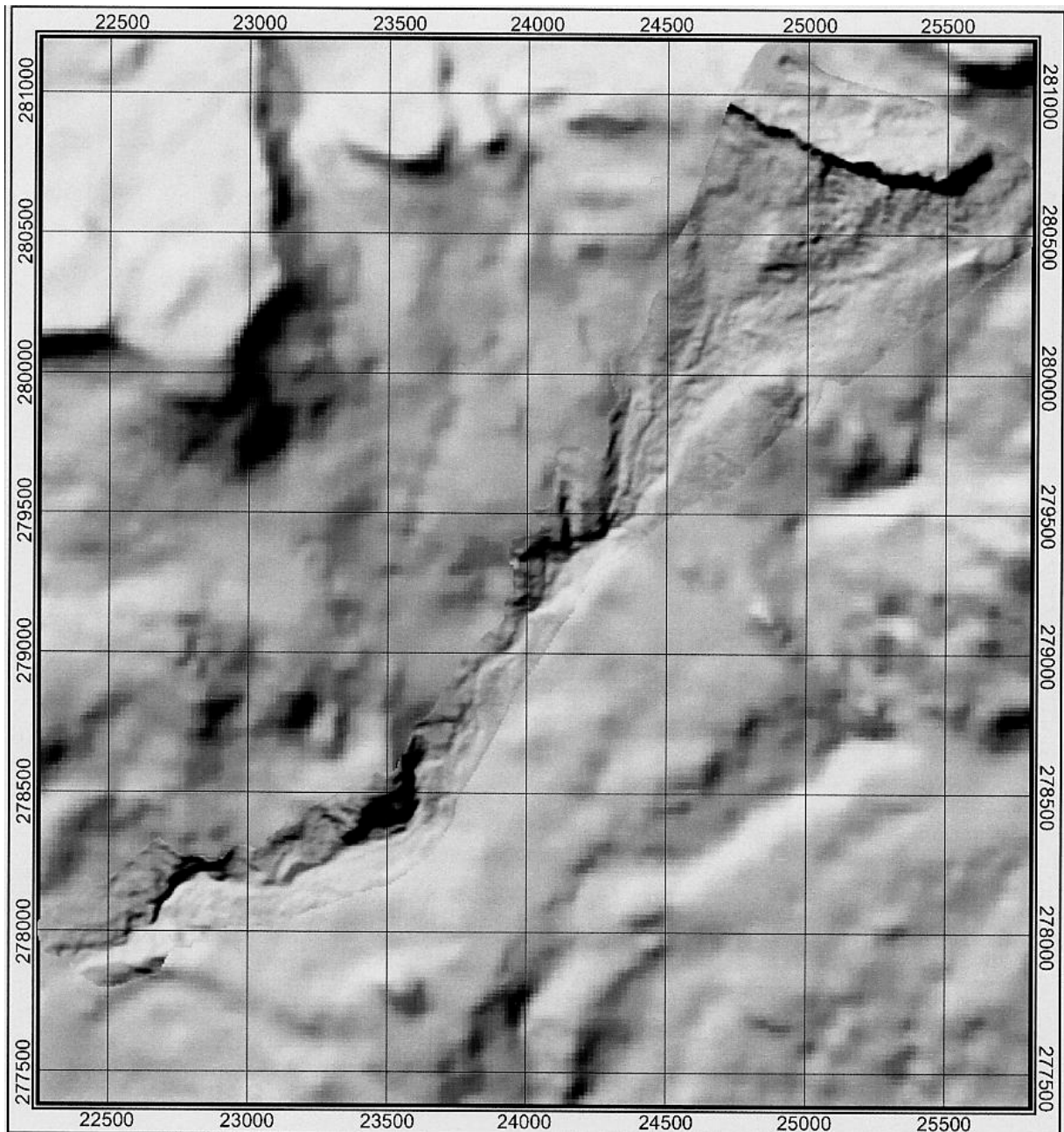


**Figure 10.** Shaded relief map from GIS enhancement of a 1:50,000 DEM of the Stambach landslide. West is to the left. Compare with Figure 2.

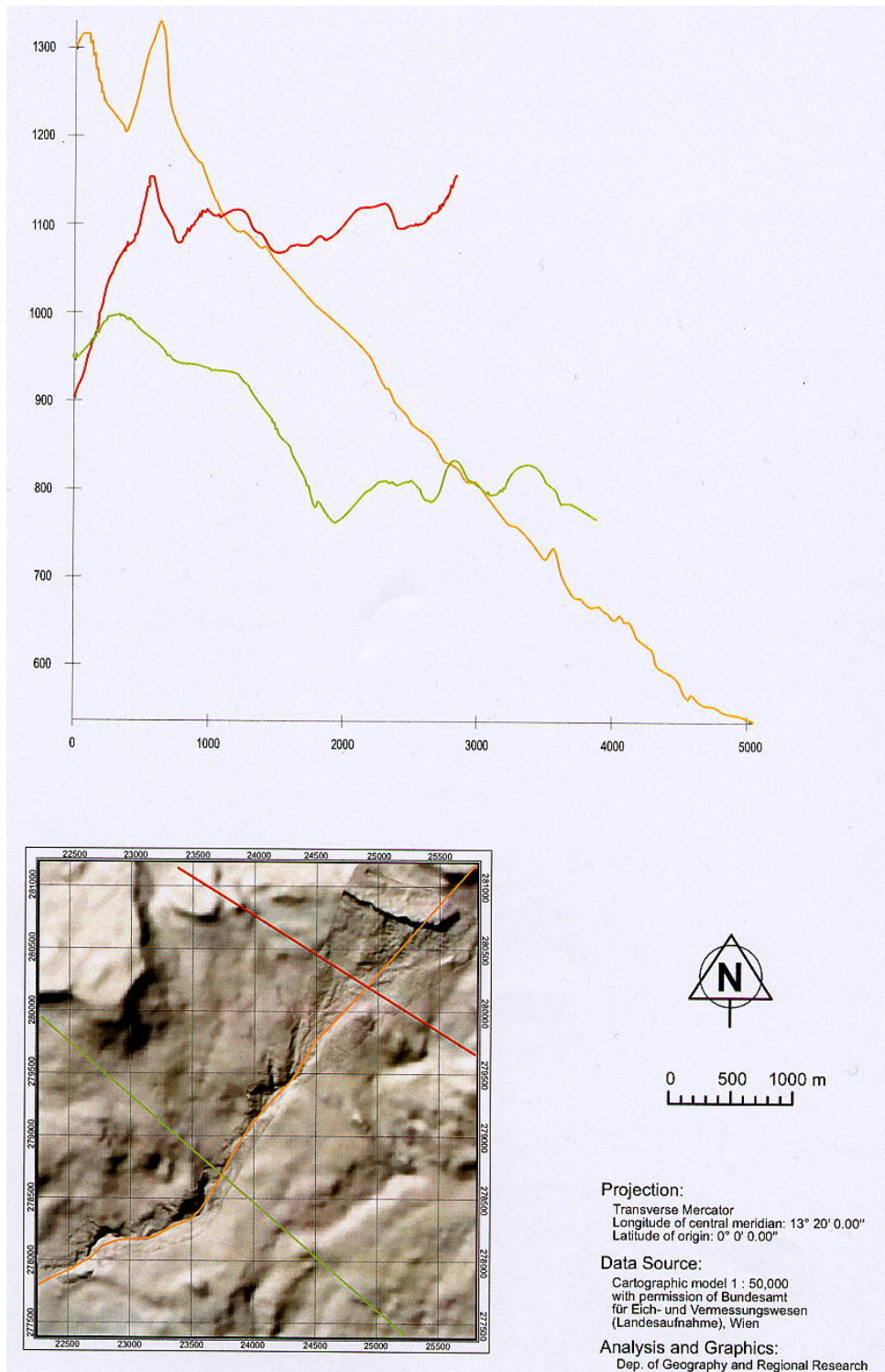


**Figure 11.** Sample profiles across the Traun valley obtained from GIS analysis.

## References

- Bieniawski, Z. T. 1974. Geomechanics classification of rock masses and its application to tunnelling. *Proceedings of the Third Congress of the International Association of Rock Mechanics*, Denver, Colorado. **2-A**, 27-32.
- EPOCH (European Community Programme) 1993. *Temporal Occurrence and forecasting of landslides in the European Community*. Flageollet, J. C. (Ed), 3 volumes, Contract No. 90 0025.
- Hutchinson, J. N. & Bhandari, R. 1971. Undrained loading: a fundamental mechanism of mudflows and other mass movements. *Geotechnique*, **21**, 353-358.
- Varnes .D. J. 1978. Slope movement types and processes. In: R. L. Schuster and R. J. Krizek (eds), Special Report 176: *Landslides: Analysis and Control*; Washington, TRB, National Research .

## 9. The Barranco de Tirajana Basin, Gran Canaria, Spain

### Introduction

The Barranco de Tirajana (BdT) Basin is a 25 km<sup>2</sup> amphitheatre cut into the southern side of Pico de Las Nieves, the highest point on Gran Canaria (1949 m). The Basin is a major erosive feature formed since the Pliocene by large landslides. The eroded material consists of interbedded volcanic lava flows and pyroclastic units which, erupted since the Miocene (14.5 million years ago), cover a total range in composition from basanite and nephelinite to trachyte, rhyolite and phonolite.

The BdT contains at least 28 landslides, some with volumes exceeding 1 km<sup>3</sup>. Several generations of movement can be recognised, typically consisting of a major primary failure of the bedrock, followed by a succession of smaller, secondary displacements due to sliding from the primary body. Following primary failure and emplacement, the landslide materials suffered a progressive weathering and weakening, so that second-generation and younger bodies typically display a broken and disorganized texture. Most reactivations have occurred along the initial planes of failure, which themselves developed exclusively within levels dominated by volcanic tephra (tuffs, ashes, ignimbrite and basaltic pyroclasts), rather than lava flows.

Modes of displacement have included examples from most types of mass movement, including slides (rock-, earth-, and debris-slides), rock avalanches, and debris slumps and flows. Altogether, 23 of the 28 landslides have involved a major translational component, notably 12 rockslides, 5 debris slides and 2 earth slides.

The most recent movements have been concentrated in the Rosiana area (flanked by San Bartolomé and Santa Lucía) where displacements exceeding 10<sup>6</sup> m<sup>3</sup> have been recorded since 1879, often following intense rainfall. The last rapid slide, in 1956, destroyed houses and communication lines, and prompted the evacuation of 250 people. Slow movement continues in the area and is being monitored by a newly-installed ground-deformation network. Simultaneous plans for raising public awareness of landslide hazard are described in Chapter 13.

### New 1:25,000 Geomorphological map of the BdT

The BdT has been completely remapped at a scale of 1:25,000. Shown on the accompanying CD ROM, specific features to note about the map are as follows.

#### *Geomorphological features of the bedrock*

The bedrock has been considered as an only rocky whole, where only have been differentiated some recent volcanic landforms, i.e. calderas and craters, pyroclastic cones and deposits, and a lava flow. Erosive processes worked in an intense way on the bedrock. They produced many incised ravines and rocky escarpments, and leave some structural surfaces on the upper areas of the rocky massif, as platforms.

#### *Slide landforms*

Slide masses, considered as one unit and demarcation boundary have been drawn to distinguish them from the bedrock. There are high scarps behind the upper parts of the landslides, sometimes jointed the ones to the others.

Landslides have very variable forms and sizes. Although, some specific features have been individually distinguished in the field and represented on the map. These are: slide scars and escarpments, elongated depressions named “grabens” in landslide terminology, landslide contours and slide directions. As a result, landslides do not follow a regular or simple pattern.

The Rosiana landslide (discussed below) has been specially pointed out as an active slide. Meanwhile, the zones with present rock-falls have been represented as active scree.

#### *Sedimentary deposits*

Sedimentary deposits in the BdT basin are always directly or indirectly related to landsliding. Three basic units have been recognised: (1) slide masses have been considered as one type of them, like a result of erosive processes; (2) a huge number of debris deposits appear on the upper part of the slides, that came from the upper escarpments produced by the slides; and (3) main alluvium that has been produced by an intense erosion of the recent landslides. In addition, some obstruction deposits have been also recognized and drawn. They were produced when a ravine was closed by a slide. This slide-obstruction relationship is clear in the case of La Manzanilla landslide.

The detailed geomorphological survey and map can be used in the future as an important tool to prepare a hazard zonation or risk-map in this area, in order to forecast future events of sliding or rock-falling; it can also be very useful for local developers and authorities.

#### **The Rosiana landslide**

The active Rosiana landslide is located at the bottom of the BdT and corresponds to the lower part of a group of old large landslides (Lomoschitz and Corominas, 1997a). Still active, the landslide has moved at least four times since 1879 (1879, 1921, 1923 and 1956).

The last important movement occurred in February 1956 following a period of intense rainfall (272 mm in 24 hours). Within days, some 3 million cubic metres of material destroyed an arterial road and bridge (Macau, 1956), severely damaged buildings across an area of 0.3 km<sup>2</sup> and provoked the evacuation of 250 people. Significantly, this destruction resulted from a net downslope motion of only 7 metres. It is a translational slide according to Varnes' classification with a surface-parallel failure plane at a depth between 12 and 25 m. Due to erosion along a ravine, especially during periods of heavy rainfall, the toe of the slide is unbuttressed and so favours new displacements (Lomoschitz and Corominas, 1997b).

#### **Monitoring the Rosiana landslide**

A three-stage strategy has been designed for monitoring movements along the Rosiana landslide: (1) definition of the geomorphological context of the slide; (2) geophysical and bore-hole surveys; and (3) installation of a local EDM geodetic network, which can be integrated into the larger-scale GPS network for the whole BdT (Chapter 11).

#### *Geomorphology and composition of the Rosiana landslide*

The Rosiana district has been mapped at a scale of 1:6,250 (Figure 1). The M-shaped headwall consists of two merging arcuate scars, 200-250 m across. The slide is confined by bedrock to the northwest where its margin, marked by an escarpment, runs 500 m downslope and meets the road by the present bridge. The eastern scar is delineated by a series of small escarpments, from which the landslide margin runs some 750 m to the road. Mean surface dips decrease downslope from 35° to 20°, although relief is irregular due to step-wise displacements that become shallower downslope. The central part of the slide dips at angles decreasing downslope from 25° to 14-18°; cut by a ravine, its eastern margin has near-vertical slopes 3 m thick. The distal zone of the landslide has

advanced as a tongue over shallow slopes, invading cultivated land. Altogether, the slide reaches 450 m across, extends 855 m, and covers an area of 0.33 km<sup>2</sup>. In addition to geomorphologic indicators, local directions of movement can be inferred by deformation of buildings and tilting of palm trees, all of which indicate a broad southerly movement for the slide (Figure 2).

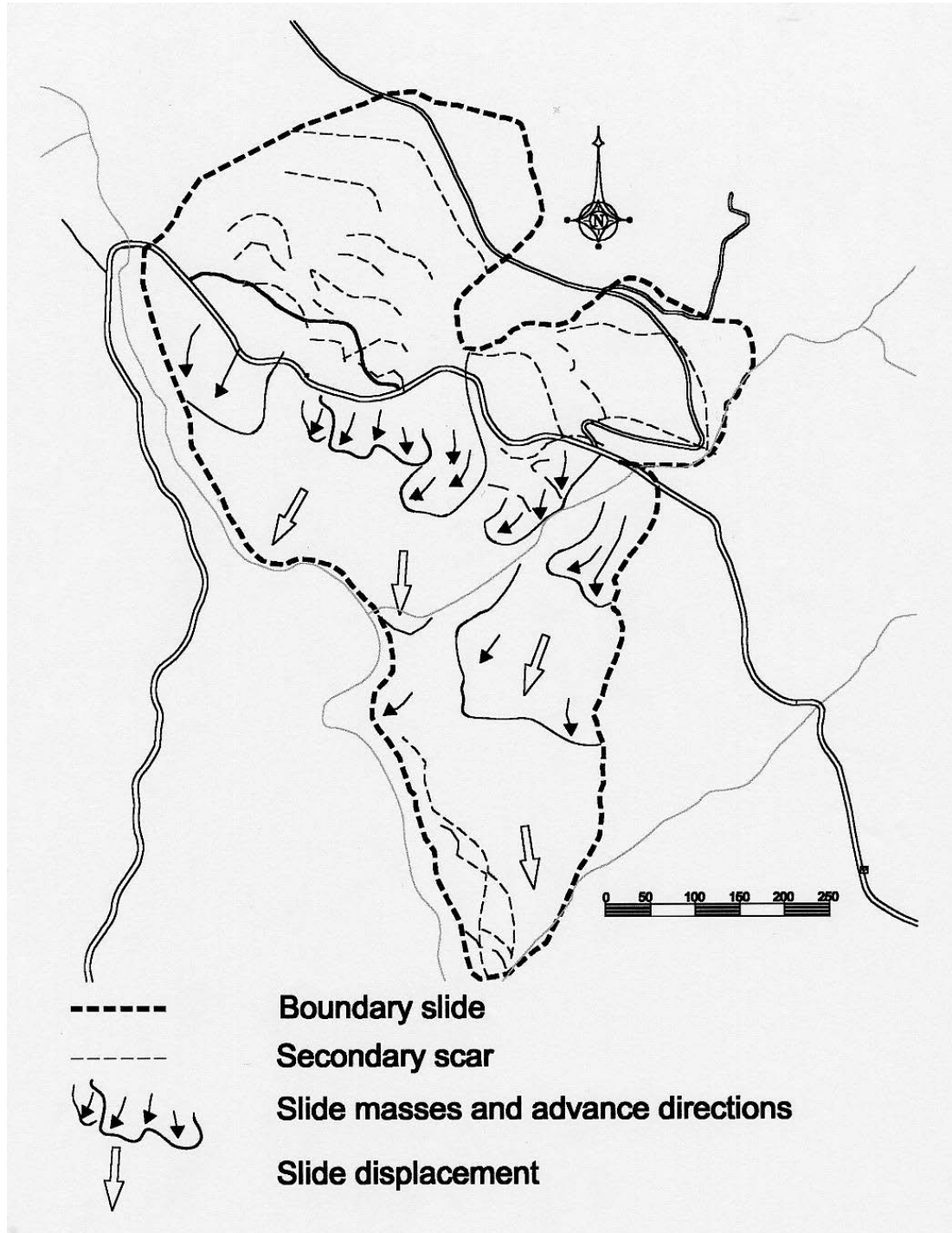


**Figure 1.** Geomorphological units within the Rosiana landslide.

Compositionally, the Rosiana slide consists of broken volcanic material, mostly derived from Miocene and Pliocene trachyte-rhyolite-phonolite formations. Natural

cross-sections reveal a chaotic internal structure, composed of heterogeneous, angular fragments (from gravels to boulders) supported by a matrix of clayey-gravel (gravel, sand and clay). Although some sections contain almost exclusively large fragments, most contain some 40% of matrix, a typical particle size distribution being 58% coarse fragments, 20% sand and 22% silt and clay. When the failure occurred the silt-and-clay mixture was cohesionless with a friction angle between  $17.7^\circ$  and  $21.6^\circ$ .

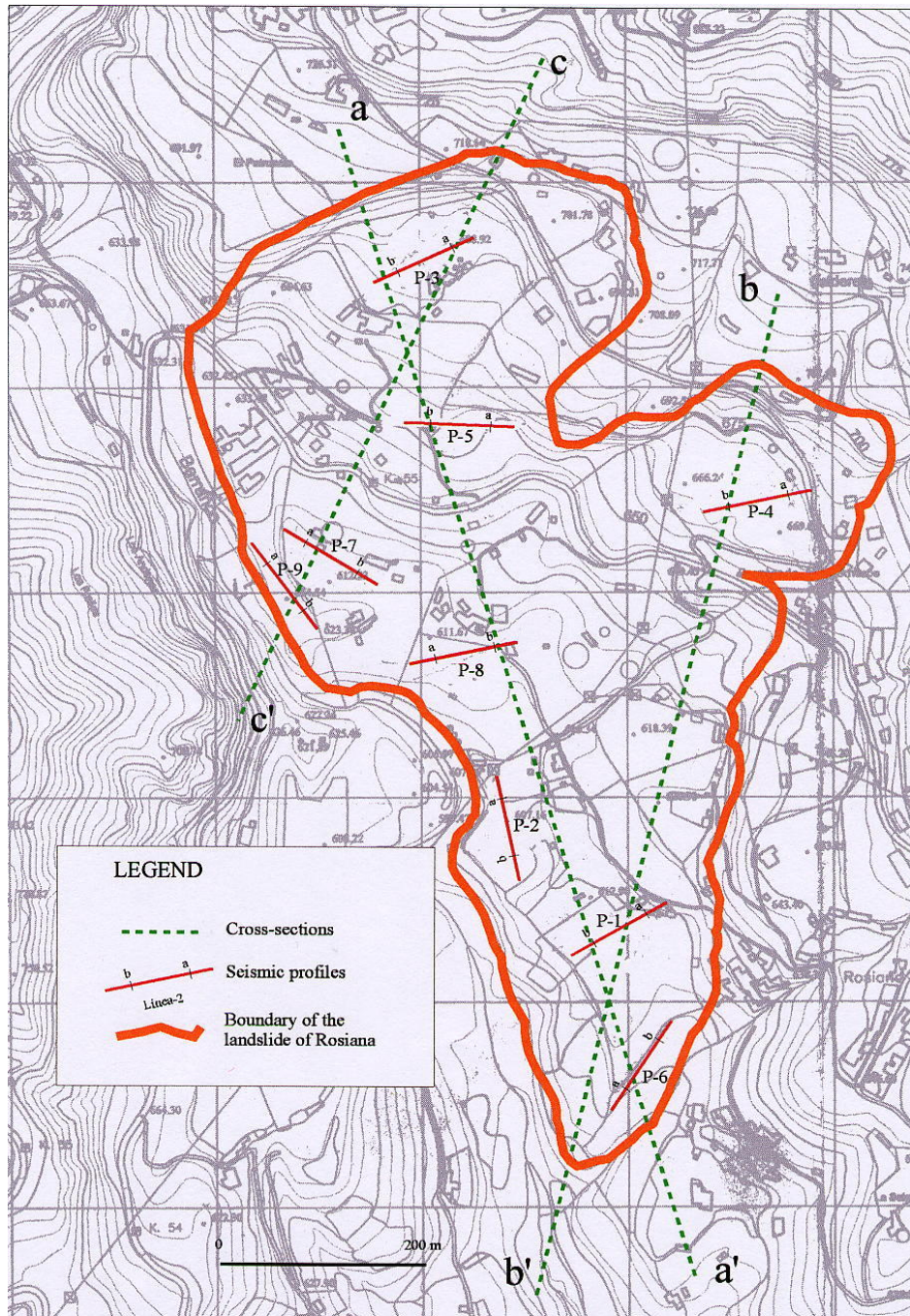


**Figure 2.** Location of the 9 seismic profiles within the Rosiana landslide.

### Geophysical and bore-hole surveys

Directed by the geomorphological features of the landslide, nine seismic profiles, each 55 m long (Figure 2), were measured using an EG & G1225 Geometrics multichannel seismograph. Data are analysed by the Wave Front method using Sesview and Gremix software. This technique is frequently used in engineering geology, and the results can be well interpreted if: (1) the depth of the layers does not exceed about 20 m; and (2) real differences appear among the collected seismic velocity data.

Bedrock in general has been well detected, about 5-13 m deep with seismic velocities of 2,185-3,363 m s<sup>-1</sup>, except at the crown of the slide where velocities decrease notably to less than 2,200 m s<sup>-1</sup>. In addition, within the landslide material there are two different layers: a variable colluvium layer 1-4 m thick, underlain by the slide mass proper that is 4-9 m thick (Figure 3).

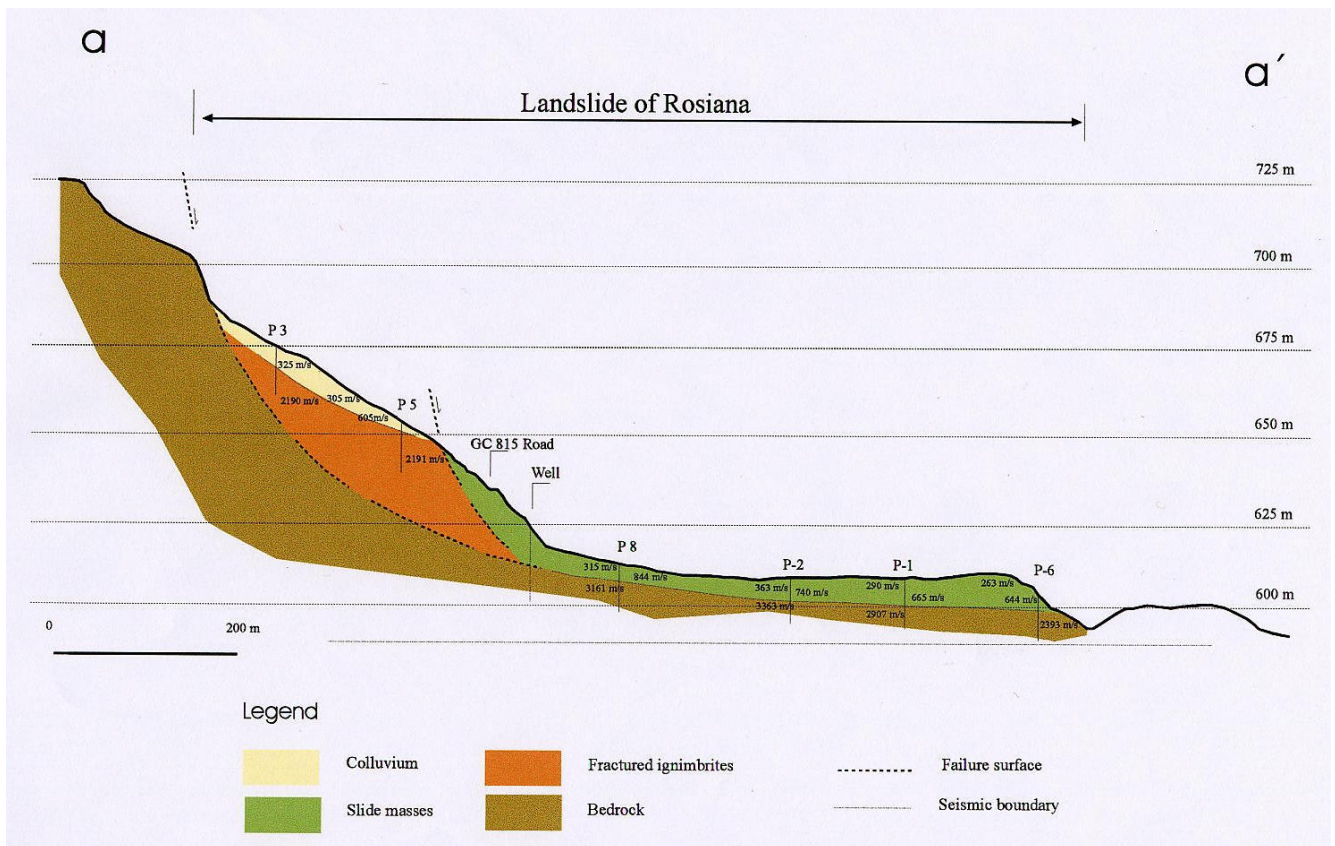


**Figure 3.** Interpretative a-a' seismic profile across the Rosiana landslide.

Three boreholes have been drilled into the Rosiana landslide. They are located in the mid-lower part of the landslide and they are 10, 13 and 20 m long. Three stratigraphic sections have been obtained but direct interpretation is not possible due to the variability in lithology and weathering of the materials (Figure 4). Within two boreholes a piezometer, extensometer and a data logger have been installed for periodic and continuous measurements (1 per 15 minutes) of the watertable level and displacements across the slide.

*Evaluation of the EDM geodetic network*

Since installation of a local EDM network across the landslide, repeated surveys have been undertaken using a TC-1610 Leica distance meter, Wild T2 theodolites and a GSS1 Sokkia GPS station (Chapter 11). The utm reference system was USED on the WG 584 ellipsoid. The main network (reference points) has 4 bench marks around the landslide, located on stable terrain, which are visible to each other. Twenty-four markers were put in the field (object points) according to the morphology of the landslide, providing seven traverses, both along and across the direction of movement. Planimetric sights were obtained by a combination of the polar and bisection methods from the four reference points to each marker. This methodology maximises reliable measurements and minimizes potential errors (Figure 5), yielding an accuracy of  $\pm 2$  cm the local topographic network as a whole. After calculation, only measured displacements greater than 2.8 cm can be interpreted as real movements.

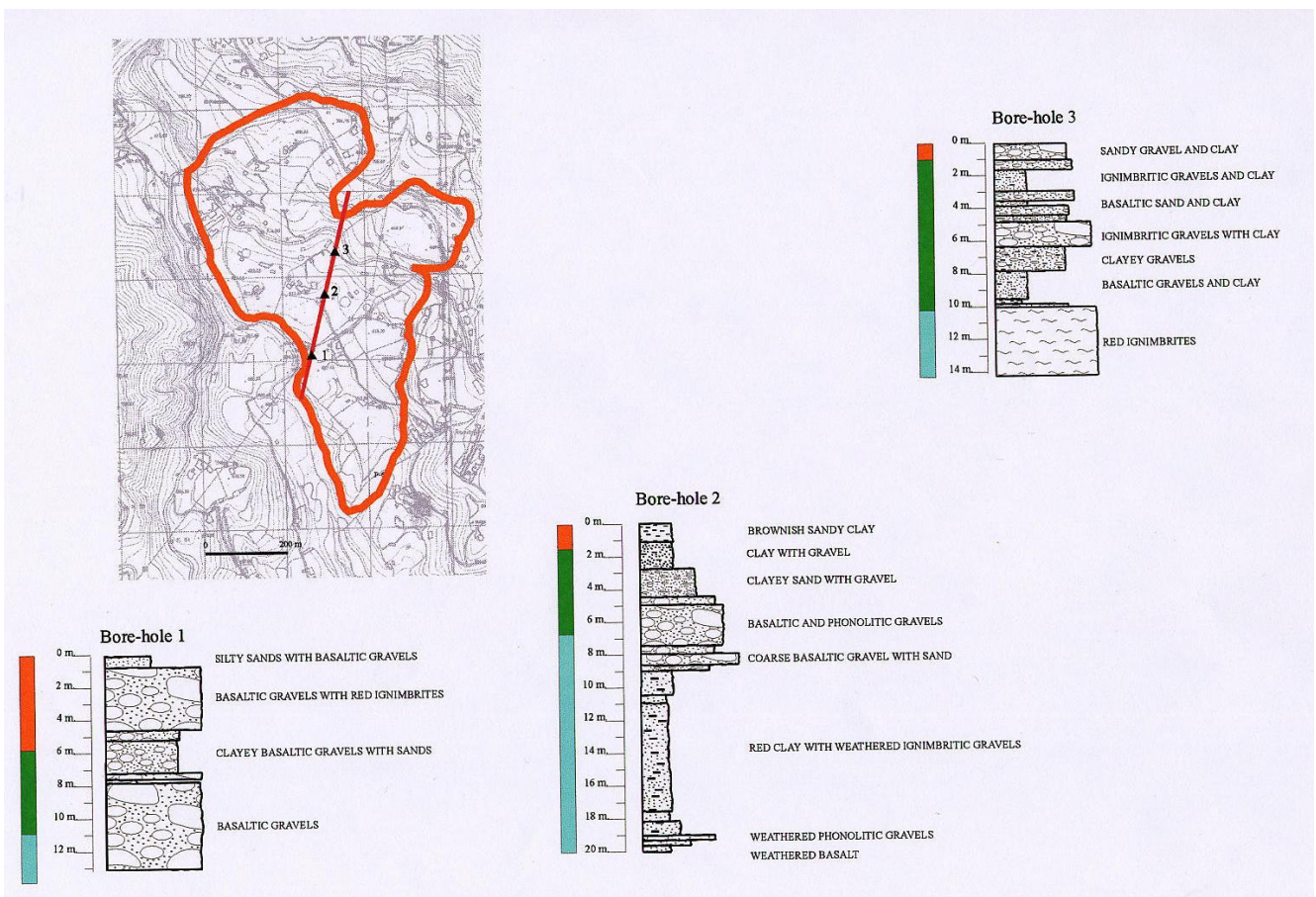


**Figure 4.** Location of the 3 bore-holes and their stratigraphic sections.

Four surveys have been conducted in April 1998, December 1998, May 1999 and December 1999. The time interval covered by these surveys included 2 rainfall periods (rainfall normally occurs between November and February). The results indicate no significant displacement of the landslide, in agreement with the static results obtained from the larger GPS network (Chapter 11). A fortnight per survey has been needed, one week for field work and another for calculations. Following recent modifications, it should be possible in future to detect displacements with an accuracy of  $\pm 2$  cm.

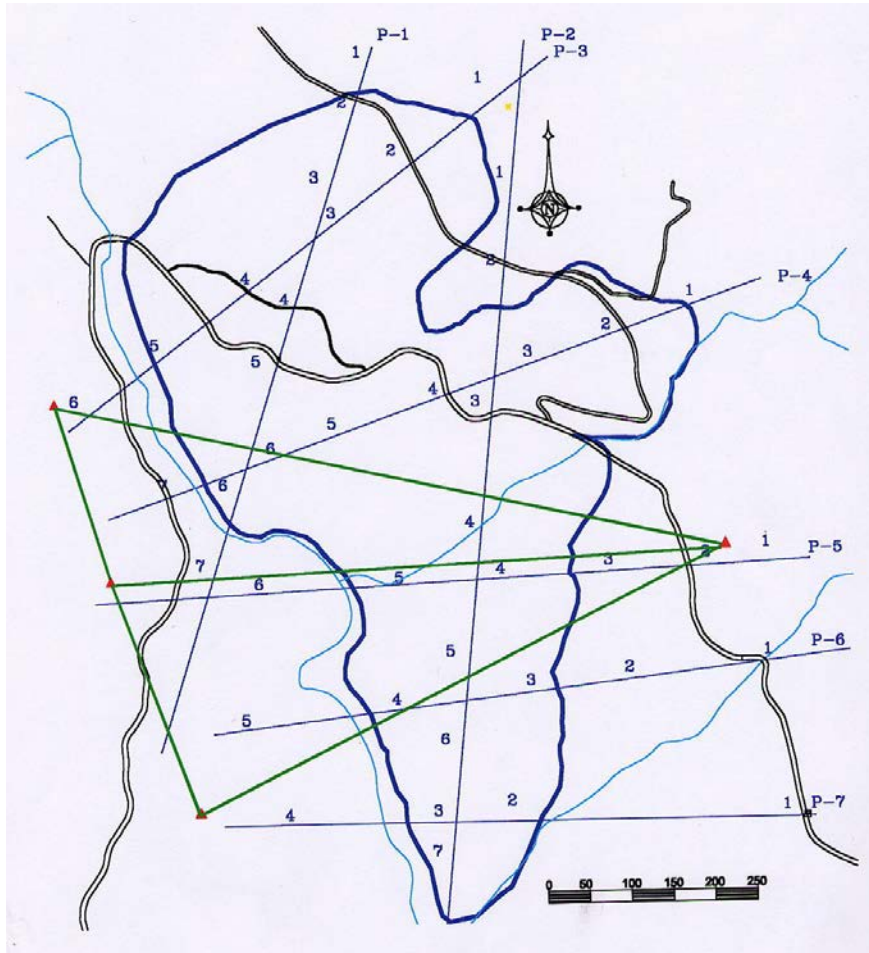


**Figure 5.** Local surveying network placed on the Rosiana landslide.  
P-1 to P-7 are the topographic profiles across the slide

### Conclusions

Although the Rosiana slide has been creeping at a mean rate of 1 cm per year since its last major reactivation in 1956, no significant displacements have been measured during the two years since installation of a new EDM geodetic network. This may reflect either that the current accuracy of the network is insufficient to record significant movements less than 2-3 cm, or that movement since 1956 has been episodic. Continued surveying should resolve this uncertainty. The slide remains potentially unstable when wet, indicating that hazard assessments in the medium term can be guided (a) by the expected return times of extended torrential rainfall, and (b) by the historical frequency of reactivation (4 times in 100 years). The latter factor alone suggests that the next reactivation may be imminent.

## References

- Lomoschitz A, Corominas J 1997a. La depresión de Tirajana, Gran Canaria. Una macroforma erosiva producida por grandes deslizamientos. Cuat Geomorf, 11: 75-92
- Lomoschitz A, Corominas J 1997b. Actividades histórica y características de los movimientos de ladera de Rosiana, Gran Canaria. Bol Geol Min, 108: 807-818.
- Macau F 1956. La muerte de un joven enfermo. Análisis de las causas de la destrucción del puente Rosiana en la carretera de Las Palmas a San Bartolomé de Tirajana (Gran Canaria). Rev Obras Pub, Madrid Nov 1956: 584-594.

## 10. The stability of episodically reactivated landslides: Stambach, Austria, and Tessina, Italy

### Introduction

The Tessina and Stambach landslides (Fig. 1; Chapters 6-8) are combined earth-and-debris flow systems that are prone to reactivation after collapses at their headscarps. Both landslides threaten Alpine communities (Bad Goisern below the Stambach landslide, and Funès and Lamosano by the Tessina landslide) and so it is essential for hazard mitigation to understand the conditions triggering reactivation. The geotechnical data obtained for each landslide are discussed in detail in Chapters 6 and 8. They are here used for comparative analyses of slope stability.

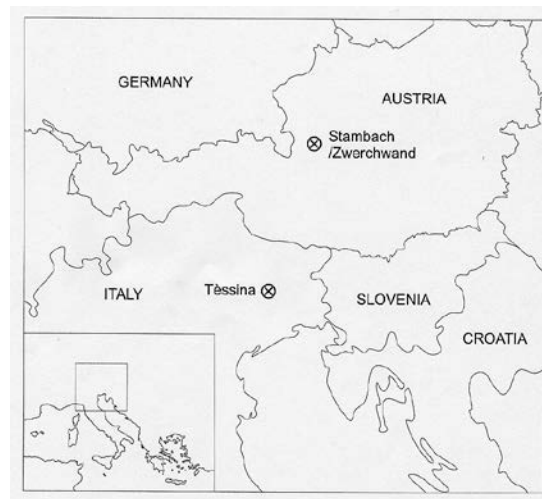


Figure 1. Location of the Stambach and Tessina landslides

Using the rock mass rating (RMR) method of Bieniawski (1974), the materials collapsing at the headscarps range from “good” and “very good” for Stambach to “poor” at Tessina. Independent from initial material conditions, however, the matrix of the debris that forms the bulk of each landslide has the geotechnical properties of a clay with *low to intermediate plasticity*. In particular, the Tessina matrix has remoulded cohesion values of 0-18.4 kPa and friction angles of 17.9-22.6°. The matrix thus behaves as a weak soil when remoulded and so is prone to re-activation during periods of high groundwater levels. The matrix also has low liquid limits of 41-44%, which means that it will behave as a fluid at relatively low moisture contents. Indeed, it is notable that even in summer the field moisture content of these soils was 23-36%, in excess of the plastic limit of 17-19%.

Matrix material in the Stambach landslide is stronger than that found at Tessina, and values for cohesion and friction angle lie in the ranges 6-31.9 kPa and 15.6-21.2°. Such values are consistent with a higher clay content than at Tessina. Plastic limits and liquid limits are 20-24% and 35-61% respectively and the field moisture content ranges from 18.1 % to 39.1 %. The higher strength of the Stambach matrix, combined with the higher liquid limits partly explains why re-activation of this landslide occurs less frequently than at Tessina.

Slope stability analyses based on the new geotechnical data suggest that both landslides are normally stable with high factors of safety. However, Monte Carlo simulations that incorporate the observed ranges of geotechnical data indicates that instability can be expected at high groundwater levels. At Tessina, movement patterns can be explained by the natural variation with water content in the shear strength of the soils. At Stambach, however,

intermittent movement requires the additional influence of head loading due to pillar collapse (Chapter 8).

### **Sampling strategy and sample analysis**

The aim of sampling during fieldwork was to obtain sufficient material to understand the geotechnical properties of the soils and rocks which form the landslide. The sampling strategy adopted can be divided into three stages

(1) Hand shear vane tests were undertaken at 200 m intervals along the length of both landslides, depending on outcrop availability with three readings being taken at each site. This led to 110 measurements being made along the length of the Tessina landslide, and 120 measurements along the length of the Stambach landslide. Use of this field technique enabled the collection of a large number of low-precision measurements of the shear strength of surface materials, thus allowing an estimate of the spatial variability of the strength of the soil down the track of each landslide.

(2) A sample was collected from each location to measure the moisture content. The shear vane results showed only a very weak correlation with the moisture content, which, given the normal relationship between water content and shear strength, tends to suggest that the readings taken of the surface materials were being strongly influenced by clods formed at the surface. The formation of clods is partly linked to wetting and drying. If soil particles had locked together to form larger aggregates of soil material (or *peds*), then these larger particles may be acting as a granular material. If this was the case, the moisture content observed within the clods would bear little relationship to the amount of water found between clods, as opposed to between soil particles.

(3) Six major samples of 20–50 kg were collected from each landslide. These were used to investigate the geotechnical properties of as nearly *undisturbed* material as was feasible given the condition of the landslide.

Care was taken to ensure that samples did not dry between collection and testing. Each sample was sealed within two plastic bags, which were then placed into a plastic container. The container was then topped up with clay, to which a few drops of water were added (as well as silicon sealant in the case of the major samples). The lid of the containers was then covered in tape and then sealed in a plastic bag. Structural information was recorded on 1:2,000 field slips, on sketch maps, and in a field notebook. In addition to general geological observations, attention was focused on joint patterns, water conditions and bedding relations. No evidence was found at either landslide of any stratigraphic inversions.

### **Laboratory analysis**

Laboratory tests were conducted to determine the *moisture content*, *Atterberg limits* (plastic limits, liquid limits and plasticity index), *particle size distribution* and *bulk density* of key samples. These index tests define the activity of clay-rich soil masses. Soil strength was determined from *direct shear* tests and *triaxial compression* tests. All tests were carried out in accordance with British Standard 1377 and with reference to Eurocode 7.

#### *The Atterberg limit test*

Tests have been undertaken on the major samples to determine the Plastic Limits (PL), using the cone penetrometer method and Liquid Limits (LL), in accordance with BS 1377 : Part 2 : 1990. The PL is the moisture content above which the sample behaves plastically and the LL

is the moisture content above which the sample behaves as a liquid, i.e. it flows under its own weight. From the PL and LL the Plasticity Index (PI) and activity index were calculated using the equations

$$PI = LL - PL \quad (1)$$

$$\text{Activity Index} = PI / (\% \text{ Clay}) \quad (2)$$

#### *Particle size distributions*

Particle size distributions were determined for the major samples. Samples were wet sieved and split into gravel, coarse sand, fine sand and silt-and-clay fractions. The fine grained components were differentiated using the hydrometer method in accordance with BS 1377, Part 2, 1990.

#### *X-Ray diffraction*

X-ray diffraction was carried out using a Phillips Diffractometer with a Cu  $\alpha$  radiation source. The intensity of the resulting diffraction patterns was written to disk and stored as an Excel worksheet. Standard diffraction patterns for common clay minerals were then overlaid on the trace and the clay minerals were identified. XRD was carried out on four sets of samples: (1) untreated samples; (2) samples treated with ethylene glycol to detect swelling clays; (3) samples heated to 300° C (which will cause the collapse of some common clay minerals, e.g. vermiculite); and (4) samples heated to 600° C (which will cause the collapse of all clay peaks except gibbsite and brucite).

#### *Direct shear testing*

The apparatus for the direct shear test is shown in Fig. 2. The test methodology is outlined in British Standard 1377 and only a brief summary is given here.

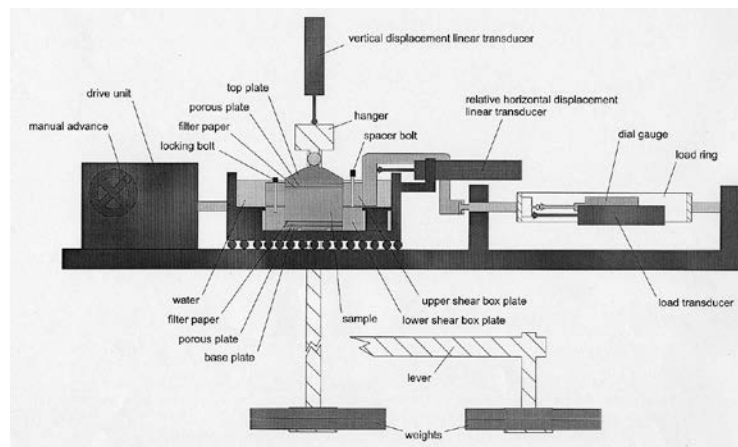


**Figure 2.** Direct shear test apparatus

The direct shear test involves samples being placed in a square, or in the case of rock core, circular steel box. Two stresses are then applied. The first is a normal stress applied through a vertical load. The second is the shearing stress which is applied through a gearing system which moves the split steel box. The lower half of the box is displaced, while the upper compartment remains stationary causing shearing along a known plane. The value of this test is that the stresses are easy to resolve, and the location of the shear plane is known.

Therefore, it is possible to test pre-existing shear surfaces. Unfortunately, it is difficult to monitor pore water pressure effects in samples.

Different normal stresses can be applied to the sample in order to calculate material cohesion and friction angle. With the application of different loading rates it is possible to test samples under *drained* (allowing pore water pressures to dissipate during testing) or *undrained* (not allowing pore water pressures to dissipate during shearing) conditions. These tests were carried out at shearing rates of approximately 0.04 mm/minute. This rate was chosen on the basis of the time taken for primary consolidation to occur when the initial vertical load is applied to the soil. This shearing rate can be assumed to be allowing the test to be carried out under drained conditions.

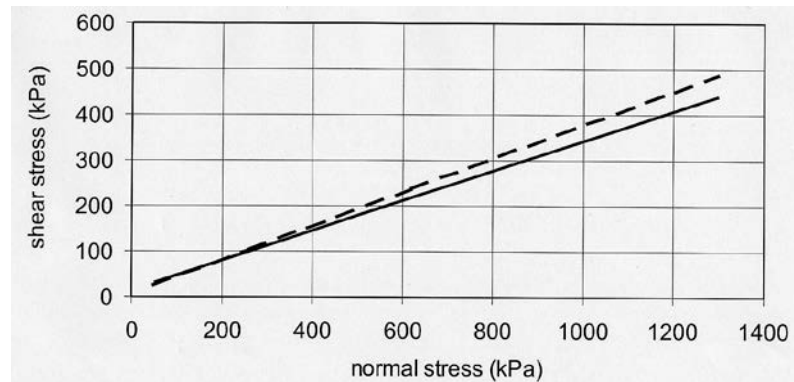


**Figure 3.** Mohr-Coulomb failure envelopes for the Stambach (*solid line*) and Tessina (*broken line*) landslides.

Two direct shear tests were used. The first used a sample with a cross sectional area of 60 mm x 60 mm, the second test setup has cross section dimensions of 305 x 305 mm. These two different experimental setups were used to allow for differences in stress conditions and particle size distribution in accordance with existing guidelines.

Samples were tested at normal stresses of 50, 260, 520 and 1300 kPa. These stress ranges were chosen in order to bracket the range of depths at which the landside shear surfaces are found. Figure 3 shows the Mohr-Coulomb strength envelopes derived from direct shear testing of samples collected during fieldwork. It can be seen that both soils show similar strength conditions. The data were used in the slope stability analyses described below.

**Table 1.** Comparative geotechnical data for the Stambach and Tesina landslides (see also Chapters 6 and 8)

<i>Property</i>	<i>Tessina</i>	<i>Stambach</i>
<b>Cohesion, <math>c'</math> (kPa)</b>	8.0	14.2
<b>Friction angle, <math>\phi</math> (<math>^{\circ}</math>)</b>	20.3	18.1
<b>Unit weight, <math>\gamma</math> (<math>\text{kN m}^{-2}</math>)</b>	19.7	19.5
<b>Factor of safety, F</b>	1.48	0.98 (20-m shear plane) 1.10 (40-m shear plane)
<b>Plastic limit (%)</b>	17.8	21.4
<b>Liquid limit (%)</b>	42.8	48.2
<b>Plasticity index (%)</b>	25.3	26.4
<b>Activity index (%)</b>	1.2	0.7
<b>Moisture content (%)</b>	27.5	37.3
<b>Mean clay fraction (%)</b>	25	30
<b>Particle <math>D_{60}</math> diameter (mm)</b>	0.02	0.06

## Comparative analyses

The mean geotechnical properties of the Tessina and Stambach landslides are shown in Table 1 and Figure 3 (further details can be found in Chapters 6 and 8). Compared with the Tessina material, the Stambach matrix is more cohesive and plastic, and has a higher clay concentration and moisture content.

Mineralogically, X-ray diffraction shows the presence of three clay groups: kaolinites, illites and members of the smectite group. Such components are consistent with observed matrix plasticity (Fig. 4): all the samples plot above the A-line (*i.e.*, they are inorganic rather than organic soils) and the majority lie in fields where the plasticity would suggest a mixture of montmorillonitic, kaolinitic and illitic minerals. Figure 4 also shows that while the Tessina samples cluster within a similar plasticity field, those from Stambach show a clear increase in plasticity with position downslope (from samples BG5a to BG2). As discussed in Chapter 8, the Stambach trend is consistent with the bulk downslope change in landslide behaviour from a debris flow to an earth flow.

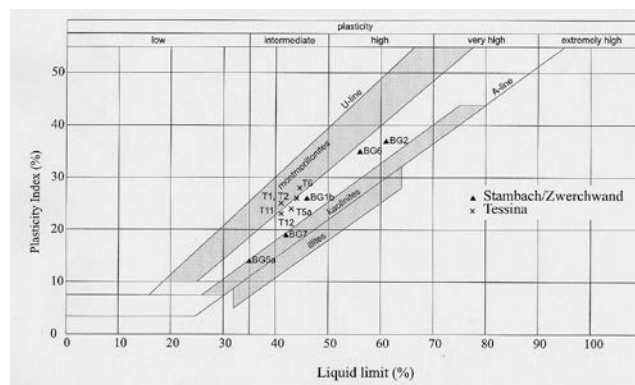


**Figure 4.** Variation of plasticity with clay composition for the Stambach and Tessina matrix material

## Slope stability: the infinite slope model

The stability of the Tessina and Stambach landslides were investigated using standard slope stability models. Both landslides lend themselves to the use of the relatively simple *infinite slope* model. This is one of a group of models used in slope engineering in which the stability of a potential landslide system is modelled as a rigid block sliding on a discrete shear surface. Such surfaces may be planar, circular or non-circular. These models are inherently deterministic in their approach (*i.e.*, single value inputs yield single value outputs). Although not ideal for discriminating *changes* in the spatial distribution of material properties, the infinite-slope model can be used to compare mean conditions and is easy to interpret.

In addition to approximating a landslide to a simple block, the infinite-slope analysis also assumes that (1) the shear surface is parallel to the ground, (2) the phreatic surface is parallel with the ground and flow orientation is in the downslope direction (*i.e.*, no seepage occurs), and (3) no interslice force calculations are necessary, since the landslide moves as a rigid block. The result of the model is a single value measuring slope stability, the Factor of Safety (F), which can be written for the failure plane as:

$$F = (\text{Shear strength})/(\text{Applied shear stress}) \quad (3)$$

From the Mohr-Coulomb failure criterium, the shear strength ( $\tau$ ) can be written as

$$\tau = c' + \sigma' \tan\phi \quad (4)$$

where  $c'$  is the cohesion,  $\phi$  is the angle of internal friction and  $\sigma'$  is the effective normal stress, given by

$$\sigma' = \sigma - u \quad (5)$$

where  $\sigma$  is the actual normal stress and  $u$  is the pore water pressure along the plane of failure.

Combining Eqs (3) to (5), the factor of safety can be expressed in terms of material properties as

$$F = [c' + (\gamma - m\gamma_w) z \cos^2\alpha \tan\phi] / (\psi z \sin\alpha \cos\alpha) \quad (6)$$

where  $\gamma$  is the unit weight of the material which forms the slope,  $\gamma_w$  is the unit weight of water,  $m$  is a pore water pressure coefficient ( $m = 0$  when the groundwater is at the shear surface and  $m = 1$  when it coincides with ground level),  $z$  is the depth to the shear surface and  $\alpha$  is the angle of inclination of the shear surface.

Using the values of cohesion, friction angle and unit weight in Table 1, factors of safety for the two landslides were estimated assuming a 'worst-case' scenario, that is incorporating the maximum expected values of water pore pressure (thereby maximising  $m$  in Eq. (6)). For the Tessina landslide, groundwater records relate mainly to boreholes in the flysch deposits surrounding the landslide, and have limited value in attempting to understand groundwater conditions within the landslide itself. However, field observation showed that (1) even when the surface of the landslide was dry and dessicated, standing water was evident in stream channels approximately 1 m deep, and (2) seepage could be observed from the flysch at the flanks of the landslide at an elevation of 1-2 m *above* the landslide mass. These observations suggest that the phreatic surface mirrors the ground, but is markedly at the location of the landslide. It was thus decided to model the water table using a triangular distribution, with the water table at 1 m below the surface. Few systematic data have been published for the Stambach landslide, and so the worst-case scenario was taken to be a water-table coincident with the ground surface ( $m=1$ ).

Results of the worst-case analyses (Table 1) yield factors of safety greater than 1, implying that both landslides are stable. Indeed, further parametric studies show that extreme conditions are necessary (Table 2) for either landslide to become unstable if it follows the infinite-slope model. Thus, instability at Tessina requires an elevated water table some 9-10 m above the landslide itself, while for the Stambach landslide, no realistic artesian condition can induce instability, so that an additional gravitational load is required to induce movement.

The infinite-slope model assumed that each landslide is geotechnically homogeneous and can be modelled with single values of the relevant strength parameters (Table 1). It is possible that the extreme conditions inferred for instability are false results caused by the neglect of spatial heterogeneities in landslide properties.

### **Modelling geotechnical heterogeneities**

To investigate the importance of geotechnical variations in slope movement, the stability analyses were repeated, substituting discrete values for the geotechnical data with *normal distributions* for the values of each parameter (Table 3; Mostyn & Li, 1993, Murphy, 1997). Depths to shear surfaces were not modelled in this way, as these are absolute values known from field investigation.

Distributions are used instead of point values to account for the potential variation in geotechnical properties around measured values (induced either by true variations or by measurement error). The assumption of a normal distribution is made for simplicity.

Although other distributions might be more appropriate, such information is not available for the Tessina and Stambach materials. The normal distribution, however, is suitable to investigate the potential influence of geotechnical heterogeneity on slope stability. Also for simplicity, a triangular distribution has been assumed for the water table.

**Table 2.** Shear-surface and water-table parameters used as input into slope-stability models

<i>Depth to shear surface, z (m)</i>	<i>Depth to water table, dw (m)</i>	<i>Shear surface angle, <math>\alpha</math></i>	<i>Factor of safety, F</i>
<b>Stambach</b>			
20	0	12.4	0.98
	5	12.4	1.13
	10	12.4	1.31
	20	12.4	1.68
40	0	9.7	1.10
	5	9.7	1.20
	10	9.7	1.32
	20	9.7	1.55
	30	9.7	1.79
	40	9.7	2.03
Triangular distribution for water table depths			
20	1	9.7	1.56
40	1	9.7	1.41
<b>Tessina</b>			
30	-10	8.0	0.99
	-5	8.0	1.21
	0	8.0	1.43
	5	8.0	1.65
	10	8.0	1.86
	15	8.0	2.08
	20	8.0	2.30
	25	8.0	2.52
	30	8.0	2.74
Triangular distribution for water table depths			
30	1	8.0	1.48

Monte Carlo simulations (10,000 iterations) were run to select values at random from the assumed normal distributions. As for the previous infinite-slope model, the water table was assumed to lie 1 m below the landslide surface. The results (Table 4) show ranges in calculated factors of safety of 0.95-1.28 for Tessina and 1.27-1.55 and 1.48-1.62 for failure planes at depths of 20 and 40 m within the Stambach landslide. Bearing in mind that factors of safety less than 1 correspond to failure and greater than 1.25 correspond to long-term stability, the simulations indicate that only at Tessina could geotechnical heterogeneity contribute to reactivating the landslide. Once again, remobilisation at Stambach must require the addition of a gravitational load.

**Table 3.** Characteristics of normal distributions assumed for geotechnical parameters

<i>Sample</i>	<i>Cohesion c' (kPa)</i>	<i>Friction Angle <math>\phi</math></i>	<i>Unit Weight <math>\gamma</math> (kN m<sup>-2</sup>)</i>	<i>Plastic Limit (%)</i>	<i>Liquid Limit (%)</i>	<i>Plasticity Index (%)</i>	<i>Activity Index</i>	<i>Moisture Content (%)</i>
<b>Stambach</b>								
<b>Mean</b>	14.16	18.12	19.52	21.40	48.20	26.40	0.73	37.34
<b>Standard deviation</b>	10.75	1.89	0.08	1.95	10.83	10.16	0.24	8.09
<b>Minimum</b>	5.30	15.60	19.40	20.00	35.00	35.00	0.35	18.10
<b>Maximum</b>	31.90	20.20	19.60	24.00	62.00	62.00	0.97	49.70
<b>Tessina</b>								
<b>Mean</b>	7.98	20.30	19.57	17.83	42.83	25.33	1.16	27.45
<b>Standard deviation</b>	9.11	1.92	0.14	0.98	1.47	1.75	0.72	6.23
<b>Minimum</b>	0.00	17.90	19.40	17.00	41.00	23.00	0.68	20.00
<b>Maximum</b>	19.80	22.60	19.80	19.00	44.00	28.00	2.60	49.40

**Table 4.** Minimum, maximum and average values for F calculated from the uncertainty in geotechnical data. The 10%-values give the factor of safety for which there is less than a 10% probability of F being smaller than this value.

<i>Factor of Safety, F</i>	<i>Stambach (20-m failure plane)</i>	<i>Stambach (40-m failure plane)</i>	<i>Tessina</i>
<b>Minimum</b>	1.27	1.48	0.95
<b>Maximum</b>	1.85	2.12	3.00
<b>Mean</b>	1.55	1.79	1.75
<b>10% value</b>	1.40	1.62	1.28

## Conclusions

If the geotechnical properties of the soils and rocks are considered in isolation, there is little to suggest that these two large volume slope failures are anything unusual. Each landslide has a debris component with a significant fraction of clay in its matrix. Both landslides are therefore cohesive in nature, they are of low to intermediate plasticity, and within the sliding mass, they are generally at residual-strength conditions. As expected, they also show considerable variability in their strength parameters.

The Tessina landslide is activated by changing groundwater levels within the landslide mass. The properties of the soil materials are well understood, and the risk of reactivation can be readily established with a more detailed understanding of the variation in the geotechnical properties of the rocks and soils comprising the main slope units. The principal problem associated with the initiation of movement is the route by which water enters the upper part of the slope. It is clear that groundwater is fed from the limestone aquifer; however the hydrogeological interaction between the tectonically-juxtaposed limestone and flysch is complex. This interaction makes it difficult to predict movements of the flysch rock mass at the upper portions of the slope at Tessina, and since there is clear evidence that these rotational rock slope failures can give rise to reactivation of the debris flow component of the landslide (Chapter 6), understanding the link between hydrogeology, the limestone-flysch boundary conditions and the changes in pore water pressure are vital.

The geotechnical evidence shows that the landslide is the result of a poor rock mass which was *probably* reactivated at what was initially believed to be the time of first movement in 1960. Geomorphological evidence of the slopes along the mountain front suggests that a series of rotational landslides exist, which may be reactivated by construction. The debris flow component is composed of low plasticity clays with a significant proportion of coarse grained materials. Strength parameters give a range of values with mean cohesion and friction angle of 7.1 kPa and 20°. Slope stability analysis suggests that the landslide mass is stable except under conditions when the phreatic surface is very close to the ground. Since the hydrogeology of landslides is a complex issue, *in situ* piezometers within the landslide mass may give short term forecasts of landslide re-activation on the basis of groundwater changes fed from the limestone aquifer. Since extensive monitoring is currently in place (Chapter 6), it seems unlikely that further monitoring equipment would significantly reduce the hazard from this landslide. It is also unlikely that an engineering solution could be found easily to stabilise the landslide at Tessina because of the hydrogeological properties of the limestone massif found at the back of the landslide.

The Stambach landslide is a different situation. Compared with Tessina landslide, movements along the landslide threatening Bad Goisern remain poorly understood. At least two dynamic components have been recognised. Firstly, there is the rockfall component from the crown of the landslide. This would normally reactivate a debris flow type landslide on the basis of head loading and undrained loading. With the Stambach landslide, however, these are not necessarily sequential events. After the rockfalls of 1980 and 1981, reactivation of the debris flow section of the landslide did not occur until 6 and 10 months later. This delay suggests the action of some other process ongoing apart from simple head loading or undrained loading. As discussed in Chapter 8, the delay may reflect the time to equalise negative pore-water pressures induced by pillar collapse, or it may simply reflect the earliest time after collapse when precipitation has raised pore-pressures sufficiently to induce movement. In either case, loading by pillar collapse is a prerequisite for reactivating the landslide. Stabilisation of the headwall might thus significantly reduce the landslide hazard (Chapter 8).

## References

- Bieniawski, Z. T. 1974. Geomechanics classification of rock masses and its application to tunnelling. *Proceedings of the Third Congress of the International Association of Rock Mechanics*, Denver, Colorado. **2-A**, 27-32.
- BRITISH STANDARD 1377, 1990. British standard methods of test for soils for civil engineering purposes. Part 2. Classification tests. British Standards Institution, London.
- Mostyn, G. R. & Li, V. S. 1993. Probabilistic slope analysis - state of play. In: Li, K. S. & Lo, S. C. R. (Eds) *Probabilistic Methods in Geotechnical Engineering*, 89-110, Balkema, Rotterdam.
- Murphy, W. 1997. Sensitivity of palaeoseismological estimates derived from landslides to variations in geotechnical and geological inputs. *Journal of the Geological Society of China*, **40**, (1), 185-208.

## 11. Surface Deformation Monitoring using rapid static GPS

### Introduction

GPS ground-deformation networks have been established around two potentially active landslide areas: the Barranco de Tirajana (BdT) in Gran Canaria (Chapter 9) and Tessina in the Italian Alps (Chapter 6). The new networks augmented the existing small-scale EDM networks that were already established at the sites and provided information on: (1) ground deformation in a wide area around each site, and (2) the application of GPS to a small semi-permanent dynamic network. Each network was installed in 1998 and then re-occupied twice to assess annual and bi-annual displacements. The results revealed two very different deformation rates. The BdT appears inactive, results showing no coherent deformation which may be attributed to landsliding. The Tessina valley, in contrast, is very active with as much as 9 m of deformation occurring during the period of investigation. Both networks provide a baseline from which future deformation may be measured, and station descriptions are given on the accompanying CD ROM.

### The Barranco de Tirajana landslide

The GPS network was successfully established using the International GPS Service benchmark in Maspalomas as a fixed point. During the measurement of the network, however, there was a persistent problem with multipath errors. This is an external problem with GPS whereby satellite signals are received by the ground antenna from both a direct source and via reflective surfaces adjacent to the instrument. In addition, the high cliffs surrounding the basin, block signals and reduce satellite coverage. This was further hampered by a poor orbital coverage over the Canary Islands during a one-hour period of the day, when only 3 or 4 satellites were visible.

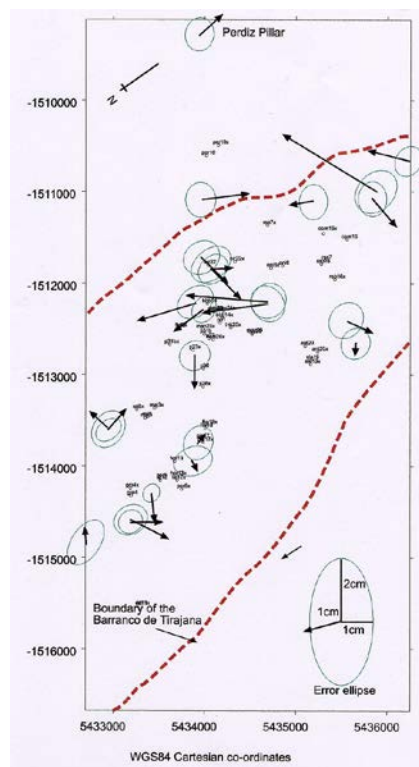


**Figure 1.** Vector displacements in the Barranco de Tirajana GPS network between November 1998 and April 1999.

The measurement procedure uses a predominately radial approach with Hot13 as a primary reference station. The network was then subsequently reinforced by using other survey stations as reference stations for secondary occupations. The vector changes between November 1998 and April 1999 are illustrated in Figure (i). The vector displacements recorded do not reveal any coherent patterns of displacement, which may be attributed to real displacements. Although the vector changes are above the expected 10 mm, the poor repeatability is interpreted to be a result of the extensive multipath experienced. The EDM data (Chapter 9) concur with these findings and confirm the inactivity of this landslide. The results indicate that the BdT is not currently undergoing active landsliding. However, the results do not preclude the possibility of landslide reactivation, especially at the most recently active Rosiana landslide (Chapter 9)

### **Ground deformation monitoring of the Tessina landslide, Italy**

The Tessina valley is situated in the Chies d'Alpago region of north-east Italy, 80km north of Venice (Chapter 6). The area is in the pre-Dolomites, the dominant geology comprise mainly weak layers of limestone and clays, Flysch, glacial moraines and screes. Figure 2 illustrates the location of the Tessina Valley and the city of Graz in Austria where a fixed GPS benchmark is used to locate the network.



**Figure 2.** The location of the Tessina Valley

### **A brief introduction to the landslide area.**

The Tessina landslide is a complex landslide, divided into an upper rotational slide and a lower recurrent mudflow. The upper section extends from 950m to 1150m; the arced head of the landslide divides into multiple rotational slides (Fig. 3; Chapter 6). The edges of the scarp can be divided into eastern, central upper and western areas, a classification that reflects

distinct magnitudes of deformation recorded over the area (Chapter 6). A small buttress that forms the eastern boundary of the primary major landslide in 1960 divides the western and eastern sections. The rotational landslides form around the detaching zone. There are numerous small scarps (0.5-2m) which are the head walls of multiple small rotational collapses. They are activated by high rainfall that saturates the clay layers within the Flysch formation, increasing pore fluid pressures. These separate bodies descend into the upper accumulation zone where the amassed material is mobilised by the active spring forming mudflows which continue downwards through the connection canal. By measuring the deformation of the ground within and around the landslide, this study seeks to distinguish the discrete lobes around the apparent landslide, and to examine different rates of deformation around the perimeter of the disturbed ground within the known landslide.



**Figure 3.** The eastern wall of the headscarp of the Tessina landslide.

### **Existing ground deformation networks**

The reactivation of the Tessina landslide in 1990 and 1992 threatened the villages of Funes and Lamosano and destroyed the Funes-San Martino road. When the landslide is next activated there will be a number of warning signs. The most obvious will be the detachment of the upper parts of the landslide, and the slow or rapid rotational of the scarps. Once the scarps have been dislocated and displaced into the upper accumulation zone, the material will then be reworked and transported as a mudflow towards the villages and roads below. As a response to this threat, an Electronic Distance Measurement (EDM) network was established to measure the initial ground deformation around the unstable upper flanks. The network comprises 20 EDM reflectors located within the Upper Accumulation and the Detaching Zones; these zones are defined and explained by Mantovani *et al.* (1999) and discussed below.

The automated EDM is stationed to in the southeastern part of the Detaching Zone, within a purpose built hut. The reflectors are situated around the fractured crown of the main scarp and within the active scarp itself. They are however, predominately located in the Eastern sector of the zone, this is because of line-of-sight restrictions from the automated EDM to the upper central and western parts of the landslide. The rates of deformation that have been recorded vary depending on rainfall. Periods of high rainfall often proceed intervals of greater displacement and instability. The area covered by the EDM network is divided into three displacement categories;  $>1\text{m/yr.}$ ,  $>10\text{cm/yr.}$  to  $<1\text{m/yr.}$  and  $<10\text{cm/yr.}$  (Mantovani *et al.*, 1999). The most mobile area is within the centre of the Upper Accumulation Zone; this is the source of a number of springs. The edge of the central zone is characterised by disturbed ground; featuring stepping scarps and steep slopes. This area experiences between  $>10\text{cm/yr.}$  to  $<1\text{m/yr.}$  of displacement, reflectors in this area record the fracturing and displacement of the crown of the landslide. The zone which experiences the lowest levels of displacement is situated within and just beyond the fractured crown of the landslide, there are only two EDM reflectors in this area as trees inhibit the line-of-sight

required between the EDM and the signal reflector. The network is measured from a single location on the western edge of the main scarp of the landslide, within the Detaching Zone. Although the western edge of the scarp is visibly more stable than the eastern edge, the actual stability is not measured. The location of the permanent housed EDM means that it can only 'see' stations on the eastern edge of the landslide. The Global Positioning System network aims to overcome these problems through the combination of a *dynamic ground deformation network* (Moss, in press) with the automated EDM.

### **The role of the Global Positioning System network**

A *dynamic ground deformation network* is an array of semi-permanent survey stations located within an unstable area. A detailed explanation of the Global Positioning System (GPS) is given below. The fundamental defining characteristic of a dynamic ground deformation network is that the area under investigation is an unstable environment that may be undergoing continuous or near-continuous ground displacement. Flexibility is built into the network through the use of cheap and readily available, semi-permanent survey station markers such as metal rods or survey nails. The consequent versatile nature of the network enables it to expand and develop as the terrain undergoes alteration. Although prevalent opinion recommends the use of permanent concrete survey pillars for precise GPS surveying (Hofmann-Wellenhof *et al.*, 1997), extensive studies have found that the set-up accuracy of semi-permanent survey station is only 2-4mm when using a fixed tripod and tribrach mount. This is therefore suitable for rapid-static surveying (Moss *et al.*, 1999; Moss, In Press). As the survey markers are small, detailed site descriptions and three-dimensional co-ordinates are used to locate the survey stations for each occupation. The primary goal of the GPS survey is to extend and compliment the existing topographic network. Since GPS is not limited by line-of-sight to adjacent survey stations, the GPS network will extend into the area directly beyond the current EDM network. The EDM network is limited by the line-of-sight required between the instrument and the reflector. Therefore the EDM network is only located within the eastern part of the landslide and the reflectors are positioned in front of the line of trees which edge the active scarp.

The specific aims of the GPS study were therefore to (1) identify the current boundary of the active landslide, (2) to determine the rates of deformation zone directly beyond the detaching zone, (3) to detect any deep-seated structural mechanisms responsible for the slope displacement, and (4) to establish a baseline topographic network from which to measure future deformation. These aims were achieved by the installation of a broad GPS network. This entailed the establishment of survey stations within detaching area, beyond the fractures at the crown of the landslide and along the flanks. This extends the measurement of ground deformation to each side of the landslide and further back over 100m from the current edge. The occupation of the survey stations was undertaken three times in July 1998, July 1999 and November 1999. These enabled annual and bi-annual rates to be compared to the daily and monthly rates measured using the EDM. This periodic reoccupation of survey stations determined survey station velocity and azimuth of displacement. The comparison of EDM data from the detaching area with GPS data enabled re-evaluation and subdivision of <10cm deformation zone determined by Mantovani and co-workers (1999).

### **GPS data collection and analysis**

The Global Positioning System is a satellite positioning system used to locate unknown positions on the surface of the Earth. Detailed descriptions of GPS data collection and processing may be found in Hofmann-Wellenhof *et al.* (1997). In simple terms, GPS locates an unknown survey point on the Earth's surface by calculating the distance or range from the satellite-signal receiver located at the unknown survey point, to a number of satellites located

along known orbits. The range between the satellite and the receiver is measured by comparing the departure time of a satellite-transmitted signal with the arrival time at the ground-based receiver. The exact length of the signal is calculated and the times are compared. As the distal point of each satellite range forms a spherical contour extending from the satellite, the three dimensional point is identified by combining the ranges of four different satellites, so the point is identified by the meeting point of the four spheres.

The principal task of the GPS software is to measure the number of full and partial wavelengths between the satellite and receiver and the time taken for the signal to travel. The biggest sources of error are due to satellite and receiver clock errors and the inaccurate measurement of the remaining fraction of the wavelength. Processing therefore primarily seeks to calculate these sources of error and remove them from the data. As outlined above, four satellites are required for a point position; therefore, if two receivers observe four common satellites then the satellite clock offset can be determined by comparing the ranges from both receivers to each satellite. Furthermore receiver clock offsets can be derived from comparing the ranges from each satellite to the pair of receivers; this is called *double differencing*. Further ambiguities to both the satellite and receiver are cancelled by examining the common ranges in successive epochs.

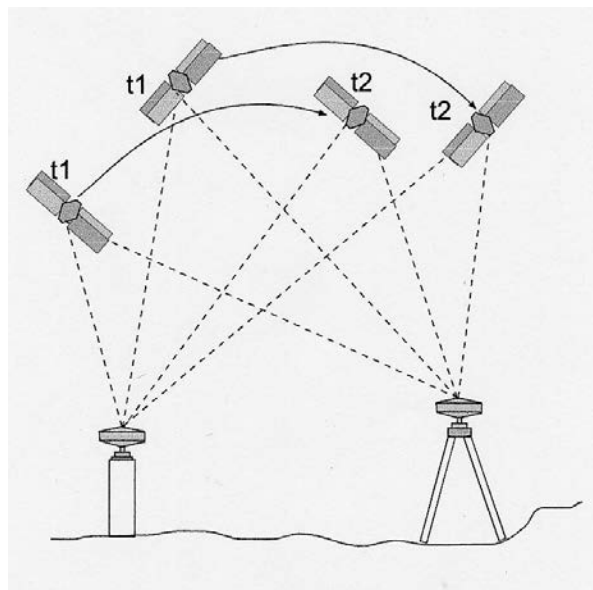


**Figure 4.** GPS receivers tracking common satellites for 2 epochs

The receiver compares the received satellite signal with a receiver generated duplicate signal; this identifies the satellite number, its position and the number of signal wavelengths. There are two main types of processing using the signal code and its carrier phase, these use the binary modulation of the carrier wave and the cycle of the wavelengths respectively. Phase solutions are used in precise positioning and are accurate to approximately 5-50mm depending upon measuring conditions.

### **The Global Positioning System: rapid static and static GPS**

The GPS surveying method employed was the rapid-static or fast-static technique. The aim of rapid static GPS surveying is to measure the network in a short time to a high accuracy. The technique uses two or more GPS receivers, where one receiver is located at a known survey station as the *reference receiver* and the others move around the network occupying unknown survey stations as the *rover receiver*. The use of more than one receiver allow double

differencing (see above and relative positioning to be undertaken. Relative positioning locates an unknown site relative to a known stationary reference site. The range is may be calculated exactly, calculating the difference between the range and range plus errors gives the errors which can be used to find the exact range to the unknown position.

The use of rapid static GPS differs from static GPS in that the occupation times for the *roving receivers* is very short (5-20 minutes for baselines less than 10km) as opposed to 60-120 minutes for static GPS. This allows a large number of survey stations to be measured in a short time. Precise geodetic surveying using high precision GPS receivers is accurate to approximately to 10mm+ 1ppm for rapid-static GPS under optimal conditions. Set-up errors and the environmental influences such as multipath or tropospheric variations degrade the accuracy of GPS in the field. The application of the rapid static technique can therefore further degrade the accuracy to approximately 10-15mm  $\pm$  3ppm. In order for an occupied survey stations to be used as reference stations they should ideally be occupied at least twice, this is undertaken during the first few days of the survey when the reference station is being fixed. The reference stations used for the duration of the survey need only be stable for the duration of the survey and can be chosen for their accessibility, radio contact and safety.

## **Establishment of the Tessina network**

### *Preliminary reconnaissance*

Before the network can be installed, the area is assessed by a detailed reconnaissance. The reconnaissance commences with the examination of topographic and geomorphologic maps of the Tessina area to determine the nature and extent of the unstable region. Then the land-use and road network are considered to determine the accessibility of the area and to ascertain if there are any major natural or man-made features such as buildings, trees or radio antenna which would impede the use of GPS. Taking into account these factors, the optimal locations for survey stations are marked on the map and the site is visited for a ground reconnaissance. Each GPS site requires a good sky view for maximum satellite coverage, however a site with poor sky view may still be used where at least four or five satellites may be observed. The site also needs to be at least five metres from elevated metal structures such as pylons, chain-link fences or corrugated iron roofs, or tall trees, in order to minimise multipath. The survey station marker is then installed; the type of marker depends upon the soil and rock type. If there are no stable suitable rocks then a long metal rod, at least one metre long is hammered into the ground with about two to five centimetres showing, the rod is then marked using luminous orange tape. These rods remain firm and give a good indication of shallow soil motions in addition to larger deeper measurements. Once the station is installed then a site description is completed with bearings to prominent features and paced or taped measurements (if necessary with bearings) to adjacent rocks and trees.

### *The Tessina Network*

The GPS network was installed in the Detaching and Upper Accumulation Zones defined by Mantovani and co-workers, and approximately 500-1000m directly beyond the edge of the landslide. Around the perimeter of the detaching zone, the blocks and margin most likely to fail are bounded by young cracks, and many of the EDM reflectors are located within the cracked area. The GPS stations are located within this peripheral area and beyond where co-workers have identified further cracks and are unable to position EDM reflectors.

The first stage of survey stations occupation is to fix a base station for the duration of the survey. As post-processing is undertaken to locate the position, the precise WGS84 coordinate of the initial reference is not required at the outset, and rover receiver occupation is undertaken from the outset. For the establishment of the network the initial base station was located in the village of Funés (at survey station ffb1). The reference receiver was positioned

at this location for four days of the campaign. The rapid static technique is applied to occupy each of the survey stations in the network, in order to obtain sufficient data to position the receiver; it must occupy the site for around ten minutes observing the same satellites as the reference receiver. Once the rover occupies a survey station it can then be used as a reference point. Each survey station is measured at least twice; this provides redundant measurements for network adjustment. By occupying each survey station using reference survey stations from different parts of the network, separated by a large horizontal angle, a more statistically acceptable network adjustment is achieved. Since the network is measured during a short time period any survey station of the network may be assumed to be stable. There are 20 survey stations in the GPS network, their type, location and approximate height is listed in Table 1. Location maps are given in Chapter 6 and on the accompanying CD ROM.

**Table 1.** Survey station type and location.

<i>Survey Station</i>	<i>Date first measured</i>	<i>Type</i>	<i>Zone</i>	<i>Height (m) asl</i>
<b>Thy1</b>	1998	nail	Detaching	1132
<b>sws2</b>	1998	nail	Detaching	1225
<b>ffb3</b>	1998	rod	Stable	876
<b>smw4</b>	1998	nail	Stable	835
<b>bwm5</b>	1998	rod	Beyond Upper Accumulation -Detaching	1022
<b>sal6</b>	1998	rod	Detaching	1126
<b>dan7</b>	1998	rod	Detaching	1148
<b>chg8</b>	1998	rod	Detaching	1187
<b>rfc9</b>	1998	rod	Detaching	1191
<b>vri10</b>	1998/dead	nail	Lower Accumulation Zone	872
<b>edm11</b>	1998	pillar	Edge of Upper Accumulation -Detaching	1042
<b>wtr12</b>	1998	nail	Detaching	1124
<b>sps13</b>	1998	rod	Detaching	1108
<b>mag14</b>	1998	rod	Detaching	1149
<b>cab15</b>	1998	rod	Edge of Upper Accumulation -Detaching	1081
<b>fgy16</b>	1998	rod	Edge of Upper Accumulation -Detaching	1059
<b>des17</b>	1998	rod	Detaching	1183
<b>lvp18</b>	1998	rod	Detaching	1159
<b>top19</b>	1998	rod	Above Detaching	1258
<b>lam20</b>	1998	nail	Stable	699
<b>dob21</b>	1999	pillar	Edge of Upper Accumulation - detaching	1042
<b>ars22</b>	1999	pillar	Stable	699

The network was measured in July 1998 and the re-occupied in July 1999 and October 1999. One survey station was lost in 1999; this was vri10 situated in the Lower Accumulation Zone. This was lost due to a reactivation of the landslide in spring 1999 (Mantovani, this report). Two new surveys stations were measured in 1999 these were both pillars and provided extra control for two important survey stations; dob21 and ars22. Dob21 is situated near to edm11, these are both used a extra instrument survey stations for the EDM network, ars22 is situated near the principal stable survey station smw4 and provides a second stable position to verify the stability of smw4. In October 1999 a final survey was undertaken in order to confirm changes noted between July 1998 and July 1999 and to estimate if the rates of movement are gradual or episodic, since if displacements are episodic then the shorter time between occupations should reveal a proportional magnitude of displacement.

### *Determination of the network co-ordinates*

A detailed explanation of the GPS data processing is beyond the scope of this paper; Hofmann-Wellenhof et al. (1997), Blewitt (1997) and Moss (1999) describe the methods further. At each site, the receiver set-up information is checked and the data are examined for breaks in signal reception or a lack of data from common satellites between the reference and the rover receivers. For each session (6-8 hours), the data are processed using a combination of code and phase processing to produce an L1 code fixed double difference solution, the whole network is then combined in a network (least squares) adjustment.

The first stage of processing for the initial July 1998 data set is to locate the initial starting position of the primary reference. ffb3 was chosen due to its suitability as a base station as it is located away from the active area in an easily accessible location, with good sky-view and within radio-range for communication between the reference and rover receiver groups. The co-ordinates for ffb3 are obtained by static processing with a known fixed GPS reference benchmark located in Graz, Austria. The satellite data from GRAZ is freely available on the Internet from the Crustal Dynamics Data Information System. Data from Graz are downloaded; the GPS data correspond with the time intervals of the Tessina data occupations. The Graz data are then processed with the data from ffb3 by differential static processing, using SKI (Leica). Only one survey station is used as this was maintained as the principal base station during the campaign, the long occupation sessions enable a good static position to be calculated. The GPS data collected during the survey are processed using the precise ephemerides; this eliminates variations from the predicted satellite orbit that may have occurred during the campaign. The co-ordinates obtained for ffb3 from each of the occupation session are compared and an average position and height is attained. Figure 5 illustrates the positional and height variations measured during the five sessions between ffb3 and Graz.

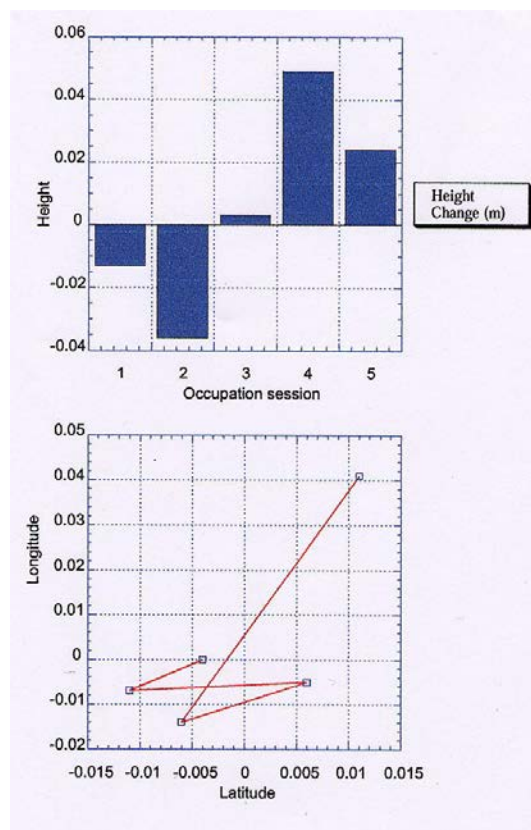


**Figure 5.** Variation in the position of ffb3 measured from GRAZ.

The position for ffb3 obtained by measurements with Graz is then held fixed in position and height, thereby allowing the differential processing of the rover occupations of the survey. SKI software from Leica is used to process the data; where a survey station has been measured more than once; a mean value is displayed. In order to examine the accuracy of the network, a least squares network adjustment is undertaken, this is the best value obtainable from a set of measurements of equal precision.

The July 1998 dataset is illustrated in Table; it may be statistically assumed that the coordinates obtained are accurate to the extent of these values. The error ellipses and its azimuth are a function of the network geometry; an elongated error ellipse indicates a skew in the measurement in either height or horizontal position.

**Table 2.** 90% error ellipse values for July 1998

<i>Point</i>	<i>Semi major axis</i>	<i>Azimuth</i>	<i>Semi minor axis</i>	<i>Height</i>
<b>bwm5</b>	0.0090	18.7	0.0077	0.0158
<b>cab15</b>	0.0118	166.4	0.0078	0.0194
<b>chg8</b>	0.0085	163.7	0.0062	0.0115
<b>dan7</b>	0.0068	171.4	0.0047	0.0112
<b>des17</b>	0.0085	151.5	0.0069	0.0161
<b>edm11</b>	0.0099	147.5	0.0085	0.0194
<b>fyg16</b>	0.0139	178.9	0.0097	0.0188
<b>lam20</b>	0.0140	86.9	0.0119	0.0241
<b>lvp18</b>	0.0100	168.5	0.0087	0.0191
<b>mag14</b>	0.0100	8.1	0.0067	0.0195
<b>rfc9</b>	0.0075	155.1	0.0062	0.0141
<b>sal6</b>	0.0094	176.8	0.0070	0.0141
<b>smw4</b>	0.0057	24.7	0.0052	0.0141
<b>sps13</b>	0.0080	8.1	0.0067	0.0144
<b>sws2</b>	0.0100	173.4	0.0093	0.0196
	0.0100	178.4	0.0078	0.0203
<b>top19</b>	0.0129	3.9	0.0093	0.0185
<b>vri10</b>	0.0118	11.8	0.0073	0.0170
<b>wtr12</b>	0.0066	5.3	0.0056	0.0130

The data from July 1999 were processed using the stable survey station smw4 as fixed in order to marry the July 1998 and July 1999 datasets. Graz was not held fixed since the measurement of six stations of the network proved too inconsistent, to fit within the geometry of the network. One interpretation may be differences in the phase centre of the two antenna, as this was not modelled. Comparisons were made using both Graz data and a fixed point within the network and it was decided to use smw4. The 90% error ellipse values for July 1999 are illustrated in Table 2.

The dataset from October 1999 was processed using Graz as a fixed control point, Graz was incorporated into the network using simultaneous occupations of Graz and Smw4, thy1, ffb3 and wtr12, these points were then processed within the rest of the network to obtain a network solution. These calculations are illustrated in Figure 6.. The error ellipses from the least squares adjustment are listed in Table 3. The poor repeatability of des17 is explained by soft spongy ground around the survey marker. In agreement to the first two surveys poor height and lateral positioning was again recorded for cab15 and fyg16, this is due to adjacent tall trees which limit sky view.

**Table 2.** 90% error ellipse values for July 1999 dataset

<i>Point</i>	<i>Semi major axis</i>	<i>Azimuth</i>	<i>Semi minor axis</i>	<i>Height</i>
ars22	0.0120	164.6	0.0115	0.0257
bwm5	0.0117	3.8	0.0084	0.0160
cab15	0.0169	2.8	0.0105	0.0228
chg8	0.0089	174.8	0.0058	0.0119
dan7	0.0123	178.9	0.0081	0.0167
des17	0.0144	166.6	0.0094	0.0241
dob21	0.0349	139.2	0.0160	0.0489
edm11	0.0274	125.7	0.0152	0.0487
ffb3	0.0060	167.4	0.0054	0.0117
fyg16	0.0142	136.9	0.0117	0.0251
lam20	0.0098	176.0	0.0074	0.0189
lvp18	0.0103	162.3	0.0084	0.0180
mag14	0.0135	133.7	0.0073	0.0182
rfc9	0.0120	169.9	0.0074	0.0157
sal6	0.0136	165.2	0.0098	0.0213
sps13	0.0107	157.1	0.0071	0.0141
sws2	0.0128	168.8	0.0087	0.0182
thy1	0.0093	165.4	0.0061	0.0130
top19	0.0123	178.1	0.0091	0.0221
wtr12	0.0098	167.8	0.0061	0.0127

**Table 3.** 95% error ellipses from October 1999.

<i>Point</i>	<i>Semi major axis</i>	<i>Azimuth</i>	<i>Semi minor axis</i>	<i>Height</i>
ars22	0.0135	140.4	0.0127	0.0234
bwm5	0.0092	44	0.0086	0.0155
cab15	0.023	18.7	0.0183	0.0358
chg8	0.0119	15.9	0.0101	0.0179
dan7	0.0153	160.9	0.0134	0.0237
des17	0.0424	7.9	0.0243	0.0477
dob21	0.023	162.8	0.0168	0.0353
edm11	0.0226	169.5	0.0163	0.0352
ffb3	0.0094	19.3	0.0091	0.0144
fyg16	0.0236	45.6	0.0181	0.0432
lam20	0.0147	172.7	0.012	0.0245
lvp18	0.0205	168.4	0.0137	0.0291
mag14	0.011	0.3	0.0095	0.0163
rfc9	0.0109	6	0.0097	0.0165
sal6	0.0102	173.8	0.0094	0.0184
smw4	0.0099	161.3	0.0093	0.0163
sps13	0.0154	2	0.0124	0.028
sws2	0.0155	21.3	0.013	0.0272
thy1	0.0098	16.2	0.009	0.0149
top19	0.0195	175.5	0.0142	0.0317
wtr12	0.011	179.9	0.0102	0.0191

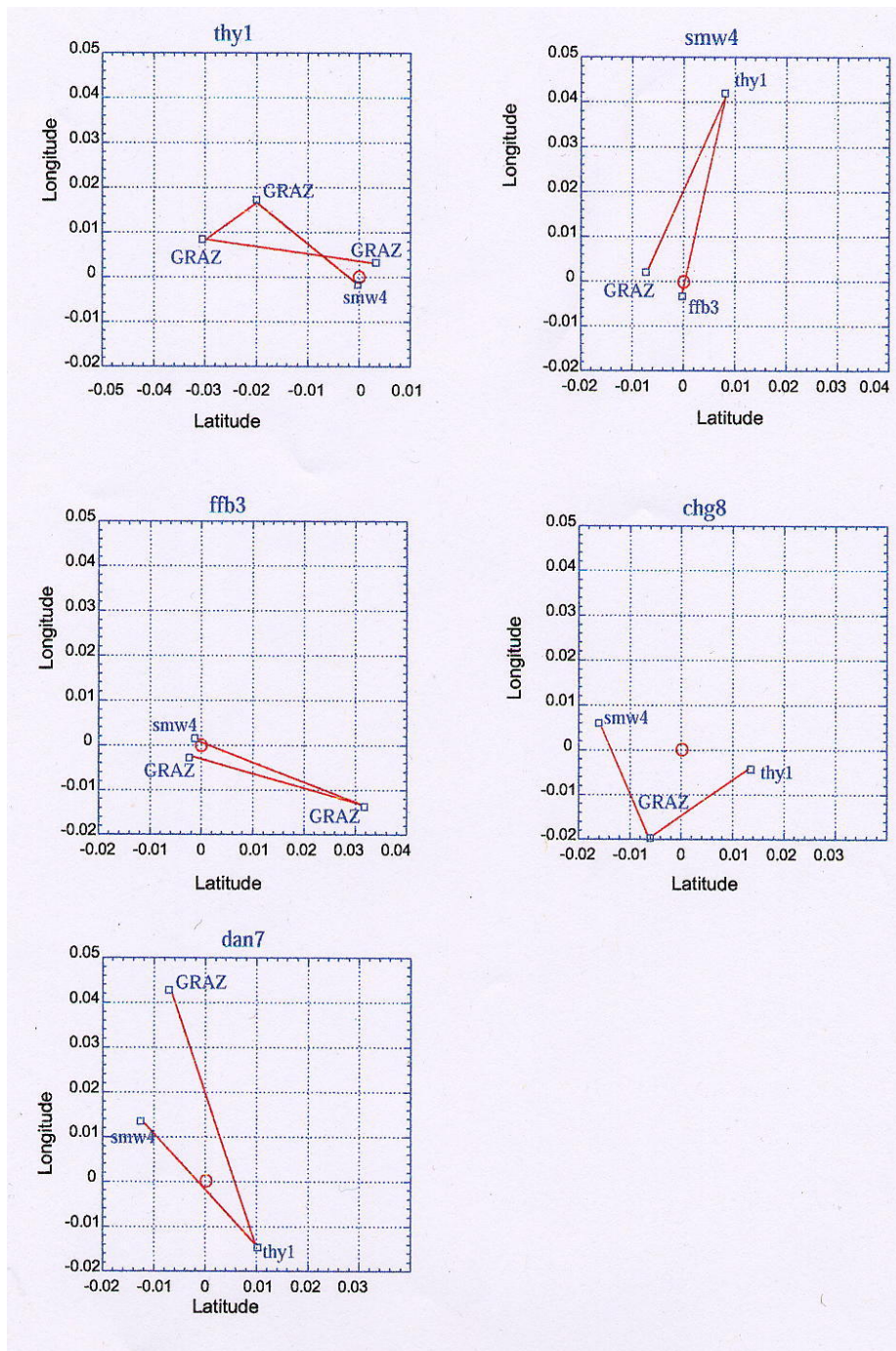


Figure 6. Variations in positioning using Graz to fix the network co-ordinate.

## Ground deformation results for Tessina 1998 & 1999

### Results of the EDM network in 1998 and 1999

The EDM network of Tessina identified distinct deformation patterns from April to September 1998; these are interpreted in two ways. Firstly, that the background state of the headwall and side scarp is steady state slow deformation, independent of rainfall variations. The peripheral deformation ceased in September and the deformation rate of the lower section of the Upper Accumulation Zone increased. The mechanism for this pattern is suggested to be the migration of ground water downslope through the landslide scarp. The alternative view is also presented that the Detaching Zone and Upper Accumulation zone behave as a single unit, but undergo deformation at differing times. The implication of this is

that there may be a large-scale underlying process that is instigating the shallow disparate failure. The GPS will determine the extent of the deformation and the total annual rate of deformation between July 1998 and July 1999. The total horizontal and vertical displacement of the individual survey stations within each zone are examined; this will allow the identification of patterns and coherent bodies or blocks.

#### *Vector changes from 1998 to 1999*

The deformation patterns recorded between July 1998 and July 1999 show two distinct displacement magnitudes: (1) small horizontal (0.03m) and vertical deformation (-0.1-0.005m), and (2) large horizontal (1-9m) and vertical deformation (1m). These distinct bands of deformation indicate that ground is somewhat stable within the zone beyond the active detaching zone, and actively moving in a new active area in the northwest area of the landslide. Although there appears to be no intermediate magnitude of displacement, this is interpreted to be a function of the spatial distribution of the network survey stations. EDM measurements in the intermediate area, on the edge of the landslide-detaching zone, reveal centimetric movements from 10 to 100cm (Mantovani *et al.*, 1999). The dataset from July 1999 to October 1999 reveals deformation of a lesser magnitude; the greatest displacement was from the central crown area within a displaced section dissected with fractures and open cracks.

From the GPS survey data, the right hand-side of the landslide appears to be more stable than the left hand-side however; a large part of the right hand-side did collapse into the landslide in early 1999. Due to this re-activation survey station vri10 that was situated within the lower accumulation zone, was destroyed. It is therefore inferred that the survey stations on the right hand-side are situated too far enough beyond the rim of the landslide to demonstrate strong deformation characteristics associated with the recent displacement events. The upper central part of the landslide shows more gradual deformation, which is to be expected on the rim of the landslide, this area lies within the >10cm to <1m zone defined by Mantovani and co-workers (1999). Large deformation recorded on the left hand-side of the detaching zone reveals an area in danger of imminent failure, this and the other areas will be examined in more detail below.

#### *Upper Detaching Zone*

This zone contains the large vertical and horizontal displacements of survey stations sps13, lvp18 and des17. This surface area of the unstable region is estimated to be between 10,000 and 30,000m<sup>2</sup> and is of unknown depth. Investigation of the area between survey stations showed an increase in the number, width and throw of existing fractures.

Des17 is located in the middle of the crown of the landslide on a sloping grassy section comprising titled Flysch deposits. It lies above the springs of the Upper Accumulation Zone. In July 1998 it was noted that there were numerous thin, deep cracks in the slope above and below the survey station. In July 1999 most of these cracks had increased to a span of approximately 30cm and a throw of 10-20cm, the distended cracks appear to be shallow and are aligned to the surface of the slope. The accumulation of the extensions may account for the 1.01m horizontal displacement of the survey station that is also aligned to the maximum slope direction and the 60cm vertical drop. Between July 1999 and October 1999, 38cm of horizontal and 24cm of vertical deformation was recorded. If this is doubled to indicate an annual rate then a displacement of ~1.15m horizontal and 1m vertical would be expected. The rates listed above for the period July 1998 and July 1999 are just below this rate, suggesting that the deformation is semi-continuous but may also reflect periodic events that induce sudden downslope displacements. The primary mechanism for the displacement is

unclear, but is most likely shallow soil creep occurring as a consequence of deep-seated block sliding. There is no evidence of a rotational element to the displacement.

From July 1998 to July 1999, 210m further to the west, survey stations lvp18 was displaced 2.7m horizontally and 1m vertically downwards. Distended existing fractures and several fresh fractures, aligned to the direction of maximum slope again surrounded this survey station. An important feature was observed to the side of the survey station, a small scarp increased in throw by around 1m. It may be interpreted that the increase in the throw of the scarp accounts for the drop in vertical position. The horizontal displacement however was downslope thus inferring that the downthrown block (defined by the scarp) dropped by 1m and was displaced laterally by approximately 3m at this point. From July 1999 to Oct 1999, lvp18 underwent significant deformation, 10cm horizontally with a 6.5cm vertical drop. This displacement is significantly smaller than the substantial deformation recorded between 1998 and 1999. The deformation is of the same azimuth with the displacement oriented to the maximum slope direction. This displacement does not reflect expected fraction of the annual displacement recorded between July 1998 and July 1999. The higher rate recorded during the 12 month period is most likely due to either a higher rate of displacement during the months with the highest rainfall or one or more sudden events that produced a sudden displacement.

From July 1998 to July 1999, 173m further downslope within the freshly downthrown block, survey station sps13 was displaced 1.6m downwards and 9m laterally (in the direction of slope), this suggests that the ground between sps13 and lvp18 also underwent ground cracking causing further lateral displacement. On field inspection the area was crossed by some cracks and many springs. This hypothesis that the scarp is the head of a recent displacement is verified by the status of wtr12 which is situated above the scarp. Wtr12 was recorded to have remained virtually stable during this period, showing a slight rise in height and a small lateral movement. Between July 1999 and October 1999, sps13 underwent a similar magnitude of displacement to lvp18 for the same period. Although the horizontal displacement was again oriented to the direction of maximum slope the vertical change during this period is only 3cm and as such as barely above the error margins of the technique. This suggests that the fault that is thought to have dropped over 1m between July 1998 and July 1999 has not been further activated from July 1999 to Oct 1999. Inspection of the scarp in Oct 1999 did not reveal any obvious recent reactivation. Survey station wtr12, which was stable from 1998 to July 1999, underwent slight displacement from July 1999 to October 1999, the recorded westerly displacement may indicate that the block is part of a new rotational slide, the soft muddy surface of the backslap may conceal the small fresh scarp.

Figure 7 illustrates the possible subsurface fracturing associated with the displacement recorded from July 1998 to Oct. 1999. The model infers that the 4.6cm westerly displacement and the 4.8cm vertical drop are a result of the rotational movement and subsequent backward tilt of the block on which wtr12 is situated. Although there is no field evidence for the small surface fracture to the west of the white rock, as stated above this may be obscured by the soft ground. The displacement of sps13 by over 9m was obvious when visiting the site and there were numerous fresh cracks between wtr12 and sps13.

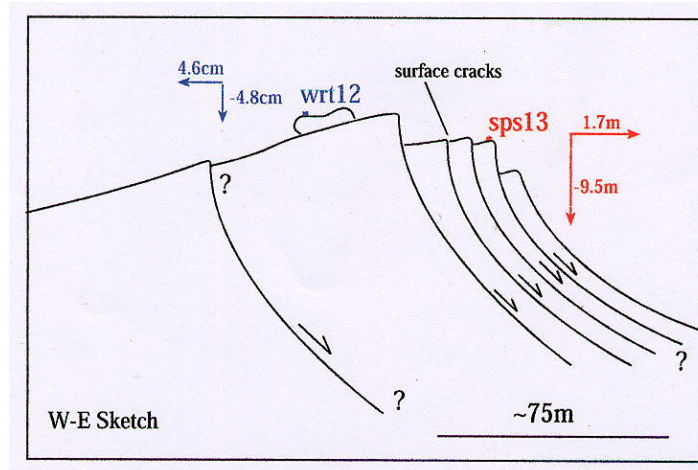


**Figure 7.** Sketch to show possible fracturing of western flank around survey stations wrt12 and sps13 and data from July 1998 to Oct. 1999.

From July 1998 to July 1999, Top19 was displaced 7cm laterally, along the direction of maximum slope and 3cm vertically downwards and from July 1999 to Oct. 1999 there was no significant displacement. It may thus be inferred that the unstable sector defined above does not extend upwards as far as top19. The unstable area may be defined as the region bounded in the west by the scarp in front of wrt12, which extends into the Upper Accumulation Zone in front of edm11 and dob21 which lie further south. The top boundary is somewhere between top19 and lvp18, geomorphological mapping by Mantovani and co-workers have found extensive cracking in this region. The eastern boundary lies either between des17 and rfc9 or des17 and lvp18, it is therefore estimated to be between 10,000 and 30,000m<sup>2</sup>. The large and concordant vertical displacement across the unstable area suggests that there has been a massive displacement along the line of the scarp that extends around 200-250m from wrt12 to lvp18. The horizontal movement follows the direction of greatest slope and is not perpendicular to the strike of the scarp at any point. The scarp that appears to have been reactivated was first displaced as a rotational slide in 1960, during the initial activation of the landslide; this initial event involved 10<sup>6</sup>m<sup>3</sup> of material. The scarp is clearly defined on the map and is illustrated in Figure 8.

There is no evidence that can irrefutably determine the nature of the deformation event. However, it is most likely a rotational or translational slip with the head of the block between lvp18 and top19 along the strike of the edge of the original landslide. The implications of this will be examined later.

At the most southerly edge of this zone is edm11, this is a pillar survey station used for the EDM to measure EDM reflectors within the body of the landslide. From July 1998 to July 1999, the pillar underwent a downward vertical displacement of 25mm, this slight displacement may either be (1) part of a trend of slow downward deformation, or (2) an error in the reading. From July 1999 to October 1999, both EDM11 and the adjacent pillar Dob21 were reoccupied. The results for edm11 show minor changes in horizontal position, and a large vertical change, this large vertical change may be attributed to the poor repeatability of the station, reflected in its higher vertical error ellipse. Multipath and the tall trees to the west of the site blocking satellite signals cause these poor data. The pillar dob21 is a few metres east of edm11 and therefore has a slightly better sky view; this was evident from faster occupation times in the field and the better error ellipse values (see Table 3). The stability of dob21 confirms that the velocity changes recorded for edm11 were an error in the readings.

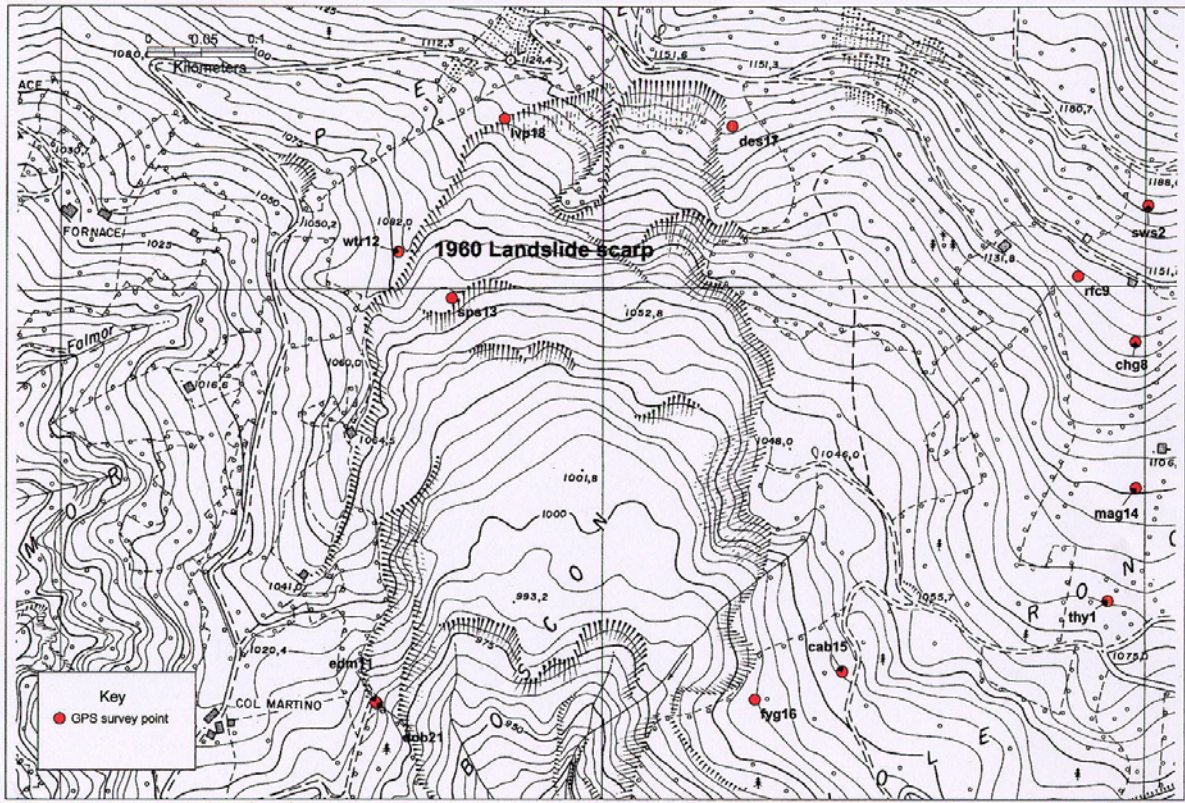


**Figure 8.** Freshly activated scarp and the outline of the original landslide.

### *Eastern Zone*

In the area near the headwall and the right-hand side lateral scarp of the landslide, lateral survey station velocity ranges from 10mm to 50mm. Between July 1998 and October 1999, there are no significant height changes, the largest drop is just 2cm and many changes are very small (2-3mm) and within the error limits of the technique. The area is defined by Mantovani and co-workers as undergoing minor deformation of <10cm per year, it may be useful to redefine this classification to a narrow one of <10cm a year and to add a new zone of <2cm. From July 1998 to July 1999, the deformation recorded for survey stations rfc9 and chg8 above the head of the landslide shows centimetre oriented to the direction of maximum slope. These small velocities are within the error margins of the survey as outlined in Table.

The survey stations furthest from the scarp, sws2, dan7, mag14, thy1 and sal6, reveal a concordant southwesterly velocity of between 5mm and 25mm. There is no apparent cause for this coherent displacement, the movements are not thought to be a consequence of the network geometry. The displacements are all minor and may be within the error margins of the technique. From July 1999 to October 1999 the survey stations of the eastern sector did not undergo any strongly significant deformation. The largest displacements recorded for sws2 show that deformation occurs neither in the direction of maximum slope or along the line of an existing fault or fracture system.

The consistent SE velocity of these survey stations suggests that there may be a geological or geomorphological source to the displacement. It is however significant that none of these survey stations showed a decrease in height during the same period. It can therefore be accepted that if any broadscale deformation occurred then it was purely on a horizontal plane and not downslope sliding. The only plausible explanations are either a common measurement error or a broad lateral tectonic displacement. These will be examined further in the conclusion section.

#### *Lower eastern edge of Upper Detaching Zone*

At the lower eastern edge of the landslide a wide buttress extends into the landslide basin and creates the neck of the connection canal. There are two GPS survey stations located on this buttress; intense tree coverage prevented a more concentrated network at this point. The survey stations are cab15 and fyg16.

The area underwent visible deformation between July 1998 and July 1999. Investigation of the area around the survey stations showed an increase in the number of ground fractures and the width and throw of existing fractures. The survey station deformation revealed just 1-2cm of coherent movement, despite being very close to the edge of the landslide basin the survey station revealed just minor creep. The velocity and magnitude of both survey stations was very similar, both were orientated to approximately 260°. Between July 1999 and October 1999 survey stations cab15 and fgy16 did not reveal any significant deformation. The relatively large height difference for fgy16 of -3.5cm may indicate significant although slight, vertical deformation.

The implications of this result are that this area is at present stable and is not undergoing significant continuous creep. Failure is therefore most likely to be constrained to periodic events, most likely induced by high rainfall or loss of material at the toe, due to emptying of the upper accumulation zone and adjacent connection canal zone.

#### *Survey stations more than 100m away from the active landslide*

From July 1998 to July 1999, two survey stations located along the east flank of the landslide, bwm4 and ffb3 both underwent minor deformation. In a similar pattern to sal6, thy1 and sws2 mentioned above, bwm4 was displaced to the SE 29mm. The survey station was not located on a SE facing slope. There was a negligible increase in height of just 8mm. From July 1999 to October 1999, the deformation pattern of the survey stations did not correspond with the pattern seen from July 1998 to July 1999. However, the overall pattern from July 1998 to October 1999 does show a general downslope displacement pattern for most of the survey stations, in particular sal6, which is situated on a steep unstable slope. The displacement of this survey station reflects the localised instability of this scarp, which although minor may cause localised landsliding.

Further south in Funés, ffb3 is located in a meadow, the survey station was primarily installed as a useful base station location and was not considered very stable. 10cm of the rod was protruding from the ground and the surrounding grass was regularly cut, it does however provide a good test of the metal survey station marker. The site was however marked with a metal stake and on inspection in July 1999 looked undisturbed. Ffb3 underwent only negligible displacement on the horizontal and vertical plane, moving just 13mm and -1mm respectively. From July 1999 to October 1999 this survey station again, underwent only slight displacement and is considered stable.

#### *Western Stable survey stations*

On the western flank two stable survey stations were occupied and a further Pillar was installed. Smw4 was used as the fixed common point to join the two 1998 and the 1999 surveys. The furthest survey station from the landslide was lam20, this survey station was located on the edge of the road, primarily as a GIS reference point, the stability of the area was unknown, the survey station underwent 4mm vertical deformation and 35mm horizontal deformation. The cause of the lateral displacement is thought to be due to the Lamosano landslide. From July 1998 to October 1999 smw4 was not held fixed, but was processed using Graz as a fixed point. This allowed the measurement of smw4 from July 1998 to October 1999. The survey station was displaced around 20mm, this is within the bounds of

the technique and probably reflects set-up errors or the long baseline fixes to Graz in 1998 and 1999. In order to assess the stability of this area as a fixed zone, an adjacent pillar asr22 was measured. The velocity of the pillar between July 1999 and October 1999 was approximately 9mm and 0.4mm in height. The pillar was measured on three separate occasions and reflects the good repeatability of the technique in a good situation away from trees and other causes of multipath.

### **Conclusions**

The Tessina landslide is currently undergoing slow continuous deformation around the detaching zone. The higher rate recorded during the 12 month period is most likely due to either a higher rate of displacement during the months with the highest rainfall or one or more sudden events that produced a sudden displacement. The reactivation in early 1999 of the upper eastern flanks and head of the landslide affected only the direct area around the head - this area is estimated to be between 50 and 100m. The area over 100m from the active scarp shows no continuous displacement attributable to the landsliding process. The largest movements were recorded in the upper western area of the landslide head near the vicinity of the primary failure in 1960 and slight reactivation in 1964.

## References

- Blewitt G. (1997) Basics of the GPS technique: Observation Equations. [In: *Geodetic Applications of GPS*, Swedish Land Survey]
- Bock Y., Wdowinski S., Fang P., Zhang J., Williams S., Johnson H., Behr J., Genrich J., Dean J., van Domselaar M., Agnew D., Wyatt F., Stark K., Oral B., Hudnut K., King R., Herring T., Dinardo S., Young W., Jackson D. and Gurtner W. (1997) Southern Californian Permanent GPS Geodetic Array: Continuous measurements of regional crustal deformation between the 1992 Landers and the 1994 Northridge earthquakes. *Journal of Geophysical Research*, Vol. 102, No' B8.
- Briole P., Gaulon R., Nunnari G., Puglisi G. and Ruegg J.C. (1992) Measurements of ground movement on Mount Etna, Sicily: A systematic plan to record different temporal and spatial components of ground movement associated with active volcanism. [In: Gasparini P., Scarpa R. and Aki K. (Eds.) *Volcanic Seismology*, pp. 120-132. Berlin Heidelberg: Springer-Verlag]
- Burnside C. D., (1991) *Electromagnetic distance measurement*, 3<sup>rd</sup> Edn. London: Blackwell.
- Davies R., England P., Parsons B., Billiris H., Paradissis D. and Veis G. (1997) Geodetic strain of Greece in the interval 1892-1992. *Journal of Geophysical Research*, vol. 102, B11.
- Delaney P., Miklius A., Arnadottir T., Okamura A, T., and Sako M. K. (1987) Motion of Kilauea volcano during sustained eruption from the Puu Oo and Kupaianaha Vents, 1983-1991. *Journal of Geophysical Research*, 98, 17801-17820
- Dikau R., Brundsen D., Schrott L., and Ibsen M-L. (Eds.) (1997) *Landslide Recognition: Identification, Movement and Causes*. John Wiley & Sons, UK. P1-13, 63-103, 213-216.
- Hofmann-Wellenhof B., Lichtenegger H., and Collins J., (1997) *Global Positioning System Theory and Practice*. 4<sup>th</sup> edition, Springer-Verlag Wien, New York.
- Holcomb R.T. and Searle R. C. (1991) Large landslides from Oceanic Volcanoes. *Marine Geotechnology* **10**, 19-32.
- Foulger G. R., Bilham R., Morgan J., and Einarsson P. (1987) The Iceland geodetic field campaign 1986. *EOS* **68**, 1801-18.
- Frei E. and Schubernigg M. (1992) GPS surveying techniques using the 'Fast Ambiguity Resolution Approach (FARA)'. *34<sup>th</sup> Australian Surveyors Congress and the 18<sup>th</sup> National Surveying Conference at Cairns, Australia, May 23-29*.
- Fukuoka H., Kodama N., Sokobiki H., and Sassa K. (1995) GPS monitoring of landslide movement. *Proceedings of the International Sabo Symposium*, Tokyo, Japan.
- Kimata F., Satomura M., Usui W., Saaki Y., (1991) Preliminary result of crustal motion monitoring by GPS in the southern part of central Japan (March 1989-1991). *Journal of Physics of the Earth*, 39, 649-59.
- Kodama N., Hamada T., Sokobiki H., Fukuoka H. (1997) GPS observations of Ground movements in large-scale landslides. *Proceedings of the International Symposium on Landslide hazard Assessment*, Xian.
- Lomoschitz A. and Corominas J. (1992) Los Fenomenos de deslizamiento gravitacional de la depresion de Tirajana (Isla de Gran Canaria). *III Simposia Nacional Sobre Taludes y Landeras Inestables*, La Coruña, Octubre 1992.
- Lomoschitz A., Quintana A., Santana F., and Martín F. J. (1998) RUNOUT Base-map of Barranco de Tirajana. Compact Disc. University of Las Palmas.
- Lomoschitz A. (1999) The depression of the Barranco de Tirajana, Gran Canaria Spanish - English edition. Ediciones del Cabildo de Gran Canaria, Las Palmas de Gran Canaria, 200 pp.

- Moss J. L. (1999a) Volcanic rift-zones and flank instability: an evaluation of ground deformation monitoring techniques. Ph.D. Thesis, Cheltenham & Gloucester College of Higher Education.
- Moss J. L. (1999b) Monitoring ground deformation in zones of active instability. In Runout first year report for the European Commission, Environment and Climate.
- Moss J. L. (In Press) Using the Global Positioning System to monitor dynamic ground deformation networks on active landslides. *International Journal of Applied Earth Observation and Geoinformation*.
- Moss J. L., McGuire W. J. & Page D. (In Press) Ground deformation monitoring of a potential landslide at La Palma, Canary Islands. *Journal of Volcanological and Geothermal Research* (In Press).
- Nunnari G. and Puglisi G. (1994) The global positioning system as a useful technique for measuring ground deformations in volcanic areas. *Journal of Volcanology and Geothermal Research* **61** 267-280.
- Nunnari G. and Puglisi G. (1996) GPS - Monitoring from space. In *Monitoring active volcanoes*. McGuire W. J., Kilburn C. R. J. and Murray J. B. (eds.) UCL Press, London.
- Quintana A. Lomoschitz A (2000) Influence of landslides on the geomorphological features of a volcanic area. A case study: the Barranco de Tirajana basin, Gran Canaria. Resubmitted: 22 December 1999 to *The International Journal of Applied Earth Observation and Geoinformation (JAG)*, ITC, The Netherlands.
- Shimada S., Fujinawa W., Sekiguchi S., Ohmi S., Eguchi T., and Okada Y. (1990) Detection of a volcanic fracture opening in Japan using Global Positioning System Measurements. *Nature* 343, 631-3.
- Sigmundsson F. (1996) Crustal deformation of Volcanoes. *Proceedings of the course the mitigation of volcanic hazards, Vulcano, Italy, 1994*. Environment and Climate Programme, European Commission.
- Sokobiki H, Fukuoka H, Sassa K (1995) GPS monitoring of landslide movement. *Proceedings XX IUFRO World Congress*, Finland.
- Varnes D. J. (1980) Slope movement types and processes. In *Landslides, analysis and control*. (Ed. Clark M.) Transportation Research Board Special Report. 176. National Academy of Science, USA.
- Zumberge J. F., Heflin M. B., Jefferson D. C., Watkins M. M., and Webb F. H. (1997) Precise point positioning for the efficient and robust analysis of GPS data from large networks. *Journal of Geophysical Research*, Vol. 102, No' B3.

## **12. Use of spaceborne remote sensing for monitoring giant landslides: Barranco de Tirajana, Gran Canaria, Spain, and Tessina, Italy**

### **Introduction**

Landslides may occur as a consequence of a number of determining and triggering factors (Varnes, 1978; Popescu, 1994). In order to assess hazard from landslides it is therefore necessary to identify and analyse the most important determining factors leading to slope failure. Approaches to landslide hazard assessment using GIS have been reported, among other authors, by Brabb (1984), Carrara *et al.* (1991), Van Westen (1993) and Leroi (1996). The applicability of various GIS methods with respect to the characteristics of the study area, the landslide type and extension, the type of data available and the mapping scale has been discussed by Soeters and Van Westen (1996). Most direct methods include landslide inventories and heuristic analysis, where the hazard assessment is made by the earth scientist using site-specific knowledge obtained mainly through photointerpretation and fieldwork.

In the literature, three types of landslide hazard assessment techniques are commonly used: deterministic, statistical and heuristic approaches.

(1) Deterministic approaches, based on stability models, can be very useful for mapping hazard at large scales, for instance for construction purposes. Deterministic landslide hazard maps normally provide the most detailed results, expressing the hazard in absolute values in the form of safety factors, or the probability of failure given a set of boundary conditions for groundwater levels and seismic acceleration. However, deterministic models require the availability of detailed geotechnical and groundwater data, and may lead to oversimplification if such data are only partially available.

(2) The combination of factors that have led to landslides in the past are determined statistically, and quantitative predictions are made for areas currently free of landslides. In these methods the use of complex statistics require the collection of large amounts of data to produce reliable results.

(3) Heuristic methods use selective criteria to decide the type and degree of hazard for each area, which need expert knowledge to be suitably applied.

In view of the data available and the characteristics of landslides in the Barranco de Tirajana basin, where hazard is not so much related to the occurrence of new landslides, but to the reactivation of existing ones, as well as to rockfalls, a heuristic approach was considered most suitable. In this approach, direct and indirect GIS-based methods were developed for assessing landslide hazard at a medium scale (1:25,000). In the direct mapping approach the degree of hazard was mapped both directly in the field and after fieldwork on the basis of a detailed geomorphological map (Barredo *et al.*, 2000). The indirect method followed an indexing approach, by which parameters including slope angle, landslide activity, landslide phases, material, proximity to gullies and reservoirs, and land use change were combined within a GIS using multicriteria evaluation techniques to produce a hazard map (Barredo *et al.*, 1999; Barredo *et al.*, 2000). The land use change maps were previously generated using satellite remotely sensed imagery.

This chapter discusses the indirect landslide hazard assessment approach and compares the resulting hazard map with that derived from direct mapping methods. Particular emphasis is placed on the use of satellite remote sensing (1) to generate land

use change maps to investigate the impact from human activities on slope instability in the Barranco de Tirajana, Gran Canaria, and (2) to investigate the potential of real-time monitoring of landslides at Tessina in the Italian Alps.

### **The Barranco de Tirajana study area**

The Barranco de Tirajana basin is located in central Gran Canaria Island, Canary Islands (Chapter 9). It has an extension of 50 km<sup>2</sup>, spreading over the municipalities of San Bartolomé de Tirajana and Santa Lucía (Figure 1). The basin is a major erosive feature formed on interbedded volcanic breccia, ignimbrites and lava flows since the Pliocene by large landslides (Lomoschitz and Corominas, 1997a). It makes up a deep oval-shaped amphitheatre, bounded by very steep slopes and cliffs reaching up to 350 m of height, which are remnants of ancient, large landslide scarps. Altitudes range from 1949 m. in the northernmost sector to 300 m. in the southern end, with differences of up to 900 m on slopes next to the basin boundaries. The basin is mainly drained by the Barranco de Tirajana stream and its tributaries, all with seasonal or intermittent flow. Average annual rainfall ranges from 370 mm at the bottom of the basin and 890 mm near the cliff tops, although much of it concentrates within days. It is believed that rainfall is responsible for the major landslide reactivations occurring this century (Lomoschitz and Corominas, 1997b). The site includes two major villages and numerous scattered houses. It contains artificially irrigated orchards within extensive shrubby areas and bare ground (soil and rock outcrops) with some coniferous patches. Tourism is also starting to flourish because of its proximity to a major beach resort.

The Tirajana basin contains at least 28 large landslides, some with surfaces exceeding 400 hectares and volumes over 1 km<sup>3</sup>. Main landslide types include rockslides, debris slides, earth slides, debris flows and rockfalls (Lomoschitz and Corominas, 1997a). Several phases of movement since the Pleistocene can be recognised, typically consisting of a major primary failure of the bedrock, followed by a succession of smaller, secondary displacements due to sliding of the primary body. Following primary failure and emplacement, the landslide materials suffered from progressive weathering and weakening, so that further phases show a fragmented structure.

Recent slope movements in the basin have been reported, particularly an earth slide seriously affecting the village of Rosiana in 1956 after intense rainfall (Lomoschitz and Corominas, 1997b). Active rockfalls have been observed on cliffs, landslide scarps and denuded gully sides.

### **Creation of the GIS database**

In order to utilize the heuristic landslide hazard approaches in the Barranco de Tirajana area, an extensive GIS database was generated in collaboration with the ULPGC and ITC teams using photointerpretation, fieldwork, satellite image processing techniques and digitising of base maps. Special attention was given to the investigation of human impact on slope instability by including dynamic land use data in the GIS database. These data were derived from classification of visible-infrared multitemporal Landsat TM imagery.

Spatial data including topography, landslide boundaries and major landforms, bedrock and surficial deposits (talus, scree, colluvial and alluvial deposits), drainage networks, paved roads and groups of buildings were first transformed into ARC/INFO vector format. These layers were further reprojected, rescaled, edited and rasterised, where appropriate, for integration with remote sensing products, for GIS hazard analysis and for illustration of mass movement risk to infrastructure and urban settlements.

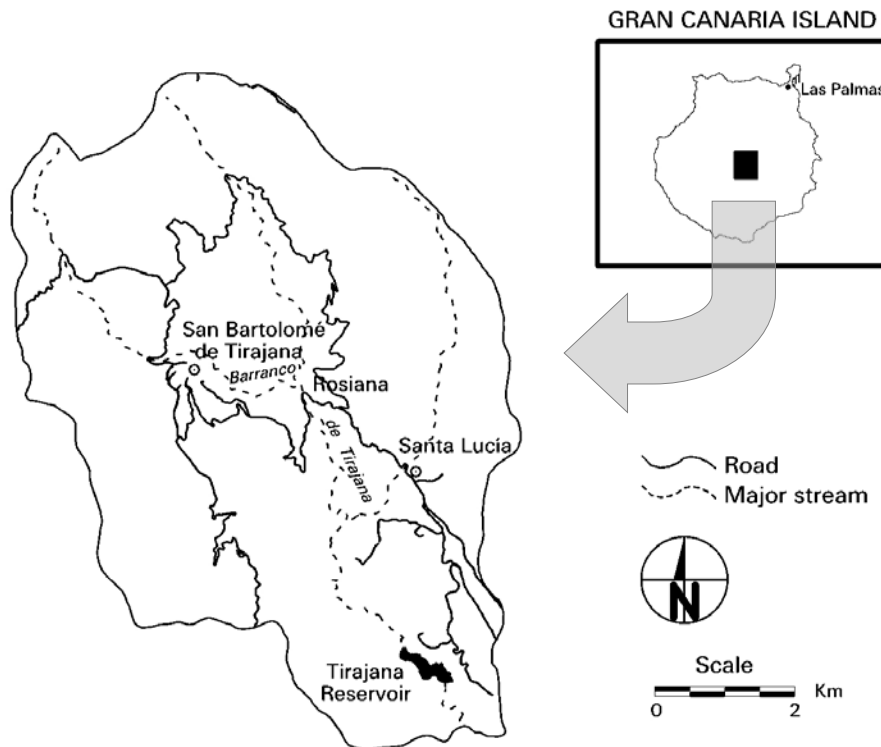


**Figure 1.** Location of the Barranco de Tirajana basin

### **DEM generation**

As input to various image and GIS processes, a raster digital elevation model (DEM) was produced for the Barranco de Tirajana basin. A raster DEM consists basically of a regular grid of elevation values often stored as a raster file. To generate a raster DEM of the study area a triangulated irregular network (TIN) was first produced from vector-format 5m-interval contours and elevation points. The TIN is a terrain model that uses a sheet of continuous, connected triangular facets based on Delaunay triangulation of irregularly spaced nodes or observation points representing XYZ values. The information defining each of these triangles as a set of nodes together with the triangle's adjacency with the other triangles form the topological structure of the TIN. The raster DEM was then generated through a lattice (surface) created by a linear interpolation of the  $z$  values of the irregular set of triangle nodes. Finally, the lattice was resampled to a raster layer with a user-defined pixel size.

Spurious effects due to errors found in some contour elevation values were corrected through interactive analysis of perspective views from the DEM. 2m, 4m and 30m pixel raster DEMs (termed DEM2, DEM4 and DEM30 respectively), matching the resolution of the remotely sensed images below, were produced for a number of tasks including image corrections, GIS-based landslide hazard assessment, and generation advanced image and map visualisation products for landslide delineation and risk illustration.

### **Generation of land use and land use change maps**

In order to investigate human impact on slope instability in the Barranco de Tirajana basin, land use and land use change maps need be generated. These maps can further be integrated in a GIS for comprehensive assessment of landslide hazard.

Satellite remote sensing methods can be effective to derive not only up-to-date land use maps but, because of their repetitive observation capabilities, to detect land use changes in recent times, and thus study their possible relationship with recent slope instability. In addition, the information provided by multispectral remote sensors in the visible to infrared regions make them well suited to discriminate most common land cover types at medium scales, including some determining factors of landsliding. The remote sensing approach used in this research has been summarised in Hervás *et al.* (1999).

To best distinguish between different classes of land cover and usage, primary factors for selecting the images were the spectral coverage of the satellite sensors, absence of cloud cover over the Barranco de Tirajana basin and the prevailing cover of natural vegetation and crops. A priori constraints for discriminating land use classes on steep slopes from adverse seasonal sun illumination effects were investigated with a raster digital elevation model (DEM30), by simulating shaded relief images with sun azimuth and elevation values corresponding to the acquisition dates and times of the available imagery.

The digital images finally elected were Landsat TM subscenes acquired on 04/07/84, 04/08/95 and 05/3/98. These images cover most of Gran Canaria Island at 30m resolution in 6 spectral bands from the visible through the middle infrared (1: 0.45-0.52  $\mu\text{m}$ ; 2: 0.52-0.60; 3: 0.63-0.69; 4: 0.76-0.90; 5: 1.55-1.75; 7: 2.08-2.35), and 120m resolution in band 6 (10.40-12.50  $\mu\text{m}$ ). It would have been desirable to have a more recent Summer image, but it was not possible because, since 1995, the appropriate satellite receiving station has been operating only from January to March each year. At the same time, other archive images available for early Spring or late Winter were not sufficiently old to extend significantly the data from the selected images.

An up-to-date land use raster map for the Barranco de Tirajana basin was generated from classification of the 1998 Landsat TM multispectral image. Changes in land use from 1984 to 1995 were also mapped using the classified images from those years. The method employed included three major steps as follows.

#### *Image pre-processing*

Images acquired under different atmospheric and illumination conditions must be pre-processed before analysis. On Landsat TM imagery this implies radiometric corrections mainly for sensor, illumination and atmospheric effects, and geometric corrections to georeference the images to a map projection. Accordingly, the following pre-processing sequence was applied (Figure 2):

All three Landsat TM images, supplied as system-corrected radiance values, were corrected for detector-generated stripping and spurious noise. Stripping was removed by means of an along-line convolution algorithm (Crippen, 1989). Spurious noise was removed by applying a selective median filter replacing noisy pixels by median values within the filter window.

The image of 05/03/98 was geometrically corrected with reference to 1:25,000 topographic maps by selecting suitably distributed ground control points (GCP) on those maps. A 2nd-degree polynomial transformation was applied to the image, whose coefficients were calculated from the UTM coordinates of the GCP selected. The other two TM images were then georectified to that of 05/03/98 applying also a 2nd-degree

transformation, and generating UTM-georeferenced images. A RMS value of less than 1 pixel was obtained for all three corrected images.

A subsene of each dated image covering the basin was orthorectified using the DEM30 and the pixel location relationship between the raw and the georeferenced 1998 TM image.

A semi-empirical slope-aspect illumination correction procedure (Itten et al., 1992; McCormick, 1997) was applied to the orthorectified images to correct mainly for shadowing effects with the help of the DEM30 and image training areas.

All 3 images were then corrected for atmospheric effects (Richter, 1990) notably due to aerosols, water vapour and the atmosphere's optical depth.

The pre-processed images consisted of reflectance values scaled from 0 to 255 for each band. The image pixel values could thus be statistically compared between different dates as well as between different bands within each image.

### *Image classification*

A pixel-based multispectral classification was performed on the pre-processed TM images by using a maximum likelihood supervised classification algorithm. Every image pixel was allocated to a previously defined spectral class in a n-band feature space by establishing a parametric decision rule. Spectral class statistics were defined from training areas, that is, areas in the image whose land cover type was known. In the process, however, the *a priori* pairwise separability of classes was statistically evaluated using the transformed divergence index (Swain and Davis, 1978). This index also allowed the best band combinations (bands 1, 2, 4 and 7 for the 1998 image) to be selected for final classification process. In parallel, non-supervised iterative clustering was performed to help estimating the spectral classes that could be discriminated on the image.

Classification of the 1998 TM image allowed discrimination of 19 land cover classes, which can be grouped into 9 more relevant thematic classes in relation to slope instability (Figure 3). Inspection of the resulting map shows that the illumination correction procedure employed did not fully correct for shadowing effects in slopes where the incident solar illumination angle (the angle between the sun illumination and the normal to the surface) was greater than 80 degrees, thus saturating pixels on those areas. As this effect is only apparent for cliffs, such pixels could generally be assumed to belong to the class "rock outcrops + patches of soil". The so-called "unclassified" class included mainly strongly shaded areas, which were not suitably corrected during pre-processing. In addition, the classification has introduced noise in the form of scattered pixels classified differently from the surrounding, much larger area class. Although this effect can be of natural origin (the so-called "scene noise"), it is often the result of misclassified border pixels, and has been smoothed out by applying a majority statistical filter to the classified images. The final 1998 TM thematic image shows an overall accuracy of 90.8 % (Table 1) which, obtained from sampling the training area pixels used in the classification procedure, is superior to that expected from other sampling procedures.

**Table 1.** Confusion matrix for the classified 1998 Landsat TM image

		Data Classification										
		Built-up	Irrigated crops	Bare Soils	Rock outcrops + patches of soil	Soil-dominated mixture of rocks, trees, shrubs and grass	Shrubland with scattered trees	Pine trees	Water	Unclassified	Total (pixels)	Producer's Accuracy %
Reference Data (training data sets)	Built-up	24				1					25	96
	Irrigated crops		158		1	7		1			167	94.61
	Bare soils		2	119		3					124	95.97
	Rock outcrops + patches of soil				91	7	3	5			106	85.85
	Soil-dominated mixture of rocks, trees, shrubs and grass		7		1	564	3	18			593	95.11
	Shrubland with scattered trees		3		8	21	119	26			177	67.23
	Pine trees					8	8	213			229	93.01
	Water								18		18	100
	Unclassified									12	12	100
	<b>Total (pixels)</b>	<b>24</b>	<b>170</b>	<b>119</b>	<b>101</b>	<b>611</b>	<b>133</b>	<b>263</b>	<b>18</b>	<b>12</b>	<b>1451</b>	
<b>User's Accuracy %</b>	<b>100</b>	<b>92.94</b>	<b>100</b>	<b>90.11</b>	<b>92.31</b>	<b>89.47</b>	<b>80.99</b>	<b>100</b>	<b>100</b>			

*Change detection*

The maximum likelihood classification procedure was also applied separately to the 1984 and 1995 TM images. The transformed divergence index suggested using bands 1, 2, 4 and 7 for the 1984 image and 1, 3, 4, and 7 for the 1995 image. The overall classification accuracy was 83.7 % and 82.5 % for the 1984 and 1995 images respectively. A land use change image was generated from these two classified images by cross-tabulation. This image was later transformed into a parameter map for GIS analysis (see Figure 5).

The higher classification accuracy achieved for the 1998 TM image with respect to that of 1984 and 1995 was due to the better separability of most land cover types in the area in Spring. Built-up areas, for instance, are better discriminated from soil-dominated mixture of rock, trees, shrubs and grass in the Spring image. Built-up areas are more easily distinguished from vegetated areas in Spring because of their high spectral contrast with plants showing high leaf reflectance and low water stress in this season. Unfortunately, no sufficiently-old Spring images were available for change detection. Because of their 30m-pixel resolution, however, small isolated buildings cannot normally be identified in either the Spring or summer TM images.

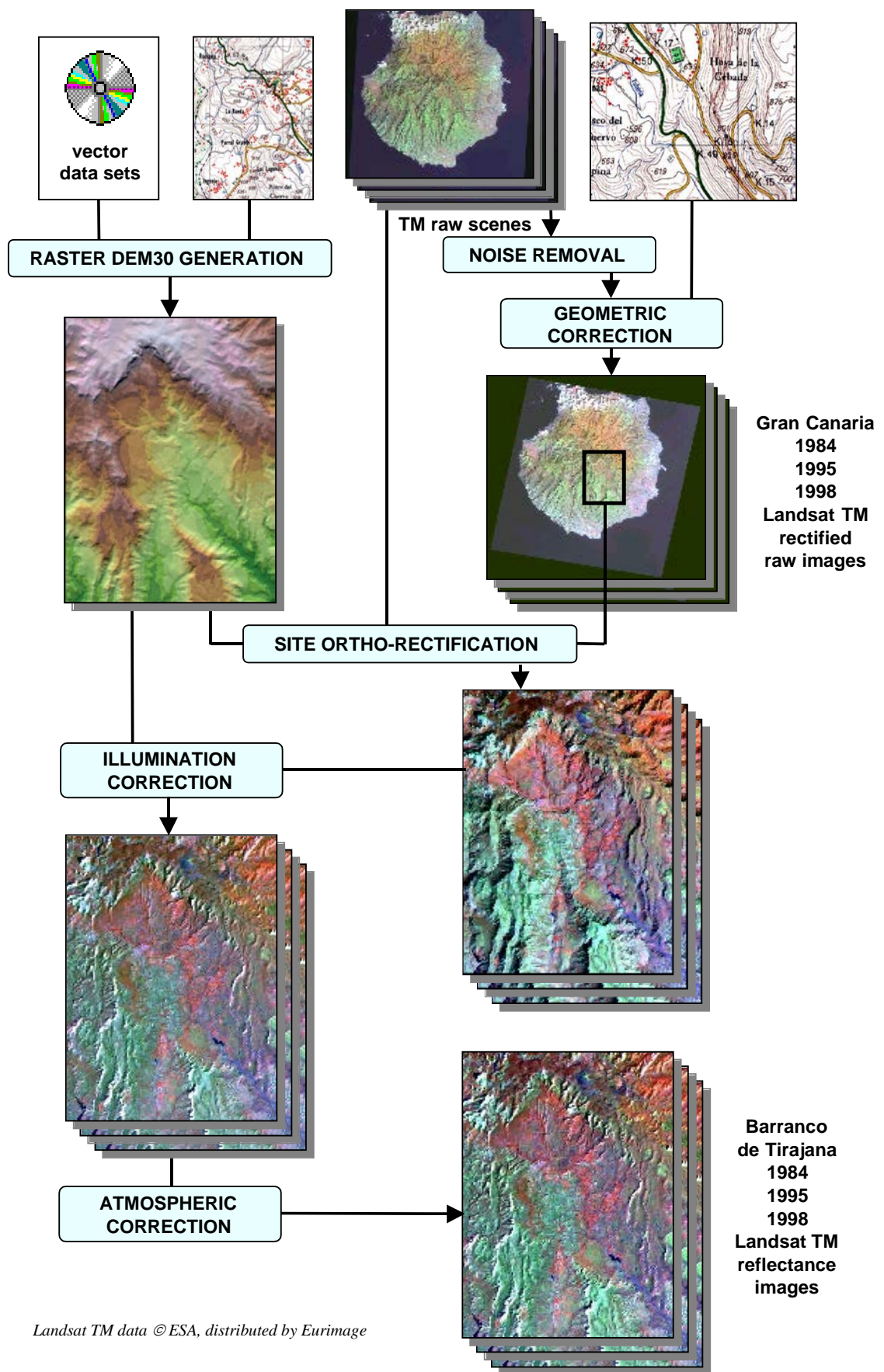


**Figure 2.** Landsat TM image pre-processing chain for the Barranco de Tirajana basin

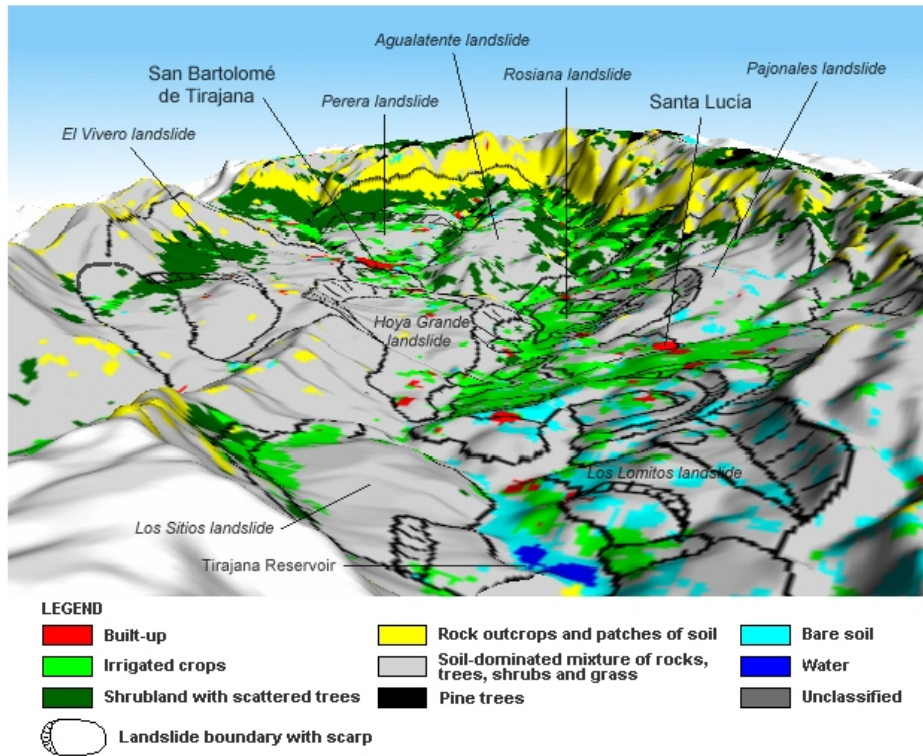


**Figure 3.** Three-dimensional representation of the land use map of the Barranco de Tirajana basin, illustrating the location of land use classes with respect to landslides. Widespread irrigation practices are observed on the Santa Lucía and adjacent landslides

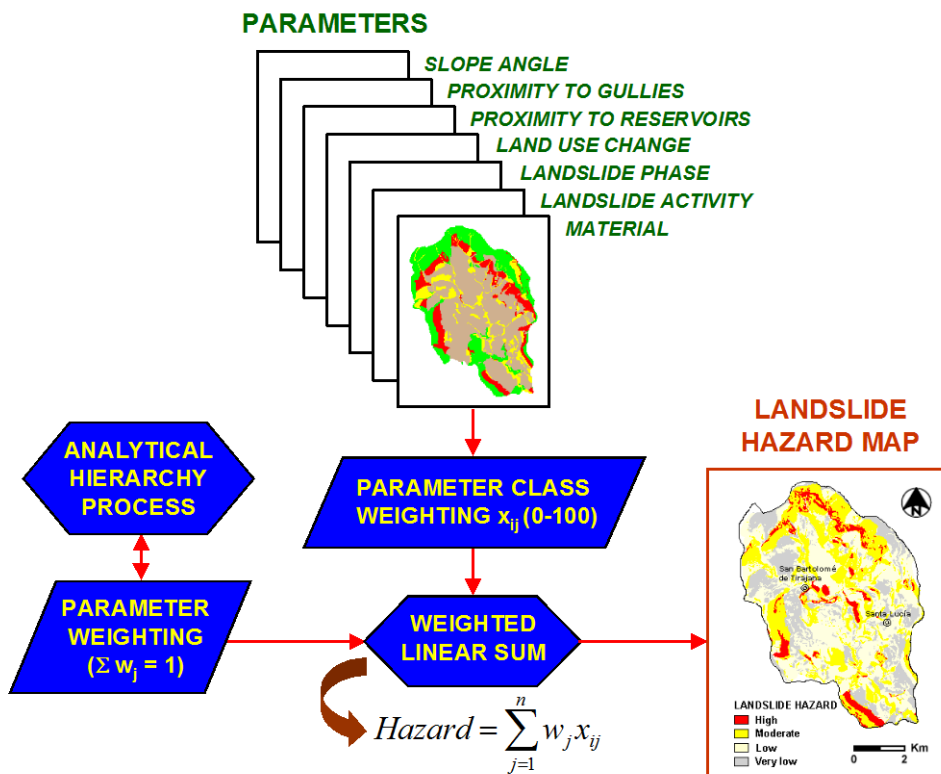


**Figure 4.** Landslide hazard assessment in the Barranco de Tirajana basin using a GIS-based indirect mapping approach and multicriteria evaluation techniques

### **Indirect hazard mapping approach**

Over 60% of the Tirajana basin is covered by landslides, which makes it difficult to apply statistical methods to assess landslide hazard, since no new landslides with similar sizes as the existing ones are expected to happen in presently landslide-free areas. This constraint, together with the unavailability of geotechnical and groundwater data, necessary for applying deterministic methods, suggested considering an alternative indirect hazard mapping approach. To this end, a GIS indexing approach has been developed (Figure 4).

Firstly, the previously constructed database has been used to generate a number of terrain parameter maps, considered the most important determining factors of slope instability in the area. Next, each parameter map has been classified into a number of significant classes based on their relative influence on mass movements. Weighting values have been subsequently assigned to each class. The relative importance of each terrain parameter as a determining factor of slope instability has been quantitatively determined by pairwise comparison using the so-called analytical hierarchy process (AHP) (Saaty, 1980). The integration of the various factors in a single hazard index has been accomplished by a procedure based on their weighted linear sum (Voogd, 1983) as follows:

$$H = \sum_{j=1}^n w_j x_{ij}$$

where:  $H$  is landslide hazard,  $w_i$  is the weighting of parameter  $j$ , and  $x_{ij}$  is the weighting of class  $i$  in parameter  $j$ .

The continuous landslide hazard raster map thus generated was eventually thresholded into four hazard classes. In multicriteria evaluation techniques the weighted linear sum is considered a compensatory procedure. The derived value of each alternative is primarily a function of the weight assigned to the parameters and, secondarily, of the weight of each parameter class (Barredo, 1996). In this approach, however, subjectivity is involved both in the assignment of weight values to classes and, although quantitatively less significantly, in the pairwise comparison of the parameters relevance. Expert knowledge is therefore required in this phase.

### **Terrain parameters**

Seven terrain parameters determining slope instability were selected (Figure 5).

#### *(1) Landslide phases*

The 10 landslide phases mapped by ITC (Barredo *et al.*, 2000) were weighted from 10 to 100. To this end, and because of its spatial and temporal relationship with the surrounding landslide complexes, phases I, II and III of La Filipina could also be reinterpreted as VI, VII and VIII of Santa Lucía and Las Lagunas landslides, and therefore assigned weights of 60, 70 and 80 respectively.

#### *(2) Landslide activity*

From field observations and historic records three classes of activity have been distinguished, namely active, partially active and inactive. Each class has been allocated maximum (100), intermediate (50) and zero weight values respectively. In the absence of displacement records, except for the active Rosiana earth slide, it has also been considered as active the areas including inclined palm trees and the sectors of landslide

deposits showing tension cracks, both resulting from recent shallow movements. Active sites are also considered the cliffs, landslide scarps, very steep slopes and gully sides displaying evidence of rockfalls. Partially active landslides include the bodies or parts not assigned to the class above. The remaining areas in the basin have been classified as inactive.

### (3) *Slope angle*

Slope angle has been derived from a raster digital elevation model (DEM30) following digitising of 1:5,000 topographic maps. A raster layer of continuous angle values has thus been generated. Weights related to mass movement occurrence have been linearly assigned in the range from zero to 100, corresponding to the minimum and maximum slope angle value respectively. Highest weights have therefore been allocated to cliffs bounding the basin, secondary landslide scarps and gully sides.

### (4) *Material types*

The material map produced by ITC and ULPGC teams was reclassified into 4 units: bedrock (with a weight of 30), alluvial-colluvial deposits, residual soils (weighted as 50), landslide deposits (with a weight of 70) and scree/rockfall material (with a weight of 100).

### (5) *Land use changes*

Land use change maps were derived from classification of multitemporal (1984-1995) Landsat TM data, as reported earlier. Highest weighting values were given to areas covered by irrigated crops on artificial terraces, recently abandoned agricultural land and the reservoir. Lower weights were assigned progressively to permanent soil cover, new and permanent soil cover with mixed vegetation, and new and permanent built-up areas and shrubby vegetation cover. Areas reforested with *pinus canariensis* were given a zero weight.

### (6) *Proximity to gullies*

It has been assumed that the intermittent flow regime of the streams and gullies in the basin encompasses remarkable erosive processes, which, in turn, are the cause of intense, superficial mass wasting phenomena in areas adjacent to drainage channels. The gullies were taken from the geomorphological map produced by ITC. Weights were calculated linearly from the gully bottoms (as taken from the stream vector map) to the side slopes within their mapped area of influence.

### (7) *Proximity to reservoir*

Instability hazard has also been considered from high pore-water pressures in the very fragmented landslide deposits making up the Tirajana reservoir banks, following possible rapid drawdown. Weight values have been linearly assigned, decreasing from the average shoreline of the reservoir up to a distance of 200 m.

## **Parameter weighting**

Although there exists a variety of procedures for establishing parameter weights, the AHP permits to evaluate the consistency of the parameter pairwise comparison. In this procedure a value comprised between 9 ("extremely more important than"), 1 ("equally important as") and 1/9 ("extremely less important than"), is assigned to each pair of parameters in a square reciprocal matrix by rating rows relative to columns (Table 2).

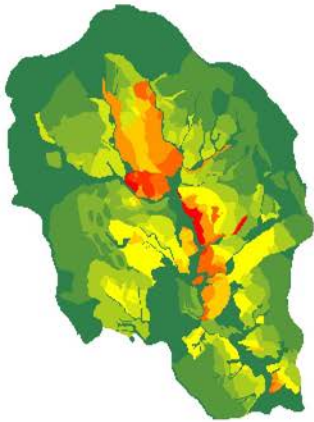
Weights of parameters are derived by taking the principal eigenvector of the parameter matrix. The procedure requires the principal eigenvector of the matrix to be computed to produce a best-fit set of weights. The procedure offers an advantage over other weighting methods, since it produces a *consistency ratio* (CR) which reveals the degree of consistency that has been used when developing the ratings. The CR indicates the probability that the matrix rating was randomly generated. Saaty (1980) suggests that matrices with CR greater than 0.10 should be re-evaluated.

The hazard map was produced by multiplying the weights of the classes with the weights of the parameter maps, and summing up all weights for each pixel, as explained earlier. The resultant scores were thresholded into four classes: very low, low, moderate and high (see Figures 4 and 5).

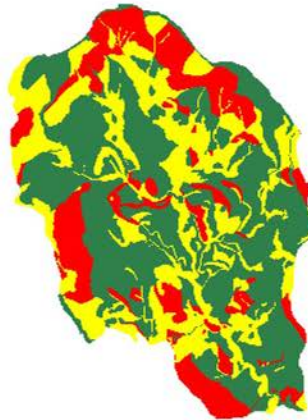
**Table 2.** Parameter weight assignment based on the analytical hierarchy process (consistency ratio=0.03).

	Slope angle	Proximity to gullies	Proximity to reservoirs	Land use change	Material	Landslide activity	Landslide phase	Weight
Slope angle	1							0.22
Proximity to gullies	1/4	1						0.06
Proximity to reservoirs	1/2	2	1					0.13
Land use change	1/3	2	1/2	1				0.07
Material	1/2	2	1	3	1			0.14
Landslide activity	2	4	3	3	2	1		0.29
Landslide phase	1/3	2	1/2	2	1/2	1/3	1	0.09

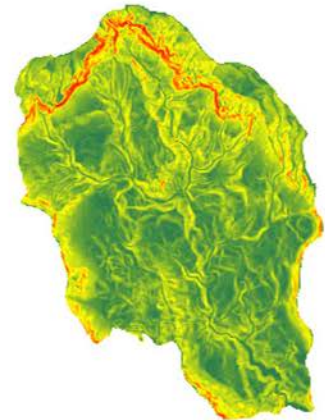
**Landslide phases**



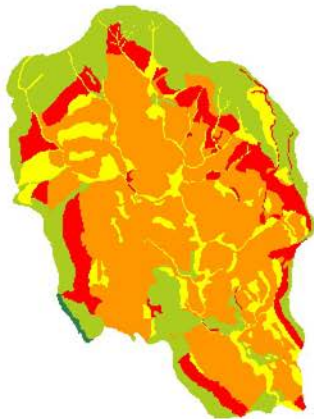
**Landslide activity**



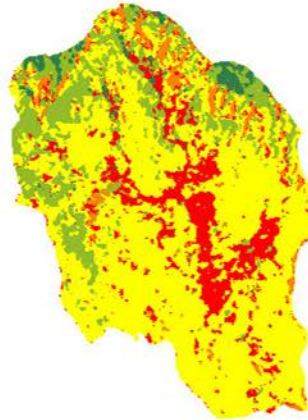
**Slope angle**



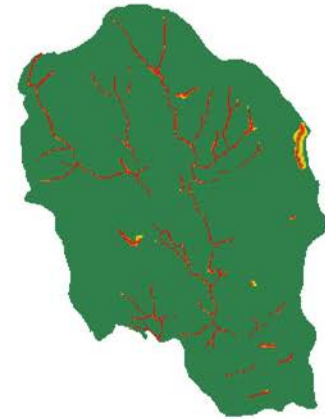
**Material types**



**Landuse changes**



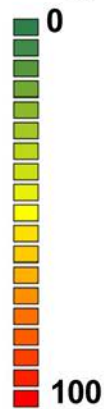
**Proximity to gullies**



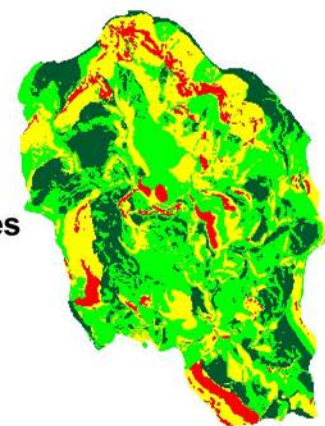
**Proximity to reservoir**



**Weight values**



**Classified hazard map**



**Hazard classes**  
Very low  
Low  
Moderate  
High

**Figure 5.** Terrain parameters used for indirect landslide hazard mapping in the Barranco de Tirajana basin. Colours represent class weights. The resulting hazard map is shown in the bottom-right

### Discussion of results

As a result of the analytical hierarchy process, terrain parameters such as landslide activity and slope angle largely outweigh others like proximity to gullies and land use change. As a consequence, the highest landslide hazard, as derived from the indirect assessment method, corresponds to rockfall occurrence on cliffs and scree, and on some talus deposits partly covering primary landslide headwalls. A number of sectors on gully sides in the most recent generation of landslides also show high hazard of instability, most likely in the form of shallow movements and small falls of the uncovered rock fragment deposits during heavy rainfall periods. Most of the ancient large landslide bodies do not appear to be subject to a major reactivation though. Some human activities, especially crop irrigation on terraced hillsides, also suggest a moderate susceptibility to small shallow displacements. No hazard from large, deep-seated landslides could be inferred, mainly because of the lack of subsurface information in most of the basin. However, such hazard is believed to be very low.

The hazard map derived from the indirect method was combined with that from the direct method produced by ITC in a GIS, and the overlap of the classes was calculated (Table 3). As can be seen from this table, there is a striking difference in the percentages of the four hazard classes between the two maps. The direct map indicates more areas as high hazard as well as very low hazard, as compared to the indirect map. The high hazard class in the indirect map (6.5 %) is much less than in the direct map (20.1 %). The indirect map has much more area classified in the intermediate classes low and moderate.

From joint interpretation of results with ITC, the differences between the two maps could be explained by a number of factors including (1) the fact that the indirect method did not differentiate between the various types of mass movements; (2) a considerable degree of generalisation which is inherent to the use of the indirect mapping approach. With the direct hazard mapping method it is possible to evaluate each polygon separately, based on the unique set of factors that are present in the polygon, whereas the indirect method has to use the same weight values for all locations with the same factors; (3) the addition of weight values gives the tendency to "flatten out" the result. The combination of many factor maps with moderate weights makes that the effect of a high or a low weight is less pronounced, and (4) the classification thresholds of the scores used for the indirect map, which have to be selected arbitrarily, and might have excluded too much area as having low hazard or high hazard.

**Table 3.** Comparison between the hazard maps made using the indirect and direct methods. The number of pixels of each overlap is given, as well as the percentage of the entire map in brackets.

Indirect hazard Mapping method	Direct hazard mapping method				
		High	Moderate	Low	Very low
High	2790	565	62	0	3417 (6.5 %)
Moderate	6833	3852	5001	102	15788 (30.2 %)
Low	920	2926	8605	9810	22298 (42.6 %)
Very Low	2	126	2427	8179	10865 (20.8 %)
Total	10545 (20.1 %)	7469 (14.3 %)	16095 (30.7 %)	18091 (34.6 %)	52368 (100 %)

### **Image processing techniques for delineating slope instability and landslide risk**

Suitable satellite image processing methods coupled with today's computer visualisation technology can effectively complement traditional aerial photo-interpretation, field mapping techniques and two dimensional map representations for delineating slope instabilities and illustrating their risk to local population and infrastructure. These methods can also help understanding landscape evolution due to geomorphological processes such as mass movements and soil erosion. They are as well particularly useful to explore remote slopes in mountainous areas. Whereas visualisation does not solve landscape simulation problems requiring, for instance, extensive field experiments for calibration, it helps to narrow the path to solutions (Mitas *et al.* 1997).

Most useful products for geomorphological exploration and risk illustration in Barranco de Tirajana integrate satellite images, base and thematic maps, and DEMs in either two- or three-dimensional representations. To this end, a high-resolution colour image of the basin was previously derived from fusion of Landsat TM and KVR-1000 images

### **Fusion of Landsat TM and KVR-1000 satellite images**

Image fusion can be simply defined as the combination of two or more images to form a new image by using a certain algorithm (Van Genderen and Pohl, 1994). Image fusion aims to integrate different data to obtain more information than can be derived from each of the single sensor data alone (Pohl and Van Genderen, 1998). As input to simulated perspective view products of Barranco de Tirajana, the 30m-resolution Landsat TM multispectral image of 05/03/98 was merged with a 2m-resolution KVR-1000 panchromatic image (0.51-0.76  $\mu\text{m}$ ) of 19/03/91. The latter was acquired by a photographic camera on board a Russian Cosmos satellite and delivered as a scanned 8-bit image. This was the only very-high resolution satellite image of the area publicly available at the time of the selection.

Three data fusion methods were attempted: principal component analysis (PCA), adding and multiplication (Figure 7). Prior to merging images acquired by different sensors, their resolution, geometry and radiometry need be harmonised (Pohl and Van Genderen, 1998). To avoid undesired geometrical distortions due to high relief differences within the study area, previously generated Landsat TM and KVR-1000 orthoimages were used. Prior to the fusion process, the Landsat TM image was resampled to match the resolution of the KVR-1000 image. However, to avoid the undesired blocky appearance of products from fusion of images with very different spatial resolutions, both images were first resampled to 4m-pixel size. The enlarged Landsat TM image was then smoothed out using a 7x7 kernel mean filter (Chavez, 1986).

The original KVR-1000 image was very noisy. Most of the nearly periodic line noise patterns irregularly distributed throughout the image were successfully removed by applying wedge mask filters in the Fourier (frequency) domain. However, the dotted-like noise affecting the whole image could not be removed without a significant loss of spatial detail.

The KVR-1000 image brightness values were normalised to those of the Landsat TM image to reduce variations due to different sun illumination angle and atmospheric conditions. To this end, a regression procedure (Jensen *et al.*, 1995) was carried out between the KVR-1000 image and channel 3 of the Landsat TM image, since the spectral range of TM channel 3 is comprised in that of the KVR-1000 image, lying also in the centre of the range of the latter image. Applying a regression equation to the KVR-1000 image predicts what a given brightness value would be if it had been

acquired under the same conditions as the Landsat TM image (Jensen *et al.*, 1995). The regression equation was built by correlating the brightness of a set of pixels in both images. To this end, 20 pixel values were sampled from wet (water) and dry (bare soil) image patches (Figure 6). A regression coefficient ( $R^2$ ) of 0.94 was obtained. As a result of the regression, the following equation was used for normalising the digital values (DN) of the KVR-1000 image to those of the Landsat TM image (see Figure 7C).

$$DN_{Normalised}(KVR-1000) = 0.215 * DN(KVR-1000) + 12.282$$

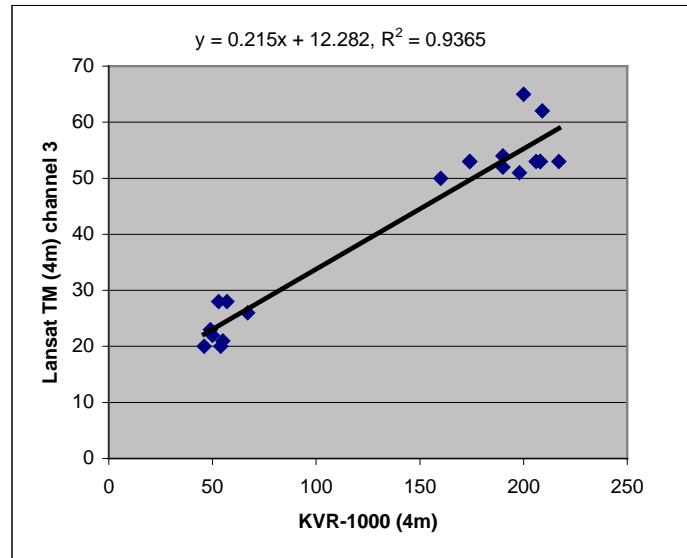


**Figure 6.** Linear regression between samples of pixel values in the KVR-1000 (4m) and Landsat TM smoothed channel 3 (4m) images

***Principal component analysis (PCA) method***

In the PCA fusion method at least three bands of the multispectral image (here the Landsat TM image) need be used as input to a PCA transformation. The panchromatic image (the KVR-1000) is stretched to have approximately the same variance and mean as the first principal component (PC1). The stretched panchromatic image replaces the PC1 image before the data are transformed back into the original space (Chavez *et al.*, 1991). These authors assume that the PC1 image and the stretched panchromatic image are approximately equal, therefore the latter can replace the former. This assumption, however, does not stand for our data, since the correlation between the KVR-1000 image and the original TM channels is low (Table 4). As a consequence, the correlation of the KVR-1000 image with the first principal component of the TM image is also low. The low correlation can be mainly explained by the large difference in spatial resolution between the two data sets, the long period elapsed between image acquisitions (seven years), and spectral window differences.

**Table 4.** Correlation coefficients of the KVR-1000 (4m) image with the TM smoothed (4m) channels.

	TM smoothed (4m) channels					
	1	2	3	4	5	7
KVR-1000 (4m)	0.37	0.35	0.39	0.05	0.30	0.34

### ***Adding method***

This method has been reported by Chavez (1986) to be successfully applied to merging Landsat TM images and high-altitude panchromatic aerial photographs. Following this method, our two data sets have been added on a pixel by pixel basis as follows:

$$\text{Fused image} = (TM1 + PAN, TM2 + PAN, TM3 + PAN, TM4 + PAN, TM5 + PAN, TM7 + PAN)$$

Where  $TM_n$  is the Channel  $n$  of the Landsat TM image, and  $PAN$  is the Panchromatic image (KVR-1000). The resulting new image channels were linearly stretched to 0-255 digital values (see Figure 7E).

### ***Multiplication method***

In the multiplication method the two data sets are multiplied pixel by pixel as follows:

$$\text{Fused image} = (TM1 * PAN, TM2 * PAN, TM3 * PAN, TM4 * PAN, TM5 * PAN, TM7 * PAN)$$

As in the adding method, the resulting image channels were linearly stretched to 0-255 digital values (see Figure 7F). This method was successfully applied, amongst other researchers, by Yesou *et al.* (1993) to merge Landsat TM and SPOT panchromatic images. The possibilities of combining the data using band multiplication or summation, however, are manifold (Pohl and Van Genderen, 1998).

### **Discussion of image fusion products**

The quality of the image fusion products can be assessed either statistically or visually, depending on the application pursued. Ideally, the method used to merge images should not distort the spectral characteristics of the higher-spectral resolution image (Chavez *et al.*, 1991). To this end, the statistical comparison focused on correlation analyses between the spectral characteristics of the fused images and those of the original Landsat TM image. Three PCA fusion procedures, resulting from selecting Landsat TM channels 1 3 4, 3 4 5 and 1 3 4 5 respectively as input to the PCA, were tested. The correlation coefficients between the first principal component of each of these PCA images and the KVR-1000 image are shown in Table 5. From these low correlation coefficients it can be expected that the image retransformed into the original spectral space will also show low correlation with the original TM channels.

**Table 5.** Correlation coefficients of the KVR-1000 image versus the first principal component (PC1) image made up from Landsat TM input channels 1 3 4, 3 4 5 and 1 3 4 5

	PC1-TM 1,3,4	PC1-TM 3,4,5	PC1-TM 1,3,4,5
KVR-1000 (4m)	0.27	0.28	0.30

The PCA-, adding- and multiplication-fusion images were also statistically compared with the original channels of the Landsat TM image (Table 6).

**Table 6.** Correlation coefficients of the 4m-resampled and smoothed Landsat TM channels with respect to the corresponding channels of the fused images using the PCA, adding and multiplication methods. (\*) Highest correlation coefficient for the Landsat TM channels.

Fused images	Landsat TM channels					
	TM1	TM2	TM3	TM4	TM5	TM7
PCA-134	0.35	-	0.55	0.35	-	-
PCA-345	-	-	0.45	0.46	0.35	-
PCA-1345	0.30	-	0.46	0.46	0.40	-
Adding	0.81*	0.72	0.83*	0.81*	0.95*	0.91*
Multiplication	0.65	0.73*	0.81	0.67	0.84	0.89

From the statistical point of view, the adding method was superior to both the multiplication and PCA methods in preserving the spectral information of the original TM image, since the resulting image shows the highest correlation with the TM channels. However, the adding method notably degraded the information content of the original KVR-1000 image, thus producing the lowest quality images from a visual point of view (see Figure 7E). On the contrary, the PCA method ranked at the top in terms of visual quality, since it best preserved the fine linear and textural details (e.g. roads, buildings, crop fields, shrubland) originally contained in the KVR-1000 image, despite losing some of the spectral information provided by the TM image (see Figure 7D). As reported by Bethune *et al.* (1998), the PCA method can generally be used to produce good looking colour composites if preservation of spectral information content is not a prerequisite, or when the resolution ratio between the multispectral image and the panchromatic image is too high to expect realistic results. In all three methods, however, some image artifacts as a result of local land cover differences between the acquisition dates of the two input images could not be prevented. False colour composite images derived from the PCA fusion method have been used to simulate perspective views of Barranco de Tirajana.

### Visualisation products

Effective visualisation products for the Barranco de Tirajana basin include shaded relief images, perspective views, 3D animations, and texture-segmented images.

#### *Shaded relief images*

Shaded relief images can be generated from a DEM raster image by first computing, for each pixel, a vector representing a unit normal to the surface from a 3x3 pixel window centred at that pixel. Light reflectance is then modelled by the dot product of the unit vector and the user-defined sun vector (azimuth and elevation).

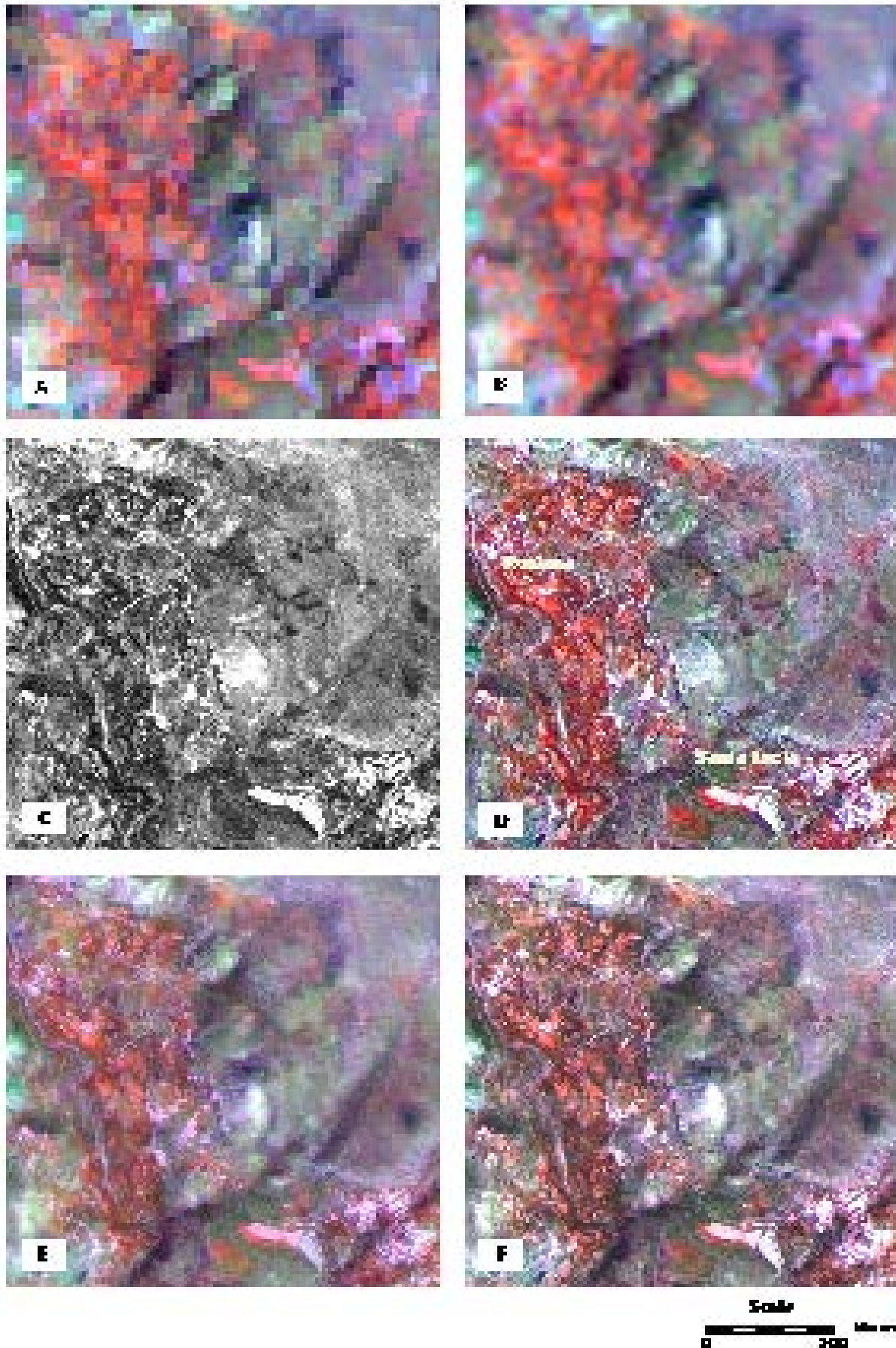


**Figure 7.** Fusion of Landsat TM and KVR-1000 satellite images over the Rosiana–Santa Lucía area, Barranco de Tirajana. (A) Original Landsat TM false colour composite image (30m) from bands 4, 5 & 3 (RGB). (B) Same image after resampling to 4m-pixel and smoothing. (C) 4m-resampled and radiometrically normalised KVR-1000 image. (D) PCA-fused image (channels 4,5,3 as above) from Landsat TM input channels 1,3,4 & 5. Buildings and some roads are shown in white; irrigated crops and healthy vegetation are shown in red; cyan and greenish hues denote shrubland and bare soil. Single eucalyptus can be distinguished along the road connecting Santa Lucía and Rosiana. (E) Adding-fused image (channels 4,5,3). (F) Multiplication-fused image (channels 4,5,3).

Shaded relief images are relatively simple products that can be used to enhance subtle topographic detail. Landslide features such as scarps and backtilted-block-derived depressions can be readily delineated from simulated shaded relief views of high-resolution DEMs. Since these images are georeferenced products, they can help to precisely map (and therefore better delineate) landslide features already drafted on base maps from aerial photointerpretation and fieldwork. In addition, shaded relief maps can be directly integrated with base or thematic maps to help illustrating landslide occurrence, as well as risk to infrastructure and urban settlements (Figure 8). The effectiveness of using shaded relief images for landslide investigations largely depends on the resolution of the DEM and on the type and size of landslide surface features. For high relief areas like Barranco de Tirajana, 5m is considered as the minimum contour interval of topographic maps to derive raster DEMs that can be effectively used for landform mapping, irrespective of the raster sampling interval chosen.

#### *Perspective views*

Georeferenced remotely sensed imagery and thematic maps can be displayed either separately or combined together and draped over a DEM to produce realistic three-dimensional representations of the landscape. In addition, dynamic visualisation tools allow for interactive manipulation, where the user is involved in altering parameters and viewing results in real time (Davis and Keller, 1997). Such parameters typically include sunlight (azimuth and elevation angles together with scene brightness), relief exaggeration and, chiefly, view point. The capability of interactively viewing a virtual landscape from any point of view can be specifically applied to understanding the geomorphology of very hilly terrain. Simulated perspective views are thus one of the most effective visualisation tools for exploration of landscape processes and presentation to both specialists and non-specialists.

The use of satellite imagery draped over a DEM proves to be particularly valuable to generate 3D views of extensive areas, while showing landscape spectral features beyond the visible range. Medium-spatial resolution multispectral images such as 30m Landsat TM (or alternatively 23m IRS-1C LISS and 20m SPOT XS, amongst others) can thus be used to produce false-colour panoramic views of the whole Barranco de Tirajana basin (Figure 9A). Until the very recent launch of the Ikonos satellite, high-resolution multispectral images showing finer ground detail could only be generated from the fusion of lower resolution multispectral imagery such as Landsat TM and higher-resolution panchromatic imagery including IRS-1C PAN (5.8m), SPOT PAN (10m) and, as done in this experiment, KVR-1000 (2m).

In order to analyse and illustrate the emplacement of major landslides in the Barranco de Tirajana, simulated perspective views have been interactively generated both from DEMs alone and from 4m-pixel Landsat TM-KVR1000 fused images. Figure 9B thus shows the same view as Figure 9A, but with much higher detail. Figure 10 displays a 3D view of the Rosiana-Santa Lucía district revealing major scarps as a result of the various movement phases of the Pajonales rock slide, including the Rosiana earth slide, which is considered to be the last phase of Pajonales landslide. The location of landslides with respect to land use classes has been illustrated in Figure 3. In this figure, one can observe not only the setting of built-up areas on major ancient landslides, but also intensive crop irrigation over landslide bodies in the neighbourhood of the towns of Santa Lucía and Rosiana. Such irrigation practices might become a triggering factor of shallow local slope movements affecting some houses.

### *3D Animations*

Cost-effective computer-generated animations, although typically not suited to interactive analysis, are another means to illustrate relevant landscape features both to specialists and non-specialists. The animation process requires the compilation of a set of perspective view images that will be the frames of the movie sequence. Animations can be created using a number of methods. Two methods have been used in the project: the first consisted of the time-consuming generation of still perspective view images of every single frame, as reported earlier, by selecting the appropriate viewing parameters for each frame. These sequential frames were later combined in a movie file using an inexpensive commercial package. In the second, most efficient method, irregularly spaced single views and smooth interpolations between them were created using a professional geographic imaging package (Erdas Imagine).

A moving viewpoint perspective computer animation was created simulating a flythrough of the central part of the Barranco de Tirajana basin. The demonstration movie consists of 300 frames of 285x204 pixels portraying perspective views of the basin by draping a false colour composite Landsat TM image of 05/03/98, made from bands 4 (near infrared), 5 (short-wave infrared) and 3 (blue), over the DEM30 previously generated. The movie has been sampled at 16 frames per second and included in AVI format in the project's CD-ROM.

### *Textural segmentation methods*

The application of semi-automatic textural segmentation methods to high-resolution remotely sensed imagery has been reported successful to discriminate landslide hummocky surfaces and other slope instability features, hence being valuable for landslide mapping (Hervás and Rosin, 1996). A supervised texture discrimination technique was attempted on the KVR-1000 image. This technique consisted of calculating similarity between a reference texture spectrum (obtained from training samples) and spectra from moving image windows.

Results were however unsatisfactory, as it could be somehow expected from the noisy appearance of the KVR-1000 image. Unfortunately, no other high-resolution image, including IRS-1C PAN, was available for Gran Canaria. The resolution of Landsat TM imagery was inadequate for applying textural segmentation procedures for landslide discrimination.

### **Lineament mapping**

The possible spatial relationship between major landslide features in Barranco de Tirajana and volcanic or tectonic structures in Gran Canaria was investigated. To this end, lineament maps of the island were derived from the geometrically corrected Landsat TM image of March 1998. Kirsh filters (e.g. Suzen and Toprak, 1998) were applied in the four major directions to TM bands 4, 5 and 7, followed by image smoothing to remove some noise introduced by the directional filtering. Next, a majority filter together with contrast stretching was applied to enhance image edges. Relevant lineaments were extracted interactively from interpretation of these images with the help of available geological and topographic maps. In the absence of major tectonic structures in the island, preliminary results did not show a significant correlation between landslides in the Barranco de Tirajana basin and either major circular or radial volcanic structures.

**Figure 8.** Shaded relief image of the Rosiana-Santa Lucía district in Barranco de Tirajana, illustrating the location of major landslide features with respect to roads and houses (simulated sun azimuth: 90 deg.; elevation: 40 deg.)

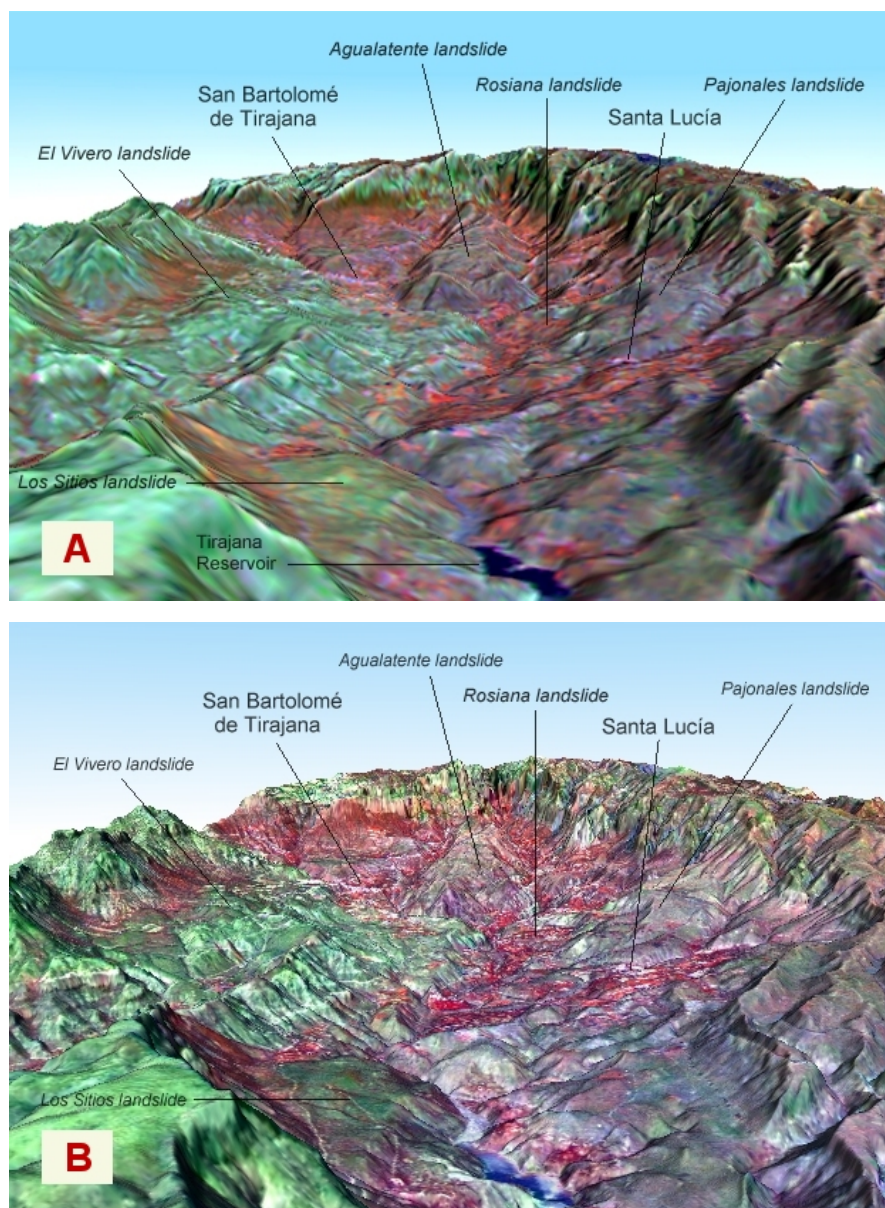
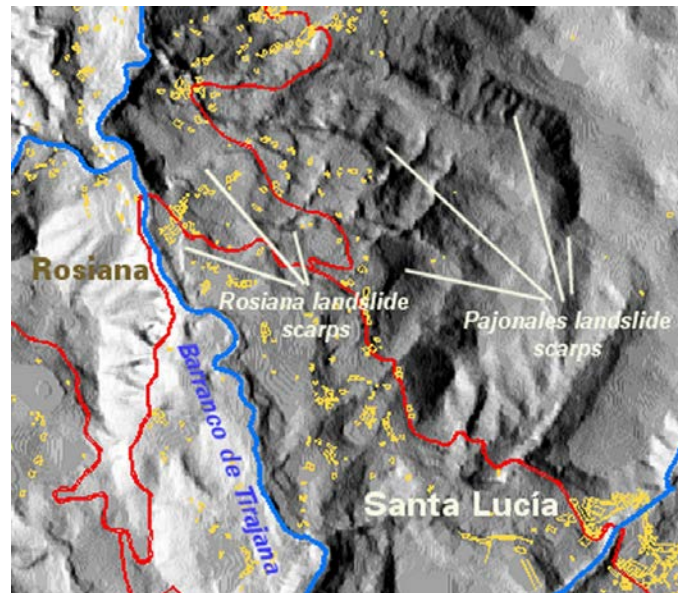
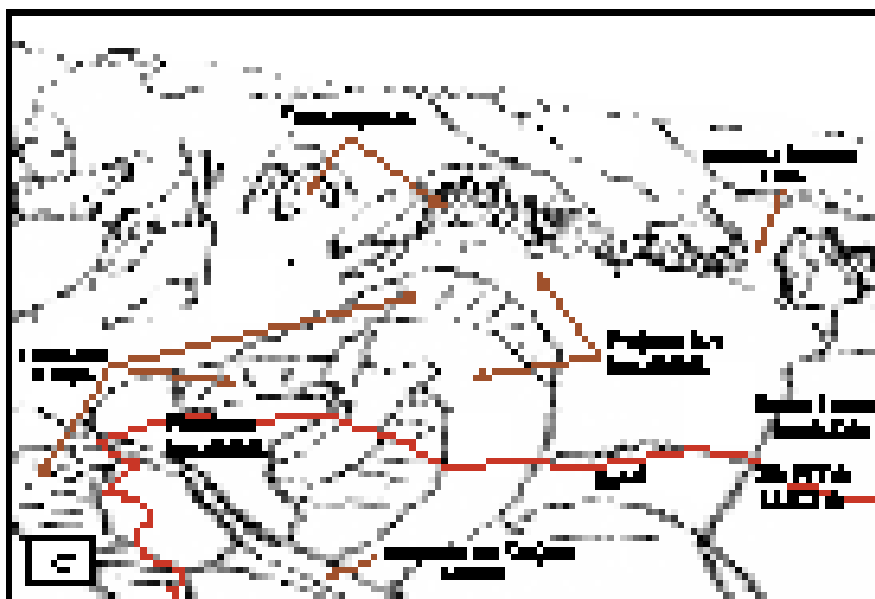
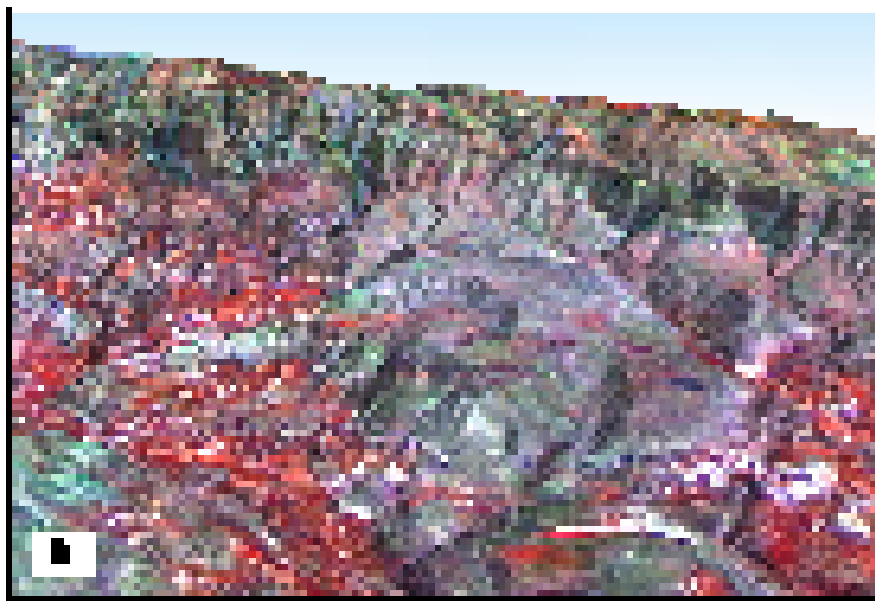
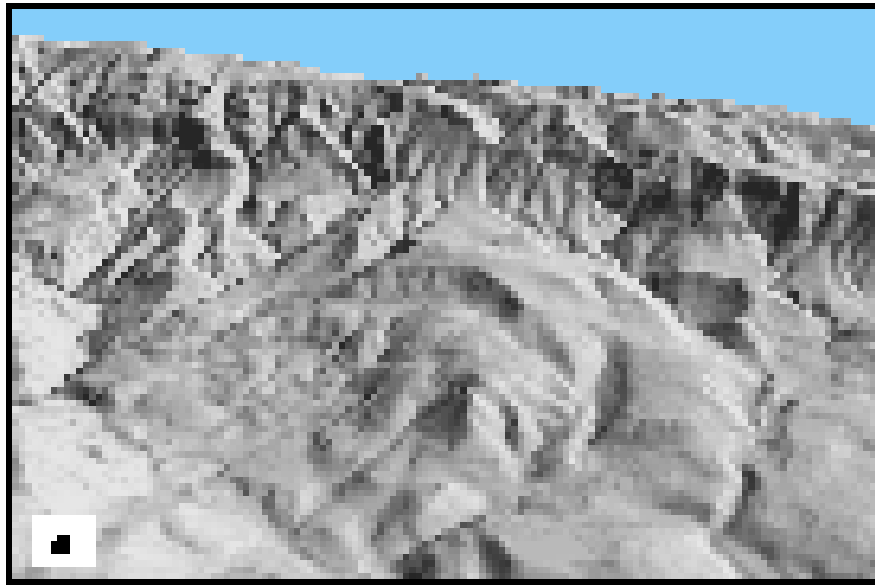


**Figure 9.** Simulated perspective views of the Barranco de Tirajana basin, made from (A) a false colour composite Landsat TM 4,5,3 (RGB) image of March 1998 and (B) a Landsat TM-KVR1000 PCA-fused image, both draped over DEMs at different resolutions. Although it is not possible to unequivocally assign colours to land cover types in these products, orchards and dense bushes are generally shown in reddish hues, shrubby vegetation in green, bare soil in magenta, and major villages in pinkish blue.



### **Monitoring landslides using optical remote sensing**

Optical (visible-infrared) satellite remote sensing has hardly been used so far for direct landslide monitoring. A major reason for this has been the insufficient spatial resolution provided by most spaceborne earth observation systems. Efforts have thus mainly concentrated on extracting possible indirect landslide indicators such as land cover pattern disruption and specific sun-shading features (Hervás *et al.*, 1996). The very recent launch of the Ikonos-2 satellite, the first commercial very-high resolution earth observation system, together with other planned missions, opens however new perspectives for landslide monitoring from optical spaceborne systems over extensive areas.

To evaluate the potential application of new satellite images at 1m resolution to detect major changes in landslides, as a possible alternative to both electronic distance measuring (EDM) and GPS methods over extensive areas, trial simulations have been conducted on existing aerial photographs over the Tessina area in Belluno province, Italy (Chapter 6).

The Tessina landslide is a complex movement developed on Eocene flysch deposits composed of marl, sandstone and calcareous units overlaying Jurassic limestone, affecting an area covered mainly by grassland and woodland with scattered small urban settlements. The movement consists of a series of rotational slides at its head quickly transforming into a 2km-long mudflow. Surficial Quaternary deposits including colluvium and glacial till have also been mobilised by the landslide. The Tessina landslide, which was first triggered in 1960, has since undergone a number of movement episodes, some of which have disrupted communication and threatened various villages. The landslide has been intensively monitored since 1992 by means of EDM stations, directional bars, wire-extensometers, echometers, and video cameras (Pasuto *et al.*, 1997).

Photographic prints of Tessina exist from a number of flights from 1954 to 1994, therefore spanning several reactivation periods. Many of them, however, cannot be suitably used for image processing since either diapositives (for precise scanning) or camera calibration certificates are not available. It was thus decided to focus this experiment on mapping ground surface changes in the Tessina landslide body and adjacent areas as a consequence of the latest major reactivation in 1992, for which black and white aerial photographs acquired in 1988, 1989 and 1994 at 1:75,000 scale were available. The photograph diapositives were scanned at 14 micron to produce the 1m-pixel digital images used in the experiment.

To automatically detect changes on multitemporal images, these must be geometrically registered and radiometrically comparable. Mapping ground surface changes has thus entailed the following image processing sequence (Hervás *et al.*, 2000).

### **DEM generation**

A digital elevation model of the Tessina area has been generated from an aerial photograph stereo pair using digital photogrammetric techniques. To this end, the 31/08/89 photographs were used because of their lower shadowing affects. The process encompassed first the aerial triangulation for the block of the two photographs to establish the geometry of the camera relative to objects on the ground surface. Triangulation typically includes two steps, interior and exterior orientation of the camera. The former was accomplished taking the fiducial marks as reference. The exterior orientation was established using 12 ground control points (GCPs) distributed across the overlapping area of the photograph stereo pair. GCPs' XYZ coordinates were

extracted from 1:5,000 topographic maps. Considering the accuracy of the base maps used ( $\pm 2.5\text{m}$ ), the accuracy of the triangulation (standard deviation of unit weight: 0.4; RMS 3.3m for X, 3.6m for Y and 3.6m for Z) was regarded acceptable. A better accuracy could however be obtained using GPS measurements.

A pattern-matching algorithm was used to locate the same ground features on the photograph stereo pair. Triangulation information was then used to calculate XYZ values for each correlated feature. Two XYZ ASCII-value DEMs were interpolated at 5m and 20m ground intervals respectively. They were then rasterised to 5m- and 20m-pixel DEMs. The former showed some errors on the hills located in the most peripheral areas of the overlapping section of the photographs, as a result of low correlation in these areas. This constraint could have been overcome using also matching information extracted from stereo pairs of the adjacent photograph strips. The 20m-pixel DEM did not show these correlation errors because of its coarser resolution. For producing orthophotographs, using the 20m-pixel DEM was considered adequate.

### **Aerial photograph orthorectification**

Large geometric distortions are common in aerial photographs because of their central projection; for Tessina these effects are aggravated by notable altitude differences within the photographs, even for the high-altitude flights selected. To digitally analyse photographs acquired at different dates, they must be orthorectified to remove both projection and relief displacement effects.

Orthorectification was first accomplished for one of the photographs of 31/08/89 (used for constructing the DEM) by applying a geometric transformation using the 20m-DEM values and pixel positions resulting from the triangulation process. Orthophotos were produced from photographs of 28/09/88 and 07/10/94 using the same DEM and the orthophoto of 31/08/89 as reference for GCP collection. 6 GCPs for each photograph were sufficient to achieve sub-pixel accuracy in the orthorectification process of the small area common to both the aerial photographs and the DEM.

### **4.3 Radiometric normalisation**

Differences in illumination (and therefore also in shadowing), atmospheric conditions and sensor/camera (and film) response may cause remarkable pixel brightness variations for a target on remotely sensed images acquired at different dates. These effects are usually higher between flights than for sun-synchronous satellite images, since aerial photographs are often available from different seasons and at different times of day. For change detection analyses on remote sensing images, these variation effects may be corrected either by absolute calibration of the single images or by pixel brightness normalisation between the images (Chuvieco, 1996). For aerial photographs, the latter approach appeared more feasible.

A relative radiometric normalisation procedure was performed between the orthoimages of 28/09/88 and 07/10/94. These two images had been selected in our final analysis since their dates were more similar in relation to illumination effects and vegetation phenology. In this procedure, the 1994 image was normalised to the 1988 image by applying gain ( $a_1$ ) and bias ( $a_0$ ) coefficients derived from regression analysis between the two images (Hall *et al.*, 1991), following the simple equation:

$$NI_{1994} = a_0 + a_1 * I_{1988}$$

Where:  $NI_{1994}$  are the pixel values of the 1994 orthophotograph radiometrically normalised to those of the 1988 orthophotograph,  $I_{1994}$  are the raw pixel values of the 1994 orthophotograph, and  $a_0 = 26.655$  and  $a_1 = 0.7482$ .

The main statistical parameters for all the images are shown in Table 7. As a result of normalisation, the mean of the corrected 1994 orthoimage became almost equal to that of the 1988 orthoimage. However, statistical differences are still apparent. These are mainly explained by land cover changes between the two dates including those owing to mass movements. Minor contribution from remnant differential illumination effects may also be possible. Both 1988 and normalised 1994 images can now be digitally compared to investigate changes caused by mass movements.

**Table 7.** Main statistics of the Tessina orthophotographs before and after radiometric normalisation

Aerial photograph	Mean	Standard deviation	Min	Max
<b>28/09/88 (reference)</b>	90.72	29.98	34	250
07/10/94	85.71	33.22	28	255
Radiom. normalised 07/10/94	90.33	24.82	47	217

### Change detection process

To map land surface changes as a result both of reactivation of the Tessina landslide and of other possible undocumented movements in the area during the 1988-1994 period, image change detection methods were applied to the normalised orthophotographs of both dates. The methods included the creation of an image expressing the differences in pixel brightness between the two input images, followed by thresholding to discard differences possibly related to non-surface changes (Singh, 1989; Eastman *et al.*, 1994).

Two pre-classification techniques have been attempted to derive pixel value variations between the images, namely ratioing and differencing. Both techniques assume that a change in land cover will produce a change in pixel brightness, with in many cases holds true.

The ratio procedure involves a simple ratio operation between the 1994 and 1988 images. By this operation, more weight is progressively given to the pixel differences closer to zero. As a result of image ratioing, the numeric scale is neither symmetrical nor linear, thus making the subsequent thresholding process difficult. To ease thresholding, a log transformation can be applied to the ratio image, thus making the scale linear and symmetrical about zero.

Image differencing involves the subtraction of pixel values between both images. Unlike the ratio technique, the difference method highlights all cases of change to the same extent. Using statistics theory, a number of thresholding procedures could then be applied to the straight change images to discriminate “true-change” image pixels from “no-change” pixels. Since both the natural-log transformed ratio image and the difference image show normal distributions, a standard deviation based thresholding has been applied. According to the normal model, 95 percent of all differences fall within 1.96 standard deviation on either side of the mean. Applying thresholds from a few small variations of this value were checked in the field, confirming the 1.96 SD threshold as most suitable. Using this thresholding procedure only 2.5 percent of change values at the tails of the histogram were retained as significant. Thresholding the natural-log ratio image resulted in a noisy “change” image compared to the thresholded difference image. Since the difference image also accounted equally for any pixel value change, this was finally selected as “change” image (Figure 11). Further thresholding

between positive and negative brightness changes was undertaken to discriminate new soil outcrops from growing (or new) vegetation patches during the elapsed period (Figure 12). Although with some caution, these two classes could generally be assumed for Tessina to be associated to ground instability and stability conditions respectively.

### **Discussion of results**

Figure 12 illustrates positive pixel brightness changes in red. Within the Tessina landslide body, these represent ground change patterns mostly associated with the reactivation occurred in 1992, documented by Pasuto *et al.* (1997). Two major change areas can be observed: the area detached in 1992 at the head of the landslide, which produced a landslide surface increase of 45,000 m<sup>2</sup>, and new runout material at the mudflow toe, near Lamosano. Pixels in yellow, in turn, appear mostly associated with either soil moisture increase or simple land cover changes, including the growth of natural vegetation on temporarily stable sectors of the landslide body. While vegetation growth may be an indicator of ground stability, soil moisture conditions (which can change dramatically over short periods of time) conceal the brightness properties of the underlying ground, especially on panchromatic images. As shown in the figure, the ground area detached by the 1992 movement could not be fully mapped using automatic change detection techniques. This may be explained by the high resemblance between the surface characteristics of the formerly stable ground at some specific locations and those of some upstream blocks displaced as far as the geographical location of the originally stable patch. In addition, because of the long time elapsed between the photographic shots, some remobilised sectors within the landslide body could appear as “negative” changes (meaning stability) as a consequence of vegetation growth during the stability period comprised between the 1992 movement and the 1994 image take.

Numerous changes are also apparent throughout the area, away from the Tessina landslide. Most of them can be explained by man-made land use changes. Although 1m-resolution remotely sensed imagery has been proved useful to map landslide-related surface changes at scales of the order of 1:10,000, typically less time spaced observations than those provided by available aerial photographs would be needed to more precisely monitor ground surface dynamics. This constraint is expected to be greatly surmounted by the new generation of high-resolution earth observation satellite systems. In addition, the multispectral imaging capabilities to be provided by some of these systems will help to better discriminate surface changes exclusively due to slope movements. The availability of archival aerial photographs over most areas, however, makes these very useful to automatically extract relevant landslide-related surface changes during the last decades. Finally, image processing techniques on digital aerial photographs must also be used with caution, since, unlike images acquired by satellite or airborne scanners, pixel values are not calibrated.

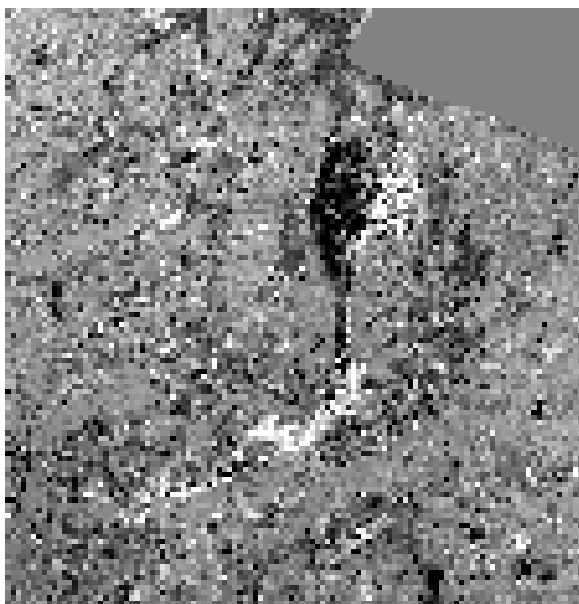
a) 27-02-1978 Orthophotograph



b) Stereoscopic 07-10-1998 Orthophotograph



c) Difference image



d) Thresholded difference image

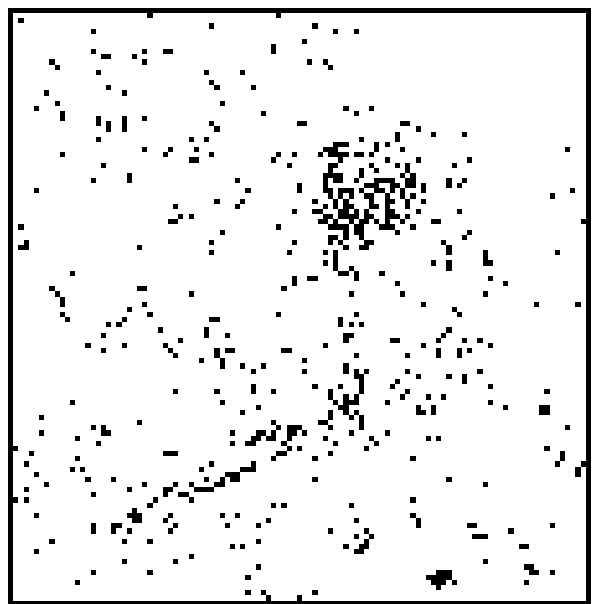


**Figure 11.** Change detection in Tessina landslide from digital aerial photographs, using the image differencing method. Change areas are illustrated in black on (D).

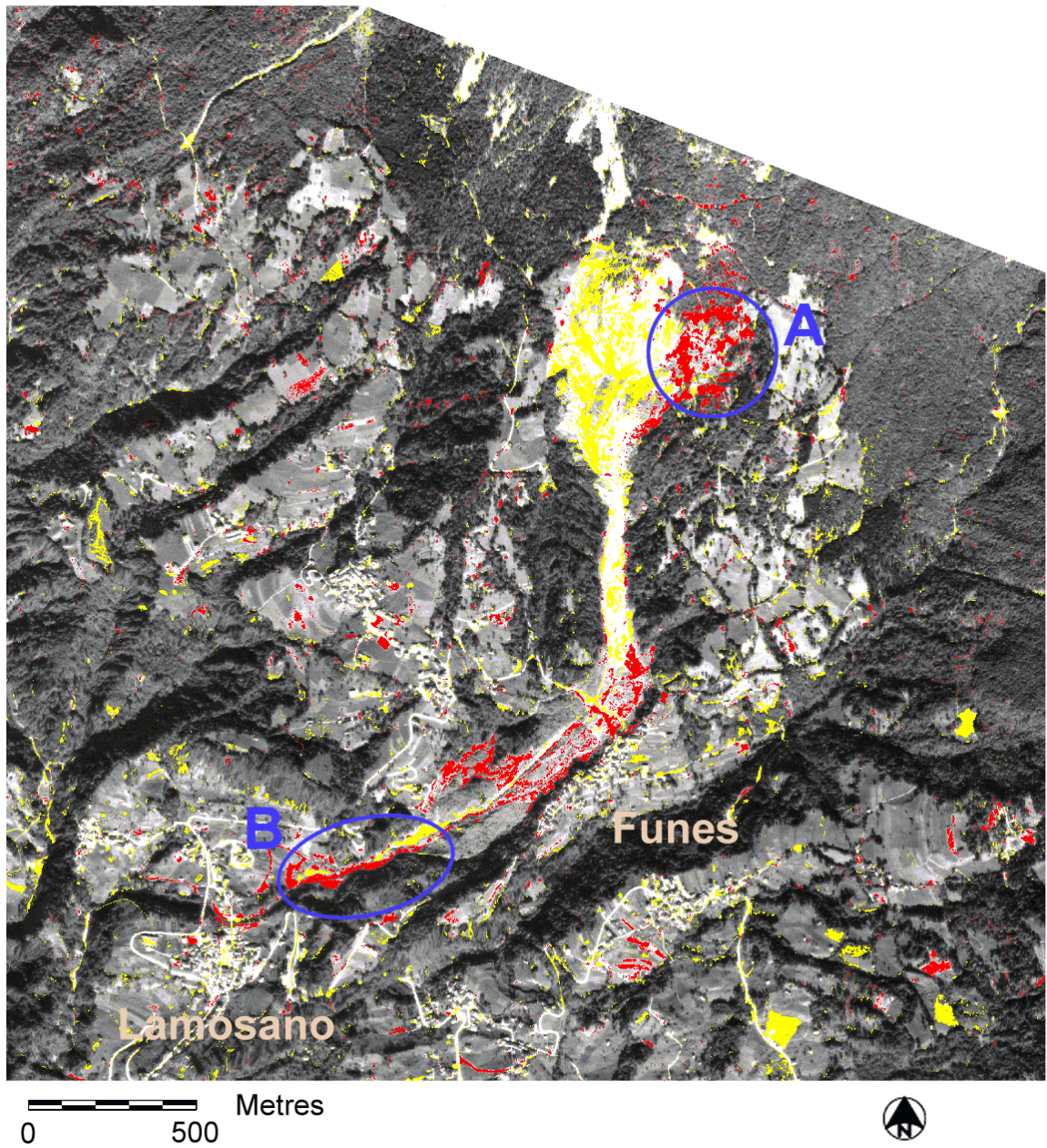


**Figure 12.** Changes undergone in the Tessina landslide between 1988 and 1994, overlaid on the 1994 orthophotograph for illustration. Red pixels within the landslide body represent changes often associated to landslide reactivation. Changes due to soil moisture increase and vegetation growth are depicted in yellow. The zone detached in 1992 has been highlighted in A; new runout material in B.

## **Conclusions**

The use of optical spaceborne remote sensing and its integration with spatial data has proved valuable to a number of investigations regarding large-volume landslides.

GIS-based heuristic approaches including direct and indirect mapping methods have revealed useful and cost-effective for assessing landslide hazard at medium scales (1:25,000 to 1:50,000) when costly geotechnical and groundwater data are not available. Although direct hazard mapping techniques may be time consuming, they may give detailed results since each area is evaluated individually. An indirect hazard mapping method using multicriteria evaluation techniques to assign weights to selected terrain parameters and classes has also proved a valid alternative to direct hazard mapping methods, and especially to statistical methods, in areas like the Barranco de Tirajana basin, where the dominant landslide occurrence prevents the use of robust sampling strategies. Both methods, however, involve a certain degree of subjectivity either when mapping hazard directly or when allocating weights to the parameter classes, therefore requiring high analyst expertise. Nevertheless, in the indirect method designed the allocation of parameter weights can be eased using an analytical hierarchy process.

The contribution of land use change maps, derived from classification of multitemporal visible-infrared Landsat TM images, has demonstrated of relevance to the GIS indirect hazard assessment approach. In particular, these maps highlighted possible hazard from shallow mass movements to scattered houses in irrigated areas.

Shaded relief images and dynamic three-dimensional representations of high resolution DEMs and computer-enhanced satellite images are effective visualisation techniques not only for exploring major slope instability and erosive processes (therefore helping to delineate major landforms), but also for understanding the spatial relationship between landslides and land use. These products are also very useful to illustrate mass movement risk to built-up areas and major infrastructure. Whereas typically more than a single simulated perspective view or 3D map needs be produced to cover a hilly area entirely, these products are easy to understand, particularly for a non-specialist decision-maker. These techniques however do not substitute but complement traditional aerial photointerpretation and field surveys.

The application of automatic image change detection methods to simulated high-resolution multitemporal satellite imagery using digital aerial photographs has proved useful to map landslide-related land cover changes, despite some limitations mainly due to both the temporal and spectral resolution of available aerial photographs.

Because of the repetitive observations starting to be provided by high-resolution satellites, including multispectral capabilities, satellite image processing methods can be regarded as complementary to EDM, GPS and other ground-based techniques for landslide monitoring over extensive areas at scales of the order of 1:10,000. A major research effort, however, will still be needed to derive landslide movement rates from optical satellite imagery, especially for landslides involving high internal deformation.

## References

- Barredo, J.I., 1996. *Sistemas de Información Geográfica y Evaluación Multicriterio en la Ordenación del Territorio*, Madrid: Ra-Ma.
- Barredo, J.I., Benavides, A., Hervás, J. and Van Westen, C.J., 2000. Comparing heuristic landslide hazard assessment techniques using GIS in the Tirajana basin, Gran Canaria Island, Spain. *International Journal of Applied Earth Observation and Geoinformation* (in press).
- Barredo, J.I., Hervás, J., Lomoschitz, A., Benavides, A. and Van Westen, C.J., 1999. Landslide hazard assessment using GIS and multicriteria evaluation techniques in the Tirajana basin, Gran Canaria Island. *Proc. 5<sup>th</sup> EC GIS Workshop*, Stresa, Italy, 28-30 June 1999. European Commission (in press).
- Bethune, S., Muller, F. and Donnay, J.P., 1998. Fusion of multispectral and panchromatic images by local mean and variance matching filtering techniques. *Proc. Conf. Fusion of Earth Data*, Sophia Antipolis, France, 28-30 January. 31-36.
- Brabb, E.E., 1984. Innovative approaches to landslide hazard and risk mapping, *Proc. 4<sup>th</sup> International Symposium on Landslides*, Vol. 1, 307-324. Canadian Geotechnical Society: Toronto.
- Carrara, A., Cardinali, M., Detti, R., Guzzetti, F., Pasqui, V. and Reichenbach, P., 1991. GIS techniques and statistical models in evaluating landslide hazard, *Earth Surface Processes and Landforms*, Vol.16, 427-445.
- Chavez, P.S. (Jr.), 1986. Digital merging of Landsat TM and digitized NHAP data for 1:24,000-scale image mapping, *International Journal of Remote Sensing*, Vol. 52, 1637-1646.
- Chavez, P.S. (Jr.), Sides, S.C. and Anderson, J.A., 1991. Comparison of three different methods to merge multiresolution and multispectral data: Landsat TM and SPOT panchromatic, *Photogrammetric Engineering and Remote Sensing*, Vol. 57, 295-303.
- Chuvienco, E., 1996. *Fundamentos de Teledetección Espacial*, tercera edición revisada, Madrid: Rialp.
- Crippen, R.E., 1989. A simple spatial filtering routine for the cosmetic removal of scan-line noise from Landsat TM P-tape imagery. *Photogrammetric Engineering & Remote Sensing*, Vol. 55, No. 3, 327-331.
- Davis, T.J. and Keller, C.P., 1997. Modelling and visualizing multiple spatial uncertainties, *Computers and Geosciences*, Vol. 23, 4, 397-408.
- Eastman, J.R., McKendry, J. and M. Fulk, M. (eds.) 1994. *Change and time series analysis. Explorations in GIS Technology*, Vol. 1, Geneva, Switzerland: UNITAR
- Hall, F.G., Strebel, D.E., Nickenson, E. and Goetz, S.J., 1991. Radiometric rectification: toward a common radiometric response among multirate multisensor images, *Remote Sensing of Environment*, Vol. 35, 11-27.
- Hervás, J., Barredo, J.I. and Lomoschitz, A., 1999. Use of Landsat TM imagery for investigation of landslide hazard from human activities in the Barranco de Tirajana area, Gran Canaria Island, *Geophysical Research Abstracts*, Vol. 1, No. 4, 836.
- Hervás, J., Barredo, J.I., Mantovani, F., Pasuto, A. and Silvano, S., 2000. Mapping recent activity in the Tessina landslide, Italy, by digital processing of aerial photographs. *Proc. European Geophysical Society XXV General Assembly*, Nice, France, 25-29 April 2000 (in press).
- Hervás, J. and Rosin, P.L., 1996. Landslide mapping by textural analysis of Daedalus ATM data. *Proc. Eleventh Thematic Conference on Applied Geologic Remote Sensing*, Las Vegas, Nevada, 27-29 February 1996. ERIM, Ann Arbor, Michigan, USA, Vol. 2, 394-402.

- Hervás, J., Rosin, P.L., Fernández-Renau, A., Gómez, J.A., and León, C., 1996. Use of airborne multispectral imagery for mapping landslides in Los Vélez district, south-eastern Spain. In: Chacón, J., Irigaray, C. and Fernández, T. (eds) *Landslides*, Balkema, Rotterdam, 353-361.
- Itten, K.I., P. Meyer, T. Kellenberger, R. Leu, S. Sandmeier, P. Bitter and K. Seidel, 1992. Correction of the impact of topography and atmosphere on Landsat-TM forest mapping of alpine regions. *Remote Sensing Series*, Vol. 18, University of Zurich-Irchel, Switzerland, 48p.
- Jensen, J., Rutchey, K., Koch, M. and Narumalani, S., 1995. Inland wetland change detection in the Everglades water conservation area 2A using a time series of normalised remotely sensed data, *Photogrammetric Engineering and Remote Sensing*, Vol. 61, 199-209.
- Leroi, E., 1996. Landslide hazard - Risk maps at different scales: Objectives, tools and developments, In: Senneset (ed) *Landslides*, Proc. 7th International Symposium on Landslides, Trondheim, Norway, 17-21 June 1996, Rotterdam: Balkema, 35-51.
- Lomoschitz, A. and Corominas, J., 1997a. La depresión de Tirajana, Gran Canaria. Una macroforma erosiva producida por grandes deslizamientos, *Cuaternario y Geomorfología*, Vol. 11, No. 3-4, 75-92.
- Lomoschitz, A. and Corominas, J., 1997b. Actividad histórica y características de los movimientos de ladera de Rosiana, Gran Canaria, *Boletín Geológico y Minero*, Vol. 108-6, 553-568.
- McCormick, N., 1997. Automated forest stand mapping by spatial analysis of satellite imagery. Proc. Int. Workshop on Application of Remote Sensing in European forest monitoring, Vienna, Austria, 14-16 October 1996. EUR 17685, Joint Research Centre, Brussels, Belgium, 411-415.
- Mitas, L., Brown, W.M. and Mitsova, H., 1997. Role of dynamic cartography in simulations of landscape processes based on multivariate fields, *Computers and Geosciences* Vol. 23, 4, 437-446.
- Pasuto, A., Silvano, S., Tecca, P.S. and Zannoni, A., 1997. Convenzione tra la Regione del Veneto e l' IRPI-CNR per lo studio della frana del Tessina in Comune di Chies d'Alpago (BL). Relazione finale della prima fase. Padua: IRPI-CNR, 135p.
- Pohl, C. and Van Genderen, J.L., 1998. Multisensor image fusion in remote sensing: concepts, methods and applications, *International Journal of Remote Sensing*, Vol. 19, 823-854.
- Popescu, M.E., 1994. A suggested method for reporting landslide causes, *Bulletin IAEG*, No. 50, 71-74.
- Richter, R., 1990. A fast atmospheric correction algorithm applied to Landsat TM images. *Int. J. Remote Sensing*, Vol. 11, No. 1, 159-166.
- Saaty, T., 1980. *The Analytical Hierarchy Process*, New York: McGraw Hill.
- Singh, A., 1989. Digital Change Detection Techniques using Remotely Sensed Data, *International Journal of Remote Sensing*, 989-1003.
- Soeters, R. and Van Westen C.J., 1996. Slope instability recognition, analysis and zonation, In: Turner, K. and Schuster, R.L. (eds) *Landslides Investigation and Mitigation*, Transportation Research Board Special Report 247, Washington DC: National Academy Press, 129-177.
- Suzen, M.L. and Toprak, V., 1998. Filtering of satellite images in geological lineament analyses: an application to a fault zone in Central Turkey. *Int. J. Remote Sensing*, Vol. 19, 6, 1101-1114.
- Swain, P.H. and S.M. Davis, 1978. *Remote Sensing: The Quantitative Approach*. McGraw-Hill, New York, 396 p.

- Van Genderen, J.L. and Pohl, C., 1994. Image fusion: Issues, techniques and applications. Intelligent Image Fusion, Proceedings EARSeL Workshop, Strasbourg, France, 11 September 1994. Enschede: ITC, 18-26.
- Van Westen C.J., 1993. Application of geographic information systems to landslide hazard zonation, ITC Publication, Vol. 15. ITC, Enschede, The Netherlands.
- Varnes, D.J., 1978. Slope movement types and processes, In: Schuster, R.L. and Krizek, R.J. (eds) Landslides Analysis and Control, Transportation Research Board Special Report 176, Washington DC: National Academy Press, 11-33.
- Voogd, H., 1983. Multicriteria Evaluation for Urban and Regional Planning, London: Pion.
- Yesou, H., Besnus, Y. and Rolet, J., 1993. Extraction of spectral information from Landsat TM data and merger with SPOT panchromatic imagery-a contribution to the study of geological structures. ISPRS Journal of Photogrammetry and Remote Sensing, 48, 23-36.

### 13. Raising public awareness on landslides in the Barranco de Tirajana, Gran Canaria, Spain.

#### Introduction

The Barranco de Tirajana (BdT) is the only short-term landslide prone area in the Canary Islands (Chapter 9). The basin has an "inverted-drop" shape, 10 Km long and 6.5 km wide, opening to the southeast through a 7 km gorge. It has a total catchment area of 64 km<sup>2</sup>. Several seasonal rivers cross the zone, the major one being the 22-km long Barranco de Tirajana. Large slope movements in the BdT have continued since at least the Pleistocene to the present. Historical movements have been focussed on the Rosiana slide, near the centre of the basin (Chapter 9) which has been reactivated four times since 1879. The last destructive movements at Rosiana occurred in 1956 and further activity can be expected in the future. Since engineering control measures are not cost-effective, risk-mitigation depends on preventative land-planning and on raising public awareness of potential landslide hazards.

#### Social structure of the Barranco de Tirajana

The economy within the BdT is very poor and relies heavily on agriculture, notably the growth of fruit, olives and almonds. Administratively, the basin is divided into two municipalities (Fig. 1): Santa Lucía, (1995 population of 38,445) and San Bartolomé de Tirajana (1991 population of 60,316). The main centres are two villages with the same names as their municipalities. The population of the BdT has risen rapidly since 1900 (Table 1), especially following the expansion of tourism in the 1970's which led to the growth of the coastal resort Maspalomas, outside the BdT but within the municipality of San Bartolomé de Tirajana. As a result, much of the BdT's original population has moved to the coast in the search of jobs, generating a big drop in numbers during the week, but creating a "weekend peak" in occupation when people return to their family houses (*e.g.*, the 1,300 population of Santa Lucía increases 3-4 times at weekends).

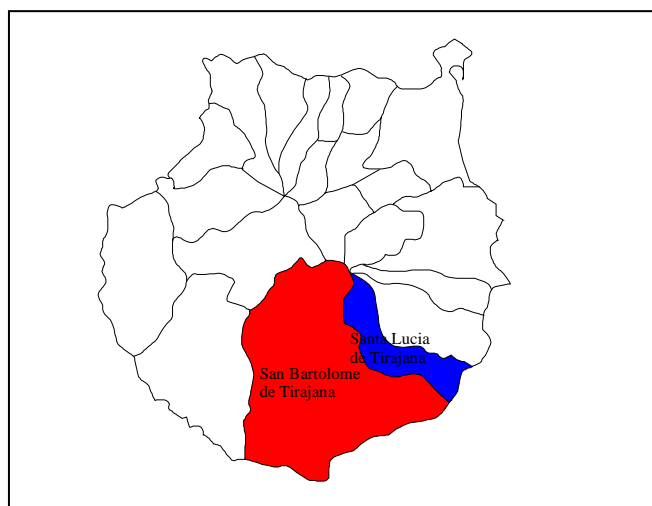


**Figure 1.** The municipalities of San Bartolomé and Santa Lucía de Tirajana.

The BdT population is spread across the basin, with local concentrations around a handful of villages. Due to the abrupt topography and the steepness of the walls that surround the basin, most of those villages are at elevations between between 450 and 1000 m asl.

**Table 1.** Population growth in the municipalities of San Bartolomé de Tirajana and Santa Lucía.

<i>Year</i>	<i>San Bartolomé de Tirajana</i>	<i>Santa Lucía</i>
<b>1900</b>	4633	2713
<b>1910</b>	4611	3092
<b>1920</b>	5750	2783
<b>1930</b>	6370	3521
<b>1940</b>	8960	6321
<b>1950</b>	8809	7020
<b>1960</b>	13384	11081
<b>1970</b>	19846	18589
<b>1981</b>	52836	26498
<b>1991</b>	60316	32732

By virtue of its dispersed nature, the BdT population is especially vulnerable to interruptions in communications, from the blocking of roads to the failure of telephone and power lines. The categories of road cross the BdT:

- Primary routes with one line of traffic in each direction, and minimum and average widths of 5 and 6 m. The daily traffic flux ranges from 2,000 to 10,000 vehicles at a maximum authorised velocity of 90 km per hour.
- Secondary routes with minimum and mean widths of 4.5 and 5 m, daily traffic fluxes of less than 2,000 vehicles and speed limits of 60 km per hour or less.
- Unpaved tracks.

Most routes are vulnerable to rockfalls, while the primary route that crosses the BdT from the coast passes through Rosiana and was interrupted by the 1956 movement. A key implication is that access by motor vehicle is likely to be disrupted during any future reactivation of the slide.

### **Reducing the vulnerability of the population**

Although current landslide studies are focussing on possible reactivations of the Rosiana slide (Chapter 9), slow movements are continuing throughout the BdT. A key example is the village of Santa Lucia, in which many buildings are progressively cracking due to slope creep. Although the hazard is not catastrophic, it may in the long-term result in considerable expense for structural repairs. Similarly rockfalls, which are another frequent but low-intensity hazard, can provoke considerable long-term expense when they block roads or disrupt power and telephone lines.

At the other extreme, faster, short-term reactivations of the Rosiana slide have occurred intermittently since 1879, typically in response to extended periods of intense rainfall. Although more damaging, the decadal intervals between reactivations have produced a low level of awareness of potential future hazards. Indeed, local authority records indicate that the 1956 event was considered to be a one-off occurrence and no formal contingency plans are available in case of future activity. Of special note is the lack of understanding of secondary effects due to landslide reactivation. For example, one of the two petrol stations serving the San Bartolomé – Santa Lucia district is located along the edge of the Rosiana slide. Although movement of the slide may not threaten the station directly, any leaks from storage

tanks induced by rapid displacement pose a significant hazard to houses in the immediate vicinity. Similar implications follow from the possible disruption of stored gas supplies, currently distributed across the BdT in domestic canisters.

### **Hazard and vulnerability at Rosiana**

Formed by reactivation of the toe of the much larger Pajonales landslide, the Rosiana landslide is the most important historical large landslide in Gran Canaria. Persistently active since 1879 (Table 2), its most dramatic movement to date occurred in February 1956, following a period of intense rainfall (272 mm in 24 hours). Within days, some 3 million cubic metres of material destroyed an arterial road and bridge, severely damaged buildings across an area of 0.3 km<sup>2</sup> and provoked the evacuation of 250 people. This destruction resulted from a net downslope motion of only 7 metres. It is a translational slide with a surface-parallel failure plane at a depth between 12 and 25 m. Due to erosion along a ravine, especially during periods of heavy rainfall, the toe of the slide is unbuttressed and so favours continued displacement.

**Table 2.** History of the Rosiana landslide

<i>Date</i>	<i>Phenomenon</i>
1879, December	Rosiana slide activated after large storms. Bed of ravine moved at toe of slide.
1896, May	Extension of road Las Palmas-San Bartolomé requires design of bridge across ravine at toe of Rosiana slide.
1921	Mass movement after heavy rainfall breaks one keystone of bridge, later partially repaired.
1923	Mass movement after heavy rainfall disables bridge. A replacement girder bridge with reinforced concrete was built 200 m upstream.
1956	Mass movement (3 x 10 <sup>6</sup> m <sup>3</sup> ) destroys road and old bridge, 250 people evacuated.
1956-Present	New buildings constructed on mobile zone, even though toe continues to creep forward.

Although the toe of the slide has been slowly advancing since 1956, it has become increasingly built upon and today supports over 200 dispersed buildings. Based on periodic measurements of the position of the surviving pillars of the old bridge destroyed in 1956, it appears that the slide has extended by another c. 0.5 m (*i.e.*, a mean rate exceeding 1 cm per year). The key point is that the slide remains as active in a creeping mode as it was during the decades before the 1956 event. Thus, another rapid movement remains a strong possibility, especially after periods of heavy rainfall.

The fast rates of advance (centimetres per hour) were accompanied by ground cracking (producing cracks metres long, 0.5-1 m wide and metres deep) as well as by the collapse of buildings. Rotational surface movement also induced uplift, disrupting the primary road south from Rosiana. At the peak of activity, the bridge crossing the ravine just north of the toe of the slide was submerged by the swollen river.

Despite the destruction and loss of primary escape routes (the bridge flooded to the north and the road interrupted to the south), the rates of movement were sufficiently slow to allow spontaneous evacuation of the zone without injury. A similar evacuation can be expected during future reactivation. However, preventative measures today could substantially reduce the cost of future movements, from the reinforcement of vulnerable buildings to construction of emergency vehicle routes should the primary road again be disrupted. The fact that such measures are not already in place reflects the low local awareness of landslide hazard. For example, only eye-witnesses of the 1956 event – and some immediate relatives – recognised

that the Rosiana zone remains an active landslide. Similarly, in Santa Lucia, built on another ancient landslide 1 km southeast from Rosiana, the common cracking in buildings is virtually always attributed to the poor quality of construction material: rarely has any connection been made to creep movements of the hillside.

### **The awareness of vulnerable populations to landslides**

Preliminary surveys of the BdT revealed that many of the BdT population (typically those too young to remember the 1956 Rosiana reactivation) were either unaware that landslides pose a hazard within the basin, or that events such as at Rosiana were one-off occurrences without a possibility of recurrence. Given the low level of awareness, a detailed questionnaire (Appendix 1) was prepared and distributed throughout the BdT in order to assist plans for raising awareness of landslide hazard and for designing by local consensus appropriate preventative measures.

The questionnaire was designed to obtain databases on:

1. Public knowledge of what landslides are and where they occur.
2. Public impression on possibilities of future events.
3. Impression of landslide threat to interviewees.
4. Expected reaction in case of land movements on their property.

The results (Table 3) compare the responses among the population of Rosiana (sample of 29 homes) and of the rest of the BdT (sample of 69 homes). Overall, they show a modest understanding of landslides but a poor profile in the responses expected during landslide reactivation. Although awareness of landslide hazard was greater in the the Rosiana zone, this was also the zone with lower level of appropriate response.

While many people claimed to know what a landslide is, they failed in relating different types (just 36% BdT and 17% Rosiana respondents viewed both rockfalls and large slope movements as landslides). Almost all respondents knew that the BdT has experienced landslides and most viewed that future events were possible. In Rosiana, most assumed that future events would occur again at Rosiana, while the BdT group related activity to steep slopes in general. Most respondents also acknowledged that they they could be affected by future landslides, although some 50% in the BdT and 67% in Rosiana expect movement to be slow.

There is a general awareness that rainfall is an important factor triggering landslides. Fewer numbers associated instability with other causes, such as earthquakes and deforestation. Some 14% of BdT respondents conjectured wind to be a potential landslide trigger. In the case of future movement such as occurred at Rosiana in 1956, between 25% (BdT) and 49% (Rosiana) relied on evacuating their family by car despite the high possibility that roads might be disrupted. Half or more would seek to help disadvantaged members of the community, while only about one half thought to turn off power supplies before leaving. Hardly any respondent elected to seek advice by the radio (or television if functioning), a clear indication in lack of dependency on any official response.

**Table 3.** Results of the BdT landslide questionnaire spread in Tirajana.

Question	Answers	BdT (%)	Rosiana (%)
1 Do you know what a landslide is?	No	6	0
	Rockfall	12	21
	Big movements of land	29	46
	Small movements of land	23	11
	All movements	36	17
2 Do you know if there has been any movement in the Barranco in the past?	No	19	10
	Yes	81	90
3 Do you think it could happen in the future?	No	10	21
	Yes	87	76
	Dk/Da	3	3
4 Where do you think could happen?	Rosiana	13	45
	Slopes	26	10
	Everywhere	16	10
	Ravines	22	7
	Other		
5 Do you think they will be dangerous	No	7	24
	Yes	88	73
	Dk/Da	3	
6 Which velocity do you think they could have?	Fast (not able to escape)	48	35
	Slow (could escape)	54	62
	Dk/Da	4	7
7 What size do you think a future landslide could have?	<car	16	0
	<House	30	21
	House	30	3
	School	6	3
	Football ground	20	17
	>Football ground	19	59
8 Do you know which of those processes can trigger landslides?	No	4	0
	Rain	91	93
	Earthquakes	23	17
	Wind	14	0
	Deforestation	6	0
9 Would you Know what to do during a Landslide?	No	49	24
	Yes	40	52
	Dk/Da	6	24

**Table 3 continued.**

<b>10</b> If the land will start moving slowly you will:	See what neighbours does	7	7
	Take everything in my car and go	25	39
	Listen tv/radio for news	12	4
	Go out of the house	20	32
	Phone relatives/friends to see what to do	7	0
	Help elders/handicap/ill	72	50
	Walk to council/police to seek information	32	32
	Go to border of ravine to see if flooding	4	0
	Walk in comfortable clothes to safe place	15	4
	Turn off gas, power and leave	45	58
	Wait in door of house	1	0

In most of the questions, answers have been similar: while very few people will go nearby the ravine to see the level of the water, will act depending on the neighbours or will try to phone, also very few people will listen radio or TV in search of news or will change to comfortable clothes before leaving. In both of the cases the most common action was helping people that will need and switch off power, water and gas. But many people (25% in the Barranco and 39% in Rosiana) claim they will use the car. Just 32% will go to the Council or Police in search of advice.

### **Public information programme**

Results from the first questionnaire were used to design a public information pamphlet has been designed and will be distributed through the local authorities. The pamphlet has the format of a comic and will be used to inform the population on the nature of landslides, when and where they occur in the BdT, how to use local signs to warn of possible reactivation, and what to do in case of future activity. The pamphlet (see accompanying CD ROM) will be available on the BdT's municipal websites. A second questionnaire (Appendix 2) will later be distributed to evaluate the impact of the pamphlet on raising hazard awareness and in determining appropriate modifications:

## Appendix 1. First questionnaire

---

### CUESTIONARIO 1- Poblaciones del Barranco de Tirajana

¿Sabe qué es un deslizamiento de ladera?

- No  Si:
- La caída de rocas de las laderas
  - Grandes movimientos de tierras
  - Pequeños movimientos de tierras
  - Todos los anteriores
  - Otros

¿Sabe si existen /han existido movimientos en el barranco? No  Si

¿Cree que podría pasar en el futuro? No  Si

¿Dónde cree que podrían ocurrir?

Si existieran, ¿Cree que serían peligrosos? No  Si

- ¿Cómo cree que serían? Rápidos (No podría escapar a pie)
- Lentos (Podría escapar andando)
- Grandes
- Del tamaño de una casa
  - Del tamaño de un colegio
  - Del tamaño de un campo de fútbol
  - Mayor que un campo de fútbol
- Pequeños: Menor que una casa
- Menor que un coche

¿Sabe cuándo se producen deslizamientos?

- No  Si:
- Cuando llueve mucho
  - Cuando hay terremotos
  - Por el viento

Otros

¿Sabría qué hacer si se encontrase en medio de un deslizamiento?

No  Si

Si el terreno donde vive comenzara a moverse lentamente usted

1. Saldría a ver qué hacen los vecinos
2. Cogería en el coche las cosas que pudiera y mi familia y me iría
3. Pondría la television o la radio a ver qué dicen del deslizamiento
4. Recogería todo lo que pudiese y saldría con eso de mi casa
5. Llamaría a un amigo o amiga a ver qué piensa hacer
6. Ayudaría a los vecinos enfermos o con dificultades a salir de su casa
7. Iría andando al Ayuntamiento o al puesto de Policía mas cercano para saber qué hacer
8. Si lloviese, iría al borde del barranco a ver si corre agua
9. Antes de salir de mi casa me pondría ropa cómoda, recogería mis cosas de valor y algo de comida
10. Cortaría el gas, el agua y la luz de mi casa
11. Esperaría en la puerta de casa a ver que ocurre
12. Otros

Appendix 2. Second questionnaire

---

CUESTIONARIO 2 Valoración folleto informativo

¿Qué le ha parecido el folleto en general?

- |                           |         |           |        |
|---------------------------|---------|-----------|--------|
| • Entretenido             | - Mucho | - Regular | -.Poco |
| • Fácil de entender       | - Mucho | -.Regular | -.Poco |
| • Cantidad de información | - Mucha | -.Regular | -.Poca |
| • Longitud del folleto    | - Largo | -.Bien    | -Corto |
| • Utilidad                | -.Mucha | -.Regular | -.Poca |

Valore del 1 al 10 el folleto

¿Ha aprendido algo nuevo al leerlo?

- |      |       |         |            |        |
|------|-------|---------|------------|--------|
| - No | - Si: | - Mucho | - Bastante | - Algo |
|------|-------|---------|------------|--------|

La información le ha parecido:

1. Demasiado complicada
2. Bien
3. Demasiado sencilla

¿Le ha gustado que se haga como un tebeo? - Si - Regular - No

¿Le gustaría tener una copia en casa? - Si - No

¿Cree que lo que dice el folleto puede serle útil a usted y a los demás?  
- Si - No

Si le hubiera llegado a casa por correo

1. Lo leería y lo guardaría - Si - No
2. Lo leería y lo tiraré despues - Si - No
3. Lo guardaré para leerlo algun otro día - Si - No
4. Lo guardaré para mis hijos/nietos sin leerlo - Si - No
5. Lo leeré y lo guardaré para mis hijos/nietos - Si - No
6. Lo tiraré sin leer - Si (¿Por que?) - No

¿Qué cree que le falta o cómo cree que mejoraría?

Otros comentarios sobre el folleto

---

## 14. The development of multi-media training material for landslide hazard zonation: applications to Project RUNOUT

### Introduction

One of the aims of the educational approach within ITC is to achieve more training possibilities for participants in their own countries, making use of distance learning methods. For this purpose training packages are being developed. An example of such a training package is the training package on the use of Geographic Information Systems for Slope Instability Zonation (GISSIZ, Van Westen et al, 1993). The first version of this package was released in 1993, as a contribution to the UNESCO-IUGS GARS project (Geologic Application of Remote Sensing). Several hundreds of copies of this package have been distributed worldwide, and workshops were given with the package in Colombia, Costa Rica, Argentina, India, Nepal and the Netherlands. This package consisted of a theory book, an exercise book and a set of 10 diskettes, containing a full data set and an MS-DOS based GIS package. The opening screen is shown in figure 1.

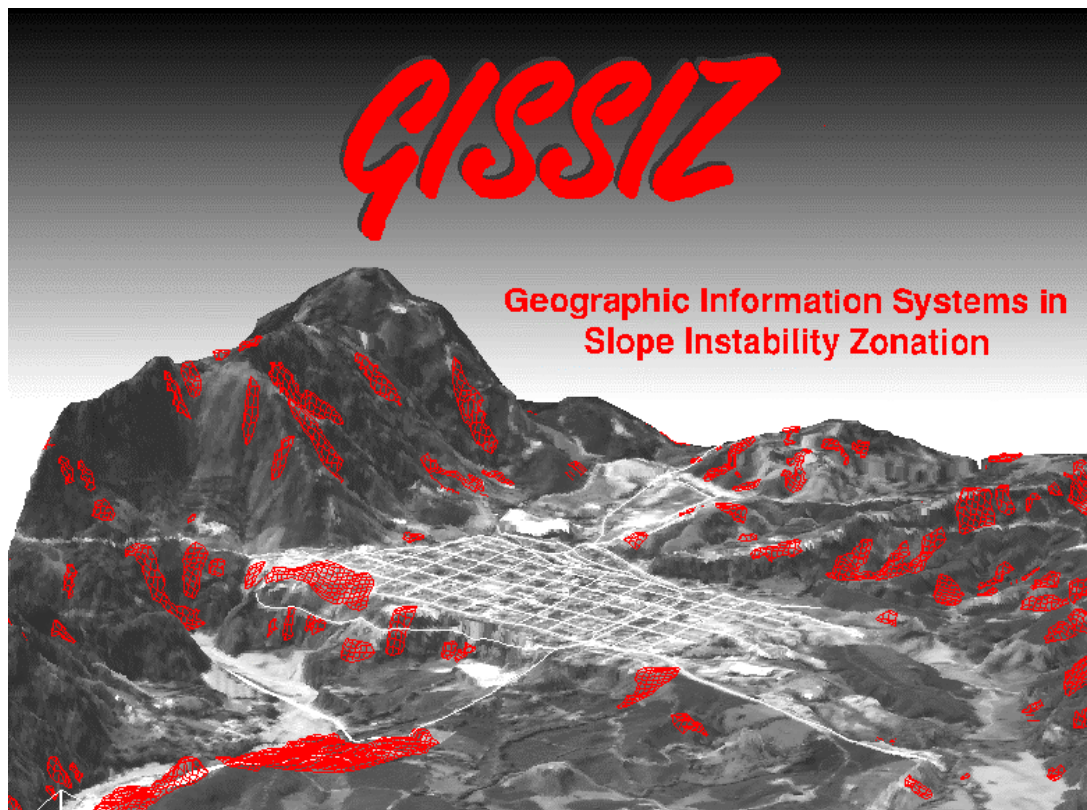


**Figure 1.** Opening screen of the MS-DOS based training package GISSIZ

For the RUNOUT project it was decided to adapt the GISSIZ package and convert it into a multi-media package, with all information on one CD-ROM, including theory, datasets and GIS software. The results of the RUNOUT project, both with respect to the test areas, as the developed methodologies would also be included in this package.

Development of the package required more than 12 man months, of which 3 were sponsored by the RUNOUT project, and started in the middle of 1999, when the first results of the project became available. Due to the late submission of material by the

various project partners, the package could not be completed before the end of the project period (December 1999). Full completion is foreseen before the second half of 2000. The package will be distributed free of charge on a CD-ROM, and will also be made available via the Internet. The opening screen is shown in figure 2.

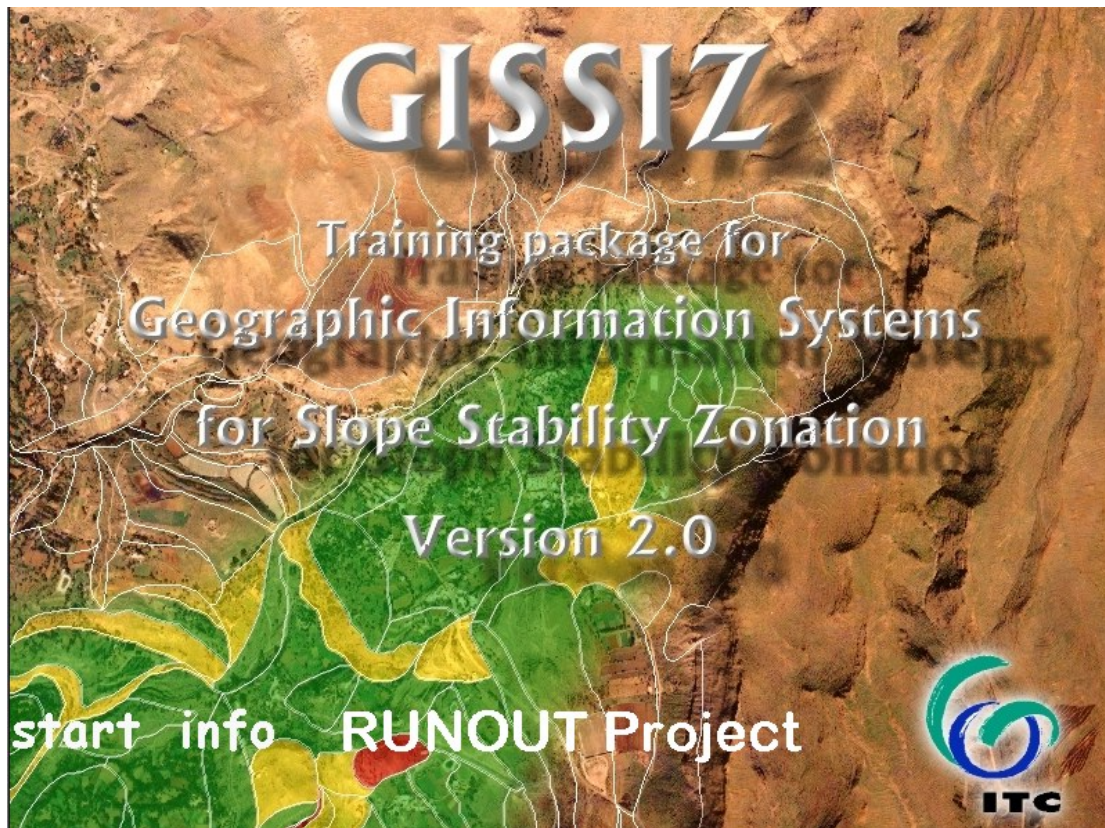


**Figure 2.** Opening screen of the multi-media version of the training package GISSIZ, for the RUNOUT project.

#### **Homesite 4.0**

The multimedia tutorial of GISSIZ is made with the program HomeSite version 4.0. HomeSite is a program, which help professional Webmasters and Web developers to build a homepage. This was the main reason to make the multimedia tutorial GISSIZ in HomeSite, because GISSIZ should also be available on the homepage of AGS.

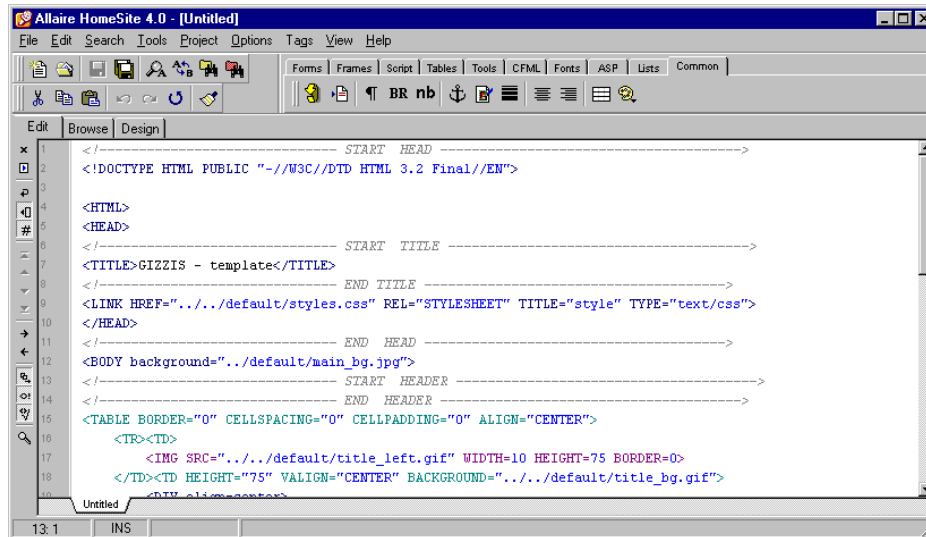


**Figure 3.-** Main window of Homesite

The program is easy to learn, especially for those that have already learned program languages (like Java, C). It is very user friendly. In other program language you must know all the scripts, in HomeSite several functions and script are hidden behind buttons. For example, when you want to insert a table into the screen you can click on the tab named Tables and several functions are shown, like adding a row, adding a column etc. This saves a lot of time. The main window of Homesite is shown in Fig. 3.

Another great difference between HomeSite and other program languages is that the running time is not so long. If you want to see the result of the script you just click on the Browse tab and the result is shown. A great advantage of HomeSite is that it allows JavaScript. When you are on the Internet and you see something you want to use, you can copy it from the source and paste it, with several changes, in HomeSite.

### **Structure of GISSIZ**

The structure of the tutorial is shown in Figure 4. This window shows the titles of the 5 chapters of GISSIZ. By clicking on the chapter-titles a submenu with subtitles appears. Clicking on the subtitles starts the page-slide of that subtitle. You can walk through this page-slide with the navigation-arrows at the bottom of Figure 4, which are not shown in the main menu. When you have finished a page-slide you return to the main menu with the up-arrow.

The window is divided into three frames. The top frame is called "master-frame". This is the frame where an arbitrary page of the tutorial can be loaded. This arbitrary page can also exist of different frames. The navigation arrows are in the frame called "slave-frame", on the bottom left of the window. With these arrows you can walk through page-slides, or you can go back to the main window. To see where you are in the tutorial there is at the bottom right of the window the third frame called "Page\_No\_frame". This frame shows the chapter title and the page-number of the in the "master-frame" loaded page. Figure 5 shows an example of an arbitrary page in GISSIZ. In the "master-frame" all the information of the arbitrary page is loaded. On the bottom left you see the three arrows of the "slave-frame". On the bottom right you see the "Page\_No\_frame". The position of the arbitrary page in the tutorial, namely page 7 of the 10 of the page-slide of the chapter Classification of landslides is shown in Figure 5.

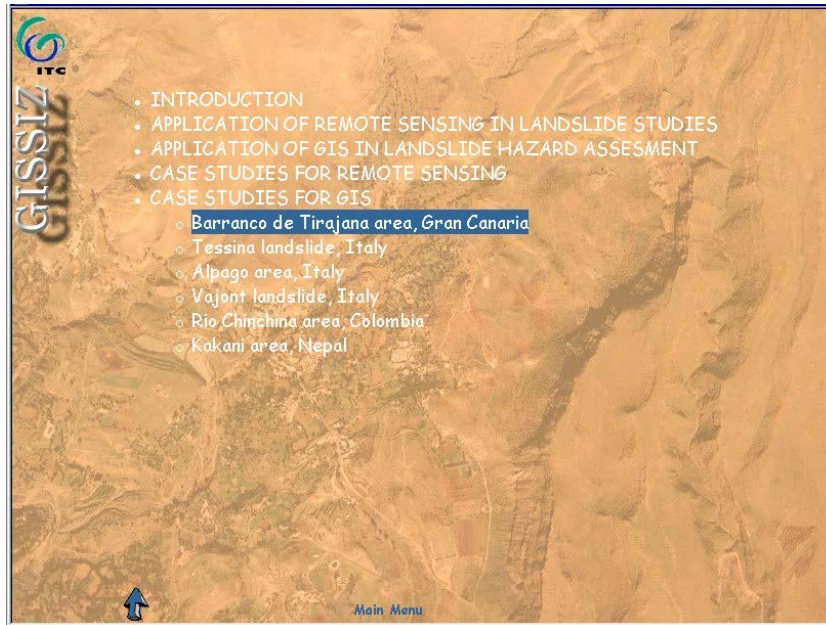


**Figure 4.** Main menu of GISSIZ, with a series of drop down menus. The menu is showing the contents of the case studies for GIS in detail.

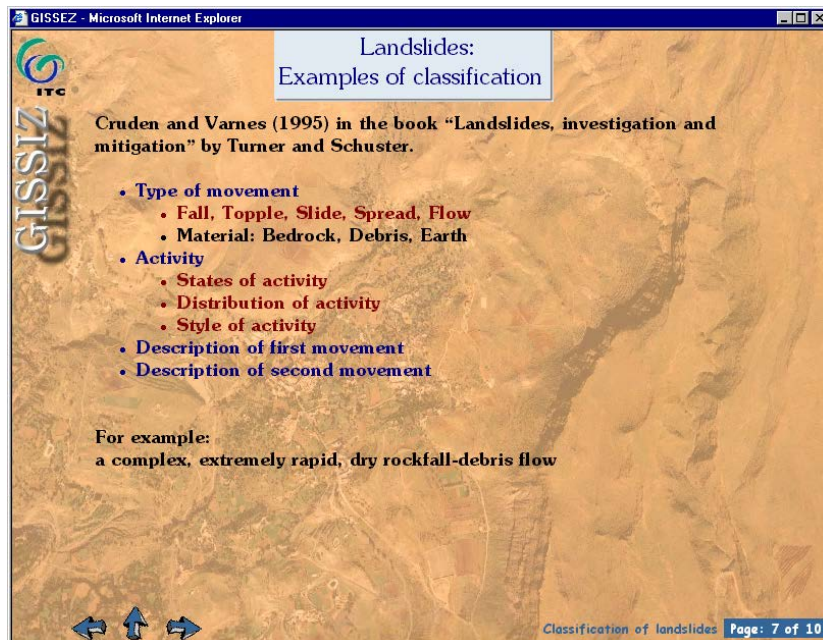


**Figure 5.** Example of an arbitrary page of GISSIZ

## GISSIZ contents

The tutorial consists of 5 main chapters:

- Introduction
- 2. Application of Remote Sensing in Landslide Studies
- 3. Application of GIS in Landslide Hazard Assessment
- 4. Case studies for remote sensing
- 5. Case studies for GIS

Each of the chapters is subdivided in many subheadings, but the user can always navigate easily through the tutorial. The first three chapters are theoretical in nature, with many examples. The last two chapters demonstrate case studies. The first chapter is subdivided in the following items:

- Natural Hazards: Definitions and Statistics
- Principles of Landslide Hazard Zonation
- Classification of Landslides
- Landslide examples

Figure 6 gives an example of the section on definitions and statistics, and Figure 7 from landslide examples.

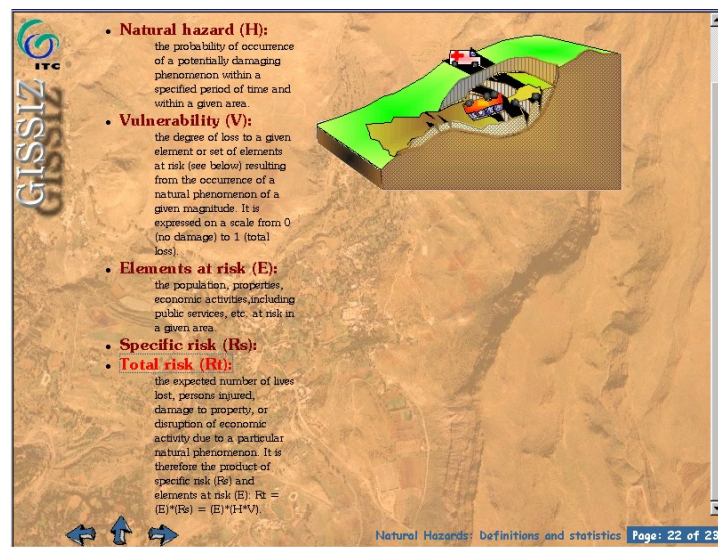


**Figure 6.** Example of a screen explaining the definitions of hazard, vulnerability and risk

These chapters are mostly filled with text and pictures. The first chapter exists of the introduction to GISSIZ. In this the information of landslides and landslide-types are displayed. The last subtitle of the first chapter shows examples of landslides. This is shown in Figure 7. The master-frame of this page is divided into three frames. One frame on the left is the overview of all sorts of landslides. At the top of the page a frame with thumbnails of an arbitrary type of landslides, here *subsidence*, is shown with, at the middle-right a frame which shows the real picture of the thumbnails.

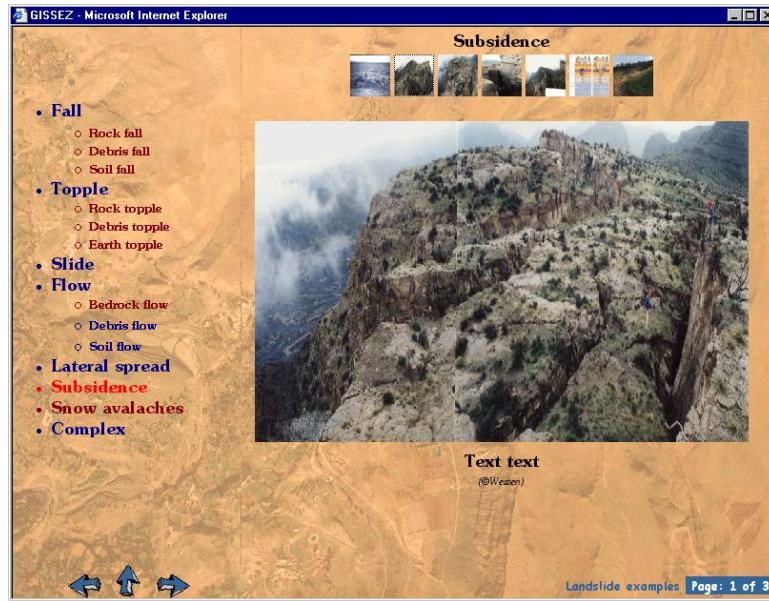


Figure 7. Landslide example

The second chapter shows the application of Remote Sensing in landslide studies. In this the interpretation of landslides from aerial photos and the characteristics of landslides that can be seen from aerial photos or satellite images is explained. Figure 8 shows an arbitrary page of the second chapter of the tutorial.

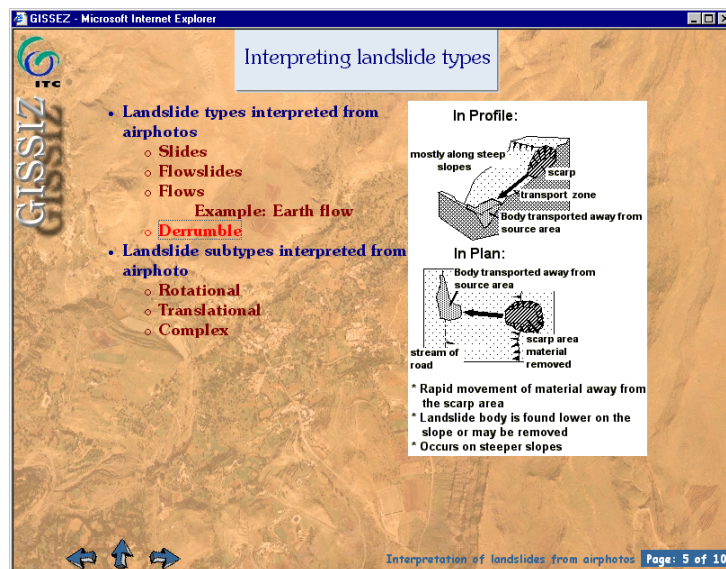


Figure 8. An arbitrary page of the second chapter

The third chapter of the tutorial shows the application of GIS in landslide hazard assessment. This chapter gives information on the phases of data collection, data entry, data management, data analysis and data output. An arbitrary page of this chapter is shown in Figure 9.

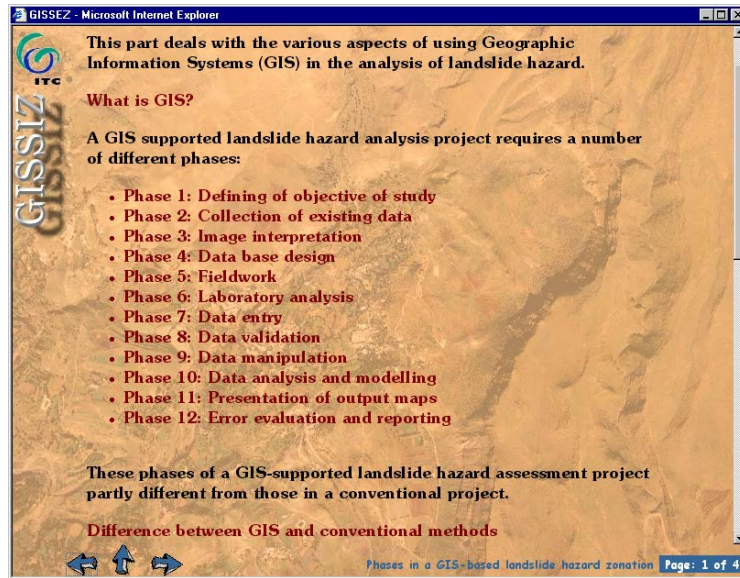


Figure 9. The first page of the chapter on GIS.

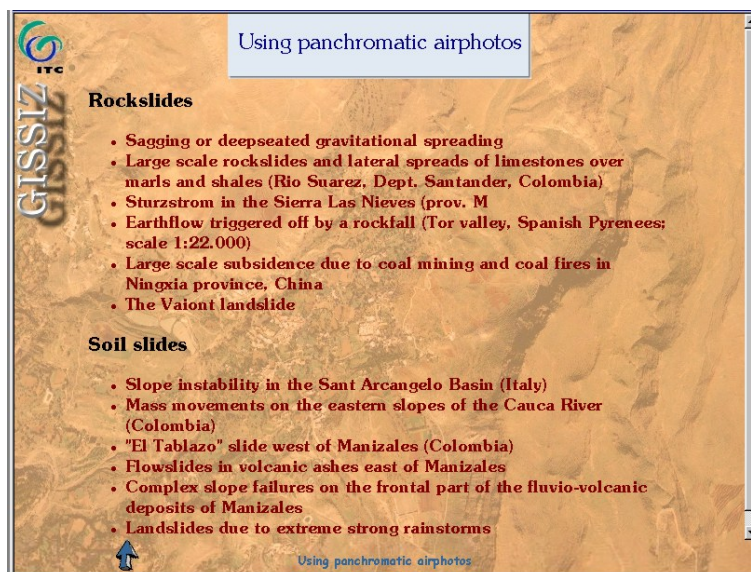
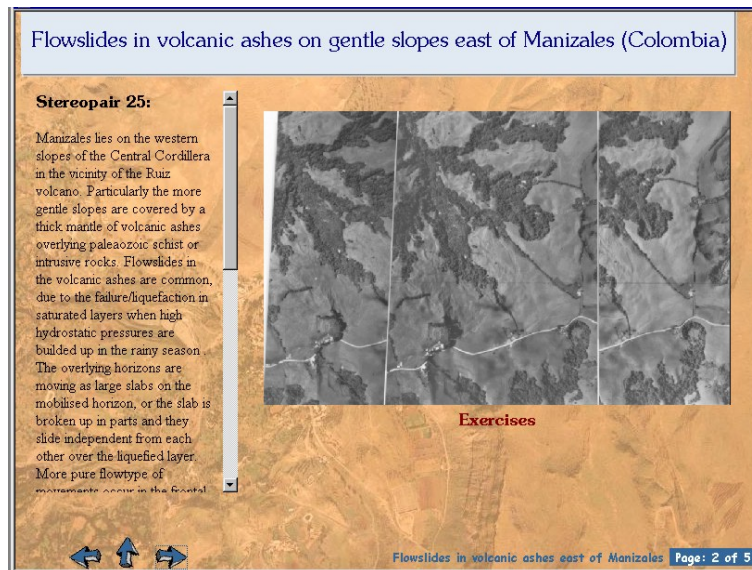


Figure 10. Screen from which a selection can be made of many different three dimensional views.

The fourth chapter, named case studies for Remote Sensing, exists of stereopairs. We used a method to convert the stereopairs into 3D red-green photos (anaglyphs), that can be viewed with inexpensive red-green glasses. So there are two possibilities to look at the stereopairs. The two possibilities are shown in Figure 11. An explanation and exercises are available for each stereopair



**Figure 11.** Example of a stereopair with a clear landslide example.

Chapter 5, named case studies for GIS, exists of several case studies for GIS and some also for Remote Sensing. In this chapter the results from the various study areas of the Runout project will be demonstrated:

- Barranco de Tirajana (Gran Canaria, Spain)
- Tessina landslide (Italy)
- Vaiont landslide (Italy)
- Stambach (Bad Goisern, Austria)
- Otztal (Köfels, Austria)

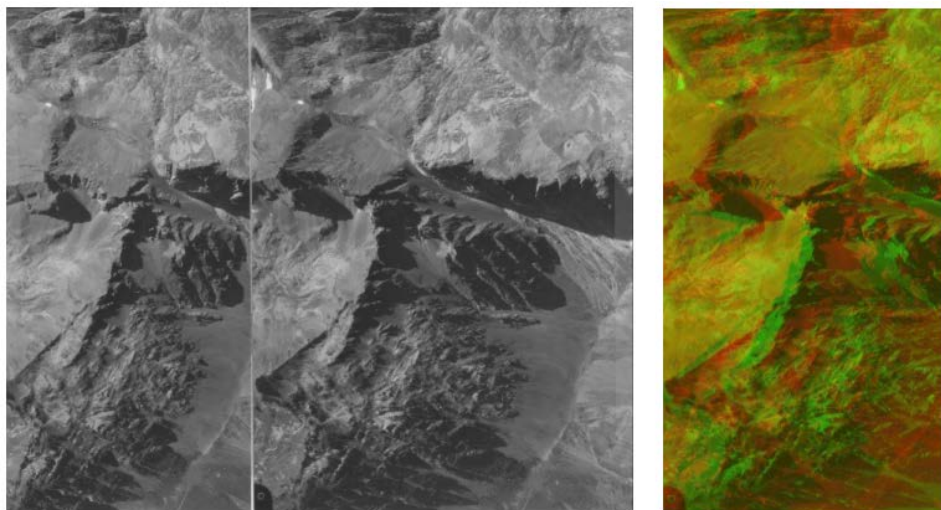


**Figure 12.** Two possibilities to look at the stereopairs. Normal black and white stereopair (left) and anaglyph image (right).

From the first moment we worked with several templates, so every page has the same structure. This is easier when you want to change something throughout the whole tutorial. You don't have to make changes in all individual pages. There is a function in HomeSite, named Extended Replace, which searches through selected pages and makes the required changes.

An advantage of HomeSite is that the layout of the whole tutorial can be changed in one file, named default. Here you can change for example the background-picture, the navigation arrows etc. Also all the fonts of the texts can be changed. This can be done in the file named styles.css, where all the fonts are defined. With Homesite - Style Edit you can open this file. Figure 13 shows the program Style Edit and the file styles.css is loaded. Here all fonts used in GISSIZ are shown.

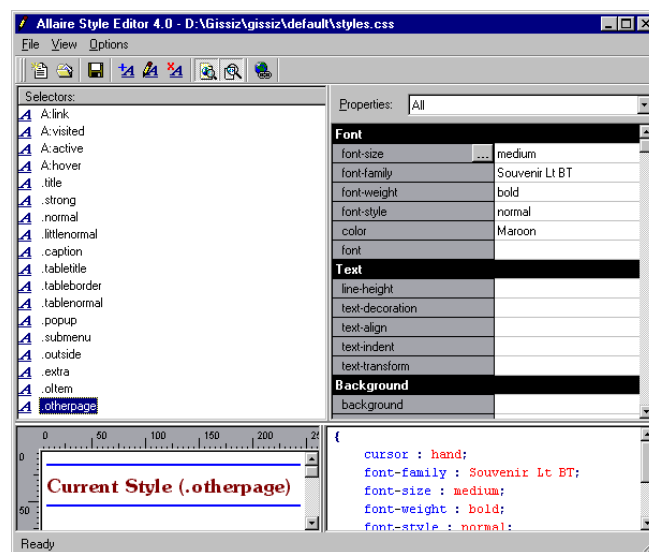


Figure 13. Styles.css in Style Edit

Another advantage of HomeSite for this tutorial is that GISSIZ has a possibility to check all the links to other pages or to pictures. Hence it is not necessary to look through the whole tutorial to find errors in these links.

The key difficulty in making the tutorial was the writing of the JavaScript for the navigation and other features, for example for the pulldown-menus. The navigation-arrows do not have to be in every page, so there was a script needed that removed or placed an arrow on the screen.

Another 4 to 6 months is expected to be required to ensure that the tutorial is completely bug-free. Preliminary versions will be made available for testing before then.

## References

- Alexander, D. 1993. Natural disasters. UCL Press Ltd., University College London. 632 pp.
- CEOS, 1998. CEOS Disaster Management Support Project, Progress Report. Committee on Earth Observation Satellites, NOAA report, 183 pp.
- International Space University, 1993. Global Emergency Observation and Warning. International Space University, Design Project Report. Huntsville, Alabama, USA. 234 pp.
- Lee, B. and Davis, I. (ed), 1998. Forecasts and warnings: programme overview. Flagship Programme sponsored by the United Kingdom National Coordination Committee for the International Decade for Natural Disaster Reduction. Thomas Telford Publishing, London, 250 pp.
- Munich Reinsurance Company, 1998. World Map of Natural Hazards. Munich, Germany, 55 pp.
- OAS 1990. Disaster , Planning and Development: Managing Natural hazards to reduce Loss. Department of Regional Development and Environment. Organization of American States. Washington, USA. 80 pp.
- UNDRO 1991. Mitigating Natural Disasters. Phenomena, Effects and Options. United Nations Disaster Relief Co-ordinator, United Nations, New York. 164 pp
- Van Westen, C.J., Van Duren, I, Kruse, H.M.G. and Terlien, M.T.J. (1993). GISSIZ: training package for Geographic Information Systems in Slope Instability Zonation. ITC-Publication Number 15, ITC, Enschede, The Netherlands. Volume 1: Theory, 245 pp. Volume 2: Exercises, 359 pp. 10 diskettes.
- Van Westen, C.J. (Ed) (1997). The ILWIS 2.1 for Windows Applications Guide. International Institute for Aerospace Survey and Earth Sciences (ITC). 352 pp.